UNIVERSITY OF SOUTHAMPTON

FACULTY OF ENGINEERING AND THE ENVIRONMENT

Water and Environmental Engineering Group

An investigation into gas transfer from bubbles into water

by

William James Nock

Thesis for the degree of Doctor of Philosophy

June 2015

UNIVERSITY OF SOUTHAMPTON

ABSTRACT

FACULTY OF ENGINEERING AND THE ENVIRONMENT
Water and Environmental Engineering Group

Doctor of Philosophy

AN INVESTIGATION INTO GAS TRANSFER FROM BUBBLES INTO WATER

by William James Nock

The current design of mass transfer systems for gas bubbles absorbing into a liquid is mainly restricted to the use of empirical relations which involve a high level of uncertainty. This is due to a lack of understanding of the interactions of gas bubbles and the liquid phase, and of how this affects the mass transfer. This work set out to enhance our understanding of the mass transfer of CO_2 from concentrated sources such as flue gases into the aqueous phase, for use in applications such as micro-algal biomass cultivation systems.

Bubble characteristics were observed using high speed imaging for single bubbles and optical fibre sensors for bubble swarms. These techniques were combined with gas chromatographic analysis of input and output gas samples to obtain a mass balance and measurements of the mass transfer. The mass transfer rate in bubble swarms was observed to be greater than that of single bubbles. For larger bubble sizes, this is partly due to the increased bubble rise velocity in bubble swarms. This was observed to increase, in part, due to the reduced drag a bubble experiences when it follows in the wake of a preceding bubble. Smaller bubbles within bubble swarms did not experience the same inhibition of mass transfer as was evident for single bubbles. This inhibition of the gas-liquid interface of single bubbles is due to the accumulation of surfactants which attach to the bubble surface, transforming the properties of the gas-liquid interface and reducing the mass transfer rate.

The reduced mass transfer in single bubbles compared to bubble swarms was more apparent at lower input concentrations of CO_2. This suggested a possible reduction in the internal circulation within the bubble, due to surfactant accumulation which reduces the gas-side resistance to mass transfer and is more apparent at a dilute gas concentration. Finally the experimental results from this work were compared with a simple finite difference model which analysed the mass balance of a rising bubble. The mass transfer coefficient of single bubbles with a mobile gas-liquid interface could be approximated by the penetration theory of Higbie (1935), while with sufficient surfactant accumulation to transform the bubble surface to an immobile gas-liquid interface the

rigid particle theory by Frössling (1938) provided a good approximation. In bubble swarms, however, the theory for a mobile gas-liquid interface based on Higbie (1935) provided a reasonable approximation throughout the range of bubble sizes studied in this work.

Contents

List of Figures

List of Tables

Declaration of Authorship

I, William James Nock , declare that the thesis entitled *An investigation into gas transfer from bubbles into water* and the work presented in the thesis are both my own, and have been generated by me as the result of my own original research. I confirm that:

- this work was done wholly or mainly while in candidature for a research degree at this University;
- where any part of this thesis has previously been submitted for a degree or any other qualification at this University or any other institution, this has been clearly stated;
- where I have consulted the published work of others, this is always clearly attributed;
- where I have quoted from the work of others, the source is always given. With the exception of such quotations, this thesis is entirely my own work;
- I have acknowledged all main sources of help;
- where the thesis is based on work done by myself jointly with others, I have made clear exactly what was done by others and what I have contributed myself;
- none of this work has been published before submission

Signed:.....

Date:.....

Acknowledgements

I owe a great deal to my supervisors Professor Charles Banks and Dr Sonia Heaven, who have gone above and beyond their call of duty over the last four and a half years. They have encouraged, challenged and supported me throughout, and provided opportunities which have helped me to reach my potential.

This work was also initiated with the support of Dr Mark Walker, who I'm very thankful for providing friendly guidance and encouragement. The approachability and advice from the technicians has been invaluable in helping to overcome many of the problems encountered in the lab, I would like to thank Ms Pilar Pascual-Hidalgo, Mr Karl Scammell and Dr Dominic Mann for all of their help. It has also been a great experience to be part of the community of the bioenergy and organic resources research group, who have a real team spirit and togetherness. I would like to thank all members for their friendliness and support.

This work was funded by the EPSRC, for which I am very grateful. The EPSRC Engineering Instrument Pool also very generously provided the high speed video camera, which is a vital piece of equipment used in this work. I would also like to thank the EC FP7 ECOFUEL project, and all members who hosted my visit to the Guangzhou Institute of Energy Conversion, including Professor Wang ZhongMing and Ms Guo Ying; I was made to feel very welcome and will never forget my time there.

I have to thank all of my friends and family for their support and understanding throughout the last few years. My parents and brother, as always, have been a 'rock' and have always been there for me.

Nomenclature

a_b	Surface area of bubble	m^2
Bo	Bond number	
C^*	Equilibrium liquid concentration	mol fraction
C_0	Bulk liquid concentration	mol fraction
C_D	Drag coefficient	
D_C	Column diameter	m
D_L	Liquid diffusivity	$m^2\ s^{-1}$
d_0	Initial bubble diameter	m
d_A	Major bubble diameter	m
d_B	Minor bubble diameter	m
d_C	Chord length	m
d_e	Equivalent bubble diameter	m
d_{or}	Orifice diameter	m
d_{vs}	Mean surface-volume bubble diameter	m
E	Ellipse aspect ratio	
Eo	Eötvös number	
e	Ellipse eccentricity	
f	Lens focal length	mm
f_E	Lens effective focal length	mm
Ga	Galilei number	
g	gravitational acceleration	$m\ s^{-2}$
H	Henry's coefficient	Pa or dimensionless
K_G	Overall gas side mass transfer coefficient	ms^{-1}
K_L	Overall liquid side mass transfer coefficient	ms^{-1}
k_G	Local gas side mass transfer coefficient	ms^{-1}
k_L	Local liquid side mass transfer coefficient	ms^{-1}
$k_L\alpha$	Volumetric liquid side mass transfer coefficient	ms^{-1}
Mo	Morton number	
N	Number of bubbles per unit volume	m^{-3}
N_A	Mass transfer rate	$(mol\ s^{-1})$
N_0	Number of orifices	
n	number of mols	

n_a	Refractive index of air	
n_p	Refractive index of perspex	
n_w	Refractive index of water	
P_c	Probability function for chord length distribution	
P_p	Probability function for probe size distribution	
P_s	Probability function for bubble size distribution	
Pe	Peclet number	
p_A	Partial pressure of A	kPa
p_{atm}	Atmospheric pressure	kPa
p_e	Pressure from surface tension force on bubble	kPa
p_T	Total pressure	kPa
Q_G	Gas flow rate	$m^3\ s^{-1}$
R	Ideal gas constant	$J\ K^{-1}\ mol^{-1}$
Re	Reynolds number	
r_A	Ellipse major radius	m
r_B	Ellipse minor radius	m
r_{B1}	Distorted ellipse upper minor radius	m
r_{B2}	Distorted ellipse lower minor radius	m
r_e	Equivalent bubble radius	m
Sc	Schmidt number	
Sh	Sherwood number	
St	Strouhal number	
s	Surface renewal rate	s^{-1}
T	Temperature	K
t	Time	s
t_{dur}	Duration of optical fibre detection	s
t_G	Time in gas phase	s
t_T	Total time	s
u_b	Bubble rise velocity	$m\ s^{-1}$
u_G	Superficial gas velocity	$m\ s^{-1}$
u_{or}	Gas velocity through orifice	$m\ s^{-1}$
u_T	Terminal velocity	$m\ s^{-1}$
V	Volume	m^3
V_b	Bubble volume	m^3
x	Horizontal ellipse co-ordinate	
x_a	Distance through air	m
x_o	Distance between optical fibre probes	m
x_p	Distance through perspex	m
x_w	Distance through water	m
x_{Ai}	Liquid phase interface concentration	mol fraction
x_{Ab}	Liquid phase bulk concentration	mol fraction

x^*	Liquid concentration in equilibrium with gas concentration	mol fraction
y	Vertical ellipse co-ordinate	
y_{Ai}	Gas phase interface concentration	mol fraction
y_{Ab}	Gas phase bulk concentration	mol fraction
y^*	Gas concentration in equilibrium with liquid concentration	mol fraction
z	Water depth	m
α	Volumetric surface area	m^{-1}
β	Scale parameter	
δf	Film thickness	m
ϵ	Energy dissipation	
ϵ_G	Gas hold-up	
ζ	Frequency of bubble path oscillation	s^{-1}
Ω	Amplitude of bubble path oscillation	
ρ	Density	$kg\ m^{-3}$
ρ_L	Liquid density	$kg\ m^{-3}$
ρ_g	Gas density	$kg\ m^{-3}$
μ	Dynamic viscosity	$kg\ m^{-1}s^{-1}$
ν	Kinematic viscosity	$m^2\ s^{-1}$
σ	Surface tension	$N\ m^{-1}$
τ	Period of bubble path oscillation	s
θ	Angle of light	

Chapter 1

Introduction

1.1 Background

At the turn of the millennium all member states of the United Nations (UN) agreed upon the Millennium Development Goals which set a series of targets for 2015 to improve the lives of the poorest people in the world, UN (2015). This included the aim to ensure environmental sustainability, which recognised the importance of climate change and the disproportionately large impact this will have on the world's poorest. The reduction of greenhouse gas emissions, principally CO_2, provides the most practical way to mitigate climate change. Reducing fossil fuel usage and switching to a decarbonised energy infrastructure is the most realistic strategy to reduce CO_2 emissions significantly, Pachauri and Meyer (2014). It has been recognised that limiting the rise in global temperatures to $2°C$ would avoid the most dangerous impacts of climate change. McGlade and Ekins (2015) recommend that no more than 20% of current global coal reserves can be used if the $2°C$ target is to be met. This needs to be achieved with a global population which is projected to increase by approximately 30% to 9 billion by 2050 and with a larger portion of the worlds population living wealthier lifestyles with a higher demand for energy and resources.

One option for mitigating the impacts of climate change is to employ carbon capture technologies. These technologies can be used to prevent CO_2 emissions from reaching the atmosphere. Although this would not provide a complete solution to the problems of climate change and the depletion of fossil fuel reserves, it could reduce the impact of climate change. Currently there is only one industrial-scale project to capture CO_2 emissions from a coal-powered plant in Saskatchewan, Canada, Saskpower (2015). The development of carbon capture projects has been limited by the large economic costs involved, due to the energy intensive processes required. There are also concerns regarding the geological storage of CO_2, with the potential risk of CO_2 leakages.

A recent study by Sanchez et al. (2015) evaluated different scenarios which explored biological carbon capture. They analysed the economics of increasing the biomass fraction in co-fired electricity generation power plants. These scenarios were based on CO_2 emission targets for 2050; however the practical aspects of the land, fertiliser and water requirements, as well as energy storage were not considered. Their definition also conflicts with the definition for carbon sequestration of the *European Commission* (*EC*), which does not recognise biomass cultivated for bio-energy as a carbon sequestration method applicable for carbon credits. Although carbon will be removed from the atmosphere during the growth of the biomass crop, this will be released back to the atmosphere upon combustion of the biomass. Nevertheless, utilising bio-energy can result in negative net CO_2 emissions: this is dependent on the replacement of fossil fuels taking into account the CO_2 usage in processing the biomass.

Conversion of biomass into biofuels for transportation use has some benefits over use in electricity generation. Biofuels offer a low carbon solution that can be incorporated into the current transportation infrastructure. Due to the scale of the transportation fuel market it is unrealistic for biofuels to replace fossil fuels, Acién Fernández et al. (2012b). The development of biofuels could help to reduce CO_2 emissions from fossil fuels, however, and provide a transition to an alternative fuel infrastructure. More recently car manufacturers have been designing flexible-fuel vehicles which use fuels with a higher biofuel blend. This is supported by legislation in the US which has promoted the use of biofuels, with some states introducing a mandatory limit for a 10 % blend of ethanol in transportation fuels, NREL (2008). The *EC* has also set a target for 10 % of all transportation fuels to be derived from renewable sources by 2020, EC (2009). This directive had to be revised, however, due to criticism regarding the competition this could create with food crops and subsequent inflation of food prices. The use of agricultural land, fresh water resources and fertiliser for the cultivation of energy crops would compete with the resources required for food production. This conflict has resulted in a move towards agricultural waste residues as bio-energy sources instead. An alternative is the cultivation of micro-algal biomass, which could be grown using wastewater or seawater and on marginal land, thus avoiding direct competition with the resources required for food production. Micro-algal biomass also has the advantage of a potentially higher growth rate than terrestrial crops and can be harvested continuously throughout the year.

Micro-algal biofuels have attracted interest from companies such as ExxonMobil, Airbus and Rolls Royce which have funded research into this area, Dyer-Smith (2011). The US Navy has also been trialling biofuels derived from heterotrophically grown algae, Solazyme (2013). There has been extensive work in Spain and Israel, Molina Grima et al. (2003), Richmond et al. (1993), while commercial scale facilities exist in California, Hawaii and elsewhere, Spolaore et al. (2006), Milledge (2010). In the UK there are several small pilot-scale projects which cultivate algae for higher value products.

Scottish BioEnergy Ventures developed a photo-bioreactor (PBR) at the Glenturret distillery in Scotland which utilises wastewater and waste CO_2 from the site to cultivate algae for animal feed. Similarly, Alliance Boots and Plymouth Marine Laboratory are collaborating to develop a PBR to cultivate algae for cosmetic products, Dyer-Smith (2011). The treatment of wastewater with micro-algal biomass would help to reduce the costs of micro-algal cultivation. Providing the end product from the micro-algal biomass is not for human consumption, the nutrient costs could be met by combining micro-algal cultivation with wastewater treatment processes.

Currently it is only economically feasible to produce high value products, such as nutraceuticals and cosmetics, from commercial-scale algal cultivation facilities, Acién Fernández et al. (2012a), Milledge (2010). The supply of nutrients to the micro-algal cells is one of the economic costs which need to be considered in cultivation of microalgal biomass for any of the above purposes. Carbon typically constitutes half of micro-algal cells, Grobbelaar (2004). Because of the relatively low concentration of CO_2 in the atmosphere, micro-algal growth is usually carbon limited. Supplementation of concentrated CO_2 could increase the micro-algal biomass yield, and thus improve the economic viability. This CO_2 could be supplied from concentrated CO_2 sources, such as flue gas from power stations, steel refineries and cement works or from biogas upgrading processes.

1.2 Motivation and Aim

For micro-algal biomass to be cultivated for fuel production, or similar low-value commodity products on a commercial scale, there are several significant engineering challenges which need to be overcome. The micro-algal biomass will need to be cultivated, harvested and processed to compete economically with fossil fuels, while minimising the consumption of freshwater, nutrient resources and use of arable land. As mentioned above the CO_2 could be supplied from waste sources, such as flue gas: this would improve the economics of micro-algal biomass cultivation.

One of the challenges of micro-algal cultivation is to reduce the energy consumption and thus the operating costs of the process. An important operation in micro-algal cultivation systems is the supply of CO_2 which could be optimised to improve mass transfer efficiency and reduce the energy requirements. The current design of mass transfer systems is based on empirical relations which provide an approximate prediction of the mass transfer rate. To optimise the mass transfer for novel designs, such as the carbonation systems in micro-algal ponds and PBRs, pilot-scale plants are often used. It is particularly important to limit the losses of CO_2 to the atmosphere and maximise the mass transfer efficiency in these systems, however, and for this purpose an improved understanding of CO_2 mass transfer is essential.

The current work is applicable not only to the mass transfer of CO_2 in PBRs for micro-algal biomass cultivation, but to the general case of mass transfer in multiphase flows. Martín et al. (2011) estimated that 25% of all chemical reactions take place in multiphase gas-liquid flows, including wastewater treatment and aerobic fermentations. In all of these cases accurate prediction of the mass transfer rate is required to ensure an efficient design of the system. This work aims to contribute to the understanding of mass transfer processes, which will help to improve the effectiveness of mass transfer designs, such as those for carbon capture in micro-algal cultivation facilities. To achieve this aim three objectives have been defined, these are outlined below.

1. To investigate the effect of different gaseous CO_2 concentrations within the bubble and dissolved O_2 concentrations within the aqueous phase on the mass transfer coefficient.

2. To examine three aqueous media (de-ionised water, tap water and synthetic seawater) with different degrees of surfactant contamination on the bubble characteristics and mass transfer rate.

3. To analyse the differences between bubble swarms and single bubbles in terms of their mass transfer behaviour.

Chapter 2

Literature Review

2.1 Introduction

The mass transfer from a gas to a liquid is important in a wide range of chemical engineering applications. Because of this there has been a significant amount of research over the last few decades on bubble dynamics and mass transfer of gases into the liquid phase. Section 2.2 briefly reviews the mass transfer of CO_2 in carbonation systems for the cultivation of micro-algal biomass. Section 2.4 goes into more detail on the dynamics of the multiphase flow and the bubble properties that determine the efficiency of the mass transfer, which is covered in section 2.5. A variety of different approaches have previously been used to measure the bubble and mass transfer properties. These are considered in section 2.6 with a review of the experimental measurement techniques to aid in the design of a methodology for the research.

2.2 Micro-algal cultivation systems

Research into large-scale cultivation of micro-algal biomass has been on-going since the 1950s. The first pilot-scale experiments were conducted in the US by Burlew (1953), with the concept of growing micro-algal biomass for food production. In these trials algal biomass was circulated through polyethylene tubing by a centrifugal pump, and a 5 % CO_2-air mixture was bubbled through the system. These initial trials experienced operational issues, however, including leakages in the tubing and sedimentation of the algal biomass.

The focus of algal cultivation research was soon directed to the purpose of growing micro-algal biomass as a fuel source. The initial proposal was to use micro-algal biomass to supply an anaerobic digester, producing methane for electricity and heat production, Golueke et al. (1957). From these early investigations into algal cultivation, it was found

that certain strains of algae had a high oil content. After the 1970s oil crisis the US government funded research into developing liquid fuels from algae. The Aquatic Species Program (ASP) ran for almost two decades. This programme examined the micro-algal cell biology and also looked at the feasibility and engineering design of large-scale micro-algal biofuel processes. The research involved trial experiments in open raceway ponds with areas up to 1000 m^2. These ponds were oval shaped, with a depth of $0.1 - 0.3$ m and used a paddlewheel to circulate the algal media around the pond. This ensured that the algal cells were kept in suspension, received an even exposure to light and that the nutrients were well distributed.

The paddlewheels mixed the algal media at velocities of $0.15 - 0.4$ $m\ s^{-1}$. During the operation of 100 m^2 and 200 m^2 raceway ponds, problems occurred with the settling of algal cells, due to dead zones in the pond where mixing was minimal. There were additional undesirable features, such as the formation of eddies after the 180° bends in the channel. This created cross flows, causing a variation in the water depth across the channel and subsequently different flow velocities, with the water on the inside flowing faster than on the outside of the pond. These turbulent hydrodynamic conditions were controlled by installing flow deflectors around the 180° bends; this also prevented dead zones from forming and reduced algal sedimentation, Weissman et al. (1989). There were similar issues in the 200 m^2 raceway pond; however the use of flow deflectors was less successful. There has been uncertainty over the ideal mixing speed of the algal media and its effect on productivity; however, increasing the mixing speed increases the power requirement, Weissman and Goebel (1985). A benefit of a higher mixing speed is the increased removal of dissolved oxygen (DO), which was reported to reach concentrations as high as 375 % or 400 - 500 % saturation of atmospheric O_2 levels, Mendoza et al. (2013), Sheehan et al. (1998). High levels of DO inhibit the productivity of algae, Molina Grima et al. (2001).

The power requirement of the paddlewheel is proportional to the cube of the velocity, Weissman and Goebel (1987) therefore a small increase in velocity results in a much larger energy requirement. As a means to improve the energy efficiency Weissman and Goebel (1987) looked at combining the supply of CO_2 with the mixing requirement by using an airlift reactor. They concluded that a sufficient head could be generated by the supply of flue gas; however there was insufficient gas to produce the required hydraulic head if pure CO_2 was used. Miron et al. (2000) and Ketheesan and Nirmalakhand an (2011) also looked at airlift-circulated algal cultures in closed and open systems, respectively. There are arguments for both paddlewheel and airlift mixed systems. Airlift systems have not yet been proven to work on a large scale in algal ponds, however, whereas paddlewheels have been shown to be successful.

During the ASP long-term micro-algal cultivation trials were conducted which ran for over a year in the raceway ponds. Attempts at cultivating an algal monoculture in the pond for more than three months were unsuccessful. Maximum productivities of

algal biomass peaked at 50 $g\ m^{-2}\ day^{-1}$; however the average annual productivity was recorded at 16 $g\ m^{-2}\ day^{-1}$. Low temperatures during the night and winter were blamed for a reduction in the yield, Sheehan et al. (1998).

As well as the more common raceway pond used in the ASP trials, alternative pond designs have been tested, such as very shallow inclined cascade ponds designed to improve light distribution through the algal medium, Grobbelaar et al. (1995). Varying head across a site can cause hydrodynamic problems for shallow ponds. The greater surface area to volume ratio also reduces the capacity for CO_2 storage, and results in greater temperature fluctuations which can be a problem depending on the local climate and algal species, Benemann et al. (1982). Deeper unmixed ponds of approximately 1.0 m depth, have also been used; these have lower productivities, but also lower maintenance and construction costs, Borowitzka (1999) and Benemann and Oswald (1996).

Another method of cultivating micro-algal biomass is to use enclosed photo-bioreactor (PBR) systems, Camacho Rubio et al. (1999). The advantages of a PBR include the separation from the outside environment and the greater control of the micro-algal cultivation conditions, such as temperature, that this allows. Separation of the micro-algal growth medium from the outside environment also reduces the risk of contamination by other micro-algal strains, or by micro-algal predators such as rotifers. Cultivating micro-algal biomass for the purpose of producing biodiesel is likely to require a micro-algal strain with a high lipid content, which can be converted into oils. The production rate of lipids within micro-algal cells is typically slower than carbohydrates, however. This causes problems for the cultivation of high lipid content algal strains in open pond systems, as they are particularly vulnerable to contamination from faster-growing species which can out-compete the selected strain for the available nutrients, Vasudevan and Briggs (2008). Micro-algal strains with a niche for particular growing conditions can be cultivated in open systems, where invasive strains do not find the open pond environment favourable and thus would not populate the cultivation system, Borowitzka (2005).

Several different methods have previously been used to supply CO_2 into micro-algal cultivation media. These depend on the design of the PBR used to cultivate the micro-algal biomass and the availability of the CO_2 supply. The ASP tested two carbonation systems. The first enclosed a section of the pond within a corrugated roof. The head space between the roof and the pond surface was supplemented with CO_2, which then dissolved into the water. The required extent of coverage of the corrugated roof over the pond depended on the absorption efficiency of CO_2. The second design comprised a sump in the raceway pond, approximately 1.0 m deep, and included a baffle which diverted the flow of the algal media to the base of the sump. A sparger was placed at the base of the sump which injected CO_2 into the algal media. This was set up either co-currently, with the gas flow following the liquid flow upwards, or counter-currently against the downward flow of algal media. The CO_2 absorption efficiency affects the

design depth of the sump. Weissman et al. (1989) tested the absorption efficiency of the sumps in the 1000 m^2 pond with a 100 % CO_2 input gas, in a counter-current flow with sump depths of 0.88 m and 0.58 m. The absorption efficiencies were very high, in the region of 80 - 90 %. For flue gas with a lower percentage of input CO_2, however, Weissman and Goebel (1987) predicted a requirement for much greater sump depths of approximately 3.0 m. This was due to the lower average absorption efficiency of 65 % for flue gas in a 1.0 m sump, Weissman and Goebel (1985). They found that absorption efficiencies varied depending on the CO_2 input concentration, sump configuration and gas and liquid flow rates. Their work also looked at recycling the unabsorbed CO_2 and at the effect of DO on CO_2 mass transfer Sheehan et al. (1998). They found that shallow sumps are more efficient per metre depth than deeper sumps, and noticed that the bubble size increases as the bubble rises up through the water. It was suggested that this increase in bubble size could be due to desorption of supersaturated O_2 in the water.

Putt et al. (2011) considered a tall, thin bubble column located separately from the pond, in which the CO_2 mass transfer would occur. They achieved an absorption efficiency of 86 % and noted the importance of the pH of the algal media to retain the dissolved carbon in the liquid phase. Similarly González-López et al. (2012) absorbed CO_2 into aqueous solutions of $NaOH$ in an absorption unit which were then pumped to the PBR to supply the micro-algae with cultivation media saturated with CO_2. Doucha et al. (2005) used a cascading open pond system, which used a porous ethylpropylenedimer membrane for the absorption of CO_2 in a separate retention tank, and achieved an absorption efficiency of 49 %.

Other studies have investigated the design of gas diffusers, Ferreira et al. (1998) and Carvalho and Malcata (2001) looked at hollow fibre modules to improve absorption of CO_2 into the algal media. Zimmerman et al. (2011) developed an energy efficient method to generate micro-bubbles to enhance the absorption of CO_2 and provide carbon for the algal cells. Preliminary studies by Zimmerman et al. (2011) found that the growth of *Dunaliella salina* showed a 30 % improvement with a 5 % CO_2 mix supplied by micro-bubbles ($d_e \approx 500\ \mu m$), compared to fine bubbles ($d_e \approx 1.3\ mm$).

Most algal cultivation systems monitor the pH of the liquid, and when the pH reaches a certain value CO_2 will be bubbled into the system. Work from Sakai et al. (1995) and Iwasaki et al. (1998) looked at the growth rate of different algal species at various CO_2 concentrations. Sakai et al. (1995) found that *Chlorococcum littorale* could grow at CO_2 concentrations up to 40 %. In these experiments, however, there was no control on the pH value. Doucha et al. (2005) performed experiments with flue gas and pure CO_2, and found that the presence of NO_x and CO in the flue gas had no detrimental effect on the growth of *Chlorella sp.* The maximum CO_2 concentration typically found in flue gas varies from $5 - 15\%$, so unless sources richer in CO_2 are utilised there may be no advantage in finding strains of algae which are tolerant to high CO_2 concentrations.

2.3 Chemistry of CO_2 dissolution

When CO_2 is dissolved in water it undergoes a series of reactions, shown in equations 2.1 - 2.4, where the gaseous and aqueous phases are denoted by the subscripts (g) and (aq), respectively. The proportion of the bicarbonate (HCO_3^-), carbonate (CO_3^{2-}) and carbonic acid (H_2CO_3) is dependent on the pH, as can be seen from figure 2.1. The concentrations of $CO_{2\ (aq)}$ and $H_2CO_{3\ (aq)}$ are difficult to measure separately and are usually classed together as $CO^*_{2(aq)}$. With a pH lower than 4 the $H_2CO_{3\ (aq)}$ reaction shown in equation 2.2 will be predominant. HCO_3^- will be formed between the pH range of $4-11$, and above a pH of 8 CO_3^{2-} will be formed. The pH of seawater is typically around 8; this corresponds to almost all of the inorganic carbon being present as HCO_3^-. When the dissolved carbon is of the form $CO^*_{2(aq)}$ it can be desorbed back into the gas phase.

$$\mathrm{CO_{2\ (g)}} \rightleftharpoons \mathrm{CO_{2\ (aq)}} \tag{2.1}$$

$$\mathrm{CO_{2\ (aq)} + H_2O_{(l)}} \rightleftharpoons \mathrm{H_2CO_{3\ (aq)}} \tag{2.2}$$

$$\mathrm{H_2CO_{3\ (aq)}} \rightleftharpoons \mathrm{H^+_{(aq)} + HCO_3^-} \tag{2.3}$$

$$\mathrm{HCO_3^-} \rightleftharpoons \mathrm{H^+_{(aq)} + CO_{3\ (aq)}^{2-}} \tag{2.4}$$

The pH of an algal cultivation system is also important for the health of the algal species and along with the alkalinity, very important for the storage capacity of CO_2. Putt et al. (2011) noticed that the pH of the algal media had an effect on the losses of CO_2 from the surface of open ponds. A higher pH system will have a greater carbon storage capacity, and if the concentration of $CO^*_{2(aq)}$ can be limited by maintaining the pH above $pH = 8$ the CO_2 losses can be reduced. There is a balance between finding a pH which is high enough for the CO_2 to be retained, but suitable for the algal species to not be affected. In the operation of large open ponds, the pH can vary throughout the pond and changes as the CO_2 concentration varies, Weissman and Goebel (1987).

The equilibrium concentration of CO_2 in seawater is slightly lower than in pure water. Two processes have an effect on this; the solvent effect is caused by the higher salt content in seawater and increases the solubility of CO_2 in seawater. The salting-out effect, however, reduces the solubility, and reduces the overall solubility to less than pure water, Tokumura et al. (2007).

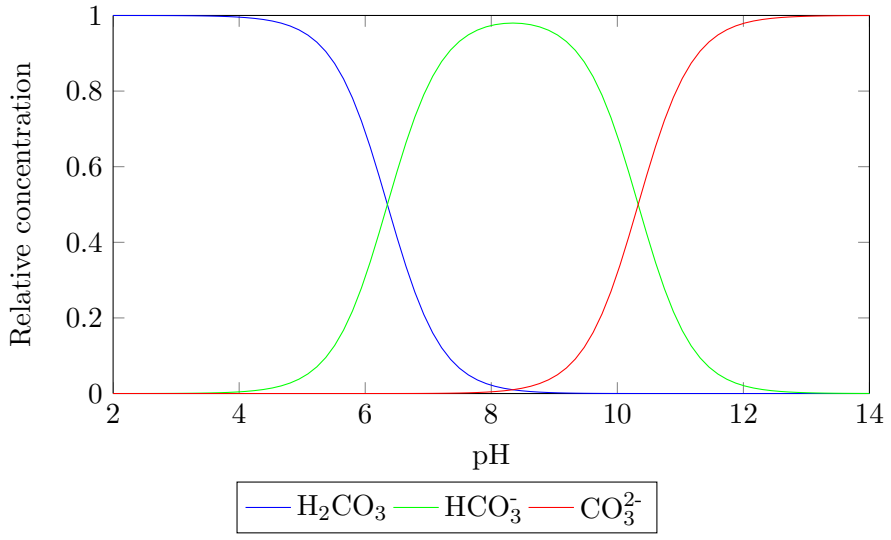

Figure 2.1: Relative concentration of dissolved carbon species with pH

The hydration chemical reactions which take place with CO_2 can also enhance the overall mass transfer of CO_2. The extent of this enhancement is due to the chemical reaction rate, in comparison with the mass transfer rate. The rate of these reactions depends on the temperature and pH. In alkaline systems CO_2 can react directly with the hydroxyl ion (OH^-); this reaction is significantly quicker than that shown in equation 2.2. The higher the pH of the system, the greater the number of OH^- ions available to react rapidly with CO_2 and the greater the enhancement factor. The enhancement factor increases exponentially at $pH > 12$, Fleischer et al. (1996). In most cases the pH in algal cultivation media is below 12 and thus the enhancement factor can be assumed to be negligible. There are also some algal species which excrete an enzyme, carbonic anhydrase, which catalyses the chemical reaction between CO_2 and H_2O, Mathews (1999). This is dependent on algal species and is not considered further in the current work.

2.4 Bubble Dynamics

Bubbles can be characterised based on their size, which is a function of the fluid properties of the gas and liquid. The bubble shape, rise velocity and mass transfer rate will be dependent on these factors. To define the bubble characteristics, the dimensionless Eötvös (Eo), Morton (Mo) and Reynolds (Re) numbers are often used. The Eötvös number is a ratio of the buoyancy forces to the surface tension force, and is often used to characterise the shape of bubbles. The Morton number describes the properties of the fluid: for water this has a value in the order of magnitude of 10^{-11}. The Reynolds number is a measure of the ratio of inertial forces to viscous forces: in this work the Reynolds number will typically range from $Re \approx 150$, for small spherical bubbles rising slowly up the column, to $Re \approx 1500$, for large oscillating ellipsoidal bubbles rising

quickly up the column. These dimensionless parameters are shown in equations 2.5 - 2.7.

Eötvös number

$$Eo = \frac{g.\Delta\rho.d_e^2}{\sigma} \tag{2.5}$$

Morton number

$$Mo = \frac{g.\mu^4.\Delta\rho}{\rho^2\sigma^3} \tag{2.6}$$

Reynolds number

$$Re = \frac{d_e u_b \rho_L}{\mu} \tag{2.7}$$

Single rising bubbles can be divided into three main categories, based on the dimensionless numbers above, or more loosely on the bubble size, Clift et al. (1978). For smaller bubbles the surface tension will be relatively large compared to the buoyancy force and the Eötvös number will be lower, $Eo \approx 0.1$. Because of the relative importance of the surface tension forces for smaller bubbles the bubble tends to a spherical shape. For bubbles of this size, the viscous and interfacial forces will be proportionally large and bubbles in this regime are sometimes referred to as being in the viscous dominated regime.

In air-water systems under normal conditions intermediate-sized bubbles with diameters (d_e), between $1.0 < d_e < 15\ mm$, or Eötvös number between $0.25 < Eo < 40$ are generally ellipsoidal, Clift et al. (1978). The bubble shape can be approximated as an oblate ellipsoid, but often lacks fore-aft symmetry and may exhibit shape oscillations. These intermediate size bubbles are affected by both the surface tension and inertia forces. As they contain a larger volume of gas than smaller bubbles, the buoyancy force is larger, but because of the ellipsoidal shape so is the drag force. Ellipsoidal bubbles can also experience path oscillations. This bubble group is often referred to as being in the surface-tension dominated regime.

Spherical cap bubbles are formed at higher Reynolds and Eötvös numbers. These are larger bubbles which have an indented base and an oscillating shape. Because of the large gas volume, the buoyancy force and hence the rise velocity is larger. Bubbles within this regime are referred to as being in the inertia dominated regime.

For a given input gas volume smaller bubbles will have a larger surface area than larger bubbles, and hence a larger volumetric surface area (α). In terms of mass transfer, an increased surface area allows a greater area of contact between the gas and liquid phases. This will result in higher mass transfer rates and is thus beneficial for mass transfer systems. Therefore this work focuses particularly on smaller and intermediate-sized bubbles with spherical or ellipsoidal bubble shapes, as these will maximise the gas-liquid interfacial area. Figure 2.2 illustrates the variation in surface area per unit

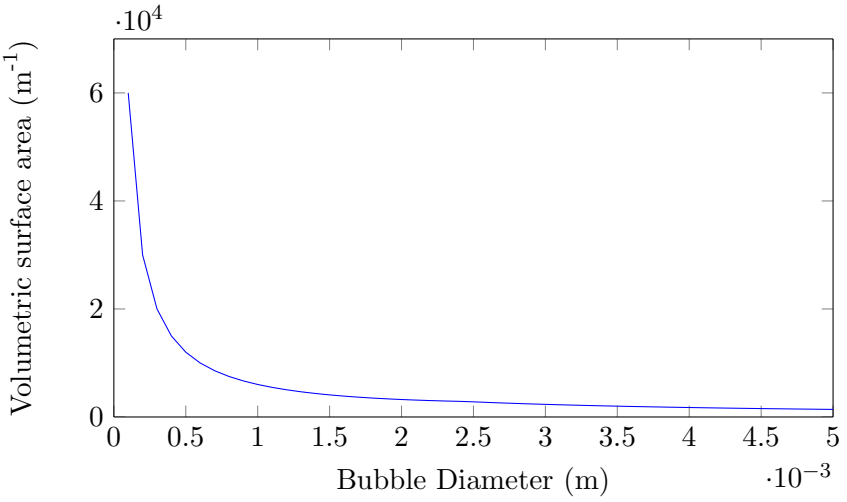

Figure 2.2: Effect of bubble diameter on gas-liquid surface area per volume of gas

volume of gas with bubble diameter. As surface area is proportional to the square of the diameter, the volumetric surface area doubles when the bubble diameter is halved. At bubble diameters of less than 1.0 mm this results in a large increase in volumetric surface area.

For calculation of the volume and surface area of intermediate-sized bubbles, for the purposes of this work it is assumed that the bubble has an oblate ellipsoidal shape. An ellipsoid can be defined by its major (d_A) and minor (d_B) axes. For comparison between the size of ellipsoidal and spherical bubbles, the equivalent diameter (d_e) can be used. This is defined in equation 2.8 and, unless specified otherwise, in this work the bubble diameter for ellipsoidal bubbles will refer to the equivalent bubble diameter.

$$d_e = \sqrt[3]{d_A^2 \times d_B} \tag{2.8}$$

The volume of an ellipsoid is given by equation 2.9, where r_A and r_B are the major and minor ellipsoidal radii, respectively. For a distorted ellipse the minor radii can be defined as r_{B1} and r_{B2}, the upper and lower minor ellipsoid radii, respectively. To calculate the surface area of an oblate ellipsoid equation 2.10 can be used, where the eccentricity is as defined in equation 2.12. The definition of the aspect ratio (E) varies in the literature; in this work, however, the aspect ratio has been taken as the minor diameter over the major diameter, as shown in equation 2.11. The inconsistency in the literature is usually due to the aspect ratio being taken as the inverse of equation 2.11. A perfectly spherical bubble will have an aspect ratio $E = 1$, while an ellipsoidal bubble will have an aspect ratio $E < 1$.

Bubble Volume:

$$V_b = \frac{4}{3}\pi \frac{(r_A^2 r_{B1}) + (r_A^2 r_{B2})}{2} \tag{2.9}$$

Surface Area:

$$a_b = 2\pi r_A^2 \left(1 + \frac{1-e^2}{e} tanh^{-1}(e)\right) \tag{2.10}$$

Aspect Ratio:

$$E = \frac{d_B}{d_A} \tag{2.11}$$

Eccentricity:

$$e = \sqrt{1 - \frac{d_A^2}{d_B^2}} \tag{2.12}$$

There are also alternative ways to express the average bubble size. The equivalent bubble diameter (d_e) is based on the geometric bubble size, shown by equation 2.8. The bubble size can also be defined by the volume-surface mean bubble diameter (d_{vs}), also known as the Sauter mean bubble diameter. This is defined as the diameter of a sphere which has a volume-to-surface area ratio equal to that of the bubble, as shown in equation 2.13. The volume and surface area of the bubble are defined as V_{bub} and a_{bub}, respectively.

$$d_{vs} = 6\left(\frac{V_b}{a_b}\right) \tag{2.13}$$

2.4.1 Bubble Size

There are several factors which affect the bubble size, including the gas and liquid properties and the bubble generation process. A number of relations have been proposed in the literature to estimate the size of bubbles. Akita and Yoshida (1974) proposed a relation for the initial Sauter mean bubble diameter ($d_{vs,i}$) from single orifice spargers. They tested different liquids (including water, methanol, glycol and sodium sulphate solution) and orifice sizes ($1.0\ mm - 8.0\ mm$) and found that the orifice diameter (d_{or}) and the gas velocity through the orifice (u_{or}) were the two factors affecting the initial bubble size.

Sherwood et al. (1975) described the bubble size produced by a slow gas flow rate, which is also applicable to single bubbles being produced from an orifice. The bubble is released from an orifice once the buoyancy force overcomes the surface tension force, which holds the bubble surface to the orifice. With air-water or similar systems using simple methods of gas injection through an orifice, the bubble produced has a minimum size, dependent on the surface tension.

Martín et al. (2009) proposed a relation applicable for spargers, which incorporates the gas flow rate, Q_G, and the number of orifices, N_0 in the sparger. Their relation is based on a model of the detachment of bubbles from orifices, Martín et al. (2006). The relations for the initial bubble size (d_0) are listed in table 2.1 and shown in figure 2.3.

These relations take g as the gravitational acceleration, σ as the surface tension and $\Delta\rho$ as the difference in density between the gas and liquid phases.

Table 2.1: Relations from literature for the bubble size

Reference	*Relation*
Akita and Yoshida (1974)	$d_{vs} = 1.88 d_{or} \left(\frac{u_{or}}{\sqrt{g d_{or}}}\right)^{1/3}$
Sherwood et al. (1975)	$d_e = \left(\frac{6 d_{or} \sigma}{\Delta\rho g}\right)^{1/3}$
Martín et al. (2009)	$d_e = 138 d_{or} \left(\frac{Q_G}{N_0}\right)^{0.26}$

The relations for the bubble diameters from Sherwood et al. (1975) and Martín et al. (2009) plotted in figure 2.3 have been corrected for the Sauter mean bubble diameter. The relation from Akita and Yoshida (1974) shows a relatively constant bubble diameter with increasing orifice diameter. The relation proposed by Sherwood et al. (1975) shows a more pronounced increase in bubble diameter; while the relation from Martín et al. (2009) shows the largest increase, with an almost linear relationship between the bubble diameter and orifice size. These relations are only for the initial bubble size, and the effects of coalescence, break-up and the hydrodynamics of the system will add a further degree of variability to the average bubble size. Nevertheless there is clearly still a large degree of uncertainty over the initial bubble size formed from an orifice or sparger.

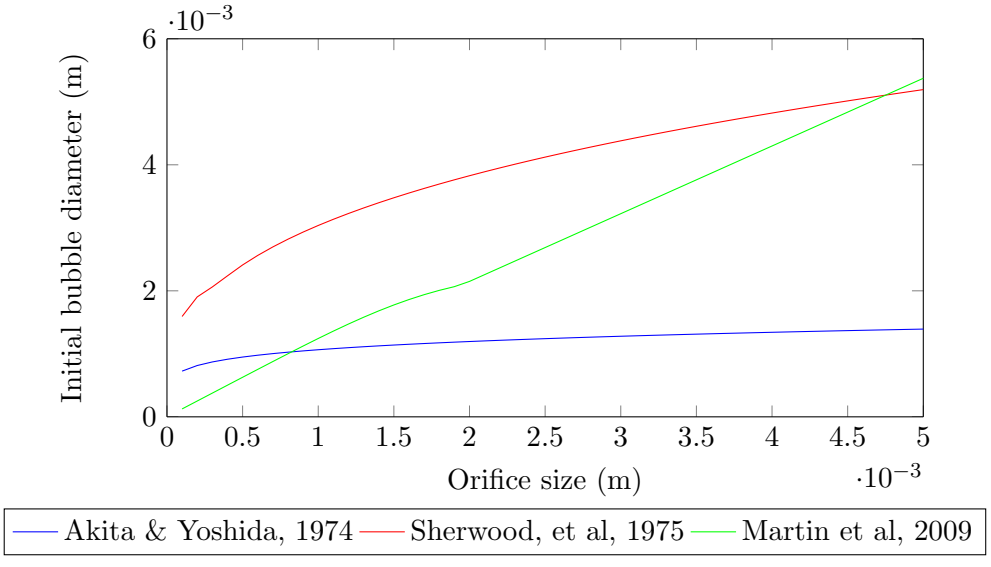

Figure 2.3: Relations for initial bubble diameter with orifice size

In bubble column systems with multiple bubbles, the effect of orifice size on initial bubble diameter is more limited. Sherwood et al. (1975) recognised that at larger gas flow rates, the orifice size is not as significant in predicting the bubble size. This is due to the inertial effects which affect the bubble release. Akita and Yoshida (1974) also looked at the average bubble size in the column, taking into consideration a number of additional variables such as column diameter, and including the effects of bubble coalescence and break-up. They found that the orifice diameter did not have a significant role in determining the average bubble size, because of the more influential effects of bubble coalescence and break-up. The superficial gas velocity, however, did have an effect. The column diameter was also important, as this influences the superficial gas velocity and bubble size.

Koynov and Khinast (2005) compared simulations of the dynamics of individual and multiple bubbles rising through a liquid. They looked at the effects of neighbouring bubbles on the hydrodynamics and bubble-bubble interactions. The bubble path and rise velocity were affected when the bubble followed in the wake of preceding bubbles. This also altered the bubble-bubble interactions, promoting bubble coalescence. The authors also found from the simulations that smaller bubbles in bubble swarms are more likely to become irregularly shaped, than are single bubbles. This work illustrated some of the key differences between the characteristics of single bubbles and bubbles rising in a bubble swarm.

Gas flows in bubble column reactors can be classified into either homogeneous or heterogeneous flow regimes, Kantarci et al. (2005). The homogeneous flow regime occurs at lower gas flow rates, with gentle mixing and little bubble coalescence or break-up. In this regime, with a typical superficial gas velocity $u_G < 0.5\ m\ s^{-1}$, the sparger design and gas flow rate will determine the average bubble size. An increased gas flow rate results in the heterogeneous flow regime with larger bubbles, greater liquid re-circulation and bubble coalescence and break-up. The hydrodynamics of these two regimes are very different and as a result the bubble size in a heterogeneous regime is often affected by different parameters, such as the energy dissipation. With an increased gas flow rate, larger bubbles are produced and, due to the increase in both coalescence and break-up, the bubble size distribution is wider in heterogeneous flow regimes.

2.4.2 Gas Holdup

In bubble columns the interfacial area (α) or gas-holdup (ϵ_G) is often used to quantify the gas distribution, rather than the bubble size. This is due to the comparative ease of measuring the gas holdup in bubble columns, compared to the bubble size. The gas holdup is often used to characterise the hydrodynamics of bubble columns and is frequently derived from empirical data. The gas holdup is defined as the ratio of the volume of gas to the volume of the system, as shown by equation 2.14 where V_G and V_L

are the gas and liquid volumes, respectively. Reviews by Shah et al. (1982) and Kantarci et al. (2005) provide an overview of the most widely used relations to estimate the gas holdup in bubble columns.

$$\epsilon_G = \frac{V_G}{V_G + V_L} \tag{2.14}$$

The gas holdup can be linked to the volumetric surface area by the volume-surface average diameter as shown in equation 2.15, Akita and Yoshida (1974). Table 2.2 shows relations to estimate the gas holdup from gas and liquid properties, as proposed by Hughmark (1967a), Akita and Yoshida (1973) and Kawase et al. (1992). The gas holdup relations from Hughmark (1967a) and Akita and Yoshida (1973) are based on empirical measurements. Kawase et al. (1992) developed their relation based on the energy dissipation rate in bubble columns, which is usually used to derive the heat transfer.

$$\alpha = 6\frac{\epsilon_G}{d_{vs}} \tag{2.15}$$

Figure 2.4 shows the three gas holdup relations listed in table 2.2 plotted for values of superficial gas velocity $u_G < 0.1\ m\ s^{-1}$. The gas holdup increases with the superficial gas velocity. The superficial gas velocity is different from the bubble rise velocity u_b and is calculated from the gas flow rate divided by the cross-sectional area of the bubble column. The relations from Hughmark (1967a) and Kawase et al. (1992) predict similar values of ϵ_G, while the relation from Akita and Yoshida (1973) predicts a higher ϵ_G for the range $0.02 < u_G < 0.1\ m\ s^{-1}$ shown in figure 2.4.

The relation from Akita and Yoshida (1973) takes into consideration the bubble column diameter, unlike the relations from Hughmark (1967a) and Kawase et al. (1992). A review of ϵ_G relations from Kantarci et al. (2005) showed that the column diameter

Table 2.2: Gas Holdup (ϵ_G) relations from literature shown in figure 2.4

Reference	*Relation*
Hughmark (1967a)	$\epsilon_G = \frac{1}{2+(0.35/u_G)(\rho_L\sigma_L/72)^{1/3}}$
Akita and Yoshida (1973)	$\frac{\epsilon_G}{(1-\epsilon_G)^4} = 0.2\left(\frac{gD_c^2\rho_L}{\sigma_L}\right)^{1/8}\left(\frac{gD_c^3}{\sigma_L^2}\right)^{1/12}\left(\frac{u_G}{\sqrt{gD_c}}\right)$
Kawase et al. (1992)	$\frac{\epsilon_G}{(1-\epsilon_G)} = 0.0625\left(\frac{u_G^3}{(\mu_L/\rho_L)g}\right)^{1/4}$

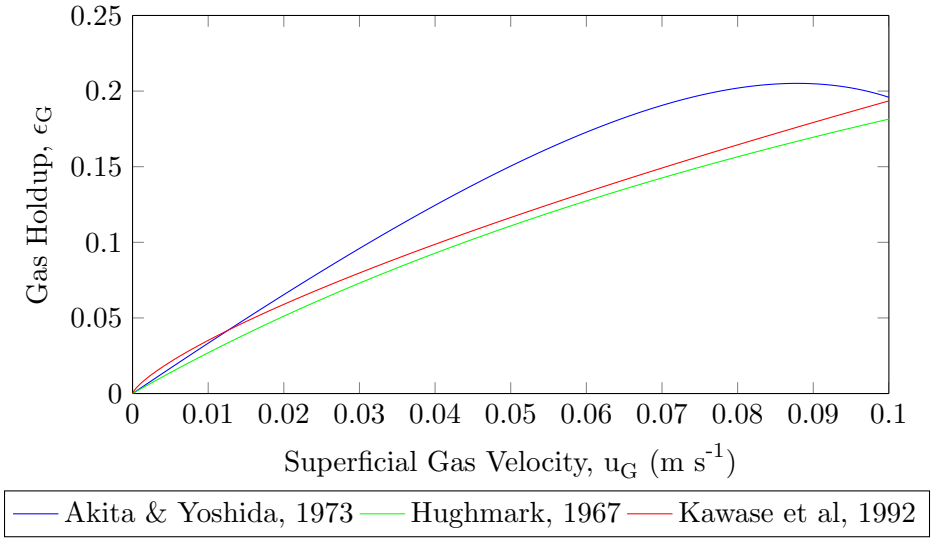

Figure 2.4: Relations for gas holdup with superficial gas velocity

affects the gas holdup to a degree, with smaller columns increasing gas holdup. The bubble size also has an effect on ϵ_G, with smaller bubbles resulting in an increased ϵ_G due to their lower rise velocity. The lower bubble velocity results in an increased bubble residence time, and thus larger gas holdup. One reason for the difference between the relations of Akita and Yoshida (1973) and Hughmark (1967a) and Kawase et al. (1992) could be due to the presence of surfactants in the liquid phase, Kantarci et al. (2005).

The review by Kantarci et al. (2005) found that smaller bubbles contributed more to the overall gas holdup. Kantarci et al. (2005) also found that holdup for small bubbles is dependent on solids concentration; however there were differences between experiments conducted with solid particles and with microbial cells. Krishna et al. (1997) found that solid particles reduced the holdup of the small bubbles; while Prakash et al. (2001) performed experiments with yeast cells and found that an increase in the cell concentration resulted in an increase in velocity of larger bubbles, but a decrease in velocity for smaller bubbles. This illustrates the different effects that solid particles and cells can have on bubbles and the complexities in their interaction with bubbles of different sizes. Generally an increase in cell concentration increases surfactant concentration, which reduces the bubble rise velocity and inhibits bubble coalescence, which in turn reduces the average bubble size and increases ϵ_G.

2.4.3 Internal Circulation

Individual gas bubbles can be generalised as either behaving as a rigid or fluid particle. This is mainly dependent on the gas-liquid system and the size of the bubble, Haberman and Morton (1953). Smaller bubbles with low Reynolds numbers can be better approximated as rigid spheres. In this case the assumption of mass transfer occurring through

diffusion from the gas phase to the liquid phase is reasonable. For larger bubbles the approximation of the bubble as a fluid particle is more reasonable. In this case the internal circulation of gas molecules within the bubble can also be taken into account. The gas molecules within the bubble will be effected as the bubble rises through the liquid. This will be caused by the particles at the surface of the liquid moving against the gas particles at the surface of the bubble creating a shear force. This will be transmitted to the gas particles within the bubble which will move with the direction of the surface flow. This results in the outer gas particles in the bubble moving downwards, which pushes gas molecules at the base of the bubble upwards, forming a vortex. This is described in more detail by Rosso (2005) and illustrated in figure 2.5.

2.4.4 Effect of surfactants on bubble characteristics

The surface chemistry of bubbles has a large effect on the rise velocity and bubble characteristics. Concentration of surfactants are present in tap water and in almost all liquids considered in environmental engineering applications. Surfactant molecules are usually composed of a hydrophilic group and hydrophobic group at opposite ends of the molecule. This causes the surfactant to adsorb at the gas-liquid interface with the hydrophilic tail positioned inside the gas bubble and the hydrophobic head in the liquid phase. The surfactant molecules act to reduce the surface tension between the gas and liquid phases. During the rise of a bubble surfactants present in the liquid phase will attach to the bubble surface. As the bubble rises through the liquid the surface flow around the bubble will re-distribute the surfactants towards the base of the bubble. This will generate a surface tension gradient on the bubble surface. The surface tension will be lower at the base of the bubble and higher at the top of the bubble. The resulting surface tension gradient results in the generation of the Marangoni force, described by Marangoni (1872) in McGrew et al. (1974):

"If for any reason differences in surface tension exist along a free liquid surface, liquid will flow toward the region of higher surface tension"

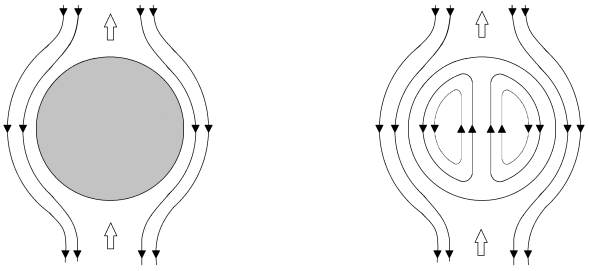

(a) Stokes Flow (b) Hadamard & Rybczynski

Figure 2.5: Flow around solid particle and fluid particle

The surface of a bubble rising through the liquid with surfactants accumulated at the base will therefore experience a Marangoni force opposing the direction of the surface flow. For small bubbles which have a lower rise velocity the opposing Marangoni force is strong enough to oppose the surface flow, resulting in a reduced flow at the bubble surface causing the bubble surface to become rigid, Harper et al. (1967).

Only a small concentration of surfactants in the liquid phase are required to rigidify the bubble surface, which does not cause a detectable change in liquid properties, Clift et al. (1978). Surfactants also inhibit bubble coalescence, which has the benefit of maintaining a higher gas-liquid surface area in bubble swarms. Overall, surfactants are often suggested as the explanation for the poor reproducibility of bubble column experiments conducted with tap water. Because it is so difficult to keep the liquid phase free from surfactants in industrial applications, the presence of surfactants must be accepted. This will certainly be the case for algal cultivation media, where a high concentration of surfactants is likely. The micro-algal biomass maybe cultivated in seawater, saline water or wastewater as well as including nutrients for algal cultivation and possible exudates from the micro-algal cells.

2.4.5 Bubble Rise Velocity

Bubble velocity is an important consideration in the design of mass transfer systems. The bubble velocity is required to calculate the bubble residence time, and has an important effect on the mass transfer coefficient. Martín et al. (2011) noted that the local velocity profile in the fluid surrounding a bubble is important in determining mass transfer rates. At the terminal bubble rise velocity, the bubble buoyancy and drag forces will be in equilibrium. By equating these forces a term for the bubble terminal velocity (u_T) can be derived, as shown for a spherical bubble in equation 2.16.

$$\begin{aligned} C_D \frac{1}{2} \rho_L u_T^2 \frac{\pi d_e^2}{4} &= (\rho_L - \rho_g)\, g \frac{\pi d_e^3}{6} \\ u_T &= \sqrt{\frac{4\,(\rho_L - \rho_g)\, g d_e}{3 C_D \rho_L}} \end{aligned} \tag{2.16}$$

In equation 2.16 ρ_L and ρ_G are the liquid and gas densities, respectively. Knowledge of the drag coefficient (C_D) would allow calculation of the terminal velocity of the bubble. The terminal velocity of a bubble, however, is not a clearly defined parameter due to the constantly changing conditions during the bubble rise, Celata et al. (2007). The reduction in hydrostatic pressure will affect the bubble size, while any oscillations or changes

in bubble shape or rise path will also have an effect, as will the accumulation of surfactants on the bubble surface. Alves et al. (2005) conducted experiments with air bubbles in distilled water, and found that the bubble surface contaminated rapidly during the first 60 s; it took $800 - 1000$ s, however, before complete contamination of the bubble surface occurred and a constant bubble rise velocity was achieved. There is disagreement in the literature concerning the point at which the maximum or terminal velocity is reached. This is because of the effects of different surfactant concentrations, changes in the bubble size, different bubble generation processes and alternative measurement techniques. Duineveld (1995) used a force balance to show that the final velocity for air bubbles rising in water was reached after 70 mm of bubble rise. Tomiyama et al. (2002) observed that the maximum air bubble velocity in water was reached within the first 170 mm. In surfactant contaminated liquids Sam et al. (1996) observed that the maximum velocity was reached after approximately 0.2 s, although a constant rise velocity was not reached in their experiments which were conducted in a 4.0 m column. Consideration should be given to the likely differences in measurement technique and operating conditions when comparing terminal velocity values for rising bubbles. Clift et al. (1978) used the terminal rise velocity as an approximation for the bubble rise velocity, and the same assumption is also adopted in this work.

The rise velocity of a rigid sphere was developed by Stokes in 1851 and is shown in table 2.3. Stokes' Law is applicable to determining the terminal velocity for rigid particles falling or rising through a liquid illustrated in figure 2.5a. This is a simplification, however, as the internal circulation of the fluid within the bubble is not considered. In 1911 both Hadamard and Rybczynski independently developed an equation for the rise velocity of a spherical fluid particle, also shown in table 2.3 and illustrated in figure 2.5b. The theory developed by Hadamard and Rybczynski takes into consideration internal circulation for a fluid particle within a fluid medium. The internal circulation reduces the viscous drag and consequently increases the terminal velocity by approximately 50 % compared to a rigid particle.

The rise velocity depends on the defined bubble regime. Haberman and Morton (1953) performed a series of experiments looking at the drag coefficient, C_D, for rising bubbles in different liquids. They observed that with a reduction in bubble size the C_D of bubbles becomes equal to that of rigid spheres, and that the viscosity of the liquid plays an important role in the rise velocity. They also identified the significant effect on bubble rise velocity of filtering the water to remove minute particles.

Smaller air bubbles ($d_e < 1.0$ mm) in water, which are dominated by the viscous forces, rise in a rectilinear fashion, with an increase in bubble diameter resulting in an increase in terminal velocity. For smaller bubbles the rise velocity can be calculated from Stokes' Law or the relations of Hadamard and Rybczynski, both shown in table 2.3.

The Hadamard-Rybczynski equation for terminal velocity of a bubble considers the bubble as a fluid and theorises the flow lines in the liquid around the bubble, as well as internally within it. This relation includes the term, κ, which is the ratio of the viscosity of gas in the bubble to the liquid and is applicable for small bubbles with a mobile interface. Typically the Hadamard-Rybczynski bubble rise velocity is 50 % higher than the terminal velocity calculated using Stokes' Law. In practice the surface tension has a noticeable effect on the bubble velocity; however the Stokes' Law velocity provides a closer estimate to experimental bubble rise velocity measurements. This is explained by trace concentrations of surfactants, which are present under most conditions in liquids and cause the bubble to behave in a similar way to a rigid particle. In clean (i.e. surfactant-free) conditions, however, the relation from Hadamard-Rybczynski provides a closer approximation to the rise velocity of small bubbles. As it is difficult to remove surfactants, particularly in industrial applications, smaller bubbles will generally behave as rigid particles rather than fluid spheres.

Haberman and Morton (1953) also observed that the bubble shape and C_D can be defined by Mo and Re. As mentioned previously intermediate-sized bubbles in the surface tension regime have a greater buoyancy force than smaller bubbles. This increases the rise velocity and inertial forces resulting in an ellipsoidal shape, which experiences greater drag forces than a spherical bubble. The rise velocity of bubbles in the surface tension regime can either increase or decrease with bubble diameter. This depends on the wake structure of the bubble, which is affected by oscillations and by the initial bubble generation process. The rise velocity of ellipsoidal bubbles is also complicated by the concentration of surfactants in the liquid phase. As with smaller bubbles the accumulation of surfactants on the gas-liquid interface increases the drag force and reduces the internal circulation within the bubble.

Many relations have been proposed for modelling the rise velocity of intermediate-sized bubbles in the surface tension regime. There is a high degree of variability, due to the large effect of surfactants on the rise velocity in this bubble size range. Mendelson (1967) developed a relation based on the surface wave equation, which provides a good approximation for the rise velocity of bubbles in purified systems.

Wallis (1974) conducted a review of previous studies on bubble terminal velocity and divided the bubble velocity relations into several groups based on the dimensionless bubble radius and the purity of the liquid phase. Clift et al. (1978) also summarised bubble rise velocity relations, and suggested a relation for ellipsoidal bubbles in pure systems based on work by Gaudin (1957), and in contaminated systems from Grace et al. (1976). These relations for intermediate-sized bubbles are shown in table 2.3.

The bubble terminal velocity relation proposed by Ishii and Chawla (1979) as reported by Tomiyama et al. (1998) is applicable for single bubbles rising in contaminated systems. Fan and Tsuchiya (1990) reviewed the terminal velocity relations and proposed the

relation shown in table 2.3. This is a combination of terms for smaller bubbles developed by Hadamard and Rybczynski and for intermediate bubbles, developed by Mendelson (1967). The first term from the Fan and Tsuchiya (1990) relation describes the viscous forces which dominate for smaller bubbles. The second term, which describes the surface tension forces, dominates for larger bubbles. Fan and Tsuchiya (1990) fitted the relation by selecting values for n, c and K_b for contaminated and pure water, with values of n between 1.6 and 0.8 for clean and contaminated systems. Maneri and Vassallo (2000) modified the model proposed by Fan and Tsuchiya (1990) by modifying the K_b coefficient to fit a wider set of bubble sizes and experimental parameters.

Tomiyama et al. (1998) proposed three relations, with coefficients B_1 and B_2 which are dependent on the contamination of the liquid phase. This relation covers a wide range of bubble sizes and fluid properties.

The relations shown in table 2.3 are plotted for bubble diameter $d_e < 5.0\ mm$ in figure 2.6. The empirical relations shown in figure 2.6 by Fan and Tsuchiya (1990) use the coefficients for the contaminated model, while the relation by Tomiyama et al. (1998) uses the coefficients for the uncontaminated rise velocity model. The variability between the bubble rise velocity relations is particularly noticeable for bubbles with a diameter $1.0 < d_e < 2.0\ mm$. This fits the surface tension dominated regime, which is particularly susceptible to the effect of surfactants. The empirical relations in contaminated liquids predict a lower rise velocity, while relations in pure liquids predict a higher rise velocity, at least for $d_e < 3.5\ mm$. For pure liquids the rise velocity reaches a peak value with a bubble diameter, $d_e \approx 1.2\ mm$.

Table 2.3: Bubble rise velocity relations from literature

Reference	Relation	Conditions
Stokes, 1851 from Fan and Tsuchiya (1990)	$u_b = \left(\frac{\rho_G - \rho_L}{18\mu_L}\right) g d_e^2$	Rigid spheres
Hadamard and Rybczynski, 1911 from Fan and Tsuchiya (1990)	$u_b = \frac{2}{3}\frac{g r_e^2 \Delta\rho}{\mu_L}\left(\frac{1+\kappa}{2+3\kappa}\right) \qquad \kappa = \frac{\mu_G}{\mu_L}$	Fluid spheres
Mendelson (1967)	$u_b = \sqrt{\frac{2\sigma}{\rho_L d_e} + \frac{g d_e}{2}}$	
Wallis (1974)	$u_b = u_b^* \frac{\mu_L g(\rho_L - \rho_G)}{\rho_L^2}^{1/3}$ $u_b^* = \sqrt{2}\frac{1}{Mo}^{1/12}$ $u_b^* = \sqrt{r^*} \qquad r^* = \frac{d_e}{2}\frac{\rho_L g(\rho_L - \rho_G)}{\mu_L^2}^{1/3}$	Region 4 Region 5
Clift et al. (1978)	$u_b = \sqrt{\frac{2.14\sigma}{\rho d_e} + 0.505 g d_e}$	pure systems

Grace et al. (1976)	$u_b = \frac{\mu_L}{\rho_L d_e} Mo^{-0.149}(J - 0.857)$ $J = 0.94H^{0.757}$ $J = 3.42H^{0.441}$ $H = \frac{4}{3} EoMo^{-0.149}(\mu_L/\mu_W)^{-0.14}$ $J = ReMo^{0.149} + 0.857$	$(2 < H \leq 59.3)$ $(H > 59.3)$
Ishii and Chawla (1979) from Tomiyama et al. (1998)	$C_D = max\left(\frac{24}{Re}\left(1 + 0.1Re^{0.75}\right), min\left[\frac{2}{3}\sqrt{Eo}, \frac{8}{3}\right]\right)$	
Fan and Tsuchiya (1990)	$u_b = \left[\frac{\rho_L g d_e^2}{K_b \mu_L}^{-n} + \sqrt{\frac{2c\sigma}{\rho_L d_e} + \frac{g d_e}{2}}^{-n}\right]^{-1/n}$ $K_b = max\left[12, 14.7Mo^{-0.038}\right]$	Contaminated: $n = 0.8$ Pure: $n = 1.6$ c = 1.2
Tomiyama et al. (1998)	$C_D = max\left(min\left[\frac{B_1}{Re}\left(1 + 0.15Re^{0.687}\right), \frac{B_2}{Re}\right], \frac{8}{3}\frac{Eo}{Eo+4}\right)$	pure systems $B_1 = 16,\ B_2 = 48$ slightly contaminated systems $B_1 = 24,\ B_2 = 72$

		contaminated systems $B_1 = 24,\ B_2 = \infty$
Maneri and Vassallo (2000)	$u_b = \left(u_{b1}^{-n} + u_{b2}^{-n}\right)^{-1/n}$ $u_{b1} = \frac{\rho_L g d_e^2}{K_b \mu_L} \qquad u_{b2} = \sqrt{\frac{2\sigma}{\rho_L d_e} + \frac{g d_e}{2}}$ $K_b = 148\left(1 - \exp\left[-5.31 \times 10^{10} Mo\right]\right) \frac{d_e}{d_0}^{0.425}$ $d_0 = 2\sqrt{\frac{\sigma}{(\rho_L - \rho_G)g}};\ n = 8$	

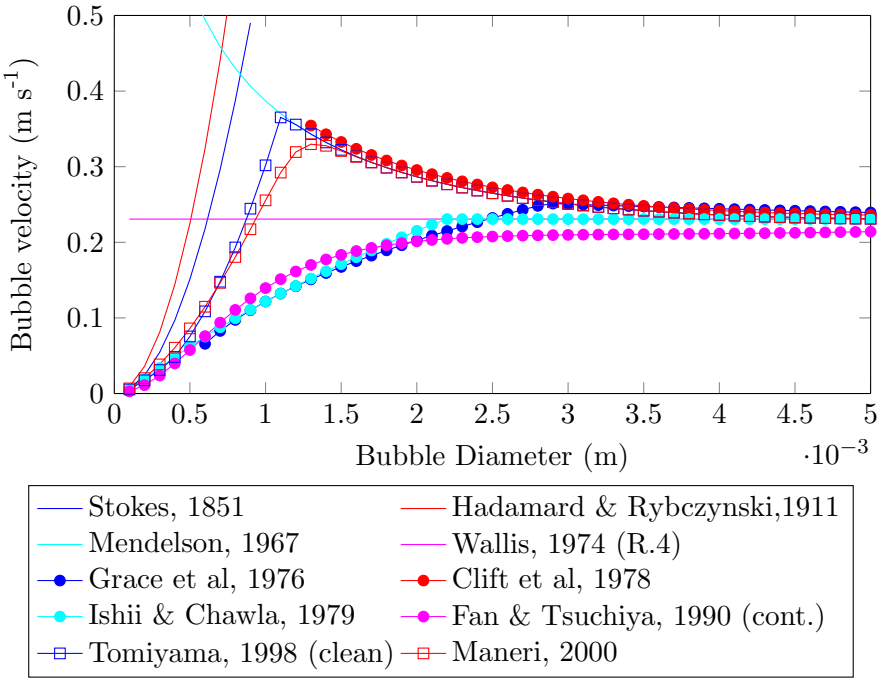

Figure 2.6: Bubble rise velocity relations for CO_2 bubble rising in water for different bubble sizes

From figure 2.6 it appears that there are two distinct curves for estimating the rise velocity of bubbles, depending on whether a system is considered contaminated with surfactants or whether it is considered pure and free from surfactants. This has a noticeable effect on the terminal bubble velocity for bubble diameters between 0.5 mm and 2.5 mm, Clift et al. (1978).

The rise velocity relations from Stokes' Law and Hadamard and Rybczynski, are suitable for small bubble diameters, $d_e < 0.8$ mm, the inclusion of the influence of internal circulation in the relation of Hadamard and Rybczynski gives an increased bubble rise velocity. The relations of Mendelson (1967) and Clift et al. (1978) for pure systems are applicable for $d_e > 1.2$ mm and match those of Tomiyama et al. (1998) and Maneri and Vassallo (2000) for the intermediate bubble size range. The relation of Maneri and Vassallo (2000) is based on the model by Fan and Tsuchiya (1990) for pure systems. The peak bubble velocity estimated by Maneri and Vassallo (2000) at $d_e \approx 1.0$ mm is slightly lower than the velocity predicted by Tomiyama et al. (1998). For contaminated systems, the relation proposed by Wallis (1974) predicts a constant bubble rise velocity, which approximates to that obtained from the relations of Ishii and Chawla (1979), Fan and Tsuchiya (1990) and Grace et al. (1976) for $d_e > 2.0$ mm. It is important that the relation by Wallis (1974) is used for the correct range of bubble sizes.

Sam et al. (1996) performed rise velocity measurements in a 4.0 m tall column and found that the bubble accelerated to a maximum velocity, before the accumulation of surfactants caused it to decelerate. The concentration of surfactants affected the rate of

deceleration from the maximum rise velocity, whereas the type of surfactant used would determine the final terminal velocity of the bubble.

Tomiyama et al. (2002), Okawa (2003) and Peters and Els (2012) showed that the bubble rise velocity depends not only on the purity of the liquid phase, but also on the initial distortion from the bubble generation process. A small initial deformation can reduce the bubble velocity, while a large deformation can increase it, Tomiyama et al. (2002). Recently Peters and Els (2012) produced both fast and slow rising bubbles in tap water by using different bubbles release methods. A slow release method allowed surfactants to attach to the bubble surface prior to release and reduced the rise velocity. A quick bubble release prevented the initial accumulation of surfactants and resulted in a higher bubble rise velocity. Okawa (2003) conducted experiments at a higher temperature and found that increasing the temperature resulted in a reduction in bubble rise velocity. The explanation for this was not clear; however it was hypothesised that this higher temperature would lead to an increase in interfacial effects from the greater vapour pressure and changes in the phase, which would have a result on the bubble rise velocity.

In comparison to the rise velocity of single bubbles, there have not been many previous studies which investigate the rise velocity in bubble swarms. Much of the research conducted on bubble columns considers the superficial gas velocity, rather than the bubble rise velocity. The velocity of the bubble swarm and the individual velocities of bubbles within a swarm, will both influence the mass transfer rate. The superficial gas velocity has been shown to have different effects on the rise velocity of different sized bubbles. The rise velocity of smaller bubbles has been shown to reduce with increasing superficial gas velocity, although it increases for larger bubbles, Prakash et al. (2001). Krishna et al. (1999a) looked at the interaction between larger bubbles and found that those rising in the wake of a preceding bubble showed an acceleration. The acceleration increased when the distance between the bubbles was reduced, and this could lead to the lower bubble catching up with the higher bubble resulting in bubble coalescence. It is thought that in bubble swarms, where every bubble is rising in the wake of previous bubbles, the rise velocities will be increased as a result of this effect. Koynov and Khinast (2005) simulated this in more detail and showed that the velocity of the lower bubble 'jumps' due to periodic vortex shedding from the leading bubble. This results in continual acceleration and deceleration, or oscillation of the bubble rise velocity. It is because of this effect, the velocity of bubble swarms is generally considered to be higher than the rise velocity of single bubbles. Bubble oscillations and the effects these have on mass transfer are discussed in more detail in the next section.

2.4.6 Bubble Oscillations

Brenn et al. (2006) observed that experimental results, including those from Saffman (1956) and Duineveld (1995) showed different bubble shapes, rise velocities and paths

for the same bubble size in water. This was considered to be due to oscillations in the rise path and fluctuations in the bubble shape. These oscillations and fluctuations were affected by the geometry of the bubble orifice, conditions of the bubble release and presence of surfactants in the water.

Smaller, spherical bubbles with a low Re rise in a straight, recti-linear fashion, without significant oscillations; whereas larger bubbles in the surface tension regime with higher Re show more instability and can oscillate in a zig-zagging or helical motion. Saffman (1956) conducted a theoretical analysis which linked the bubble wake to the path oscillations. The bubble wake and thus oscillations can be affected by the bubble and liquid properties, the presence of surfactants or the bubble generation process. When no external factors influence it, a small air bubble in water initially rises with a rectilinear motion. Given the necessary conditions this can turn into a zig-zag and, eventually, a helical motion. Saffman (1956) found that bubbles with $d_e < 1.4\ mm$ followed a rectilinear path, with zig-zag motion occurring for $d_e < 2.0\ mm$, and either helical or zig-zagging path oscillations at larger bubble diameters. Duineveld (1995) found that the zig-zagging motion occurred from $d_e > 1.8\ mm$. This inconsistency between observations by different researchers is believed to be caused by surfactants which can affect the bubble wake.

Bubble path oscillations are commonly classified by dimensionless numbers, with the zig-zagging motion occurring in water at $We_{cr} \approx 2.3 - 3.4$, Duineveld (1995), de Vries (2001). Haberman and Morton (1953) noticed that the bubble path oscillations can be correlated to Re, with rectilinear motion occurring for $Re_{cr} < 300$. It was later shown that this varies depending on surfactant concentration, with $Re_{cr} \approx 600$, for ultra clean water or $Re_{cr} \approx 200$ for untreated water, Brunson and Welleck (1970), Clift et al. (1978), Okawa (2003). The helical motion of the bubble is a secondary phase of path instability, which either occurs in the same conditions as the zig-zag motion, or develops afterwards. Shape fluctuations of the bubble have been shown to be generated only during the zig-zag oscillation and not during rectilinear or helical motion, de Vries (2001). The onset of shape fluctuations and path oscillations occurs at similar points, with $We_{cr} \approx 3.7$ identified for shape fluctuations, de Vries (2001).

Haberman and Morton (1953) propose that the oscillatory motion of bubbles is caused by periodic vortex shedding, similar to that seen for rigid spheres. Saffman (1956) reported that Marshall and Stanton (1930) observed flow past a circular disc and found the wake to be steady for $Re < 200$, although with periodic discharge of vorticity occurring for $Re \approx 200$. Ellingsen and Risso (2001) conducted experiments which showed the path oscillations develop without shape fluctuations or the presence of surfactants, indicating that the wake instability was the cause of the bubble path oscillation. Mougin and Magnaudet (2001) performed numerical simulations showing that wake instability is initiated at certain values of bubble aspect ratio, resulting in bubble path oscillations.

Surfactants can increase the drag force on the bubble which in turn affects the bubble wake, resulting in the shedding of wake vortices at a lower Re and the earlier onset of bubble path oscillations. As well as surfactants, the onset of path oscillations can also be caused by the bubble generation process, or bubble-bubble interactions, Martín et al. (2011). The bubble generation process can produce fluctuations in the initial bubble shape, which periodically result in a lower aspect ratio leading to increased bubble wake vortices and bubble path oscillations Tomiyama et al. (2002), Okawa (2003).

Haberman and Morton (1953) observed that the frequency and amplitude of the helical bubble path oscillation increases with Re. They also observed that the initial conditions affect the direction of the rise path, i.e. clockwise or counter-clockwise for helical path oscillation. Veldhuis et al. (2008) used Schlieren optics to visualise the wake of the bubble and observed shedding of bubble vortices during oscillations of the bubble surface. The vortex shedding depended on the surfactant concentration. Vortex shedding occurred more frequently in pure systems, in conjunction with the bubble shape fluctuations. With surfactants present, however, the rigidity of the bubble surface reduced the shape fluctuations, and vortex shedding only occurred at the extremes of the zig-zag bubble rise path. As a result of this the vortex shedding in pure systems occurred at a much higher frequency, while in contaminated systems it matched the bubble path oscillation frequency of approximately 6 Hz. This bubble path oscillation frequency agrees with that reported by Saffman (1956) who found a path oscillation frequency of approximately 7 Hz during the zig-zagging phase. Veldhuis et al. (2008) also observed that the bubble shape fluctuations occurred at a slightly larger bubble diameter in tap water ($d_e \approx 3.0\ mm$) than purified water ($d_e \approx 2.8\ mm$). The surfactants found in tap water will reduce the rise velocity and thus delay the onset of the bubble shape fluctuations. These authors also observed a difference in the variation in bubble rise velocity, with greater bubble acceleration in pure water than in tap water. This explained the lack of vortex shedding from bubble shape fluctuations in surfactant-contaminated tap water. The vortex shedding in tap water may also remove some of the contaminants from the bubble surface: this would have the effect of creating a variable surfactant concentration on the bubble surface.

Okawa (2003) proposed an empirical relation to predict the magnitude and frequency of the bubble path oscillations using the bubble drag coefficient, C_D. Ern et al. (2012) reported amplitudes of bubble path oscillations in the range from $3 - 5 \times d_e$. These authors also reported a slight reduction in vertical rise velocity for zig-zagging and helical oscillating bubbles, compared to recti-linear rising bubbles; however they noted that this is more clearly seen in simulations than experimental work. Tagawa et al. (2013) noted that the effect of surfactants should reduce with bubble size, and that there is an inverse relationship between the amplitude of the shape fluctuations and the bubble path oscillation. Quinn et al. (2014) also demonstrated the inverse relationship

between the bubble shape fluctuations as shown by the bubble aspect ratio, and the bubble path oscillations shown by fluctuations in the vertical bubble velocity.

Although surfactants act to increase the wake from a bubble and promote an early onset of bubble path oscillations, they also create a more spherical bubble and thus dampen the bubble path oscillations, Sam et al. (1996), Tomiyama et al. (2002), Clift et al. (1978). As well as reducing the amplitude of the oscillation, this can affect whether the oscillation is helical or zig-zagging. Lunde and Perkins (1998) and Tomiyama et al. (2002) observed that contaminated bubbles do not exhibit a helical rising motion, even when they are released with large initial shape deformations. The accumulation of surfactants onto a bubble rising in a helical path would result in the path changing from helical to zig-zagging.

The oscillation of bubbles has an important effect on the local hydrodynamics, which affect the concentration of dissolved gases and the gas-liquid interface velocity, both of which will influence the mass transfer. Martín et al. (2011) has showed that in certain cases, the increased bubble oscillation from larger bubbles can increase the mass transfer rate sufficiently to offset the reduction in the volumetric surface area. Surfactants play a complex role in this, as they dampen the amplitude but promote the early onset of oscillations. Additionally fluctuations in the shape of the bubble result in vortex shedding, although this is only observed in pure water and not in the presence of surfactants. Nevertheless the bubble shape has an important role in affecting the wake of the bubble, which in turn effects the bubble path oscillation. Empirical relations for the aspect ratio are reviewed in the following section.

2.4.7 Aspect Ratio

There is still considerable uncertainty over the relationship between bubble shape fluctuations and the bubble path oscillation. As demonstrated by Mougin and Magnaudet (2001) the aspect ratio of the bubble is an important factor which initiates wake instabilities, resulting in bubble path oscillations. The aspect ratio is also important in determining the bubble shape and resulting bubble surface area. This will have a direct effect on the available gas-liquid area and the mass transfer rate. In the absence of path oscillations, the aspect ratio (E) of the bubble can be approximated from empirical relations found in the literature. Two of these relations, proposed by Wellek et al. (1966) and Okawa (2003), are shown in equations 2.17 and 2.18, respectively.

$$E = \frac{1}{1 + 0.163 Eo^{0.757}} \tag{2.17}$$

$$E = \frac{1}{1 + 1.97 Eo^{1.3}} \tag{2.18}$$

These relations are based on the Eötvös number. It has been reported that the bubble generation process can have a large impact on the aspect ratio, Sam et al. (1996), Tomiyama et al. (2002), Wu and Gharib (2002) and Quinn et al. (2014). Celata et al. (2007) and Okawa (2003) found that correlating the aspect ratio with the Weber number also provided a good fit. We is given by equation 2.19: it incorporates the rise velocity and represents the ratio of the inertia of a bubble to the surface tension. The inclusion of a term for the bubble rise velocity, which would depend on the bubble generation conditions, may provide a more accurate estimate of the aspect ratio. Relations for the aspect ratio and We have been given by Taylor and Acrivos (1964), Moore (1965) and Wellek et al. (1966), shown in equations 2.20, 2.21 and 2.22, respectively.

$$We = \frac{d_e \rho_L u_b^2}{\sigma} \tag{2.19}$$

$$E = \frac{1}{1 + 5/32We} \tag{2.20}$$

$$We = 4E^{1/3} \frac{\left(1 + E^2 - 2E^3\right) \left[cos^{-1}E - E\sqrt{1 - E^2}\right]^2}{\left(1 - E^2\right)^3} \tag{2.21}$$

$$E = \frac{1}{1 + 0.91We^{0.95}} \tag{2.22}$$

2.5 Mass Transfer

The mass transfer rate across a phase boundary can be defined by equation 2.23, where N_A is the mass transfer rate ($mol\ s^{-1}$), α is the volumetric gas-liquid contact area ($m^2\ m^{-3}$), k_L and k_G are the individual liquid and gas side mass transfer coefficients, respectively ($m\ s^{-1}$). The concentration difference provides the driving force for mass transfer and is defined as the difference between the concentration in the bulk phase (x_{Ab} and y_{Ab} for the bulk liquid and gas concentrations, respectively) and the concentration at the interface (x_{Ai} and y_{Ai} for the liquid and gas interface concentrations, respectively).

$$N_A = k_L \alpha \left(x_{Ai} - x_{Ab}\right) = k_G \alpha \left(y_{Ab} - y_{Ai}\right) \tag{2.23}$$

In practice it is difficult to measure the concentration at the interface, however an approximation can be made using Henry's Law to find the equilibrium concentration. The interface concentration in the liquid phase x_{Ai} can be replaced with Hp_A, where p_A is the partial pressure of component A and H is the Henry's coefficient (Pa). Values

of the Henry's coefficient for CO_2, O_2 and N_2 are shown in table 2.4. For the liquid side calculation x_{Ai} can be replaced by p_A/H and for the gas side calculation y_{Ai} can be replaced with $(Hx_{Ab}p_T)$, where p_T is the total pressure. Taking into consideration the equilibrium concentration in place of the interface concentration the overall mass transfer coefficients can then be used in place of the individual mass transfer coefficients. The overall mass transfer coefficients for the liquid (K_L) and gas phases (K_G) are shown in equations 2.24 and 2.25, respectively.

$$\frac{1}{K_L} = \frac{1}{k_L} + \frac{H}{p_T\ k_G} \tag{2.24}$$

$$\frac{1}{K_G} = \frac{p_T}{H\ k_L} + \frac{1}{k_G} \tag{2.25}$$

The low solubilities for the gases considered in this work shown by the large values for Henry's coefficient in table 2.4, result in a small contribution from the gas side resistance. In this case the gas side resistance is often considered negligible and the mass transfer rate can be calculated using the mass transfer equation for the liquid phase, taking the local liquid side mass transfer coefficient (k_L) as an approximation for the overall liquid side mass transfer coefficient (K_L). The mass transfer rate for component A can therefore be calculated from equation 2.26.

Gas	Diffusion Coefficient $(m^2\ s^{-1})$	Henry's Coefficient (Pa)
CO_2	1.65×10^{-9}	1.44×10^{8}
O_2	1.96×10^{-9}	4.02×10^{9}
N_2	1.74×10^{-9}	7.94×10^{9}

Table 2.4: Diffusion and Henry's coefficients for gases in water at $293°K$, taken from Perry and Green (2008)

$$N_A = K_L\alpha(Hp_A - x_{Ab}) \tag{2.26}$$

In this work the units of the mass transfer coefficient k_L have been simplified from $mol/[(s\ m^2)(mol\ m^{-3})]$ to the velocity units of $m\ s^{-1}$. When comparing mass transfer coefficients with values reported from the literature care needs to be taken as different units are often used. The volumetric surface area $(m^2\ m^{-3})$ in equation 2.23 is sometimes defined as the gas-liquid contact area (m^2) instead. The concentration driving force can also be reported as a molar concentration rather than a mole fraction. Another complication arises when local mass transfer coefficients are used: these can be local spatially or dynamically. In the literature many theoretical models and empirical relations for k_L have been made. The values reported for k_L vary depending on the mass transfer system and are affected by many parameters. Theoretical descriptions of

k_L include the two-film, penetration and surface renewal theories, which are discussed below.

2.5.1 Two-Film Theory

The foundations for the theory of inter-phase mass transfer were developed by Whitman (1923) and Lewis and Whitman (1924). They theorised that there were two-films each side of the interface boundary where the mass transfer occurs. These films each provide resistance to the mass transfer, where bulk concentrations exist outside of the two-films. The hypothetical films are taken as having stagnant conditions where molecular diffusion drives the mass transfer.

The two-film theory is based on molecular diffusion driving the mass transfer in each film. According to this theory the mass transfer coefficient, k_L, is proportional to the diffusion coefficient (D_L) and inversely proportional to the film thickness (δf) and can be represented by equation 2.27.

$$k_L = \frac{D_L}{\delta f} \tag{2.27}$$

The film thickness itself cannot be measured and by comparison with experimental results it has been found that the assumption that the film is stagnant, with only diffusion driving the mass transfer is often too simplistic, Alvarez et al. (2001). Several modifications have been made to this theory, which change the proportional relationship between k_L and D_L.

2.5.2 Penetration and Surface Renewal Theories

The penetration theory proposed by Higbie (1935) considered the films either side of the interface to be penetrated by packets from the bulk phase. During the period of time in which each packet is in contact with the interface, mass transfer occurs from these packets across the phase boundary. Higbie (1935) proposed that k_L would be proportional to the square root of the diffusion coefficient, as well as being inversely proportional to the square root of the contact time between the packet and the interface, (t_s).

$$k_L = \frac{2}{\sqrt{\pi}}\sqrt{\frac{D_L}{t_s}} \tag{2.28}$$

This theory provides a description for unsteady state gas absorption, and has proved very successful in reliably predicting the mass transfer rate. Different approaches have

assumed different values for the time that each hypothetical packet spends at the interface. For the case of bubbles rising in a liquid many authors have taken this to be the time taken for the bubble to travel the length of its diameter, i.e. $t_s = d_e/u_T$, Leonard and Houghton (1963). Alternatively the residence time of micro-eddies has been used Nedeltchev et al. (2007) and for oscillating particles the oscillation frequency has also been taken, Brunson and Welleck (1970).

The penetration theory developed by Higbie (1935) was extended by Danckwerts (1951) who went onto assume that the time that the packets spend in contact with the interface is not constant and varies with a random distribution. This theory developed the idea that each element has a probability, depending on its age, of being absorbed or of mixing back with the bulk phase. Danckwerts (1951) used an age distribution of the surface elements, where the mass transfer coefficient is proportional to the square root of the rate of surface renewal and the diffusivity, as seen in equation 2.29, where s is the surface renewal rate.

$$k_L = \sqrt{D_L s} \tag{2.29}$$

Several other adjustments and variations have been made to these mass transfer theories, which provide models to explain the mass transfer in different systems. In addition to numerous theoretical models for the mass transfer rate, there are also many empirically derived relations. Perry and Green (2008) list dozens of relations used to model the mass transfer coefficient in bubble columns and in different mass transfer systems. From experimental studies published in the literature it has been found that k_L can be described reasonably well when the exponent of the diffusivity is taken between $1/2 - 2/3$.

2.5.3 Mass Transfer Relations

From the dozens of empirical relations describing the mass transfer rate in the literature, Perry and Green (2008), many are applicable to a certain range in bubble sizes, or related bubble flow regime. Some of these relations are also categorised depending on whether the liquid phase is contaminated with surfactants, or on the turbulence of the liquid phase. In the current work the mass transfer from single bubbles and bubble swarms is considered separately, and likewise the relations reviewed from literature have been divided into single bubble and multiple bubble relations. Most of the mass transfer relations developed from bubble columns calculate the volumetric mass transfer coefficient, $k_L\alpha$, while the relations for single bubbles often distinguish between k_L and α.

The mass transfer coefficient is often represented in the dimensionless form, known as the Sherwood number (Sh), as shown in equation 2.30. The relation for Sh often

incorporates several other dimensionless numbers, including the Schmidt number (Sc) and Peclet number (Pe), which are shown in equations 2.31 and 2.32, respectively. The Schmidt number is a ratio of the viscosity to mass diffusivity, and is often used as a representation of the thickness of the gas-liquid interface. The Peclet number represents the ratio of advection to diffusion, and can also be expressed as the product of the Reynolds and Schmidt numbers.

Sherwood number

$$Sh = \frac{k_L d_e}{D_L} \tag{2.30}$$

Schmidt number

$$Sc = \frac{\mu}{\rho_L D_L} \tag{2.31}$$

Peclet number

$$Pe = \frac{d_e u_T}{D_L} \tag{2.32}$$

2.5.4 Single Bubble Mass Transfer Relations

There have been many attempts to find empirical relations to describe the mass transfer in different systems. Despite this, there is a large variability in reported mass transfer rates, with variations in k_L by a factor of 5 typical for small bubbles, Alves et al. (2004). The mass transfer depends on the properties of the gas-liquid interface, which is significantly affected by surfactants. Frumkin and Levich (1947) identified the effect of surfactants on the mass transfer rate, while Griffith (1960) explained this in terms of the mobility of the gas-liquid interface. A mobile interface has a higher mass transfer rate and an immobile interface a reduced mass transfer rate. The higher mass transfer rates in uncontaminated bubbles can be approximated by the theory developed by Higbie (1935); whereas the reduced mass transfer rate found in contaminated liquids, which cause the bubble to behave as a rigid sphere, can be approximated by a relation proposed by Frössling (1938). Surfactants attach to the bubble surface, increasing its rigidity, while the hydrophobic tails inside the bubble reduce the internal circulation and the renewal of the gas side film, Rosso et al. (2006). Because the diffusion coefficient in gases is approximately 10^4 greater than in liquids, however, the effect of reduced internal circulation is unlikely to be significant, Clift et al. (1978). The empirical relations for k_L for these theories are shown in table 2.5.

Lochiel and Calderbank (1964) and Calderbank and Lochiel (1964) developed empirical relations from the measurements of the pressure change in a water column with a dissolving CO_2 bubble, using the methods described in section 2.6. Johnson et al. (1969) measured the change in volume as a single CO_2 bubble dissolved in a column of water. They developed a relation similar to those of Lochiel and Calderbank (1964) based on the penetration theory of Higbie (1935), with $k_L \propto \sqrt{D_L}$. For the contact time between

the gas and liquid in Higbie's theory, the time taken for the bubble to travel the same distance as its diameter was used. Due to the accuracy of the measurement technique employed in their work, the relation for k_L is also more applicable to larger bubbles, $d_e \approx 6.0 - 40\ mm$.

Clift et al. (1978) reviewed the bubble dynamics and mass transfer characteristics for a range of different system properties. They clarified the influence of surfactants, particularly with bubbles in the surface tension dominated regime. They found a large variation in empirical relations for k_L for intermediate-sized bubbles, which they explained by the different bubble generation techniques, measurement systems and system purities. Surfactant contamination was found to have a significant effect on smaller bubbles. In pure systems, with $d_e < 5.0\ mm$ k_L was observed to increase with reducing d_e, although this relation was not as clear in contaminated systems. With larger bubble sizes there was no difference between clean and contaminated systems.

The empirical relations from Clift et al. (1978) shown in table 2.5 take into consideration the oscillation of the bubble path. These empirical relations follow Higbie's theory, with $k_L \propto \sqrt{D}$. In this case, however, the frequency of the bubble path oscillation, ζ, has been used as an estimate for the gas and liquid contact time. These relations are based on work by Angelo et al. (1966) and Brunson and Welleck (1970) for mass transfer from oscillating particles. In this case, Ω refers to the amplitude of the bubble path oscillation.

Table 2.5: Relations from literature for the liquid-side mass transfer coefficient, k_L

Source	Single Bubble Relation
Higbie (1935)	$k_L = 1.13\sqrt{\frac{u_b}{d_e}}\sqrt{D_L}$
Frössling (1938)	$k_L = 0.6\sqrt{\frac{u_b}{d_e}}D_L^{(2/3)}\nu^{(-1/6)}$
Lochiel and Calderbank (1964) (spherical bubble, immobile surface)	$Sh = 0.84Re^{(1/2)}Sc^{(1/3)}$
Lochiel and Calderbank (1964) (oblate spheroid, immobile surface)	$\frac{Sh_{OS}}{Sh_S} = \left(\sqrt{\frac{A_S}{A_{OS}}}\right)E_R^{1/6}$ $\frac{A_S}{A_{OS}} = \frac{2E_R^{1/3}\sqrt{(E_R^2-1)}}{E\sqrt{(E_R^2-1)}+ln[E_R+\sqrt{E_R^2-1}]}$ $E_R = 1/E$
Lochiel and Calderbank (1964) (spherical bubble, mobile surface)	$Sh = 1.13\sqrt{\left(1-\frac{2.96}{Re^{1/2}}\right)}Pe^{1/2}$
Lochiel and Calderbank (1964) (oblate spheroid, mobile surface)	$\frac{Sh_{OS}}{Sh_S} = \sqrt{\frac{2}{3}(1+k)}\frac{A_S}{A_{OS}}$ $\mathrm{k} = -\frac{e.E_R^2 - E_R\sin^{-1}e}{e - E_R\sin^{-1}e}$

	(A_S = Spherical surface area, A_{OS} = oblate spheroid surface area, Sh_S = Spherical sherwood number and Sh_{OS} = Oblate spheroid sherwood number)
Calderbank and Lochiel (1964) (spherical cap)	$k_L = 0.0179\frac{(2E^2+4)^{2/3}}{E^2+4}\sqrt{\frac{D_L u_b}{d_e}}$
Johnson et al. (1969)	$Sh = 1.13\sqrt{Pe}\sqrt{\frac{d_e}{0.0045+0.2d_e}}$
Clift et al. (1978)	$Sh = \frac{2}{\sqrt{\pi}}\sqrt{\frac{d_e^2\zeta}{D_L}} + \sqrt{1+\Omega+\frac{3\Omega^2}{8}}$
Clift et al. (1978)	$Sh = \frac{2}{\sqrt{\pi}}\sqrt{\frac{d_e^2\zeta}{D_L}} + (1+0.687\Omega)$
Takemura and Yabe (1998)	$\frac{Sh}{\sqrt{Pe}} = \frac{2}{\sqrt{\pi}}\left[1-\frac{2}{3}\frac{1}{(1+0.09Re^{2/3})^{3/4}}\right]\left(2.5+\sqrt{Pe}\right)$
Montes et al. (1999)	$Sh = \frac{2}{\sqrt{\pi}}\sqrt{Pe}\left[1.1+0.027\sqrt{We}\right]$

Takemura and Yabe (1998) performed experiments measuring the mass transfer of O_2 into silicon oil. Because of the higher viscosity of oil their proposed mass transfer relation, which is shown in table 2.5, is suitable for $Re < 100$ and thus for smaller bubbles with a lower rise velocity.

The effect of bubble oscillations on mass transfer has gained attention recently, particularly in the work of Brenn et al. (2006), Veldhuis et al. (2008) and Ern et al. (2012). Oscillations have been shown to affect the localised liquid velocity field around the bubble and the local dissolved concentration gradient. Both of these effects have a large impact on the mass transfer rate, and greater bubble oscillations will increase the mass transfer rate. Martín et al. (2011) showed that in certain cases the increased k_L from the greater oscillation of a larger bubble can offset the reduction in α from the larger bubble size. Bubble path oscillations can also benefit mass transfer by reducing the vertical bubble rise velocity and increasing gas holdup, Martín et al. (2011). Montes et al. (1999) found that Sh was sensitive to the oscillation amplitude, which increased with bubble diameter. They developed a relation for Sh, based on Pe and We, taking into consideration the amplitude and frequency of the bubble path oscillation on mass transfer. The bubble oscillations were shown to induce convective flow around the bubble, which enhances the mass transfer rate. Their proposed relation is shown in table 2.5.

Figure 2.7 shows the k_L values plotted from a selection of the relations given in table 2.5. The k_L values have been calculated using the bubble rise velocity relation for contaminated systems from Fan and Tsuchiya (1990). It is evident that there is a large variation in predicted k_L values. The maximum difference occurs at a bubble size of $d_e \approx 1.0\ mm$, ranging from a maximum $k_L \approx 5 \times 10^{-4}\ m\ s^{-1}$ for a mobile surface and an oblate spheroid from Lochiel and Calderbank (1964), to the minimum value of $k_L \approx 1 \times 10^{-4}\ m\ s^{-1}$ for an immobile surface. The largest relation from Lochiel and Calderbank (1964) to describe a mobile, oblate spheroid in figure 2.7 is very similar to the relation from Higbie's penetration theory, while the smallest values for k_L, as predicted by the immobile surface by Lochiel and Calderbank (1964) are very similar to Frössling's relation for k_L. Nedeltchev et al. (2007) have reported that Higbie's penetration theory over-estimates k_L for ellipsoidal and spherical cap bubbles.

Schulze and Schlünder (1985a) performed experiments with a bubble held stationary in water by a downward flowing liquid, and measured the reduction in bubble size due to mass transfer. They examined bubbles dissolving from a diameter of approximately 5.0 mm, using different gases: absorption of an O_2 bubble required approximately 850 seconds, N_2 took over 1500 seconds, while CO_2 bubbles dissolved in under 20 seconds. Schulze and Schlünder (1985b) also looked at the effect of varying the concentration of gas in the liquid to reduce the concentration driving force for mass transfer from the bubble. They found the mass transfer coefficient was the same for different liquid phase concentrations.

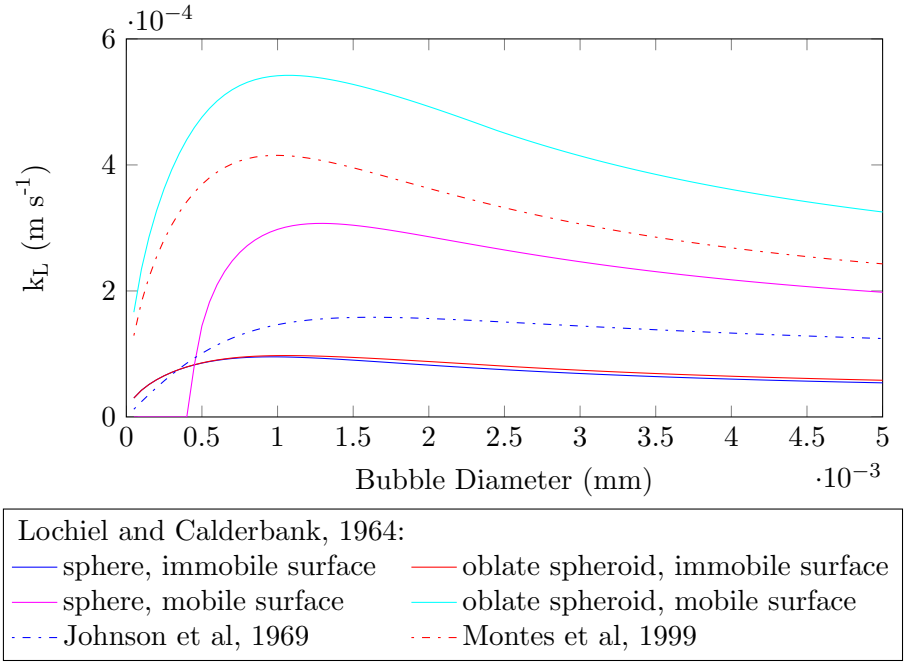

Figure 2.7: Mass transfer coefficient models from literature

2.5.5 Effect of surfactants on mass transfer

Experimental measurements by Leonard and Houghton (1963), Garbarini and Tien (1969), Schulze and Schlünder (1985a), Schulze and Schlünder (1985b), Bischof et al. (1991), Vasconcelos et al. (2002) and Alves et al. (2005) showed a reduction in the mass transfer rate with time. For gases with a high solubility, such as CO_2 Schulze and Schlünder (1985a) observed a distinct transition between the two mass transfer rates. They found the first phase of mass transfer had an absorption rate approximately three times greater than the latter phase. This is in the lower range reported by Rosso et al. (2006) who found the mass transfer rate in surfactant contaminated solutions was typically between $30 - 70$ % of those in pure systems. Bischof et al. (1991) also observed that this transition happens abruptly, and the transition diameter depends on the initial bubble diameter. This change in the k_L value has been described as the change from a mobile to an immobile gas-liquid interface by Griffith (1960) and is attributed to the accumulation of surfactants on the bubble surface.

Vasconcelos et al. (2002) and Alves et al. (2005) approximated k_L for the initial mass transfer rate in un-contaminated liquids with Higbie's penetration theory, which correlated $k_L \propto \sqrt{D_L}$. For the second and reduced mass transfer rate in contaminated liquids they approximated k_L with Frössling's theory, which correlated $k_L \propto D^{2/3}$.

Vasconcelos et al. (2002) and Alves et al. (2005) also observed that the reduction in mass transfer rate due to surfactant accumulation was more noticeable for smaller gas bubbles, as this occurs at a quicker rate. This is partly because smaller bubbles have a larger initial k_L, than larger bubbles for the same mass transfer regime, but possibly

also due to the larger surface area of larger bubbles, which requires a larger amount of surfactant to attach to the bubble in order for it to behave as a rigid sphere. Despite a reduction in k_L, smaller bubbles still have a larger surface area per unit volume and also a greater residence time, due to their lower rise velocities.

As noted previously, the bubble generation process has a large effect on the initial surfactant accumulation, which is responsible for the range of k_L values reported in the literature. Martín et al. (2007) also recognised that the bubble generation process is important as it determines the initial volume, surface area and oscillation amplitude. They observed that larger bubbles take longer to detach from the orifice, which would provide more opportunity for the accumulation of surfactants prior to bubble release. Peters and Els (2012) found that if the initial bubble velocity and Re was sufficiently large that the accumulation of surfactants in tap water would be reduced. This maintained the mobile bubble surface and higher mass transfer rate throughout the bubble rise. Alternatively a slower bubble release allowed the accumulation of surfactants and lower mass transfer rate.

In experiments conducted with wastewater, Jimenez et al. (2014) found that the measured k_L was actually lower than that estimated from Frössling's theory. The mechanism for the reduction of k_L by surfactants is still unclear. It is known, however, that surfactants reduce the flow of liquid around the bubble as well as the internal circulation within the bubble and can obstruct the diffusion through the gas-liquid interface.

2.5.6 Stagnant Cap Model

As noted in section 2.4.4, the spatial distribution of surfactants over the bubble surface is not necessarily constant. The flow around the bubble will cause the surfactants to be re-distributed towards the base of the bubble. This is especially applicable to larger bubble sizes, Ramirez and Davis (1999). The resulting surface tension gradient creates a Marangoni force which will act against the surface flow and cause the bubble surface to become rigid. The surface contamination also increases the bubble aspect ratio and reduces the internal circulation within the bubble.

Savic (1953) proposed the stagnant cap model, which is a theoretical interpretation of contaminant accumulation onto a bubble surface and takes into account the increased surfactant concentration at the base of the bubble. The bubble surface of larger bubbles remains mobile for longer, because of the greater quantity of surfactants required to reduce the bubble rigidity. This concept has been developed further by Griffith (1960), Sadhal and Johnson (1983) and Vasconcelos et al. (2002) and is illustrated in figure 2.8.

In sufficiently contaminated systems this transition between mass transfer rates was not detected as the surfactants quickly accumulated on the bubble surface, immediately inhibiting the gas-liquid interface. Vasconcelos et al. (2002) also observed that the effect

of surfactants is stronger for gases with a greater solubility. Later work by Vasconcelos et al. (2003) measured $k_L\alpha$ in bubble column and air lift reactors using the dynamic gassing-in method. This involves the desorption of DO from the water by sparging N_2 through the reactor, followed by the re-supply and absorption of O_2 and measurement of the DO concentration change. The mass transfer rate and $k_L\alpha$ can then be calculated from the rate of concentration change. Vasconcelos et al. (2003) varied the surfactant concentration in the water and found a sharp change in $k_L\alpha$. A concentration of 10 ppm was sufficient to reduce $k_L\alpha$ by half. Because there was no noticeable effect on the bubble diameter or gas holdup at the increased surfactant concentration, the surfactant concentration was the likely cause of the reduction in k_L. Once a critical surfactant concentration was reached in the liquid, further increase in surfactant concentration had little effect on $k_L\alpha$. Vasconcelos et al. (2003) found that this corresponded to the critical micelle concentration of the surfactant, and that any additional increase in surfactant over this concentration would not affect k_L.

The area of the stagnant cap depends on the concentration of surfactants in the liquid and will increase during the rise of the bubble, as surfactants accumulate onto the bubble surface. The development of a stagnant cap will also affect the distribution of the mass transfer through the bubble surface. The front of the bubble will have a higher interface velocity with a greater concentration profile, resulting in higher mass transfer, Ramirez and Davis (1999). Saboni et al. (2011) adapted the stagnant cap model, with mass transfer occurring by diffusion only through the stagnant cap, and by diffusion and convection through the mobile area of the bubble. The contamination of the interface will also modify the convection around the bubble, Cuenot et al. (1997).

Alves et al. (2004) developed a model based on the stagnant cap theory from experimental data in a stirred tank reactor. They found that in contaminated systems $k_L\alpha$ is larger in the bottom half of the tank, i.e. during the initial stages of bubble rise, due to a greater portion of gas-liquid interface of the bubble being mobile in the lower section of the tank. As the bubble rises up the column, the area of the stagnant cap increases

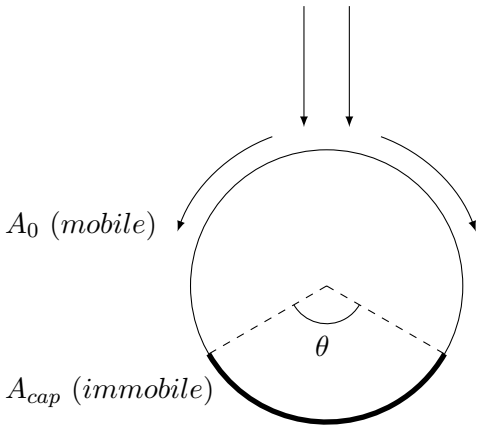

Figure 2.8: Stagnant Cap Model

and thus, the mass transfer through the bubble surface reduces. The rate at which the mass transfer reduces depends on the rate of accumulation of surfactants on the bubble surface, and thus on the surfactant concentration in the liquid phase.

2.5.7 Gas concentration

Leonard and Houghton (1963) commented that as k_L varies with time, the average measured value of k_L will depend on the duration over which the measurements are taken. Despite these authors observing a reduction in the rate of absorption with time due to surfactant accumulation, they found an increase in the rate of desorption. This has not been reported elsewhere, and is interesting as it is often assumed that in the system k_L will be the same for the desorption and absorption processes. Leonard and Houghton (1963) hypothesised that there may be an effect from the inert gas fraction which could increase the gas side resistance. This effect could be enhanced by the reduction of internal circulation within the bubble caused by surfactant accumulation.

Danckwerts (1965) adopted an analytical approach to investigate the effect of dilute gas mixtures and considered the increased surface area of a bubble with an insoluble gas, as well as the reduced partial pressure of the soluble gas inside the bubble. Danckwerts (1965) theorised that these factors would approximately cancel one another out, and that 95 % of the soluble gas would be absorbed from the dilute bubble in the time required to dissolve 100 % of the gas from a concentrated bubble. Loudon et al. (1966) performed a more thorough analysis considering different bubble shapes and sizes, and reached the same conclusion as Danckwerts (1965). The effects of the bubble hydrodynamics, however, were not fully considered by these authors.

The importance of each of these processes in the mass transfer from a bubble is not understood and further research is required to understand the mass transfer process. A better understanding of the mass transfer process in a single bubble would help in improving the design of mass transfer reactors. The differences between mass transfer from single bubbles and bubble swarms also need to be considered. In bubble column reactors the dynamics of the bubble rise and hydrodynamics of the system have a significant effect on the mass transfer. This is discussed further in the next section.

2.5.8 Multiphase mass transfer relations

As discussed previously in section 2.4.5 there are significant differences between the rise velocities of single bubbles and a bubble swarm, and this also has an effect on the mass transfer rate. Induced turbulence from bubble swarms increases the gas-liquid interface velocity, although the localised dissolved carbon concentration surrounding multiple bubbles will be larger than for isolated single bubbles. If the bubbles are undergoing

vortex shedding, however, then the localised dissolved concentration can quickly be convected away from the bubble with the shedding of the bubble vortex, Koynov and Khinast (2005). This will benefit mass transfer, by dissipating the highly concentrated liquid region away from the bubble.

Martín et al. (2011) found that overall the mass transfer rate was higher in bubble swarms, than predicted by empirical relations. There are many factors which would affect this for different flow regimes, such as the degree of bubble coalescence and break-up. This complexity is a reason for the difficulty in comparing single and multiple bubble mass transfer relations.

Many of the empirical relations proposed for the mass transfer in bubble swarms are expressed in terms of the volumetric mass transfer coefficient, $k_L\alpha$. This is due to the difficulty in measuring the volumetric surface area in multiphase flows. Depending on the flow regime, different factors will have an effect on the bubble hydrodynamics. In the homogeneous bubble flow regime ($u_B < 0.5m\ s^{-1}$) there is no bubble coalescence or break-up and gentle mixing. As a result of this the bubble size and thus mass transfer is more dependent on sparger design and system properties, Kantarci et al. (2005), Shah et al. (1982). In heterogeneous flow regimes with larger bubble velocities, the energy dissipation is often used to quantify the mass transfer, Calderbank and Moo-Young (1961). The energy dissipation rate is shown in equation 2.33, as quantified by Shah et al. (1982). This is based on Kolmogoroff's theory of isotropic turbulence, where the total energy dissipation in a bubble column is calculated by the pressure drop multiplied by u_G.

$$\epsilon = u_G g \tag{2.33}$$

Empirical relations that have been proposed for the estimation of k_L are given in table 2.6. Calderbank and Moo-Young (1961) proposed two empirical relations for small ($d_e < 2.5\ mm$) and large ($d_e > 2.5\ mm$) bubble sizes. The empirical relation for large bubbles follows Higbie's theory, with $k_L \propto \sqrt{D_L}$; while the relation for smaller bubbles follows Frössling's theory for a rigid bubble, with $k_L \propto D_L^{2/3}$. Despite this separation based on bubble size, neither of the empirical relations from Calderbank and Moo-Young (1961) uses the bubble size to calculate k_L.

Hughmark (1967a) provided a k_L empirical relation for single bubble and bubble swarms. This proposed empirical relation relates Sh to the diffusivity coefficient, $k_L \propto D_L^{0.623}$. This approach lies somewhere between Frössling's and Higbie's mass transfer theory, although it is closer to the rigid particle theory of Frössling (1938).

Akita and Yoshida (1974) proposed an empirical relation for Sh which is proportional to the Galilei (Ga) and the Bond numbers (Bo), which are shown in equations 2.34 and 2.35, respectively. The empirical relation was derived from experimental results, combining

data from single orifice spargers as well as perforated and porous plate diffusers. The mass transfer experiments were conducted with O_2 absorbing into a variety of liquids, with the mass transfer rate determined by measuring the DO concentration by titration methods. This was also combined with image analysis to quantify the bubble size and thus the volumetric surface area.

Galilei number

$$Ga = \frac{g d_e^3}{\nu^2} \tag{2.34}$$

Bond number

$$Bo = \frac{g d_e^2 \rho_L}{\sigma} \tag{2.35}$$

More recently Nedeltchev et al. (2007) proposed an empirical relation for k_L which is based on Higbie's penetration theory and is applicable to the homogeneous flow regime. They approximated the gas-liquid contact time with the ratio of the bubble surface to the rate of surface formation. As noted above, at lower gas flow rates and in homogeneous flow regimes the bubble generation process has been shown to affect the mass transfer rate. To account for this the rate of surface formation (R_{sf}) was included in the mass transfer empirical relation; this takes into consideration the major and minor bubble diameters and bubble rise velocity. The empirical relation developed by Nedeltchev et al. (2007) is suitable for intermediate-sized bubbles, $1.4 < d_e < 6.0\ mm$, and also includes a correction factor (f_c) to account for the ellipsoidal bubble shape. Surprisingly the bubble rise velocity is not always considered in mass transfer relations for bubble swarms, despite the importance of the gas velocity in determining the mass transfer rate, Chaumat et al. (2005). Hughmark (1967a) included the bubble velocity in his proposed relation; however this is not directly considered by Calderbank and Moo-Young (1961) or Akita and Yoshida (1974). Bubble coalescence and thus bubble size is also affected by the bubble velocity, which will have a large effect on the mass transfer, Jin et al. (2007). Due to the effects of bubble coalescence and break-up in heterogeneous flow regimes, the energy dissipation is often a better description of system properties, Kantarci et al. (2005).

Table 2.6: Empirical relations from literature for the liquid-side mass transfer coefficient, k_L

Source	Bubble Swarm Relation
Calderbank and Moo-Young (1961) (large bubbles)	$k_L = 0.42 \left(\frac{(\rho_L - \rho_G)\mu_L g}{\rho_L^2}\right)^{1/3} \times Sc^{-1/2}$
Calderbank and Moo-Young (1961) (small bubbles)	$k_L = 0.31 \left(\frac{(\rho_L - \rho_G)\mu_L g}{\rho_L^2}\right)^{1/3} \times Sc^{-2/3}$
Hughmark (1967b)	$Sh = 2 + 0.0187 Sc^{0.546} Re^{0.779} \left(\frac{d_e g^{1/3}}{D_L^{2/3}}\right)^{0.116}$
Akita and Yoshida (1974)	$Sh = 0.5 Sc^{1/2} Ga^{1/4} Bo^{3/8}$
Nedeltchev et al. (2007)	$k_L = f_c \sqrt{\frac{4 D_L R_{sf}}{\pi a_b}}$
	$f_c = 0.124 \left(\frac{g(\rho_L - \rho_G) d_e^2}{\sigma}\right)^{0.94} \left(\frac{\rho_G}{1.2}\right)^{0.15}$
	$R_{sf} = \pi \sqrt{\frac{d_A^2 + d_B^2}{2} - \frac{(d_A - d_B)^2}{8}} u_B$

Figure 2.9 plots the k_L values for bubbles of diameter $d_e < 5.0\ mm$ for the bubble swarm relations in table 2.6 and includes the relations of Higbie (1935) and Frössling (1938) (shown in table 2.5). Where appropriate the bubble rise velocity has been calculated from the relation for purified systems proposed by Tomiyama et al. (1998). For bubbles with $d_e < 2.0\ mm$, Higbie's relation gives a higher estimated value for k_L in comparison to the empirical relations developed for bubble columns. An increase in d_e also gives an increase in predicted k_L values according to the relations of Calderbank and Moo-Young (1961) and Akita and Yoshida (1974). The relation from Akita and Yoshida (1974) takes into consideration the bubble diameter by the inclusion of Ga and Bo. Both of these relations are suitable for the heterogeneous flow regime in bubble swarms. The relations proposed by Hughmark (1967a) and Nedeltchev et al. (2007) are more applicable to homogeneous flow regimes: in figure 2.9 it can be seen that these relations are closer to Frössling's rigid particle theory, with lower values for k_L.

There are interesting differences between the relations for k_L in bubble swarms as shown in figure 2.9 and those for single bubbles in figure 2.7. The increase in k_L with bubble size is more apparent in the bubble swarm relations. The value of k_L for single bubbles peaked at $d_e \approx 1.0\ mm$, with any further increase in d_e resulting in either a constant or reducing k_L. Conversely for bubble swarms the relations from Calderbank and Moo-Young (1961), Akita and Yoshida (1974) and Nedeltchev et al. (2007) show an increase in k_L with d_e.

The increase in k_L with d_e is more pronounced for bubble swarms than single bubbles. In terms of the engineering design of mass transfer systems, this could result in a compromise, in which a lower value of k_L is accepted in order to obtain a greater volumetric

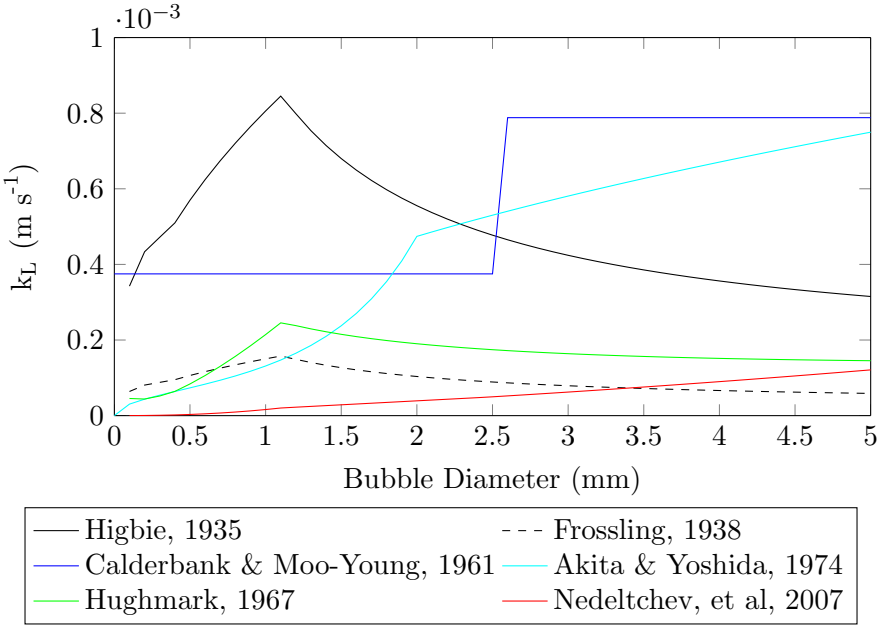

Figure 2.9: Mass transfer coefficient models from literature

surface area and thus increase overall mass transfer. Motarjemi and Jameson (1978) measured the mass transfer rate from O_2 microbubbles absorbing into tap water. They found k_L values which approximated those from Frössling's theory with a bubble diameter, $d_e \approx 0.15\ mm$, and found a slight increase in k_L with d_e. To achieve optimal mass transfer they recommended smaller bubbles, which may have a lower value for k_L, although this would be compensated by an increased volumetric surface area.

Following the same logic as that applied by Motarjemi and Jameson (1978), surfactants may provide an overall benefit to the mass transfer in bubble swarms, despite a reduction in k_L. Krishna et al. (1999a) discuss the effects of surfactants on inhibiting bubble coalescence and maintaining a smaller average bubble size. This increases the gas hold-up and gas-liquid contact area. Muller and Davidson (1995) reported increased $k_L\alpha$ values in the presence of surfactants and attributed this to the reduction in coalescence and smaller average bubble size.

2.5.9 Gas-Liquid-Solid Systems

As noted in section 7.4, Prakash et al. (2001) studied the effects of yeast cells on bubble behaviour. Interestingly it was observed when the concentration of yeast cells was increased, that the rise velocity of larger bubbles increased, although the velocity of smaller bubbles reduced. They also found that the surfactant concentration was proportional to the concentration of yeast cells.

This may not be the case in micro-algal cultivation media, where different stages in the growth cycle may correspond to varying concentrations of extracellular compounds. The growth media could also be sourced from seawater, saline or wastewater which may then be supplemented with nutrients to enhance algal growth. In such a system there is a large potential for surfactants to have an impact on the bubble dynamics and mass transfer. Kuhnhenn-Dauben et al. (2008) measured the bubble residence times in an algal system. The experiments were performed in a heterogeneous mesocosm environment and in a homogeneous environment with *Cylindrotheca closterium*, a diatom which is known to produce a mucilaginous substance. They found that the bubble residence time increased with the chlorophyll and DO concentrations. There was little relation between the bubble residence time and the dissolved organic carbon, however, suggesting that the exudates produced by *Cylindrotheca closterium* did not interfere with the bubble dynamics in this case. Kuhnhenn et al. (2006) also performed studies on the shear viscosity of liquid algal cultivation media and found that the viscosity of the liquid varied depending on species type. *Nitzshia clostterium* was found to excrete dissolved organic material (DOM) which significantly increased the viscosity of the medium, whereas there was no statistical difference in the measured liquid properties with *Thalassioira rotula*, *Thalassiosira punctigera* or *Phaeocystis sp.*

2.6 Measurement Techniques

To design a methodology to carry out this research a range of experimental techniques have been reviewed in this section. Over the last several decades a variety of different experimental techniques have been developed to investigate the bubble dynamics and mass transfer from single bubbles and multiphase flows.

For single bubble measurements the earlier experimental techniques often used global volume or pressure change measurements in a bubble column. These were sensitive enough to detect changes in the single bubble volume. Calderbank and Lochiel (1964) and Lochiel and Calderbank (1964) used a micro-manometer to measure the pressure differential caused by the introduction of a gas bubble into the water column. They combined these measurements with shadowgraph images taken underneath the bubble column to measure the bubble cross-sectional area. Johnson et al. (1969) employed a similar measurement technique, by measuring the change in volume of the total system as a single CO_2 bubble dissolved in a 3.0 m tall, 0.09 m diameter water column. The volume measurements were taken by measuring the movement of mercury in a capillary tube which fluctuated with changes in the volume of the whole system. Garbarini and Tien (1969) carried out experiments which compared the pressure change method utilised by Lochiel and Calderbank (1964) with a photographic method. They utilised a camera which could move on a vertical platform to track the rise of a bubble. They found that there was a high error in both methods and that the results were difficult to reproduce. These authors favoured the photographic method over the pressure change method, which was only found to be accurate for bubbles with a diameter $d_e > 4.0\ mm$.

Motarjemi and Jameson (1978) also used a photographic method, with two cameras used to capture images of the bubble at two different heights. From the images, the change in bubble volume could be measured and used to calculate the mass transfer rate. More recent studies on single bubbles have also employed photographic techniques, Sam et al. (1996), Takemura and Yabe (1998), Tomiyama et al. (2002), Mena (2005), Quinn et al. (2014) and Tagawa et al. (2013). These have benefited from the improvement in camera design, such as digital photography, high speed video and improved image resolutions. The photographic techniques also allow the analysis of different bubble characteristics, such as bubble shape, oscillations in the rise path and rise velocity.

A number of studies have involved visualisation of the bubble wake. Some of these have been conducted using fluorescent dyes with the Planar Laser Induced Fluorescence (PLIF) technique, Stohr et al. (2009), Francois et al. (2011) and Jimenez et al. (2014). The use of a dye in this method could have effects on the surface chemistry of the bubble, and other techniques can be used to minimise this. Montes et al. (1999) produced H_2 microbubbles generated with a tungsten wire to act as tracers for the visualisation of flow around a larger air bubble ($d_e > 1.0\ mm$). A number of authors have also employed Schlieren optics to study the wake from bubbles, de Vries (2001) and Veldhuis

et al. (2008). This technique exploits the small difference in refractive index of water at different temperatures to visualise the flow of water when a temperature gradient is applied.

A series of experiments have studied the mass transfer from a bubble which is kept stationary with a downward liquid flow, Schulze and Schlünder (1985a), Schulze and Schlünder (1985b), Vasconcelos et al. (2002) and Alves et al. (2005). This enabled photographic measurement of the change in bubble size with a stationary camera, and also allowed longer experimental runs to study the effects of surfactant accumulation on the bubble surface.

In multiphase flows the use of image analysis to measure the bubble size is limited to low gas holdups, Euh et al. (2006). A wide variety of experimental techniques have been developed for multiphase flows: Boyer et al. (2002) provide a review of many of these. The mass transfer measurements for multiphase flows predominantly use chemical analytical techniques. Many of the authors study the absorption of O_2, which enables the relatively easy monitoring of the DO concentration with a DO probe. Kulkarni (2007) conducted experiments with the oxidation of sodium sulfite by sparging air into solution and measuring the DO concentration. This was combined with Laser Doppler Anemometry (LDA) to measure the superficial gas velocity and gas volume to estimate the bubble size distribution.

Another technique that is often used to measure the rise velocity and gas holdup in multiphase flow reactors is the dynamic gas disengagement method, Kantarci et al. (2005). This involves measurement of the rate of change of gas volume in a bubble column when the input gas flow rate is switched off. Due to the different rise velocities of different bubble sizes, the gas holdup will reduce at different rates according to the bubble sizes in the column. The reduction in gas holdup will be slower with smaller bubbles. The rate of reduction in gas holdup can be analysed to determine the bubble size distribution from the rate of change of gas holdup. The gas holdup in these methods can be measured using a manometer. Jin et al. (2007) used the dynamic gas disengagement method along with electrical resistance tomography to measure gas holdup. The electrical resistance tomography technique has a low spatial resolution, but provides a visualisation of the cross-sectional profile of the gas holdup in a bubble column.

Focused Beam Reflectance measurements ($FBRM$) provide a method to measure the chord length distribution of particles. This measures the backscatter of laser light which travels back up the probe due to reflection by the particles. The chord length distribution can be analysed by measuring the time taken for the light to be reflected back to the detector. Heath et al. (2002) found that this technique was not effective with glass beads, however, due to the transparency of the particles, and this may cause problems in detection of bubbles.

Several different acoustic techniques can be applied to studying multiphase flows. Some of these require a rapid change in bubble volume, from effects such as cavitation, while others can be used with a constant bubble volume. A shadowing technique developed by Leighton (1994) relies on ultrasound waves being scattered by bubbles from which the interfacial area of bubbles can be deduced. Cents et al. (2004) used an ultrasonic spectroscopy technique to measure particle sizes from 1 μm to approximately 1 cm. As the sound wave travels through the liquid the properties of the wave change as it interacts with the particles in the fluid. The bubbles in a liquid will oscillate due to the difference in density with the continuous phase. Part of the energy of these oscillations will be converted into heat due to friction. Different size bubbles will have different dampening frequencies and from this the gas-liquid contact area can be measured, Cents et al. (2004). There are difficulties in data analysis and noise reduction, however, particularly in turbulent reactors and this may become a problem with high gas holdups, Boyer et al. (2002).

2.6.1 Optical Fibres

Optical fibre probes are an intrusive measurement technique, which can be used to measure the localised bubble size. Optical fibre sensors are able to detect whether the tip of the probe is in contact with the gas or liquid phase. This is achieved by sending an infra-red signal down the optical fibre which arrives at the tip of the probe, and is then either refracted away from the tip or reflected back up the optical fibre. This depends on the refractive index of the medium with which the probe tip is in contact. When the optical fibre tip is in contact with air, as represented in figure 2.10b, the difference in refractive index between the air and the silica of the optical fibre is large. The geometry of the optical fibre tip and the difference in refractive index results in continued internal reflection of the infra-red light at the tip of the fibre. This results in the infra-red light signal reflecting back up the optical fibre, where it can be measured by the optoelectronic unit. The detection of the light signal can then be converted to a voltage and a digital signal. When the tip is in contact with water, the difference in refractive index between the silica and water is significantly less, and as a result the internal reflection that occurs at the tip is significantly reduced. This results in a portion of the infra-red light refracting away from the tip, causing a reduction in the amount which is reflected at the optical fibre tip. The optoelectronic unit thus records a reduced signal. This process can be employed in multiphase flows to detect the quantities of gas and liquid present, as well as the properties of the bubbles. The stages in the optical fibre phase detection are shown in figure 2.10.

The time during which the tip of the optical fibre probe is in contact with the gas phase, known as the latency time, can be multiplied by the bubble rise velocity to find the bubble chord length, d_C. The chord length is the vertical length of the bubble which

comes into contact with the optical fibre probe. A representation of the bubble chord length is shown in figure 2.11. As can be seen from figure 2.11 the position which the optical fibre intersects the bubble will affect the bubble chord length. When the optical fibre pierces the bubble in the centre, the chord length will be equal to the minor bubble diameter (d_B).

There are various methods to find the bubble velocity using optical fibre probes. The

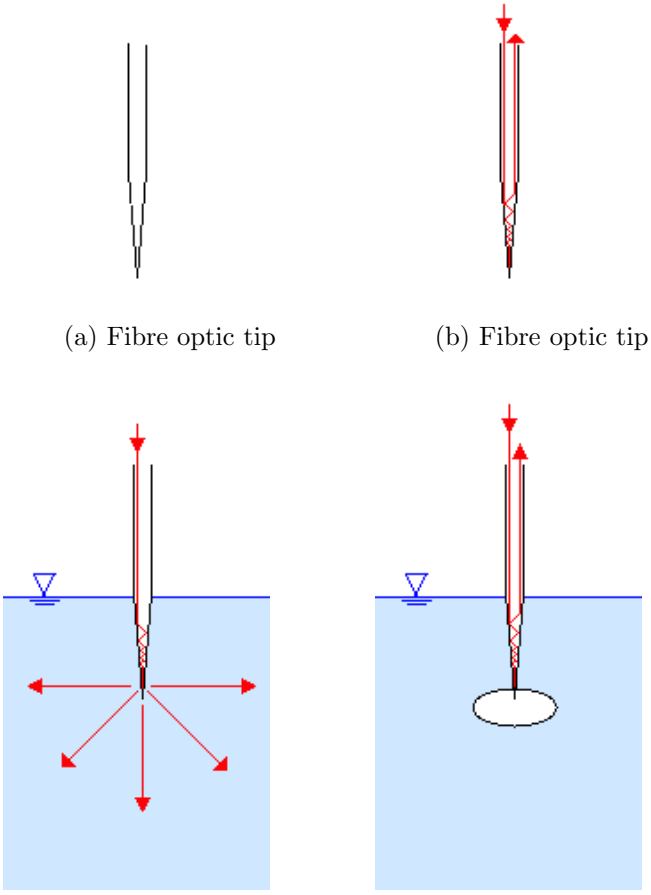

(a) Fibre optic tip (b) Fibre optic tip

(c) Fibre optic tip (d) Fibre optic tip

Figure 2.10: Stages of multiphase flow optical fibre detection

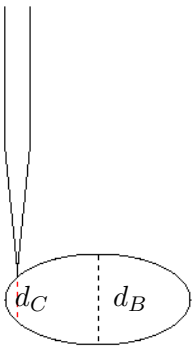

Figure 2.11: Measured bubble chord length from optical fibre probe

simplest requires two optical fibre sensors positioned a short vertical distance apart. The time difference in detection of the rising bubble measured by the two sensors can be used with the distance between the sensors to find the bubble rise velocity. Alternative methods for finding the bubble rise velocity include analysis of the gradient of the bubble detection signal, Cartellier (1992) or a modified fibre optic tip, with a groove positioned at the base of the tip to take a double measurement of the gas phase, Saito et al. (2009).

The properties of the optical fibre tip are important in achieving a sensitive detection between the gas and liquid phases. Cartellier (1990) compared different geometries and orientations of optical fibre probe tips, and measured the response time when the tip was raised in and out of water at different velocities. They found that the response time reduced with increasing velocity; at high velocities, however, the response time becomes independent of velocity. This suggests that the wetting and de-wetting time of the optical fibre probe has an influence at high velocities. Cartellier (1992) found that the probe tip geometry affects the tip drying and this can have an impact when distinguishing between the gas and liquid phases. The angle of the probe tip was found to have an effect on the duration for which the gas-liquid interface is pierced by the optical fibre tip. A lower angle between the tip and interface resulted in quicker penetration by the optical fibre.

Chabot and de Lasa (1993) conducted experiments using dual spherical bulb optical fibre sensors. The probes were made from 400 μm silica fibre optic and mounted and sealed using a synthetic porcelain cement into two stainless tubes with a vertical separation distance of 4.0 mm. The fibre optic probes were inserted at a 45° angle to the vertical. Fibre optic measurements were validated with gas hold-up readings from static pressure taps. The bubble rise velocity was smaller for bubbles closer to the wall of the bubble column. Similarly the bubble chord length reduced when the bubble was closer to the bubble column wall.

Serdula and Loewen (1998) used 1.0 mm diameter sapphire-tipped conical shaped optical fibre probes (*Photonetics Inc.*) to measure the bubble size distribution generated from breaking waves. The measurements from the optical fibre probe were compared with video analysis used to measure the bubble velocity. It was observed that the difference between the probes was more significant than the effect of changing the angle of the probe. Serdula and Loewen (1998) used a relation to find the bubble diameter from the measured bubble chord length by multiplying the chord length by a correction factor of 1.5. This makes the assumption, however, that the bubbles are spherical. Hoang et al. (2015) compared bubble size measurements from a five-point conductivity probe and high speed video. As with optical fibre sensors, the conductivity probe intersects the bubble at different locations and provides measurements of the bubble chord length. Hoang et al. (2015) analysed the chord length distribution to find the bubble size distribution. On average the measured bubble diameter was approximately 1.23 times larger than the bubble chord length. They also found that this ratio remained constant for

different flow conditions. This could vary, however, in different multiphase flow systems, different operating conditions or with different degrees of bubble coalescence and break-up.

Kiambi et al. (2001) used a double optical fibre probe to measure the local mean volumetric area and analyse the effect of the superficial gas velocity. They compared two methods to calculate the gas-liquid contact area; using the bubble chord length distribution, and analysing the signal to detect the velocity and angle of impact of bubble with the probe. This latter approach, however, assumed a spherical bubble.

Chemical measurements were combined with optical fibres by Lau et al. (2004) who coated the tip of the optical fibre with a fluorescent dye. This dye could be used to detect the DO concentration of liquid coming into contact with the tip. Light was transmitted down the optical fibre to excite the fluorescent dye at the tip; when DO molecules come into contact with the dye, energy is absorbed by the O_2 molecules and the DO concentration can then be inferred from the variation in light intensity.

Saito et al. (2009) investigated the design of the optical fibre probe. They compared a design with four tips to a wedged-shaped probe, which was designed to measure sub-millimetre bubbles and droplets. The wedge-shaped probe had a tip of diameter 52 μm which was fabricated with a femtosecond pulse laser to measure bubbles of diameter $50-100$ μm. A groove was formed at the base of the tip which allowed double detection of the air phase for velocity measurement. Using high speed video they measured the deformation of droplets to be just over 3% of the minor axis.

Vejrazka et al. (2010) looked in further detail at the deformation of the bubble as it comes into contact with the tip of an optical fibre probe. They analysed high speed video to detect modifications in the bubble shape. They found differences in the bubble and optical fibre tip interaction based on the location of the intersection of the bubble. They observed a reduction in the latency time when the optical fibre tip pierces the centre of the bubble. This was attributed to the deceleration of the bubble, and results in over-estimation of the bubble size. When the optical fibre probe intersects the edge of the bubble, the bubble is deflected slightly away from the probe. This results in a smaller fraction of the bubble being detected and a smaller bubble size measurement. Overall the average bubble size is generally underestimated. Vejrazka et al. (2010) proposed a correction factor to account for this.

Mizushima and Saito (2012) measured the localised dissolved CO_2 concentration in the wake of a CO_2 bubble using a photoelectric optical fibre probe. They also observed a slight error in the bubble chord length measurements, as a result of the bubble path oscillations and the variation in the angle of intersection between the bubble and the optical fibre. Sakamoto and Saito (2012) developed a ray tracing simulator for the optical fibre tip and bubble interface to find the optimal cutting angle of the tip to

maximise the gas phase signal: this was approximately 30°. They also identified pre-signals from the reflection of infra-red light from the bubble surface before the optical fibre tip penetrates the bubble. They attributed this pre-signal to the reflection of the rear bubble surface. Mizushima et al. (2013) used this pre-signal detection to measure the location and angle of intersection between the optical fibre tip and the bubble. This allowed them to correct the signal to estimate the bubble diameter directly from the optical fibre probe measurements. With this probe design they were able to measure bubble sizes from $0.85 < d_e < 5.0\ mm$.

Optical fibre sensors have the advantage of being able to measure the localised bubble size. By varying the axial position of the optical fibre tip in the bubble column, the variation in bubble size with height can then be measured. This could be used to give a detailed analysis of the mass transfer rate in bubble swarms. Despite the disadvantages of optical fibres due to the intrusive nature of the measurements, these measurement errors can be accounted for. Global, non-intrusive methods would be unable to provide the same detailed analysis regarding the change in bubble size in a bubble column with a high gas-holdup.

2.7 Summary & Objectives

Most of the studies reviewed in this chapter focus on the bubble characteristics or on mass transfer, either with single bubbles, or on a larger scale looking at bubble columns. This work looks at the effect bubble characteristics have on mass transfer on both single bubbles and bubble swarms. Despite differences between single and multiple bubbles, which are mainly due to the differences in the hydrodynamics of multiphase flows, a better understanding of the mass transfer from a single bubble would help to improve our fundamental understanding of mass transfer and benefit the design of industrial bubble columns.

There is uncertainty regarding the effect of a reduced CO_2 gas concentration within the bubble on k_L. Weissman and Goebel (1987) reported lower absorption efficiencies for flue gas than pure CO_2. The concentration of CO_2 in flue gases typically varies between $5 - 15\%$. Therefore there will be a substantial concentration of remaining gas, mainly N_2 or air, which would not be of interest for the mass transfer process. Leonard and Houghton (1963) suggested there may be an increased gas side resistance with a reduced gas concentration in the bubble. They also observed different mass transfer rates with absorption and desorption processes. In micro-algal cultivation systems the mass transfer rate of the desorption process is important for the removal of DO from the algal cultivation media.

The effect of surfactants has led to renewed interest in the interaction between the characteristics of bubbles and mass transfer. In particular single bubbles have been identified

as exhibiting a reduction in the mass transfer rate due to surfactant accumulation, as reported by Schulze and Schlünder (1985a), Schulze and Schlünder (1985b), Bischof et al. (1991), Vasconcelos et al. (2002), Vasconcelos et al. (2003), Alves et al. (2004) and Alves et al. (2005). This has not been identified, however, in the mass transfer rate from bubble swarms. A reason for this could be the difficulty in measuring the localised variation of k_L in bubble swarms. In surfactant-rich environments such as algal cultivation media the surfactant concentrations will reduce the mobility of the bubble surface and the mass transfer rate. For single bubbles, a smaller bubble requires less surfactant to cover all of the bubble surface, resulting in a mass transfer rate which follows Frössling's theory. For larger, single bubbles a larger amount of surfactant is required before the bubble surface becomes immobile, and the stagnant cap model can be applied to estimate the mass transfer. This will be different for bubble swarms, however, where for a given gas volume and amount of surfactant in the liquid, smaller bubbles would increase the volumetric surface area and potentially reduce the surfactant concentration on the bubble surface.

Chapter 3

Materials & Methods

3.1 Introduction

This chapter describes the materials and methods used in the methodology to investigate the mass transfer from single bubbles and bubble swarms. Experiments were conducted with different CO_2 compositions in the gas phase and different dissolved oxygen, DO and dissolved inorganic carbon, DIC concentrations in the liquid phase to examine the counter-diffusion at different mass transfer rates. By measuring the bubble size, it is possible to dissociate the mass transfer coefficient k_L from the interfacial area α. The mass transfer rate can be deduced from the change in bubble volume and the change in concentration of the CO_2, while the interfacial area can be calculated from the bubble size.

3.2 Standard Methods

The CO_2, O_2 and N_2 were each supplied from gas cylinders (BOC, UK), with a regulator and rotameter used to control the pressure and flow rate. The different gas compositions of the input gas bubbles were composed by varying levels of CO_2 and air. For the single bubble experiments the CO_2 was used to fill an impermeable gas sample bag. For the experiments with pure CO_2 the gas from the sampling bag was directly pumped into the bubble column with a peristaltic pump (Watson-Marlow, UK). Different concentrations were produced by syringing pure CO_2 from the gas sampling bag and air into another gas sample bag, which was then used to provide the gas for the single bubble experiments. For the bubble swarm experiments the input CO_2 pressure and flow rate were controlled with the regulator and rotameter. Different input CO_2 concentrations were achieved by combining the CO_2 from the gas cylinder with air from an air pump, which was mixed in the inlet tubing.

Output gas samples were collected for both single bubble and bubble swarm experiments at different heights in the bubble column and the CO_2 concentration was analysed with gas chromatography (GC). The samples were collected with an inverted funnel placed into the column, connected to a tube and syringe which stored the samples until measurement with the GC.

As well as varying the gas composition of the bubble, the effect of varying the concentration of O_2, N_2 and CO_2, dissolved in the water was tested. These gases were supplied from separate pressurised gas canisters, (BOC, UK) the pressure and flow rate were controlled with the regulator and rotameter and the gas was dissolved into the water by bubbling. During these saturated gas experiments the bubble column was sealed to prevent desorption from the free surface and an outlet was connected to a gas sample bag to ensure atmospheric pressure conditions were maintained in the column. For the O_2 and N_2 pre-saturation experiments the DO concentration was monitored with a DO probe until the desired concentration was achieved. For total dissolved carbon pre-saturated experiments, a water sample was taken and measured with the total dissolved organic/ inorganic carbon analyser.

Experiments were conducted with tap water, de-ionised water and artificial seawater. The water was replenished daily and left for approximately one hour before bubble experiments were conducted. The artificial seawater was made to a concentration of 35 $g\ L^{-1}$ from *Ultramarine Synthetic Sea salts*, (*Waterlife Research Ind. Ltd.*, U.K). The methods used for the gas chromatography, total dissolved carbon, pH and DO measurements are described below.

Gas Chromatography

A 5 ml sample of the input gas was taken either from the sample bag, inlet tubing or collected from the gas collector placed in the bubble column. The concentration of CO_2 in the input gas was measured by gas chromatography (Varian Star 3400 CX gas chromatograph (GC)), (Varian Ltd, Oxford, UK). The gas chromatograph was fitted with a Hayesep C column with argon as the carrier gas at a flow of 50 $ml\ min^{-1}$ and a thermal conductivity detector. The sample was injected into a gas sampling loop and the concentration was compared with a standard gas sample containing either 100 % CO_2, or a 65% CH_4 and 35 % CO_2 (v/v) (BOC, UK) mixture for calibration. The measurements were averaged over five repeats.

Total Dissolved Carbon

Water samples were taken before and after the single bubble experiments, from the top and bottom of the bubble column. The dissolved inorganic carbon concentration was measured from the water sample using a *Dohrman DC-190* total organic carbon analyser, *(Rosemount Analytical Inc., USA)*. This converts the dissolved carbon to CO_2 by high temperature catalytic combustion at $680°C$ in a pure O_2 environment with

platinum on alumina as a catalyst. The total inorganic carbon is converted to CO_2 by acidification in a chamber containing phosphoric acid. The CO_2 generated from both these processes is measured by a non-dispersive infrared detector (NDIR).

pH and DO measurements

The pH and dissolved oxygen (DO) concentration were measured at the top of the column throughout the single bubble and bubble swarm experiments. The pH was measured using a Jenway 3010 meter (Bibby Scientific Ltd, UK) with a combination glass electrode, calibrated in buffers at pH 7 and 9.2. The pH meter was temperature compensated and had a sensitivity of ± 0.01 pH unit and accuracy of 0.01 ± 0.005 pH units. Buffer solution used for calibration was prepared from buffer tablets (Fisher Scientific, UK) prepared according to the supplier's instructions. The pH probe was rinsed with de-ionised water in between measurements and placed into a mild acid solution to avoid cross-contamination.

The *DO* was measured with a YSI 5000 DO meter (YSI Inc., USA). The probe was maintained by cleaning the silver anode by soaking it in a 14 % ammonium hydroxide solution, rinsing with de-ionised water and lightly sanding with wet-dry paper. The gold cathode was cleaned by lightly sanding with wet-dry paper and rinsing with de-ionised water. The membrane cap was filled with potassium chloride solution and fitted around the sensors ensuring there were not any air bubbles present. The *DO* zero measurement was checked with a sodium sulphite solution. The *DO* probe includes a stirring stick, which was used in the bubble column measurements for both the pH and *DO* measurements to ensure homogeneity.

3.3 Single Bubble experimental set-up

A square bubble column, with dimensions $1.1 \times 0.2 \times 0.2$ m was used in the single bubble experiments; the schematic of the experimental set up is shown in figure 3.1. The column was constructed from 12 mm thick perspex, with the square design chosen to ensure a flat surface to reduce the distortion of photographs taken through the perspex. The internal column diameter was designed to be large enough to ensure wall effects on the bubble are negligible.

Shah et al. (1982) observed that a column diameter of 0.15 m or above was sufficient to prevent any wall effects on measurements of the gas holdup. Krishna et al. (1999b) performed experiments with single bubbles rising through a range of different column diameters from $0.01 - 0.63$ m and found that a column diameter eight times the bubble diameter did not cause any wall effects. Based on this and the bubble column used in these experiments a bubble diameter over 19.0 mm would be within the range of wall effects. The maximum individual bubble diameter in these experiments will be

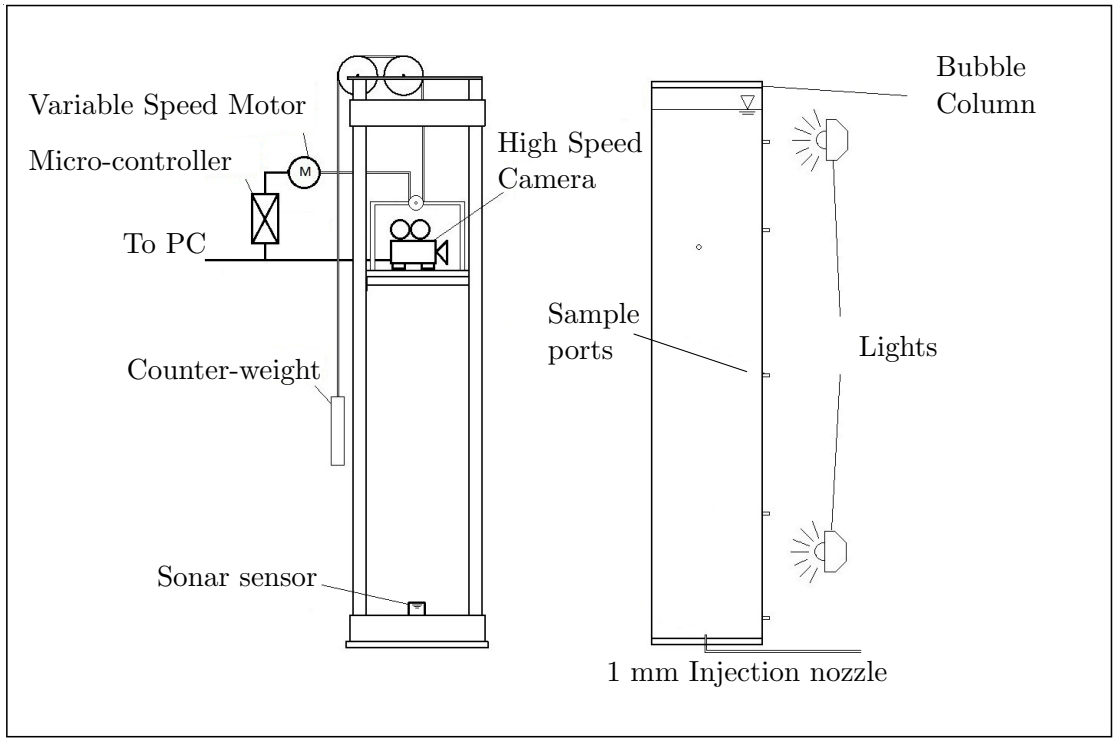

(a) Schematic of single bubble experimental set-up

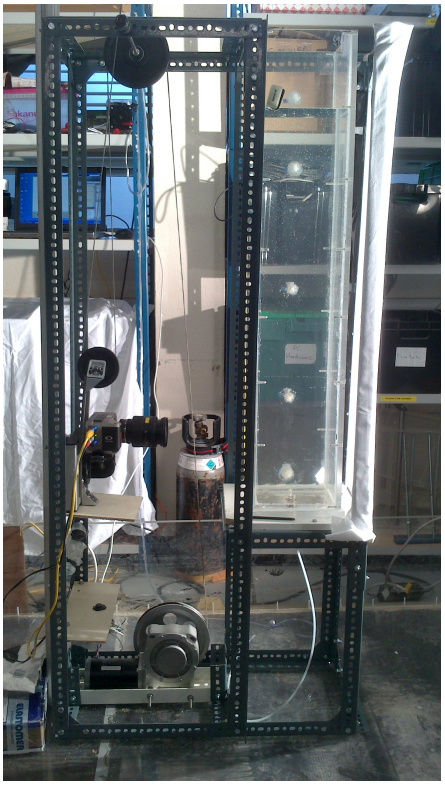

(b) Laboratory set-up of single bubble experiments

Figure 3.1: Single bubble experimental set-up

approximately 5.0 mm, therefore wall effects from this series of experiments can be assumed to be negligible.

In these experiments the input gas mixture was pumped from a gas sampling bag with a peristaltic pump into the bubble column. Recently it was found that the bubble injection system can cause an artificially greater initial mass transfer rate, by increasing the motion of the bubble as it detaches from the orifice, with smaller orifices resulting in increased disturbance in the bubble formation, Tomiyama et al. (2002), Okawa (2003), Peters and Els (2012). Work from Tomiyama et al. (2002) study the deformation after release, where the deformations consist of an early onset of the bubble shape and path oscillations. From their work it was found that larger orifices reduce the deformation of the bubbles, with a 1.0 mm orifice suitable to achieve this. The single bubble experiments in this work were conducted with both a 1.0 mm and 0.35 mm diameter orifice. All experiments were conducted under atmospheric pressure and the temperature and pH of the water was monitored throughout the experiments.

This set of experiments were designed to measure the change in volume of a bubble undergoing mass transfer. A *Phantom Miro eX-4* high speed camera (*Vision Research*, USA) was used to record images of the bubble at 400 fps. The *Phantom Miro ex-4* was loaned from the *EPSRC* Instrument Loan Pool. A *Nikkon AF Zoom-Nikkor 24-85 mm f/2.8-4D IF* lens was attached to the camera. This lens can be used with macro photography applications, with a minimum focus distance of 0.21 m and a macro focal length range between $35 - 85$ mm. Additional lighting was necessary for the high speed photography, this was provided by two 650 W halogen lights. The lights were positioned to maximise the contrast between the bubble and the background and to keep this as consistent as possible along the height of the bubble column. The camera was positioned on a platform which was able to slide along a vertical track to traverse the height of the bubble column and photograph the bubble at different axial positions. The camera lift was positioned a distance 300 mm from the bubble column. The camera platform was connected to a variable speed motor, which could control the camera movement. The recorded images from the camera were analysed with a computer in real time to track the bubble position and, depending on the relative position of the camera and bubble, the velocity of the rise of the camera could be adjusted to follow the rise of the bubble.

From these images, the size, velocity and rise path of this single bubble can be measured, with the change in volume of the bubble being estimated from the change in bubble size recorded from the images. A bubble generation frequency of between 30 - 40 bubbles per minute was used in these experiments. Work by Sam et al. (1996) showed that bubble generation frequencies between 1 - 80 bubbles per minute had little effect on the bubble size or velocity. The velocity difference between the gas and the liquid phases is an important parameter in determining the mass transfer coefficient, with higher gas velocities correlating with increased mass transfer rates. The rise velocity of the bubble

was measured with a combination of a sonar sensor and high speed imaging. An LV-MaxSonar sonar sensor (MaxBotix Inc., USA) was placed beneath the camera platform, this was able to detect the vertical position of the camera as it traversed up the vertical track. The position of the bubble in relation to the camera was interpreted from image analysis and combined with the camera position, given by the sonar sensor. The velocity of the bubble was then taken as the differential of the vertical bubble position with respect to time. As mentioned previously, the concept of terminal velocity is difficult to define for gas bubbles rising in a liquid, due to the constantly changing conditions with the vertical bubble position. Despite this, the terminal velocity is often used in literature and in many cases after initial acceleration and in some cases, deceleration, the bubble reaches a constant velocity, Sam et al. (1996).

3.4 Bubble Swarm experimental set-up

The experiments conducted in this section utilised a gas flow consisting of a CO_2-air mixture, which was introduced into a 1.0 m tall square bubble column of cross section 0.3×0.3 m by a rubber membrane sparger (Elastomer Engineering Ltd, UK). Several studies from the literature have employed square bubble columns, including Akita and Yoshida (1974), Mouza et al. (2005), Brenn et al. (2006) and Bai (2010) while many have employed circular columns, including Chabot and de Lasa (1993), Kumar et al. (1997), Chaumat et al. (2005) and Dong et al. (2010). In algal cultivation systems carbonation sumps have previously been designed with a square cross-section, Weissman and Goebel (1987), Mendoza et al. (2013). Differences between the hydrodynamics of circular and square bubble columns could have an effect on the mass transfer rate. The wall effects from the small diameter columns have been shown to effect gas hold-up and mass transfer, Shah et al. (1982). At a superficial gas velocity of $u_G = 0.08\ m\ s^{-1}$ Kumar et al. (1997) observed an increase in gas hold-up with column diameter, up to $D_C \approx 0.15\ m$. This relation between column diameter and gas hold-up was not observed, however, at a lower superficial gas velocity of $u_G = 0.02\ m\ s^{-1}$. In this work the superficial gas velocity will not exceed $u_G = 0.02\ m\ s^{-1}$, thus the wall effects have been minimised. The low gas flow rates used in this work will also allow for comparison between different shaped bubble columns.

The CO_2 was supplied from a CO_2 gas cylinder (*BOC*, UK), using a regulator and rotameter to control the pressure and flow rate. Air was supplied from an air pump and allowed to mix with the CO_2 in approximately 1.0 m length of polyethylene tubing, prior to connecting to the sparger. The CO_2 and air flow rate could be controlled to achieve the desired CO_2 input concentration and total flow rate. Gas samples of the input and output gas stream were collected and analysed using gas chromatography, as described in section 3.2. The input gas samples were taken from the tubing, prior to the bubble column. As with the single bubble experiments described in section 3.2 the

output samples were collected with an upturned funnel and syringe at the top of the bubble column.

Due to the large gas flow rate and volume of CO_2 dissolving into the water, the liquid concentration of dissolved CO_2 quickly increased. To compensate for this a continuous liquid flow was needed to supply fresh water for the CO_2 absorption. Water was circulated using two centrifugal water pumps, and was stripped of dissolved CO_2 in a series of bubble columns with a total volume of 0.1 m^{-3}. The schematic of the experimental set-up is shown in figure 3.2a. Figure 3.2b shows an image of the experimental set-up, with the larger square bubble column used to conduct the bubble size experiments on the left hand side, while the adjacent column on the right was one of those used to remove part of the dissolved carbon.

In experiments conducted with pre-saturated O_2 or N_2, the gas was sparged into the liquid prior to the experiments. Measurements of the dissolved oxygen and pH were taken at the top of both columns shown in figure 3.2 using pH and DO probes, as described in chapter 3.2.

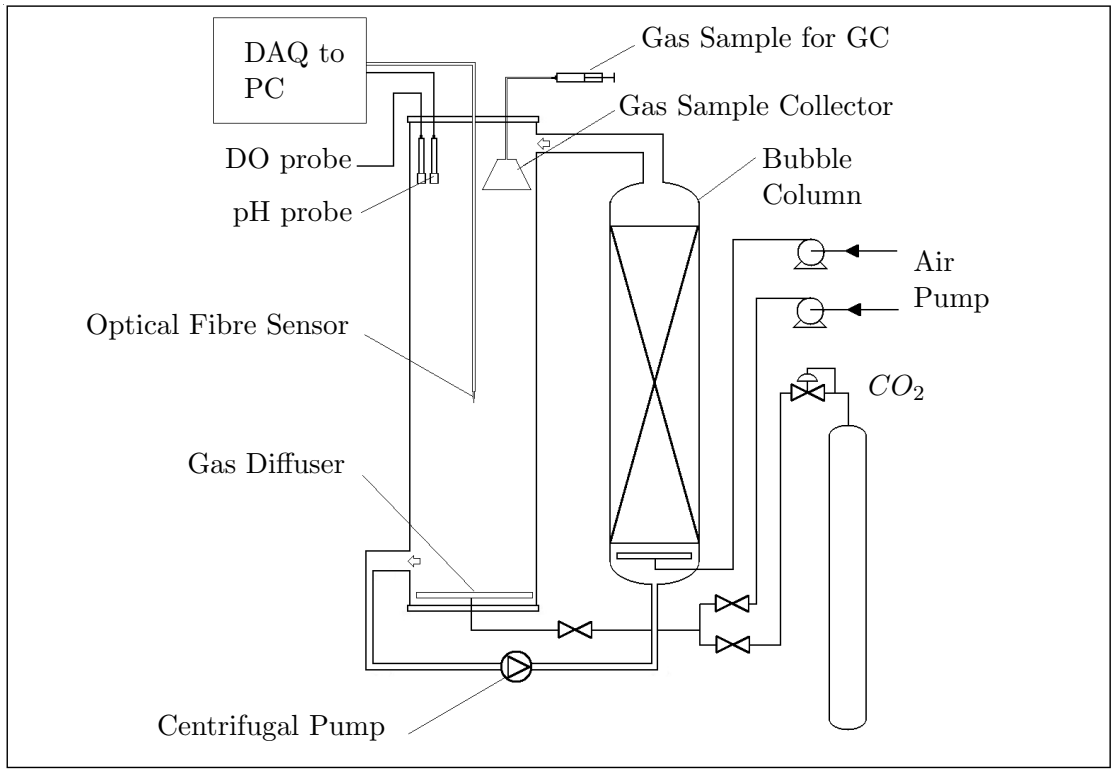

(a) Schematic of bubble swarm experimental set-up

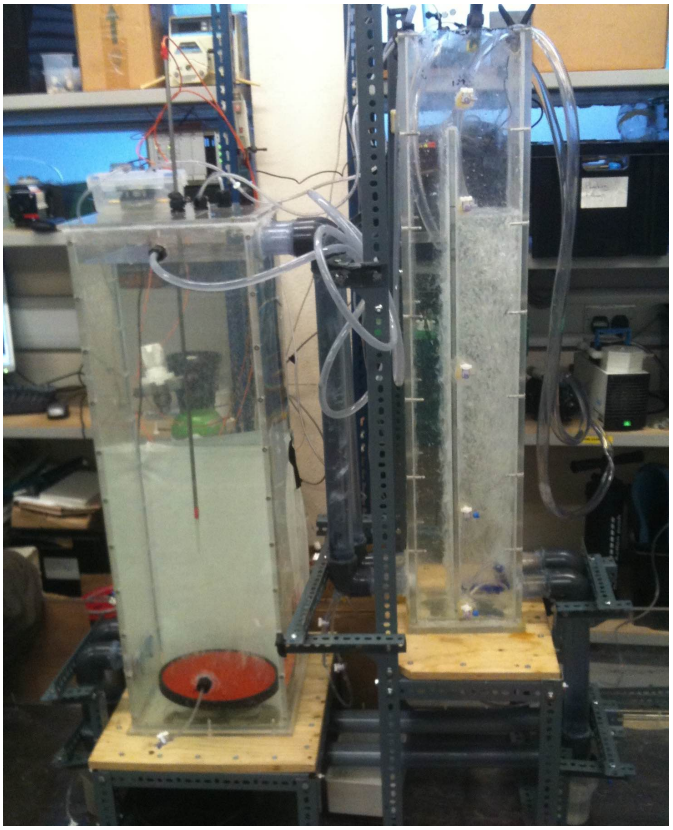

(b) Bubble Swarm experimental set-up

Figure 3.2: Bubble swarm experimental set-up

Chapter 4

Single Bubble Methodology

4.1 Introduction

This first phase of experiments consider the bubble characteristics and mass transfer of single CO_2 bubbles. This chapter describes the image analysis and methodology used to determine the bubble volume from the acquired high speed images. Section 4.3 describes a simple mass balance model to simulate the change in bubble volume and CO_2 concentration from empirical relations of k_L taken from the literature.

4.2 Image Analysis

The high speed video file was dissected into consecutive images which were analysed with tailored MATLAB software and the Image Analysis Toolbox (The Mathworks, Inc.). A flow chart of the image analysis process is shown in figure 4.1. Firstly, the file size of the grayscale image was reduced for processing by extracting a cropped section of the image taken around the initial bubble position. The initial bubble position was manually measured from the first image of the sequence. To detect the bubble within this section, background detail and uneven background lighting was removed. This was achieved by constructing a morphological dilation of the preceding image in the video sequence, which was then subtracted from the bubble image to remove the background.

To improve the definition of the bubble an iterative procedure was used to find the threshold value used to convert the image from grayscale to a black and white image. In this case, white pixels with a value of 0 represented the background and black pixels with a value of 1 represented the bubble. An iterative procedure was developed which maximised the ratio between the number of black pixels in the area of the image where the bubble was expected, and the number of pixels in the remainder of the image. The expected bubble location was calculated based on the displacement of the bubble

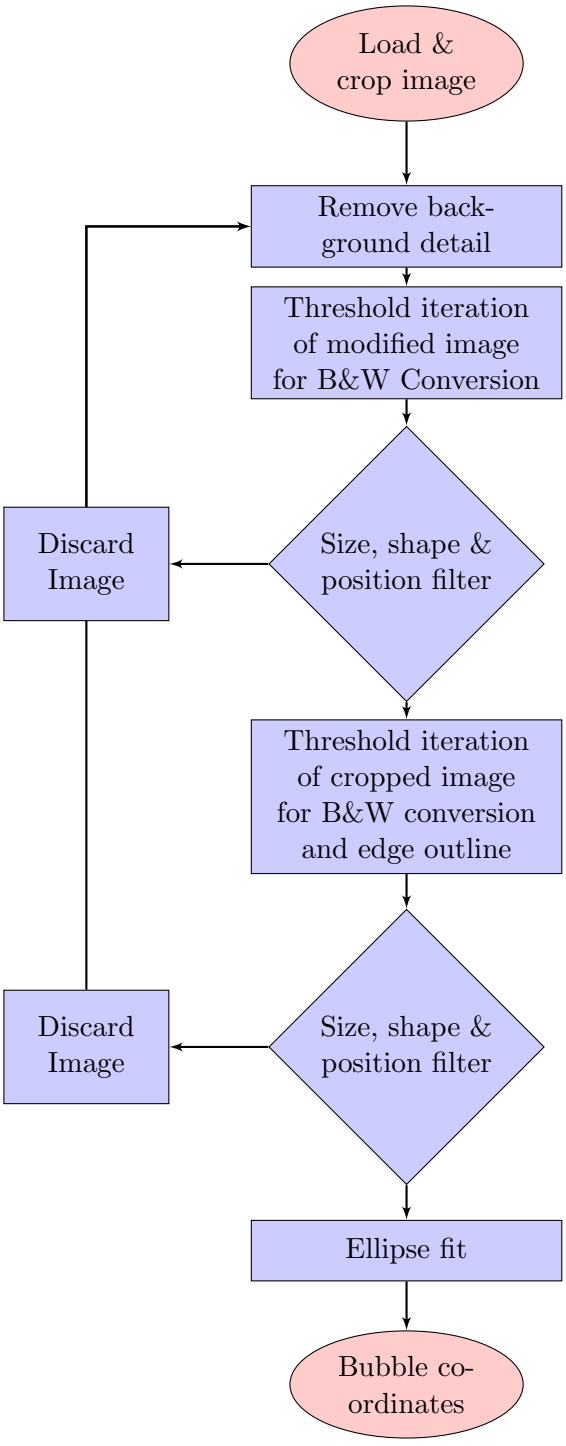

Figure 4.1: Image Processing Flow Diagram

from the present and preceding images. The initial bubble location was programmed manually from the first frame, while the displacement in the 0.0025 s between the frames resulted in small bubble displacements which could be tracked automatically by the image analysis program. The detected pixel segments were then passed through the criteria shown in figure 4.1 and programmed into the MATLAB program. This was used

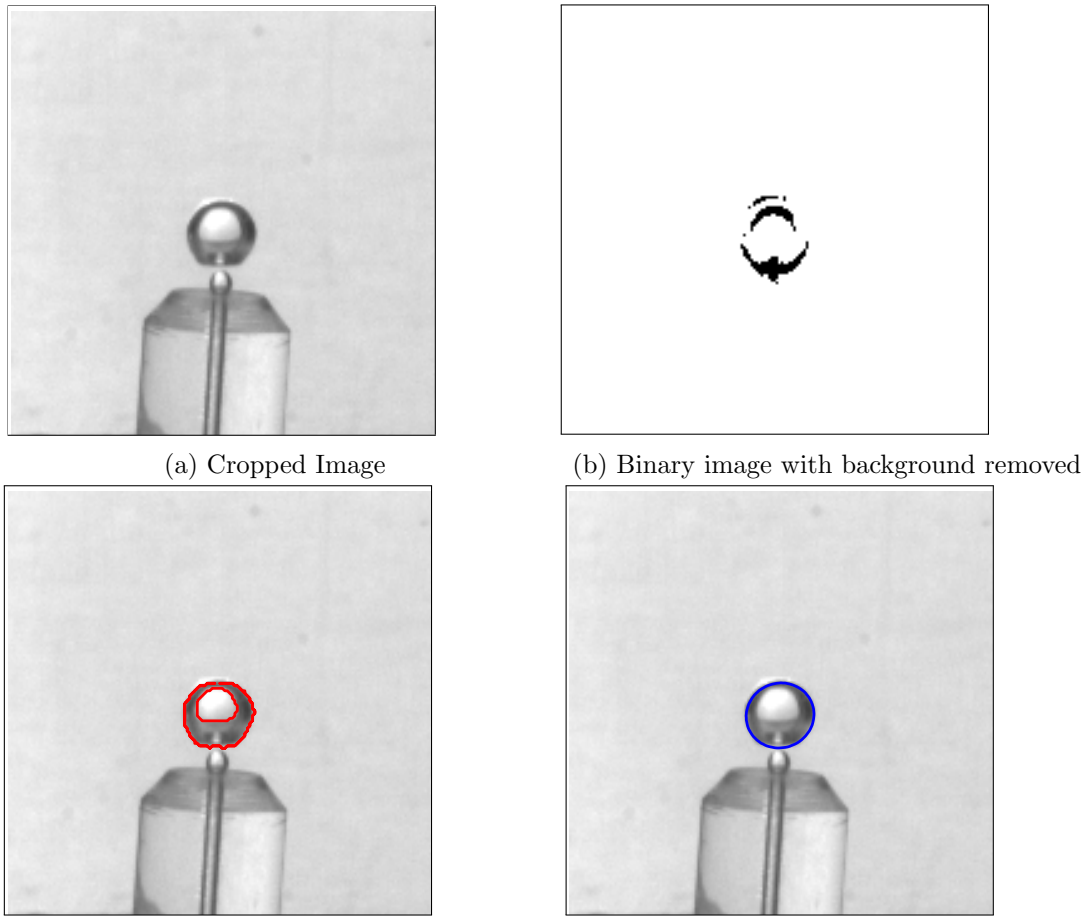

(a) Cropped Image

(b) Binary image with background removed

(c) Image with detected edge

(d) Image with fitted ellipse

Figure 4.2: Image analysis sequence

to determine whether they fitted the profile of the bubble. Because of the reflected light on the bubble, the bubble would often appear as separate segments.

The detected segments were analysed according to their size and position, both in relation to each other and to the expected bubble location, to determine which were part of the bubble and which were not. Figure 4.2 shows the cropped image and the black and white conversion. If the size and location of the segments met these requirements, the size of the bubble was then estimated.

Once the segments detected were accepted as being part of the bubble a reduced threshold value was taken, with another iterative procedure to maximise the detail of the bubble detected. Within the image analysis process a compromise has to be made to ensure the background detail is removed, but that the integrity of the bubble image is retained. A pre-programmed edge detection script from the MATLAB image analysis toolbox was then used to trace around the bubble segments. Using the data from the initial bubble detection step a set of criteria based on size, shape and location of the bubble segments was used in a series of filters to define the bubble co-ordinates.

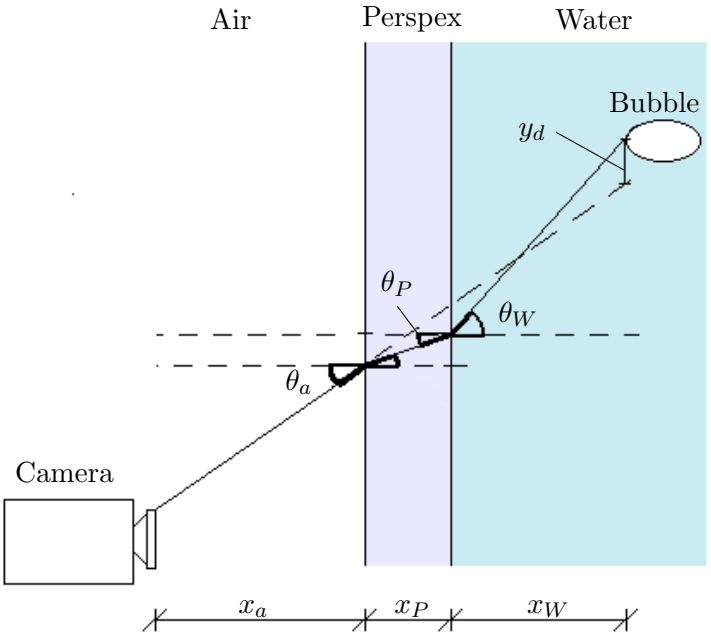

Figure 4.3: Representation of refraction through water and perspex

Figure 4.2 shows an example of the resulting bubble edge segments before and after the filters. The resulting bubble co-ordinates were then saved and an ellipse fitting routine, as described in section 4.2.2 below was performed to provide an estimate of the bubble size.

4.2.1 Calibration

The bubble co-ordinates were corrected for the refraction of light through the water and perspex. This correction was calculated using Snell's law (equation 4.1) and the refractive index of the materials, as illustrated in figure 4.3. The thickness of the perspex (x_P) and the distance between the camera and the bubble column (x_a) were measured, while the bubble was approximated as being in the centre of the column, with the distance between the bubble and the inner bubble column wall (x_W) taken as half the distance between internal column sides. The difference in the observed co-ordinates (y_d) was then calculated by trigonometry. Figure 4.4 shows the difference in y position measurement when taking into consideration the effects of refraction through the perspex and water.

$$n_a sin(\theta_a) = n_p sin(\theta_p) = n_w sin(\theta_w) \tag{4.1}$$

$$y_d = y_{meas} - [x_a tan(\theta_a) + x_P tan(\theta_P) + x_W tan(\theta_W)] \tag{4.2}$$

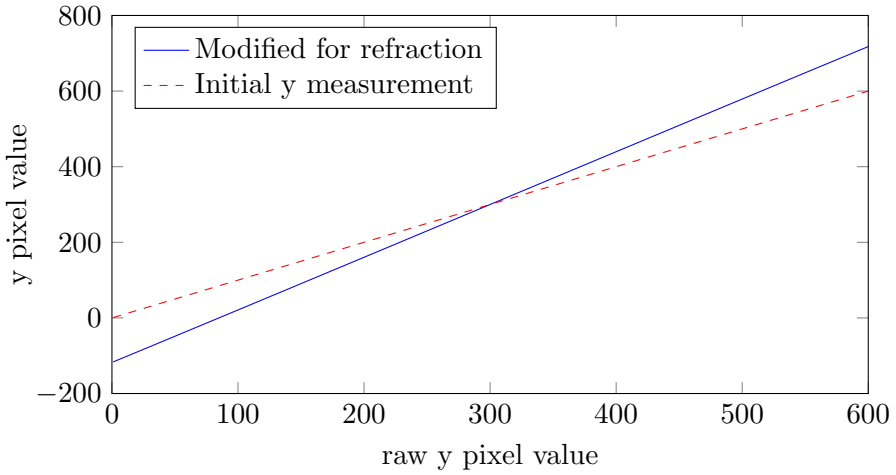

Figure 4.4: Difference in y position due to refraction

4.2.2 Ellipse Fitting

Duineveld (1995) found that the assumption of a symmetrical ellipsoidal shape can be inaccurate for bubbles with $d_e > 1.2\ mm$. This is due to the lack of fore-aft symmetry. A double ellipse fit was applied to the detected bubble co-ordinates to take into account the lack of fore-aft symmetry present in oscillating bubbles. This was achieved by combining two half-ellipses, one fitted to the upper co-ordinates and another to the lower co-ordinates. Figure 4.5 represents a double ellipse, with the two minor (r_{B1} *and* r_{B2}) and major (r_A) bubble radii shown.

To define an ellipse five parameters are required; the centre co-ordinates (x_0, y_0), the orientation θ and the major and minor axis (a, b). There are several approaches to fitting an ellipse, including those described by Shen et al. (2000), Xie and Ji (2002) and Zhang et al. (2012). The least squares method is generally considered to be the simplest and quickest approach, Chernov (2010). This can be applied either algebraically or geometrically. The algebraic technique substitutes the co-ordinate data in the equation for an ellipse (shown in equation 4.3) and minimises the sum of squares of this equation. Alternatively the geometric fit computes the differences between the estimated co-ordinates and the data points and finds the minimum sum of the squared distances; however this results in a non-linear least squares problem. The algebraic technique can be solved as

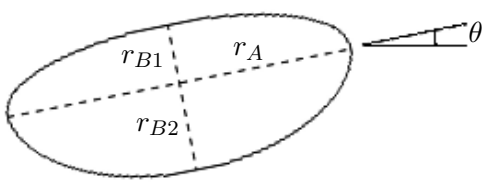

Figure 4.5: Double ellipse fit

a linear least squares problem, with the advantage of simpler equations which can be solved more rapidly. The drawback with the algebraic technique is that the fits tend to be less good than those of a geometric fit. In addition the algebraic fit often requires that a constraint is placed on the solution in order to ensure that an ellipse is fitted rather than a parabolic or a hyperbolic curve.

The reduction in the error from fitting an ellipse using the geometric method when compared to the algebraic method is small compared to the error in collecting the measurements, therefore an algebraic least squares fit was deemed suitable for this purpose. Several different ellipse fitting routines were compared including those from Fitzgibbon et al. (1999) and Taubin et al. (1992). The algebraic fit described by Gander et al. (1994) was chosen as this gave a more consistent fit when compared with alternative methods.

An ellipse can be represented by the quadratic equation shown in equation 4.3 with the coefficient b as a measure of the orientation of the ellipse. When $b = 0$ the axes of the ellipse are parallel to the horizontal and vertical axes. Ellipses were fitted to each bubble image and used as a measure of the bubble size.

$$a.x^2 + b.x.y + c.y^2 + d.x + e.y + f = 0 \tag{4.3}$$

4.2.3 Image Analysis Check

The error in the image analysis procedure was checked against the measurement of a 5.0 mm plastic bead which was dropped into the centre of the water column. The different stages of the bead image analysis procedure is shown in figure 4.6. The image analysis process of the solid bead showed more consistent results than the image analysis from bubbles. This is due to the greater contrast between the bead and the background, with the light reflection from the bubbles requiring a more rigorous image analysis procedure. From the image analysis and ellipse fitting procedure the average diameter of the bead shown in figure 4.7 was measured at 4.93 mm. A correction factor was applied from the image analysis measurements as a pixel-to-mm ratio, which was applied to the bubble measurements to adjust for the discrepancy between the measured diameter from the image analysis and the actual diameter of the bead.

4.2.4 Mass Transfer

As observed in the work of Schulze and Schlünder (1985a), Schulze and Schlünder (1985b) and Vasconcelos et al. (2002) mass transfer from the same gas bubble into a liquid can occur at different rates. These authors observed a sharp and prominent transition point between different mass transfer rates. The occurrence of two different

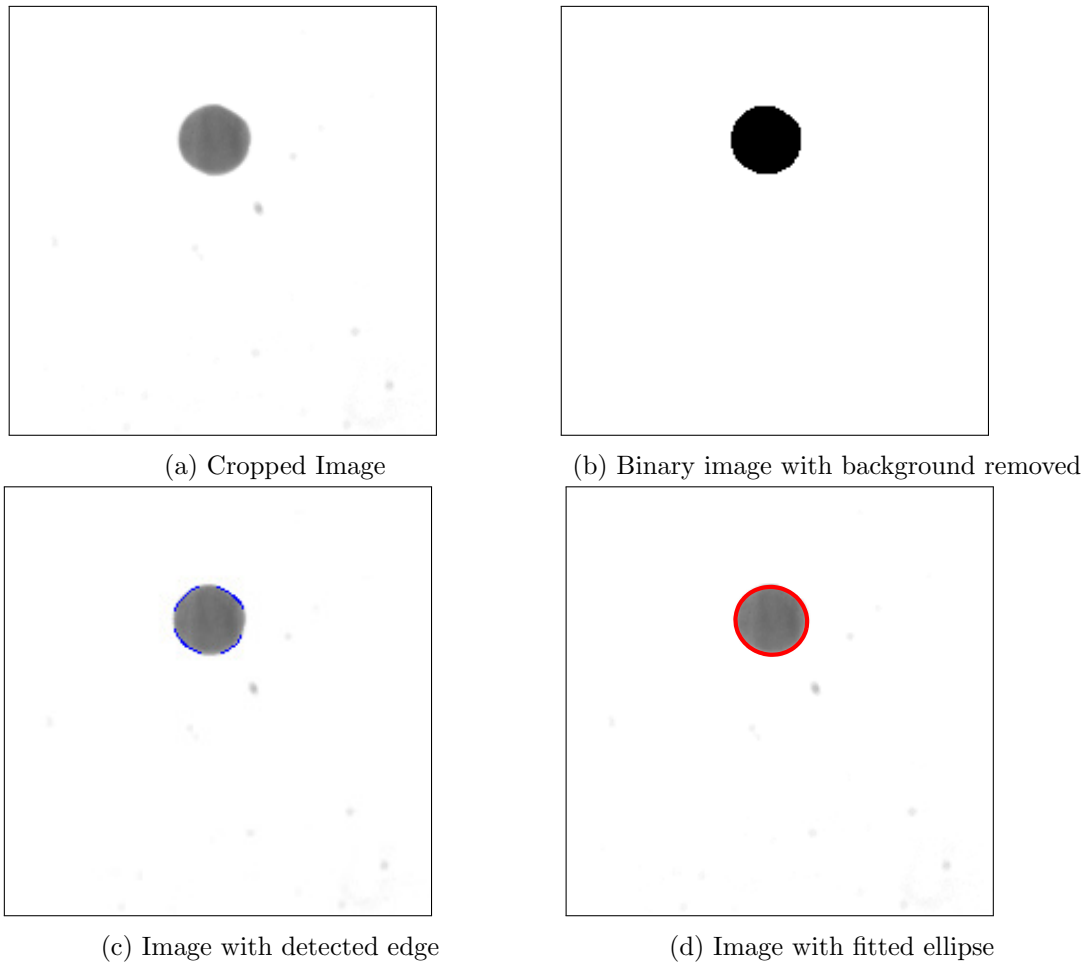

(a) Cropped Image

(b) Binary image with background removed

(c) Image with detected edge

(d) Image with fitted ellipse

Figure 4.6: Image analysis sequence of 5.0 *mm* calibration bead

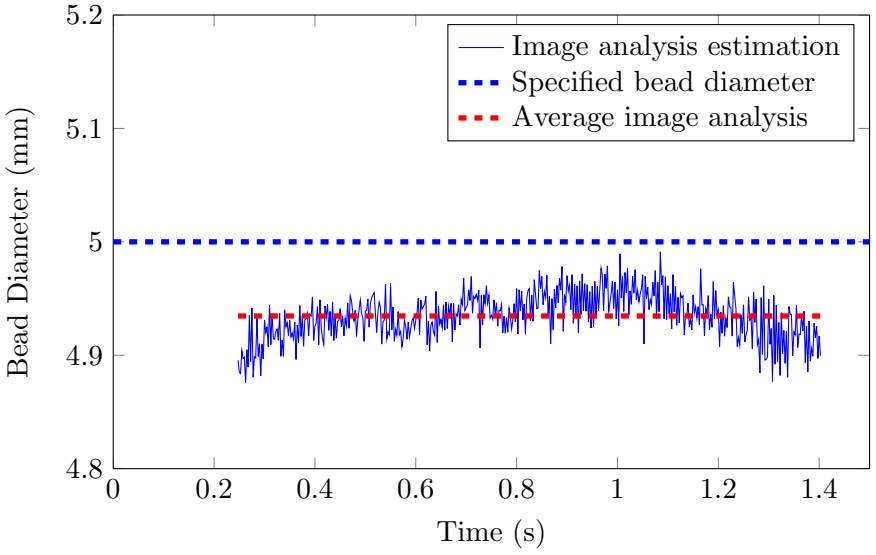

Figure 4.7: Estimation of bead diameter from image analysis procedure

mass transfer rates is dependent on the initial bubble size, CO_2 concentration driving force and surfactant concentration. As a result of this, the change in bubble diameter can be approximated by two lines of best fit. Equations 4.4 - 4.6 represent the minimisation of squares to find the two lines of best fit, while equation 4.7 represents the x value at the intersection between the first and second linear models.

$$y_1 = \alpha_1 x_1 + \beta_1 \qquad y_2 = \alpha_2 x_2 + \beta_2 \tag{4.4}$$

$$\alpha_1 = \frac{n_1 \Sigma x_1 y_1 - \Sigma x_1 \Sigma y_1}{n_1 \Sigma x_1^2 - (\Sigma x_1)^2} \qquad \alpha_2 = \frac{n_2 \Sigma x_2 y_2 - \Sigma x_2 \Sigma y_2}{n_2 \Sigma x_2^2 - (\Sigma x_2)^2} \tag{4.5}$$

$$\beta_1 = \frac{\Sigma x_1^2 \Sigma y_1 - \Sigma x_1 \Sigma x_1 y_1}{n_1 \Sigma x_1^2 - (\Sigma x_1)^2} \qquad \beta_2 = \frac{\Sigma x_2^2 \Sigma y_2 - \Sigma x_2 \Sigma x_2 y_2}{n_2 \Sigma x_2^2 - (\Sigma x_2)^2} \tag{4.6}$$

$$x_{sep} = \frac{\beta_2 - \beta_1}{\alpha_1 - \alpha_2} \tag{4.7}$$

Mass transfer rates were calculated assuming ideal gas conditions within the bubble. Based on the volume of the bubble and the calculated pressure, the number of moles of gas within the bubble can be calculated. The data from the CO_2 gas concentration analysis were used to find the mole fraction of CO_2 within the bubble (y_{CO2}). This can then be used to calculate the partial pressure and number of moles of CO_2. Equations 4.8 - 4.10 show the calculations which were performed at every time step, correlating with the frequency of bubble images every 0.0025 s.

$$n_{CO2} = \frac{p_{CO2} V_{CO2}}{RT} \tag{4.8}$$

$$p_{CO2} = y_{CO2} p_{tot} = y_{CO2} \left(p_{atm} + p_e + g[\rho_L z(1-\epsilon_G)][\rho_G z \epsilon_G]\right) \tag{4.9}$$

$$p_e = \frac{2\sigma \left(\pi \left(3(r_A + r_B) - \sqrt{(3r_A + r_B)(r_A + 3r_B)}\right)\right)}{\pi r_A r_B} \tag{4.10}$$

The number of moles of CO_2 (n_{CO2}) were calculated from equation 4.8; p_{CO2} is the partial pressure (Pa); V is the volume of the bubble (m^3), (calculated from equation 2.9); R is the ideal gas constant ($kJ\ mol^{-1}$) and T is the temperature (K). The pressure acting on the bubble is given by equation 4.9, where p_{tot} is the total pressure (Pa); y_{CO2} is the mole fraction of CO_2; p_{atm} is the atmospheric pressure (Pa); p_e is the surface tension force of the bubble, (in Pa, shown in equation 4.10); z is the depth of water

above the bubble; ρ_L and ρ_G are the liquid and gas densities ($kg\ m^{-3}$) and ϵ_G is the gas hold-up. The atmospheric pressure assumed in this work is taken as the pressure at sea level under standard conditions, being $p_{atm} = 101325\ Pa$. The altitude and climate can effect the atmospheric pressure. The experiments presented in this work were conducted at the University of Southampton, which is at an altitude of approximately 50 m above sea level, Survey. During the year a typical minimum atmospheric pressure due to the climate would be 97 kPa, while a maximum pressure would typically be 104 kPa, Office. This variation in pressure would have a small effect on the volume and size of a bubble. For instance, assuming the ideal gas law the difference in bubble volume can be calculated, a bubble with a diameter of $d_e \approx 3.0\ mm$ at an atmospheric pressure of $p = 97\ kPa$ would reduce to a bubble size of $d_e \approx 2.93\ mm$ at an atmospheric pressure of $p = 104\ kPa$. These variations in atmospheric pressure would occur over an extended period of time, therefore this would not effect the change in volume of a single bubble rising through a column in the same experiment. This could, however, be a factor in comparing experiments which were conducted under different conditions. This difference is small and although it will contribute to a slight error in the comparison between different experimental runs conducted on different days, as it does not effect the change in bubble size during the same experimental run this will be acknowledged as a contributing source of error.

The mass transfer rate of CO_2 was then calculated from the change in number of moles of CO_2 within the bubble. From the mass transfer rate, the volumetric mass transfer coefficient (k_La) can be calculated using the concentration driving force, shown in equation 4.11, where C^* is the dissolved concentration of CO_2 in equilibrium with the CO_2 in the gas phase (calculated using Henry's law) and C_0 is the dissolved CO_2 concentration in the bulk liquid ($mol\ m^{-3}$). The mass transfer coefficient (k_L) was determined by dividing the volumetric mass transfer coefficient, $k_L\alpha$, by the surface area of the bubble.

$$k_La = \frac{\Delta n}{\Delta t}\frac{1}{(C^* - C_0)} \tag{4.11}$$

Experiments were conducted with different pre-dissolved concentrations of O_2 and N_2 in the water to study the effect of counter-diffusion in more detail. These experiments were carried out under atmospheric pressure, with higher dissolved concentrations of N_2 or O_2 generated by sparging gas through the water prior to the single bubble experiments. The DO concentration was measured during the experiments to ensure that the saturated levels of O_2 and N_2 remained constant.

A higher diffusivity coefficient of a gas in a liquid will increase the mass transfer rate by increasing the mass transfer coefficient. Assuming that the mass transfer rate is consistent for absorption and desorption, the mass transfer coefficients for the counter-diffusion of the O_2 and N_2 can be calculated using the same method as for CO_2. The penetration theory from Higbie, which is applicable to bubbles with a mobile interface,

shows $k_L \propto \sqrt{D}$. Thus the mass transfer coefficients for O_2 and N_2 can be related to the CO_2 mass transfer coefficient from equation 4.12.

$$\frac{k_{L\ CO2}}{k_{L\ O2}} = \sqrt{\left[\frac{D_{CO2}}{D_{O2}}\right]} \qquad \frac{k_{L\ CO2}}{k_{L\ N2}} = \sqrt{\left[\frac{D_{CO2}}{D_{N2}}\right]} \tag{4.12}$$

The concentration difference between the liquid concentration and the equilibrium concentration of the partial pressure will determine the extent of mass transfer and have a large impact on the mass transfer rate. This is determined by the solubility of the gas and can be calculated from Henry's constant, also shown in table 2.4. The lower the value of Henry's constant, the more soluble the gas, it can be seen that at 293 K CO_2 is approximately 27 times more soluble than O_2, and 55 times more soluble than N_2. This results in the much greater mass transfer from CO_2, than either O_2 or N_2.

4.3 Mass Balance Model

A simple mass balance model was developed to simulate the change in mass transfer rate as a bubble rises through the column. There will be a spatial variation in the mass transfer from the bubble surface as described by the stagnant cap model, proposed by Savic (1953). This detail has not been considered here due to the lack of information regarding the type of surfactant and concentration from the experimental work. Studies by Schulze and Schlünder (1985a), Schulze and Schlünder (1985b), Vasconcelos et al. (2002) and Alves et al. (2005) identified the sharp transition between a higher mass transfer rate and a reduced mass transfer rate. This temporal variation in mass transfer will be approximated using the mass balance model, which will use a backward finite difference to calculate the mass transfer rate for the changing bubble size and rise velocity.

The mass transfer rate calculation is shown in equation 4.13. Where the number of moles ($n_{(i)}$) at time step (i) can be calculated from the mass transfer rate and the number of moles from the previous time step ($i-1$). The same method for calculating k_L from the experimental measurements of the bubble size were used in the mass balance model. The ideal gas law, shown previously in equation 4.8, was used to equate the number of moles from the bubble volume, which is calculated assuming an ellipsoidal bubble shape, the pressure within the bubble is calculated from equation 4.9. The k_L values are calculated from either the empirical relations proposed by Montes et al. (1999) or Frössling, 1938 as shown in equations 4.14 and 4.15, respectively. The choice between the k_L relations is dependent on the bubble diameter for single rising bubbles and is discussed in detail in chapter 6.1.

$$\frac{dn}{dt} = \frac{n_{(i)} - n_{(i-1)}}{t_{(i)} - t_{(i-1)}} = k_{L(i)}\alpha_{(i)}\left(C^*_{(i)} - C_{0(i)}\right) \tag{4.13}$$

For $d_e > 1.3\ mm$

$$k_{L(i)} = \frac{2\sqrt{Pe_{(i)}}[1.1 + 0.027\sqrt{We_{(i)}}]D_{CO2}}{\sqrt{\pi}d_{e(i)}} \tag{4.14}$$

For $d_e < 1.3\ mm$

$$k_{L(i)} = 0.6\sqrt{\frac{u_{b(i)}}{d_{e(i)}}}D_L(2/3)\nu^{(-1/6)} \tag{4.15}$$

Chapter 5

Multiple Bubble Methodology

5.1 Introduction

This chapter describes the experimental procedure used to investigate the mass transfer and bubble dynamics from a continuous gas and liquid flow. The image analysis method is limited to measuring the bubble size of single bubbles, or in systems with low gas fractions. With a gas holdup of 1 %, over 40 % of the bubbles will be overlapping in a 2D image, Lecuona et al. (2000). To measure the bubble properties in a continuous flow optical fibre sensors were used. The change in CO_2 gaseous concentration was measured by taking input and output gas samples to allow calculation of a mass balance. The mass transfer rate from the bubble swarm was measured using this data and compared with the bubble properties measured by the optical fibre sensors.

5.2 Fibre-Optic Calibration

Due to the limitations of image analysis as a method for measuring the bubble size in bubble swarms, optical fibre sensors have been used to measure the bubble properties. A double optical fibre sensor (RBI Instrumentation, France) is able to detect the difference between the refractive index of a gas and liquid, as described in chapter 2.6.1. Voltage measurements from the optoelectronic unit were measured at a frequency of 10 kHz and converted into digital signals with a Measurement Computing PCI-DAS6070 data acquisition card (Measurement Computing, USA). The voltage time series was then analysed to determine the properties of the bubbles.

The tip of the optical fibre was shaped into a conical form through a process of heating and elongation of the fibre. Two optical fibre sensors were positioned adjacent to each other, with one 6.0 mm above the other. This enabled for the same bubble to be detected twice, once by each sensor. By assuming that the bubble rises vertically and straight

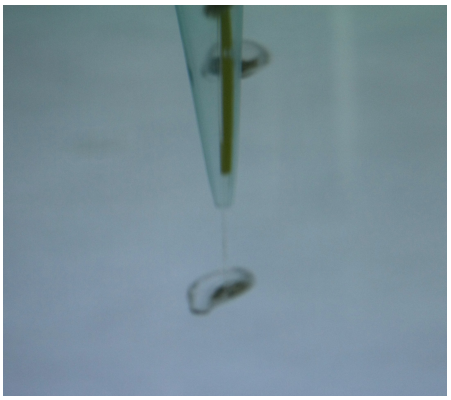

Figure 5.1: Bubble intersection of optical fibre

and knowing the distance between the two fibre tips, the difference in the detection time between the two sensors can be used to estimate the rise velocity of the bubble. The bubble velocity can then be used with the measured time during which it is contact with the optical fibre probe to calculate the bubble chord length. The orientation of the bubble will vary during its rise, as can be seen in figure 5.1. This will result in scatter in the measurements of the bubble chord length.

An example of the normalised voltage time series for a bubble detection is shown in figure 5.2. In this example the first optical fibre sensor, shown by the blue line, is positioned below the second sensor, shown in red. The bubble is first detected by the lower optical fibre, and when the tip of the fibre comes into contact with the gas phase the reflection of infra-red light increases at the tip. This results in a large increase in the voltage measurement, which continues for the period during which the optical fibre tip is in contact with the bubble. When the lower optical fibre tip comes back into contact with the liquid phase, the voltage signal returns to approximately 0. Shortly after this, the

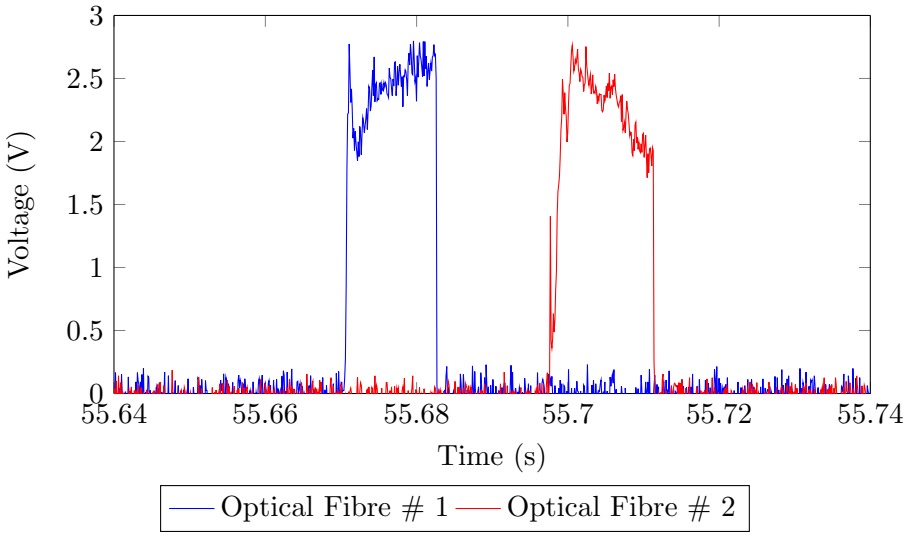

Figure 5.2: Optical Fibre Voltage Measurements

second optical fibre detects the same bubble, shown by the increase in voltage signal of the red line. The bubble is in contact with the second optical fibre tip for approximately the same duration as the first. The difference between the initial bubble contact times $(t_2 - t_1)$ was used to calculate the bubble rise velocity (u_b). The bubble velocity is then combined with the measured duration of contact with the gas phase (t_{dur}) to provide an estimate for the bubble chord length (d_C) intersecting the optical fibre. This is shown by equations 5.1 and 5.2, where x_o is the distance between the two optical fibre tips.

$$u_b = \frac{x_o}{t_2 - t_1} \tag{5.1}$$

$$d_C = t_{dur}.u_b \tag{5.2}$$

The bubble detection duration (t_{dur}) was determined by calculating the time difference when the voltage is above a threshold value. When this threshold value is exceeded, the optical fibre probe is considered to be in contact with the bubble. The threshold value was set just above the noise level shown in figure 5.2 at a value of 10 % the difference between the mean of the baseline voltage and maximum voltage. Similarly when the voltage reduced to below this threshold value, the tip of the optical fibre was considered to be in contact with water. A pre-signal can be detected prior to the voltage measurements, which has been analysed by previous authors to estimate the bubble rise velocity, Cartellier (1990), Cartellier and Barrau (1998) and bubble position with respect to the optical fibre tip, Sakamoto and Saito (2012), Mizushima et al. (2013). This is dependent on the probe tip geometry and in these experiments no further analysis of the pre-signal was conducted.

To ensure that only the same bubble was detected by the pair of optical fibre signals a restriction was applied in the data analysis which considered the second signal if it occurred within a reasonable timeframe after the first signal. The time difference between the two signals shown in figure 5.2 show that the bubble travelled 6.0 mm in approximately 0.03 s. This results in a bubble rise velocity of 0.2 $m\ s^{-1}$, which is within the range of expected bubble rise velocities and suggest the two signals are from the same bubble. Detections which occurred too close together or too far apart are considered to belong to different bubbles and were discounted from the data analysis. The gas flow rate from this work was maintained at a reasonably low level, which allowed for an easy distinction to be made between signals which occurred from the same bubble and those from different bubbles. At an increased gas flow rate, or with a variation in the direction of the bubble flow distinguishing between different signals could become an issue.

The gas holdup (ϵ_G) is frequently used in empirical relations for the volumetric mass transfer coefficient $(k_L\alpha)$. The optical fibre probes were used to measure the localised gas holdup by comparing the time for which the probe is in contact with the gas phase

with the total time the probe is in contact with both gas and liquid phases. This is shown in equation 5.3 and has been used previously to find ϵ_G with optical fibre probes, Cartellier (1990).

$$\epsilon_G = \frac{\sum t_G}{t_{TOT}} \tag{5.3}$$

5.3 Chord Length Distribution

The interpretation of bubble chord length measurements to find the actual bubble size measurements has previously involved a variety of different approaches. Serdula and Loewen (1998) correlated the mean bubble size (d_e) directly to the mean bubble chord length (d_c) from equation 5.4; however this relation is only suitable for spherical bubbles.

$$d_e = \frac{3}{2} d_c \tag{5.4}$$

Liu and Clark (1995) conducted a statistical analysis using Monte Carlo simulations to predict the relationship between the chord length distribution (CLD) and bubble size distribution (BSD). The advantage of this work was the application of simulations for ellipsoidal and truncated ellipsoidal bubbles, which is a more realistic approximation to find the BSD. Their work divided the conversion into two parts: the first section looked at finding the distribution of bubbles making contact with the probe, which will be referred to in this work as the probe size distribution (PSD). This is shown as (P_p) in equation 5.5, where E is the aspect ratio, r_e is the major radius of the bubble, P_c is the probability distribution of the chord lengths and P_c' is the derivative of the CLD. In their work Liu and Clark (1995) assumed either a Gamma or Rayleigh distribution to describe the BSD.

$$P_p(r_e) = E\left(P_c(d_c) - d_c P_c'(d_c)\right) \tag{5.5}$$

The bubbles detected by the probe are not necessarily representative of the BSD in the whole system. This is because larger bubbles have a greater cross-sectional area than smaller bubbles, and thus a greater probability of being detected by the optical fibre probe. Liu and Clark (1995) accounted for this by applying a second stage to estimate the distribution of bubbles in the system, (P_s), shown in equation 5.6.

$$P_s(r_e) = \frac{P_p(r_e)/r_e^2}{\int_{-x}^{x} \frac{P_p(r_e)}{r_e^2} dr_e} \tag{5.6}$$

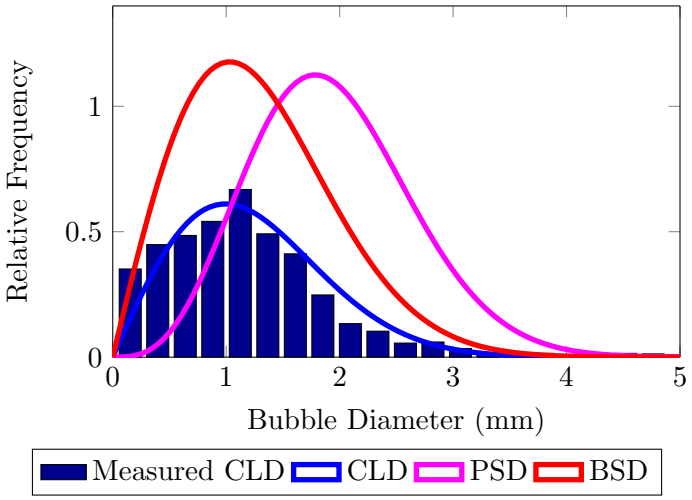

Figure 5.3: Comparison between chord length distribution (CLD), Bubble size distribution at probe (PSD) and bubble size distribution in column (BSD)

Rüdisüli et al. (2012) also performed Monte Carlo simulations of ellipsoidal bubbles and found that the mean of the increase from the CLD to the PSD and the decrease from the PSD to BSD approximately cancelled each other out. This can been seen in figure 5.3 which shows the CLD in blue and the bubble size distributions detected at the probe (PSD) and in the system (BSD) in the magenta and red lines, respectively. The mean values are not shown in the graph, although it is clear that the conversion from the CLD to the PSD increases the mean value. Conversely the conversion from the PSD to the BSD for the whole of the system gives a reduction in the mean value, which is approximately the mean value of the CLD. Because of this, Rüdisüli et al. (2012) and Karimipour and Pugsley (2011) agreed that the mean value of the CLD is a good approximation to the mean value of the BSD in the bubble column, with an error of less than 20 % between the two mean values.

The conversion from the PSD to the BSD does make an assumption on the proportion of smaller bubbles and the fit of the distribution for all the bubbles in the system. During the mass transfer of CO_2 there will be a considerable change in BSD at different heights in the bubble column. This will affect the BSD and could make choosing one distribution to represent the whole bubble column more problematic. It is also known that the BSD is affected by the liquid properties, such as viscosity. Kawase et al. (1992) noted that a higher viscosity would lead to a narrower range in the BSD.

Recently Hoang et al. (2015) validated the transformation methods from Liu and Clark (1995) to convert the CLD into the BSD, by comparing the resulting BSD from a five-point conductivity probe with bubble diameter measurements taken from image analysis from high speed video. They developed an approach which takes into consideration the different bubble shapes with bubble size. This is a more realistic approach, considering the large variation in the bubble aspect ratio with bubble size, which is discussed in chapter 6.4. Their method used a Gaussian distribution, which provided a good fit to

their data. In the current work, however, the Rayleigh distribution provided a better approximation to the BSD. Rüdisüli et al. (2012) noted that typical distributions used to describe the BSD in previous studies include the Gamma, Rayleigh and Log-normal distributions. They found the Rayleigh distribution provided the best fit as it was the most stable in the application of the transforms; this was also the fit preferred by Liu and Clark (1995). In contrast to the Gaussian distribution, the Rayleigh and Gamma distributions provide a right-skewed correlation, which represents the non-linear coalescence and break-up in bubble swarms. The work from Hoang et al. (2015) only considers the bubble distribution at the probe, and does not transform this to represent the distribution of the whole system. In this work the approach adopted by Hoang et al. (2015) has been used, which divides the CLD into different groups to consider the changes in the aspect ratio with bubble size. This has been applied with the Rayleigh distribution as opposed to the Gaussian distribution used by Hoang et al. (2015) and the transformation from PSD to BSD has also been included.

Firstly the Rayleigh distribution is fitted to the CLD, providing the scale parameter (β) as shown in equation 5.7. The CLD is then divided into different classes, which are then transformed into the BSD at the probe (P_p) and in the whole column (P_s), using equations 5.5 and 5.6 from Liu and Clark (1995), where b_E is the correction for the ellipsoid shown in equation 5.10 and the subscript i denotes the ith class. Hoang et al. (2015) calculated the aspect ratio (E) from an empirical relation based on an analysis from Bozzano and Dente (2001) who simulated bubble shapes and rise velocity by minimising the total energy. In this work the empirical relation from Okawa (2003) provided a closer match to the single bubble experimental data, and this relation has therefore been used to estimate the aspect ratio.

$$P_c(d_c) = \frac{d_c}{\beta^2} e^{-d_c^2/2\beta^2} \tag{5.7}$$

$$P_{p,i}(r_{e,i}) = \frac{r_{e,i}^3}{2b_{E,i}^4} exp\left[-\frac{r_{e,i}^2}{2b_{E,i}^2}\right] \tag{5.8}$$

$$P_{s,i}(r_{e,i}) = \frac{r_{e,i}}{b_{E,i}^2} exp\left[-\frac{r_{e,i}^2}{2b_{E,i}^2}\right] \tag{5.9}$$

$$b_{E,i} = \frac{\beta_i}{2E_i} \tag{5.10}$$

A comparison between the division of the CLD into one and two groups is shown in figure 5.4, with the CLD taken for CO_2 bubbles at the base and at the top of the bubble column. The probability function using one group provides a better fit to the initial CLD shown in figure 5.4a. Using two groups provides a better fit to the measured data

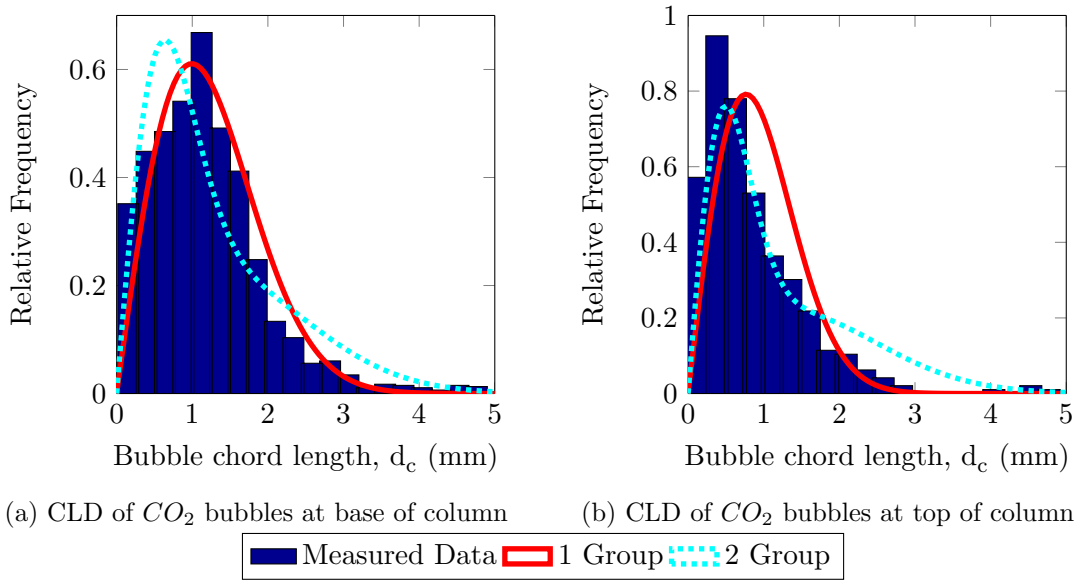

(a) CLD of CO_2 bubbles at base of column

(b) CLD of CO_2 bubbles at top of column

Figure 5.4: Chord length distribution (CLD) of CO_2 bubbles

in figure 5.4b, at least for chord lengths $d_c < 2.0\ mm$. Hoang et al. (2015) found that using three groups did not improve the fit to their data. The fit provided by either one, two or more groups would depend on the variation in bubble sizes and will vary for the different bubble size profiles in different systems.

The optical fibre probes were calibrated using image analysis from high speed video recordings of the bubbles as they came into contact with the optical fibre tip. The measurements of the bubble velocity and chord length from the optical fibre are compared with the image analysis results in figures 5.5a and 5.5b. The results from the image analysis and optical fibres agree reasonably well for the bubble rise velocity measurements. The majority of the velocity measurements are between $0.2 - 0.25\ m\ s^{-1}$. There are a few outliers which are more noticeable for the image analysis measurements.

The parity plot in figure 5.5b compares the minor bubble diameter with the bubble chord length. There is a noticeable spread in the comparison between the measured values. In both cases there does not seem to be a general relationship between the image analysis and optical fibre results. A significant contribution to the spread in measured bubble diameters is due to the fluctuations in bubble shape. Variations in the bubble major and minor diameter are clear in observations from the high speed video. The average minor bubble diameter, shown in figure 5.5b was taken over a vertical distance of approximately 100 mm in the vicinity of the optical fibre probe.

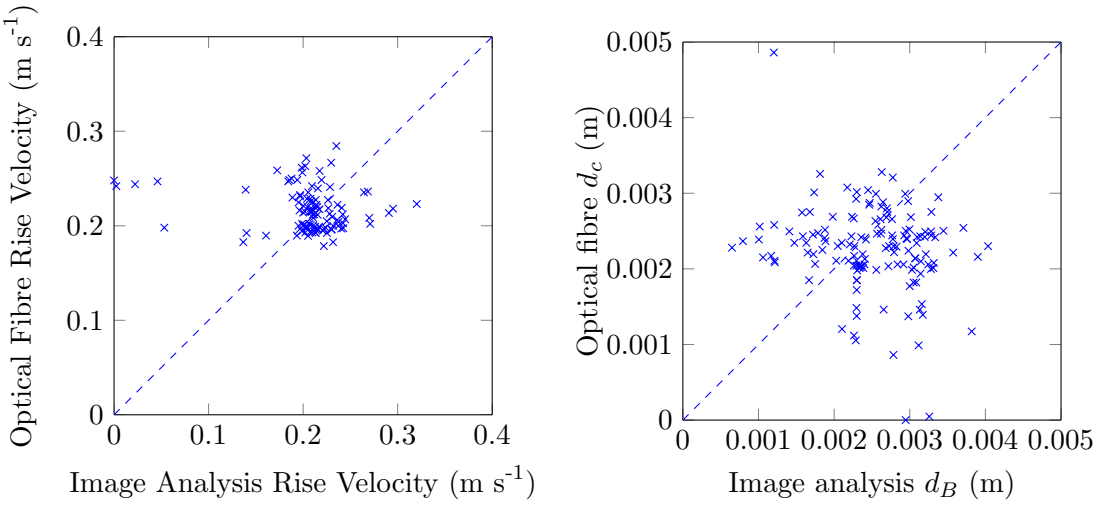

(a) Bubble rise velocity parity plot

(b) Bubble chord length parity plot

Figure 5.5: Parity plots comparing image analysis and optical fibre experiments

Chapter 6

Single Bubble Results & Discussion

6.1 Introduction

This chapter presents the results from a series of experiments using high speed imaging to track the rise of single CO_2-air bubbles in water. Image analysis allowed the measurement of the bubble size, shape, rise path and velocity. The bubble generation process and the presence of surfactants, both of which have an effect on the bubble characteristics and bubble oscillations, were also investigated. The concentration change within the bubble was measured by analysing the gas from bubbles captured at different rise heights. This allowed calculation of a mass balance of the bubble as it rises up the column, leading to estimation of the mass transfer rate. The mass transfer properties of the single rising bubble were then been correlated with the observed bubble characteristics.

6.2 Bubble Size Distribution

The bubble size distributions (BSD) for bubbles of varying input CO_2 concentration are shown in figure 6.1. The initial BSD shown in blue was measured just after release of the bubble and the final BSD shown in yellow was measured at the top of the 1.0 m column. The initial BSD for these experiments range from $2.0 - 4.0$ mm; the data shown in figure 6.1 were measured in tap water. The scenarios with bubbles containing air and 5 % CO_2 (figures 6.1a and 6.1b) show a slight increase in bubble size from the base to the top of the 1.0 m column. In both these cases the increase in bubble volume as a result of the reduction in hydrostatic pressure is expected to be greater than any mass transfer of CO_2 from the gas bubble. A large difference between the initial and final BSD can be seen with the scenario of 100 % CO_2, suggesting significant mass transfer.

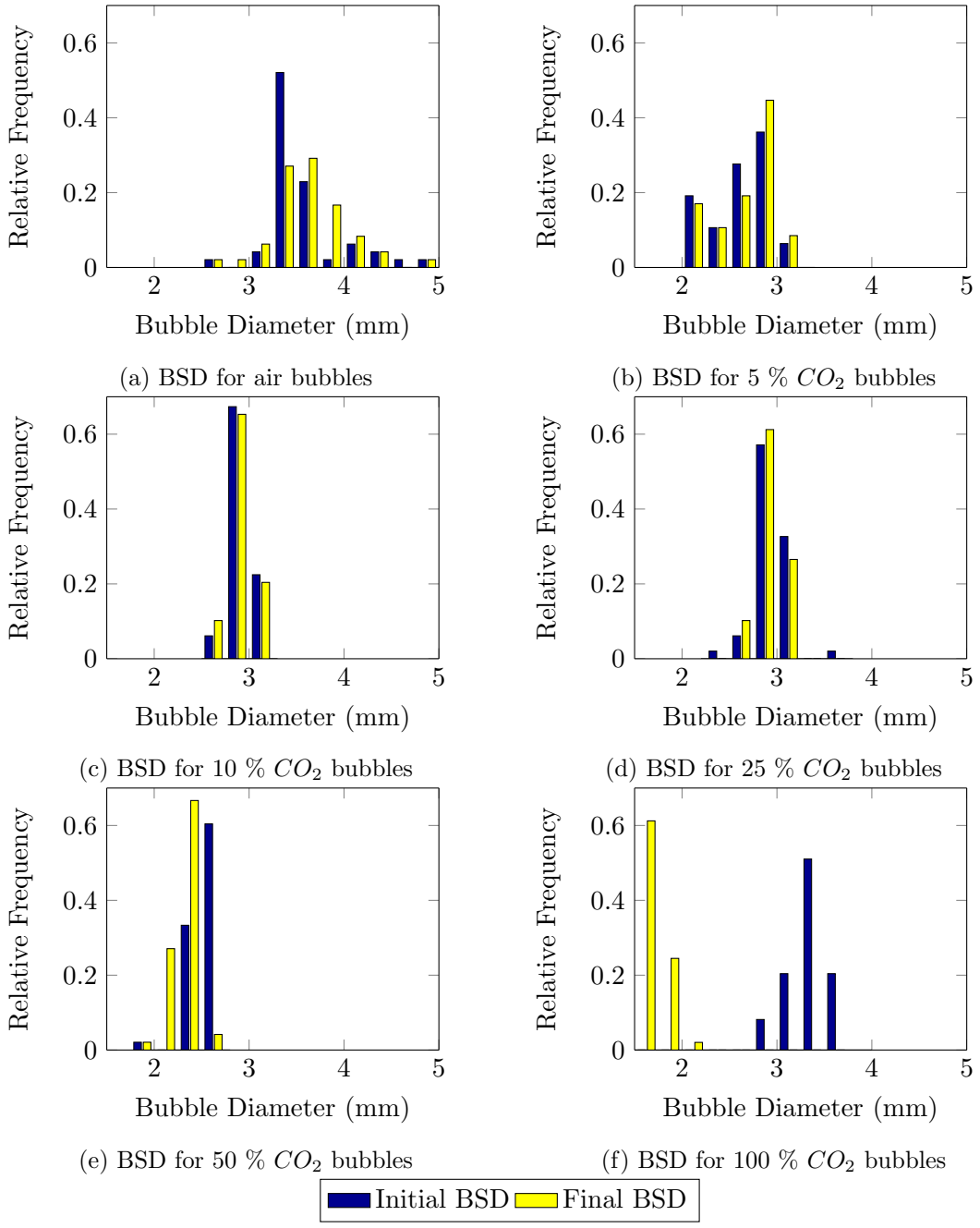

(a) BSD for air bubbles

(b) BSD for 5 % CO_2 bubbles

(c) BSD for 10 % CO_2 bubbles

(d) BSD for 25 % CO_2 bubbles

(e) BSD for 50 % CO_2 bubbles

(f) BSD for 100 % CO_2 bubbles

Figure 6.1: Comparison of initial and final bubble size distribution (BSD) after rising 1.0 m in tap water, for bubbles of different gas composition

In this case the initial average bubble diameter is between $3.0 - 4.0\ mm$ and the average final bubble diameter is under $2.0\ mm$.

The BSD shown in figure 6.1 are taken for bubbles produced by a $1.0\ mm$ orifice. This generates a bubble which rises with an initially straight path, minimising bubble deformation, at least in the early stages of the bubble rise. From observations of the bubble path, it is not always easy to detect when the bubble deformation is caused by the release of the bubble. Previous work by Calderbank and Lochiel (1964) utilised

different bubble injection methods including a method based on collecting gas in a cup before tipping and releasing the bubble, and on prior mixing with a liquid in the gas injection line before bubble release.

In the current work, however, these bubble injection procedures would increase the time in which the gas and liquid are in contact, allowing for mass transfer prior to bubble formation. It took approximately 0.05 seconds for the bubble to be formed and released from the orifice in the current work; this was found to be approximately the same throughout the experiments conducted in tap water, de-ionised water and synthetic seawater. The bubble rise time through a 1.0 m column is approximately 3 seconds, hence under 2% of the time the bubble spends in the bubble column is at the orifice. The mass transfer occurring before bubble release was therefore not considered in the current work, but will contribute a source of error in the experimental procedure.

6.2.1 Bubble Diameter

Figure 6.2 shows the measured bubble diameter of an air bubble rising up a column of water in blue and the line of best fit, shown in red. A slight increase in bubble diameter is apparent; as mentioned previously this is due to the reduced hydrostatic pressure acting on the bubble as it rises up the column of water. There is also a slight change in the gradient of the line of best fit; this is minimal, however, and does not suggest any fundamental difference in the rate of change of bubble size. There is a very noticeable spread in the bubble diameter measurements, shown by the blue line. Part of this is due to the fluctuation of the bubble shape, as well as the measurement error from the image analysis and ellipse fitting process. Because these images only represent a two-dimensional projection of the bubble, the calculation of the bubble volume from the two visible axes can show an fluctuating value, which does not necessarily translate

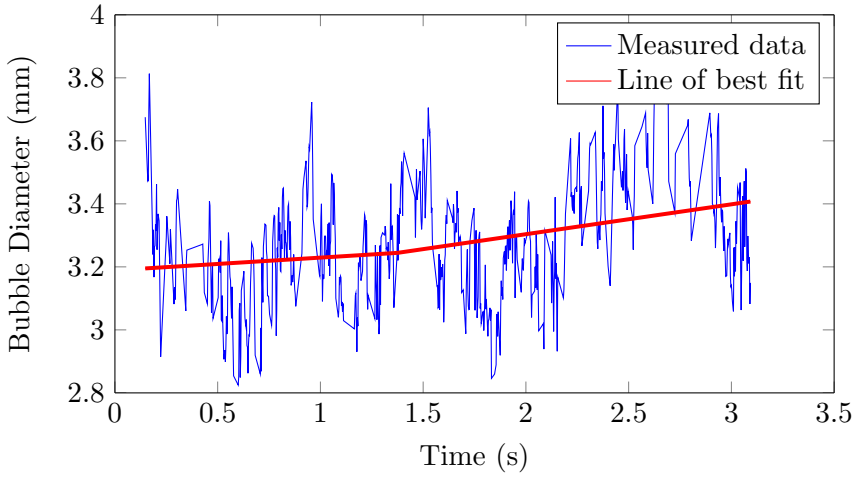

Figure 6.2: Change in bubble diameter of an air bubble rising in tap water

to a changing bubble volume, but rather an fluctuation in the bubble shape. Bubble shape fluctuations and path oscillations are discussed in further detail in chapter 6.4.

Figure 6.3a shows the change in diameter of a pure CO_2 bubble, where there is a clear reduction in bubble size due to mass transfer. There is also a clear oscillation in this example, as well as noise from the bubble diameter measurements, particularly at the beginning of the bubble rise. This is due to the image analysis, which occasionally detected background segments. This was an issue during the bubble release and early stages of the bubble rise, where the syringe or nozzle would occasionally be detected as part of the bubble in the image processing. Despite the noise and bubble oscillation, however, there is a clear gradient in the reduction in the bubble diameter, suggesting one mass transfer rate. This bubble has an initial bubble equivalent diameter, $d_0 \approx 2.9\ mm$.

Figure 6.3b shows the change in bubble diameter of a pure CO_2 bubble with a smaller initial diameter, $d_0 \approx 2.2\ mm$. As with the previous example, there is significant noise in the initial stages of the bubble size measurement. In this example, however, the bubble does clearly show two different mass transfer rates, with a larger initial rate indicated by a steeper gradient in the reduction of the bubble diameter, followed by a clear transition point to a lower mass transfer rate.

The CO_2 bubble with $d_0 \approx 2.9\ mm$ (figure 6.3a) has an average rate of change of diameter of $-0.77\ mm\ s^{-1}$, which is similar to the initial rate of change for the bubble with $d_0 \approx 2.2\ mm$ (figure 6.3b) of $-0.67\ mm\ s^{-1}$; however the final rate of change of diameter for the smaller bubble drops to $-0.15\ mm\ s^{-1}$. This indicates that the larger bubble undergoes the faster mass transfer rate during the whole rise time up the $1.0\ m$ bubble column, and that the time taken to rise the $1.0\ m$ height of the column is not sufficient for the transition to occur to the slower mass transfer rate.

This second stage of mass transfer has been attributed to the bubble surface becoming less mobile, due to the accumulation of surfactants on the bubble surface, Vasconcelos et al. (2002), Alves et al. (2005). Vasconcelos et al. (2002) found that initial bubble diameter was the sole parameter which had an effect on this transition point between the faster and slower mass transfer rates. Work by Rosso et al. (2006) confirmed that a higher interfacial velocity reduced the effect of surfactants. The interfacial velocity is related to the bubble rise velocity, which is generally higher for larger bubbles. Hence a larger bubble, with a greater velocity, would inhibit the attachment of surfactants to a greater degree than a smaller bubble with a lower rise velocity. This would explain why the larger initial bubble diameter has a later transition point to the reduced mass transfer rate. This is complicated, however, by the counter effect that the surfactants have on reducing the rise velocity. Work from Peters and Els (2012) also found that sufficiently quick bubble generation conditions managed to prevent the onset of the accumulation of surfactants. This was the case at least for the duration of the bubble rise in their experiments, which occurred for a rise height of just over $1.0\ m$, similar to that in the

current work. The findings from the initial experiments in this work, which agree with those of Vasconcelos et al. (2002), Rosso et al. (2006) and Peters and Els (2012), suggest that if surfactants are not given a chance to attach to the bubble surface before it is released and provided that the rise velocity is large enough, then surfactant attachment can be restricted for the first 1.0 m bubble rise. Once surfactants are allowed to attach to a bubble surface they will increase the drag force, reducing the rise velocity which will allow further surfactants to accumulate rapidly on the bubble surface. Once this occurs, the mass transfer rate will be inhibited. The initial bubble generation conditions and bubble rise velocity are thus critical parameters in allowing surfactant accumulation, and the bubble rise velocity is discussed in further detail in the following section.

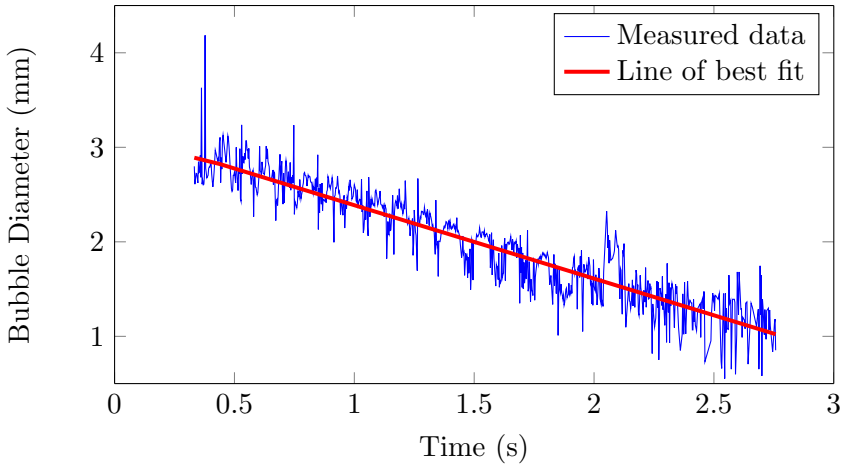

(a) Change in bubble diameter, with initial diameter $d_0 \approx 2.9\ mm$

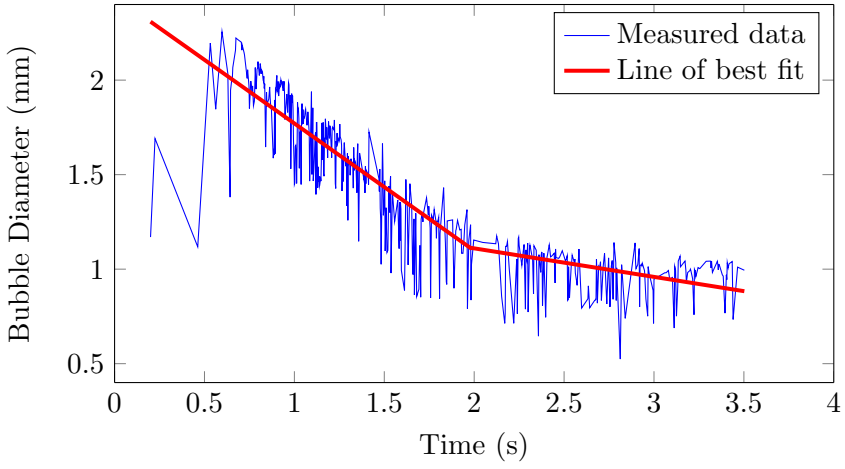

(b) Change in bubble diameter, with initial diameter $d_0 \approx 2.2\ mm$

Figure 6.3: Change in equivalent diameter of a pure CO_2 bubble rising in tap water

6.3 Bubble Velocity

Figure 6.4 shows the average rise velocity for air and CO_2 bubbles with an initial diameter $2.0 < d_0 < 3.0\ mm$ as they rise up a $1.0\ m$ column. The 95 % confidence interval is shown by the dashed line, with the results representing the average for 50 bubbles. Part of this error is due to experimental error from the sonar sensor and image analysis readings, while some is due to variation in the bubble size and bubble path oscillations. In both cases for air and 100 % CO_2, there is a very fast acceleration (not shown in the figure, due to the short time scale), followed by a slower increase, which is smaller for air than for CO_2 bubbles. A maximum velocity is reached before there is a marked reduction in the rise velocity for both bubble types. With the case of the CO_2 bubble there will be significant bubble size reduction, due to the mass transfer of CO_2. The change in bubble size will have a large effect on the rise velocity, this can be seen by the increase in rise velocity of the CO_2 bubble with a reduction in bubble size. As these measurements were conducted in tap water, this is also dependent on surfactant attachment to the bubble surface, which can have a significant effect reducing the bubble rise velocity. The reduction in the rise velocity of the air bubble is likely due to an accumulation of surfactants, increasing the drag force on the bubble. The magnitude of the effect surfactants have on the bubble rise velocity is dependent on the bubble size. The smaller CO_2 bubble at the top of the column could have a greater portion of surfactants on its bubble surface, than the larger air bubble, resulting in a greater reduction in rise velocity.

Figure 6.5 compares the bubble rise velocity measurements from this work with empirical relations for bubble rise velocity from the literature (shown in table 2.3). The ratio of

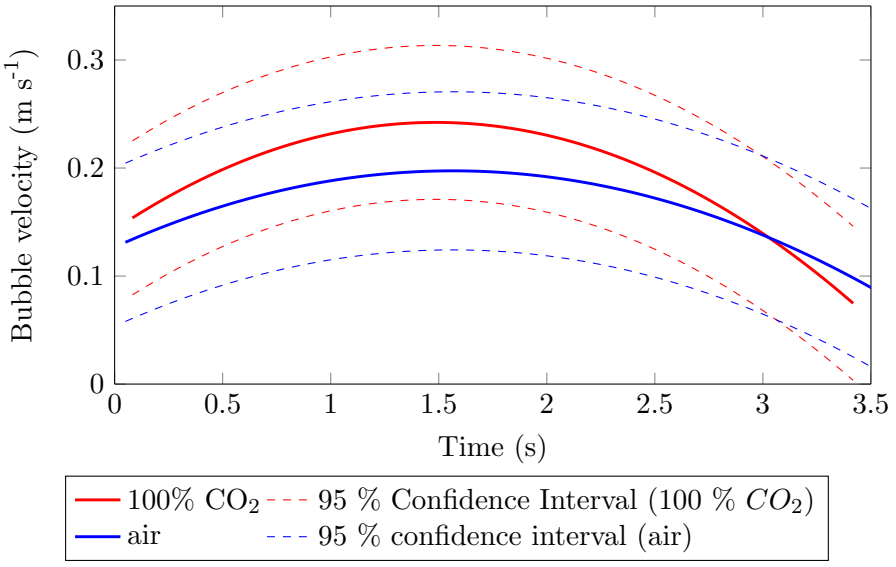

Figure 6.4: Average velocities of air and CO_2 bubbles, with initial diameter $d_0 \approx 2.0 - 3.0\ mm$, rising up a $1.0\ m$ column of tap water

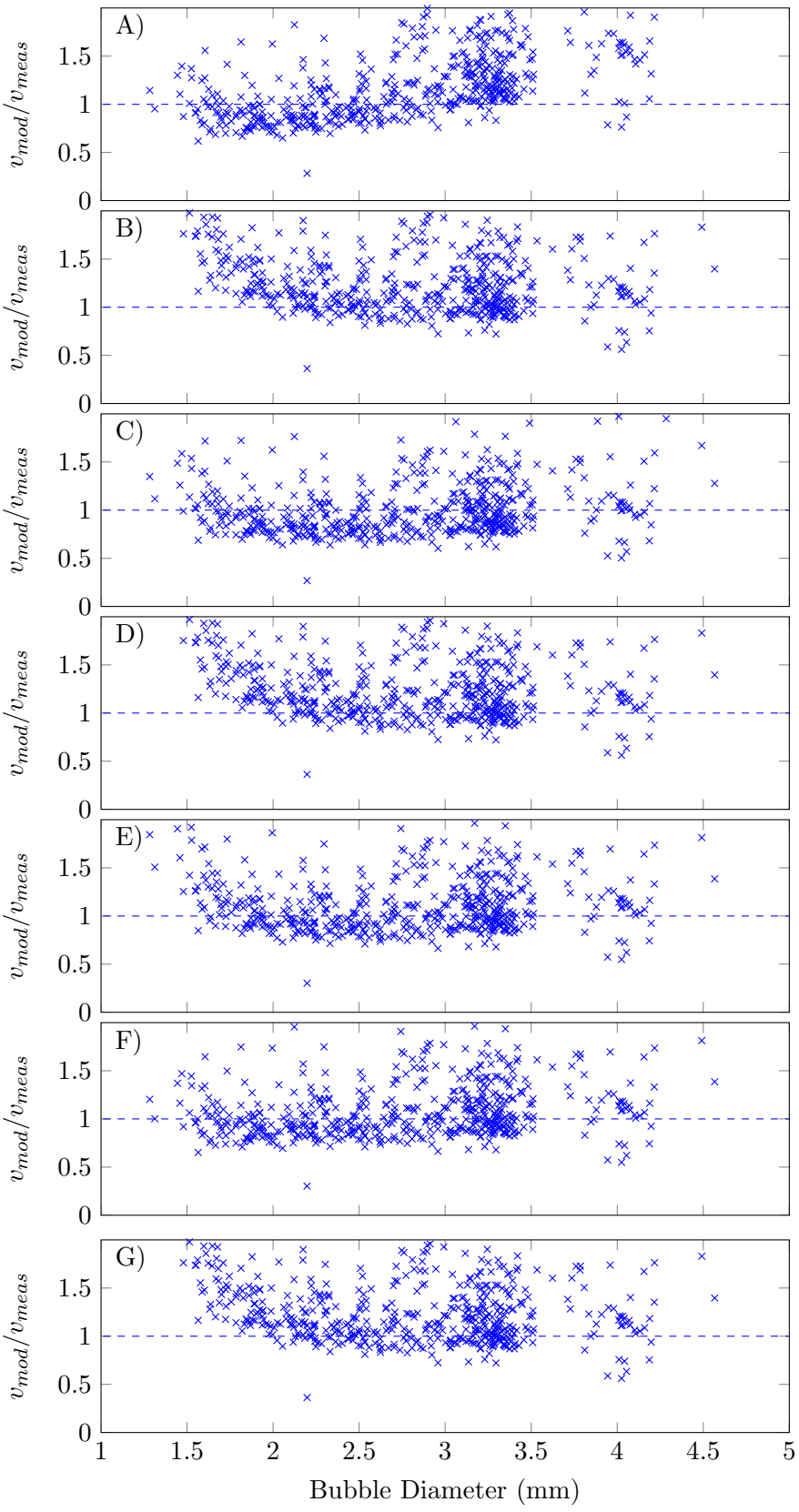

Figure 6.5: Ratio of modelled bubble rise velocity (v_{mod}) from empirical relations with the measured bubble rise velocity taken in tap water (v_{meas}) compared with average bubble diameter; A) Clift et al. (1978) B) Mendelson (1967) C) Fan and Tsuchiya (1990) D) Maneri and Vassallo (2000) E) Wallis (1974) F) Ishii and Chawla (1979) G) Tomiyama et al. (1998)

v_{mod}/v_{meas} is a ratio of the modelled bubble rise velocity as calculated from empirical relations and the measured value of the bubble rise velocity from the single bubble rise experiments. The bubble rise velocities shown in figure 6.5 were measured in tap water, for a range of average bubble diameters between $1.4 < d_e < 4.6\ mm$. These bubbles were classified as belonging to the surface tension dominated regime, characterised by an ellipsoidal shape and zig-zagging or helical rise paths. For pure CO_2 bubbles, the bubble size will often reduce to a small enough size to change from the surface tension to the viscosity dominated regime.

The empirical relations considered in figure 6.5 correspond to the surface tension regime from table 2.3, including relations from: Mendelson (1967), Wallis (1974), Clift et al. (1978), Ishii and Chawla (1979), Fan and Tsuchiya (1990), Tomiyama et al. (1998) and Maneri and Vassallo (2000). The relation from Clift et al. (1978) shown in figure 6.5A underestimates the rise velocity for the smaller bubble diameters ($d_e < 2.5\ mm$), and overestimates the velocity for larger diameters ($d_e > 3.0\ mm$). Empirical relations from Mendelson (1967), Maneri and Vassallo (2000) and Tomiyama et al. (1998), shown in figures 6.5B, D and G, respectively, on average, all over estimate the rise velocity. This is because these relations provide estimates for the rise velocity in pure systems, without the contamination of surfactants. The relations from Fan and Tsuchiya (1990), Wallis (1974) and Ishii and Chawla (1979) shown in figures 6.5C, E and F, respectively, provide estimates for the rise velocity in liquids contaminated with surfactants and show a better fit to the experimental measurements.

Surfactant contamination will also contribute to the spread of velocity measurements. As discussed previously the effect of surfactants is dynamic and will change during the rise of a bubble. Therefore, for part of its ascent the bubble may act as if it is in a pure system, until the accumulation of surfactants is sufficient enough to reduce the rise velocity. This would add to the error and spread of results when calculating the average rise velocity as shown in figure 6.5. Additionally the terminal rise velocity may not have been reached during the ascent in the 1.0 m bubble column. Sam et al. (1996) found that under certain conditions bubbles had still not reached their terminal velocities in a 4.0 m bubble column. Analysis of the bubble path oscillations would provide a better insight into the effect of surfactants, which have been shown to dampen the bubble path oscillations, as well as reducing the rise velocity, Sam et al. (1996).

Due to the large volume of the bubble column used in these experiments, it was impractical to carry out experiments using ultra pure water. Experiments were conducted with de-ionised water, tap water and synthetic seawater to look at whether the increased surfactant concentrations in these liquids have an effect on bubble characteristics. A slightly reduced average rise velocity was observed for bubbles rising in synthetic seawater compared to de-ionised water, as shown in figure 6.6. The average bubble size for both experiments is very similar. This suggests that, despite a substantial surfactant concentration already present in de-ionised water, a further increase in surfactant

concentration can still noticeably increase the drag force on the bubble. There is a large spread in measured bubble rise velocities, particularly for smaller bubble sizes, with $d_e \approx 1.5\ mm$ diameter. This could be due to the rate of surfactant accumulation, which will be almost instantaneous in the synthetic seawater, but more delayed in the de-ionised water.

6.4 Bubble Oscillations

Several external factors can generate shape oscillations, with the bubble generation process being one such method. Figure 6.7 shows the formation of two air bubbles from the 1.0 mm orifice, which result in very different bubble characteristics. Figure 6.7a illustrates a bubble being produced with a higher gas flow rate. This results in instability during the bubble detachment, seen by the 'neck-breaking' release mechanism, as described by de Vries (2001). This energetic separation from the orifice creates a faster acceleration of the rear bubble surface, causing it to deform into an inward point inside the bubble. This can initiate a water droplet to break from the point of the jet in the bubble. The momentum of the water droplet causes it to rise to the top of the bubble, where it collides with the top of the bubble surface, creating further bubble shape oscillations. High speed images from Manasseh et al. (2001) show this effect in detail.

The oscillating bubble, shown in figure 6.7a and referred to as bubble 'A', is compared with a bubble showing little shape oscillation in figure 6.7b, referred to as bubble 'B'. The

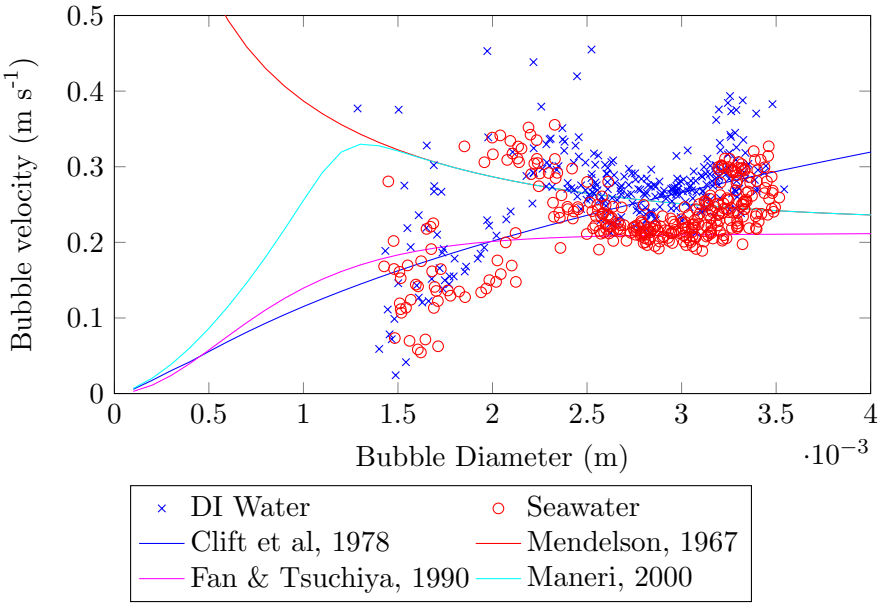

Figure 6.6: Average rise velocities (taken over 1.0 m) of CO_2 bubbles in de-ionised water and synthetic seawater

(a) 'Bubble A' - Initial 0.35 s of air bubble rise through tap water, $d_0 \approx 3.3\ mm$

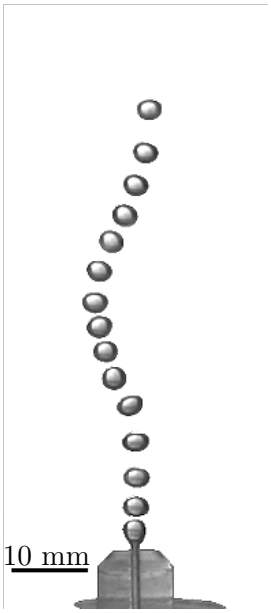

(b) 'Bubble B' - Initial 0.35 s of air bubble rise through tap water, $d_0 \approx 3.1\ mm$

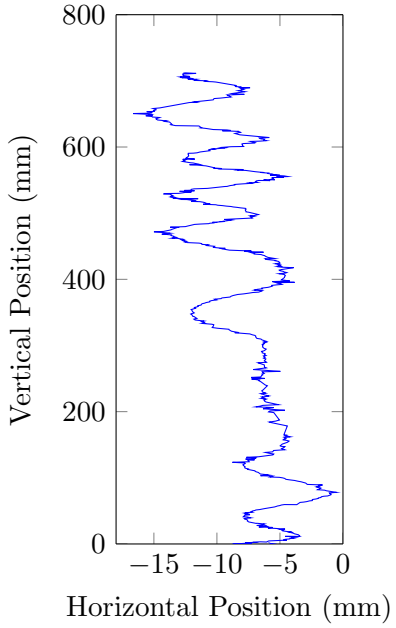

(c) 2D Tracked bubble rise path of 'Bubble A'

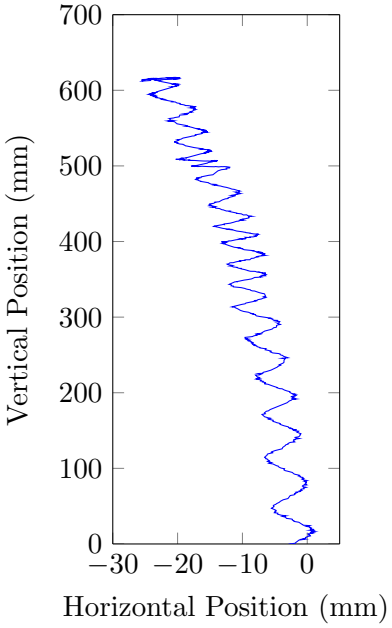

(d) 2D Tracked bubble rise path of 'Bubble B'

Figure 6.7: Image sequence and bubble path co-ordinates of two CO_2 bubbles ascending in tap water produced from 1.0 mm orifice a) $d_0 \approx 3.3\ mm$ and b) $d_0 \approx 3.1\ mm$

smooth detachment of bubble B was created by a pulse of the gas flow exiting the orifice and initiating the bubble detachment. In this scenario the bubble shape oscillations of bubble B are visibly less than bubble A. The bubble also has a more spherical shape, with the average aspect ratio of bubble B $E_B = 0.83$, compared with $E_A = 0.44$ for bubble A. This agrees with Tomiyama et al. (2002) who found that the magnitude of the initial shape deformation effects the aspect ratio, with greater deformation resulting in a lower aspect ratio. They also noticed that the initial shape deformation has a large effect on the rise velocity. In the current experiments there was also a noticeable velocity difference between the two bubbles. Figures 6.7a and 6.7b show frames taken at intervals of 0.025 s. It is clear that bubble A initially travels at a higher velocity, with the average rise velocities for bubble A and B being 0.28 and 0.16 $m\ s^{-1}$, respectively. The initial bubble diameters are $d_0 = 3.1\ mm$ and $d_0 = 3.3\ mm$ for bubbles A and B, respectively, too small a difference to be the cause of this difference in rise velocity. It is also important to consider the rise velocity when looking at figures 6.7c and 6.7d which illustrate the rise path of bubbles A and B. Despite the larger number of oscillations by bubble B seen in figure 6.7d, the slower rise velocity results in similar average oscillation frequencies of 3.4 s^{-1} and 4.6 s^{-1} for bubbles A and B, respectively. This shows the importance of the bubble generation mechanisms in determining the bubble characteristics, particularly the rise velocity and aspect ratio.

As well as manipulating the gas flow rate, the bubble characteristics can be affected by changing the size of the orifice which produces the bubbles. Figures 6.8a and 6.8b show the rise of two CO_2 bubbles produced from 1.0 mm and 0.35 mm orifices, referred to as bubbles 'C' and 'D', respectively. During the bubble detachment there is an abrupt change in shape for both bubbles, which develops into a continual shape oscillation. There is also a clear difference in initial rise velocity over the first 0.35 s of bubble rise, with bubble D travelling further than bubble C. The effect of a higher initial rise velocity for CO_2 bubbles is different for air bubbles. Comparison of the average rise velocities for the CO_2 bubbles in the 1.0 m water column shows that bubble C has a greater average velocity of 0.23 $m\ s^{-1}$ than bubble D, which has an average rise velocity of 0.17 $m\ s^{-1}$. Both bubbles have approximately the same, initial bubble diameter, $d_0 \approx 2.7\ mm$. During the course of the bubble rise, however, the change in bubble diameter is different. The higher initial velocity of bubble D, results in a greater initial mass transfer rate, and thus a greater initial reduction in bubble size. Figure 6.9 shows the change in bubble diameter for bubbles 'C' and 'D'. The approximate rate of change of bubble 'C' is 0.48 $mm\ s^{-1}$, whereas the initial rate of change of bubble D is 0.58 $mm\ s^{-1}$, which reduces to 0.27 $mm\ s^{-1}$ during the second phase of mass transfer. As a result of this larger initial mass transfer rate from bubble D, the greater reduction in bubble volume results in the bubble transforming into a spherical bubble in the viscous dominated regime. This smaller bubble exhibits a rectilinear motion at the top of the bubble column, as shown by the lack of path oscillation at the top of the bubble path in figure 6.8d. This highlights the advantage of an initially higher bubble velocity to

(a) 'Bubble C' - Initial 0.35 s of CO_2 bubble rise in tap water produced from a 1.0 mm orifice

(b) 'Bubble D' - Initial 0.35 s of CO_2 bubble rise in tap water produced from a 0.35 mm orifice

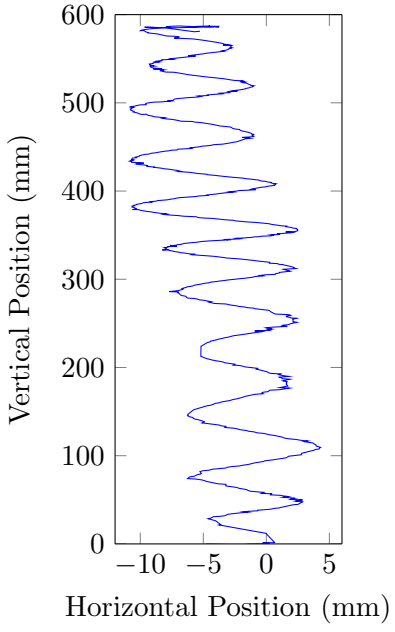

(c) 2D Tracked bubble rise path of 'Bubble C'

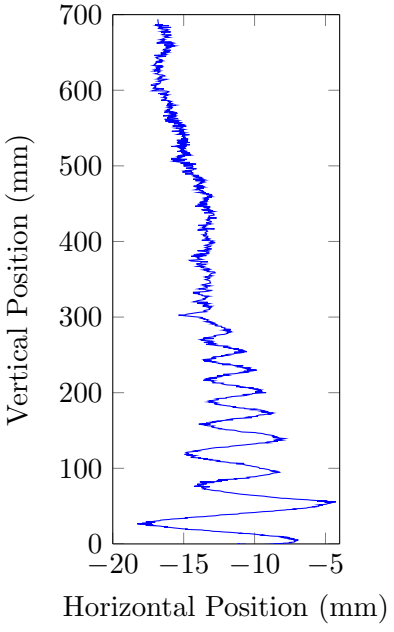

(d) 2D Tracked bubble rise path of 'Bubble D'

Figure 6.8: Image sequence and bubble path co-ordinates of two CO_2 bubbles with $d_0 \approx 2.7\ mm$ ascending in tap water from 1.0 and 0.35 mm orifices

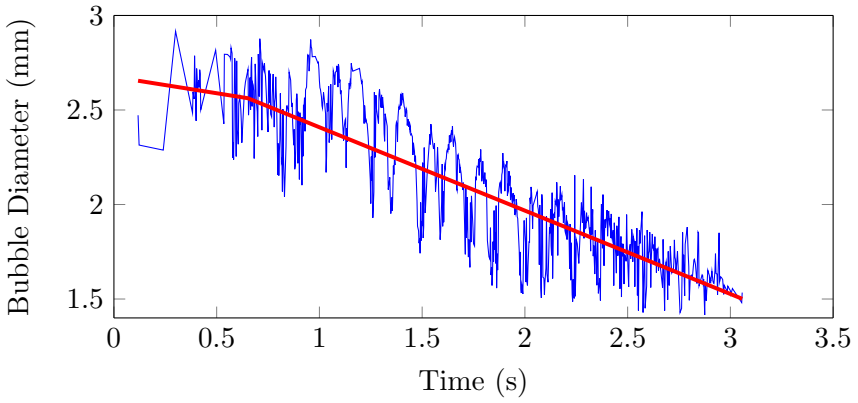

(a) Change in bubble diameter of 'Bubble C'

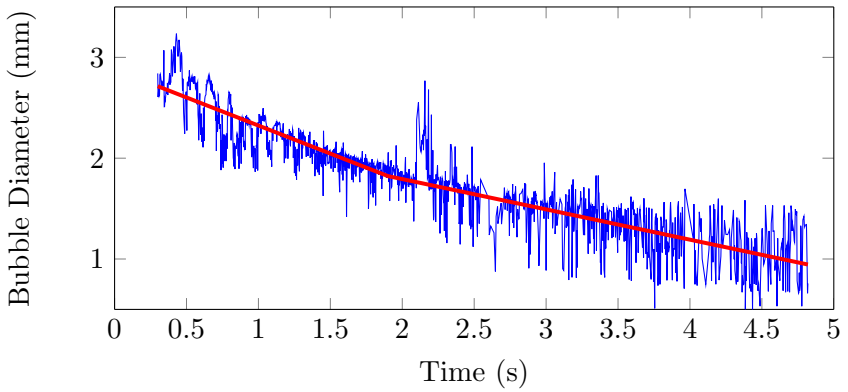

(b) Change in bubble diameter of 'Bubble D'

Figure 6.9: Comparison of bubble diameter from bubbles produced with different orifices, a) 'Bubble C' orifice diameter 1.0 mm b) 'Bubble D' orifice diameter 0.35 mm

increase the mass transfer rate, and also the difference in bubble characteristics this would create between air bubbles and pure CO_2 bubbles.

The oscillations in the bubble rise path and fluctuations in the bubble shape were considered in more detail by examining the dominant frequencies using a fourier transform. As seen in figure 6.8d the large reduction in the CO_2 bubble size, causes a change from the surface tension regime to the viscosity regime, which impedes the bubble path oscillations. Because of this change in bubble properties, the data from the bubble rise path, shape and velocity were divided into three stages, and oscillation frequencies were analysed separately for each. Prior to the fourier transform the data was de-trended to remove the underlying variation in the data and allow for the identification of any oscillations. Linear line of best fits were subtracted from the horizontal bubble position and bubble aspect ratio data, shown in figures 6.10b and 6.10f, respectively. The bubble rise velocity did not have a linear trend, however it did show an acceleration and deceleration, in this case a moving average was subtracted from the bubble rise velocity data before the fourier transform. The identified frequencies from the fourier transform were then used in a band-pass filter to remove noise from the corresponding data.

Figure 6.10 shows the fourier transform analysis for a section of the rise of a CO_2 bubble. The raw and filtered data are shown on the left hand side in figures 6.10a, 6.10c and 6.10e, while the frequency domains are shown on the right hand side in figures 6.10b, 6.10d and 6.10f. The most noticeable oscillation frequency is seen in the bubble path oscillation, with a frequency of 5 Hz. As a result of the bubble path oscillation there is a detectable oscillation in the vertical component of the bubble rise velocity which occurs at twice the path frequency at 10 Hz. This frequency corresponds to the bubble location at the extremes of the bubble rise path, showing the reduction in rise velocity as the direction of the bubble changes. The aspect ratio shows a clearer symmetry to the path oscillation frequency with a peak at 5 Hz in figure 6.10f, this is alongside a peak at, double this frequency, of 10 Hz. This indicates the fluctuations in bubble shape at the horizontal extremes of the bubble rise path.

The red lines plotted in figures 6.10a, 6.10c and 6.10e highlight the filtered data, extracting the frequencies between $5 - 10$ Hz. This highlights the importance of the oscillation to each variable, distinguishing this from the measurement noise.

The onset of path oscillations has been reported to occur at $Re_{CR} \approx 200$, Okawa (2003) for contaminated systems and $Re_{CR} \approx 600$ for pure systems, Veldhuis et al. (2008). Although the path oscillation is initiated at a lower Re in contaminated systems, these systems also act to dampen the path oscillations during the bubble rise, Sam et al. (1996). Recently, experimental work from Ellingsen and Risso (2001) and numerical simulations from Mougin and Magnaudet (2001) have shown that the path instability is initiated by instabilities in the bubble wake caused by the bubble aspect ratio, rather than oscillations in the bubble shape. The shape oscillation, however, directly results in an oscillation of the aspect ratio, as seen in figure 6.10e. A range of bubble path oscillation frequencies and amplitudes have also been reported in the literature, with an oscillation frequency of approximately $5-10$ Hz reported by Saffman (1956), while Ern et al. (2012) found an amplitude in path oscillations between $3-5 \times d_e$ for air bubbles in water. Haberman and Morton (1953) noticed that the path oscillation frequency is a function of Re. Equation 6.1 shows the relation from Okawa (2003) for the amplitude of the path oscillation (Ω). St from equation 6.1 is the Strouhal number, given by equation 6.2, and τ is the period of the oscillation.

$$\begin{aligned} \frac{\Omega}{d_e} &= C_R St^{-1} \\ C_R &= 0.1 \times \{1 - e^{-0.0061(Re - Re_{cr})}\} \end{aligned} \tag{6.1}$$

$$St = \frac{d_e}{u_b \tau} \tag{6.2}$$

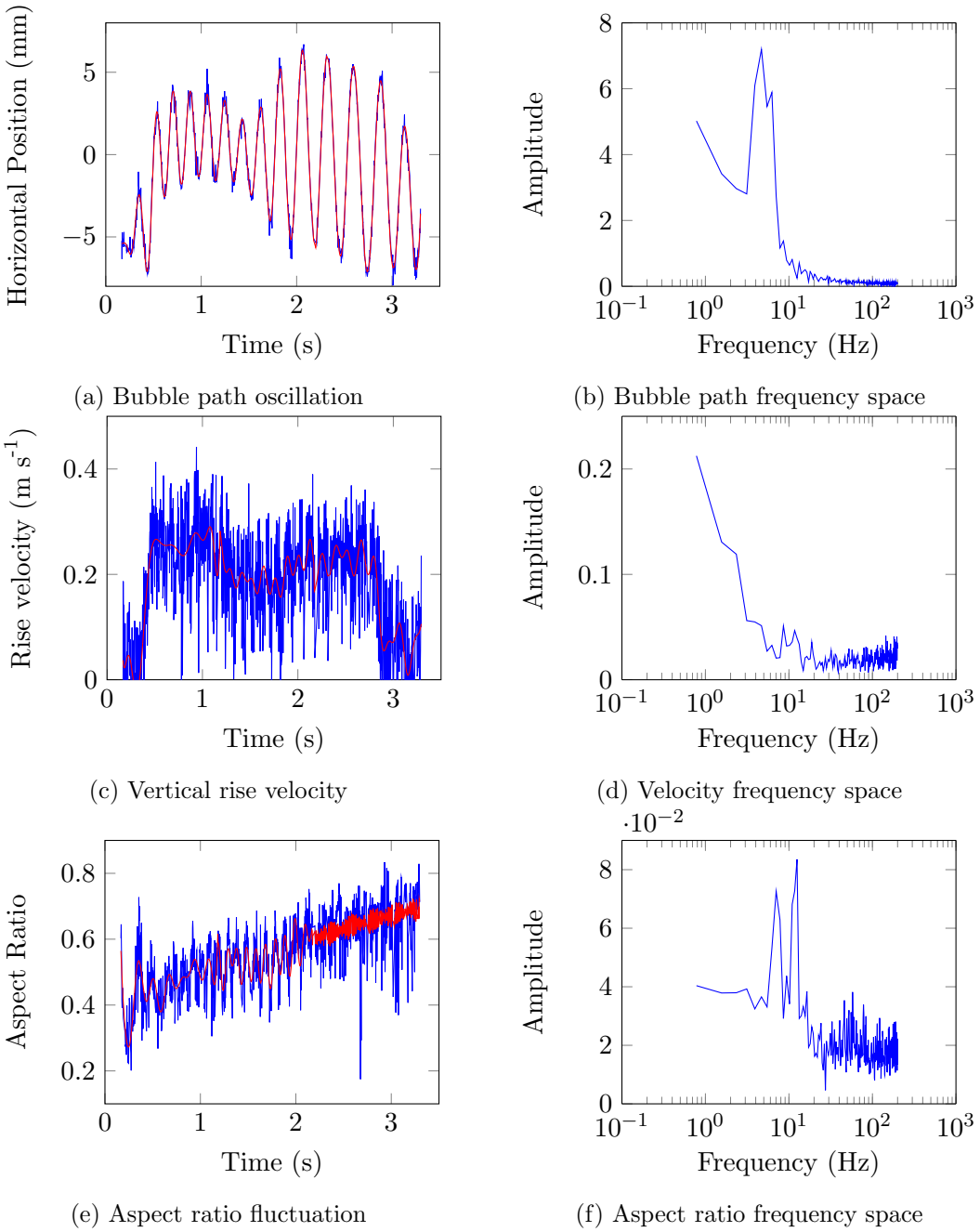

(a) Bubble path oscillation

(b) Bubble path frequency space

(c) Vertical rise velocity

(d) Velocity frequency space

(e) Aspect ratio fluctuation

(f) Aspect ratio frequency space

Figure 6.10: Fourier transform to highlight oscillation frequencies of bubble path, rise velocity and fluctuations in the aspect ratio

As can be seen from figures 6.7 and 6.8 the bubble path starts to oscillate shortly after bubble release. Figure 6.11 shows the onset of the horizontal path oscillation from a CO_2 bubble. The path oscillation in figure 6.11a occurs after $0.1 - 0.2$ s: this corresponds to an increase in $Re > 200$, shown in figure 6.11b. In this example the frequency of the bubble path oscillation was reasonably constant at around 5 Hz. This value was used in equation 6.1 to calculate the amplitude of the bubble path, which is compared with the measured path in figure 6.11c. As shown in figure 6.11, equation 6.1 provides a reasonable approximation for the maximum amplitude of the bubble path, although this is over-estimated during the earlier stages of the bubble rise. This is possibly because of the magnitude of Re, which peaks before the peak magnitude of the bubble path oscillation, as shown in figure 6.11a.

The reduction in bubble size as a result of mass transfer of CO_2 bubbles can cause a change in the bubble path from a zig-zag to a rectilinear motion. An example of this is shown in figure 6.12a, with the transition observed at $Re \approx 300 - 600$. As found in figure 6.11c the path amplitude predicted from equation 6.1 was an overestimate for most of the oscillations, apart from the maximum oscillation, which was slightly under-predicted. The over-prediction of the majority of the path oscillation amplitudes could be due to dampening of the oscillation from surfactants, as noted by Sam et al. (1996).

The relation between the bubble path oscillation frequency and bubble diameter is highlighted in figure 6.13. The reduction in bubble diameter results in a lower oscillation frequency, until the viscous forces acting on the bubble diameter become predominant and the bubble becomes spherical with no path oscillation.

6.5 Aspect Ratio

Figure 6.14 shows the frequency and amplitude of the surface area fluctuations, which are a direct result of the bubble shape, or aspect ratio fluctuations. For the size range tested in these experiments the frequency or amplitude of the surface area fluctuations does not seem to be dependent on bubble diameter.

As shown earlier in figure 6.8 and in work by Sam et al. (1996), Tomiyama et al. (2002), Wu and Gharib (2002) and Quinn et al. (2014) the bubble generation process can have a large impact on the aspect ratio. Figure 6.15a compares the aspect ratio of bubbles produced from 1.0 mm and 0.35 mm orifices. As discussed previously, the larger initial velocity of the bubbles produced by the 0.35 mm orifice, resulted in higher mass transfer rate and hence a greater reduction in bubble volume. This resulted in a change in bubble characteristics, from a larger, oscillating, ellipsoidal bubble to a smaller, spherical bubble. This change can be seen in the higher average aspect ratio, indicating a more spherical bubble, for the bubbles produced by the 0.35 mm orifice. The empirical relation proposed by Wellek et al. (1966) provides an estimate for the upper boundary of the

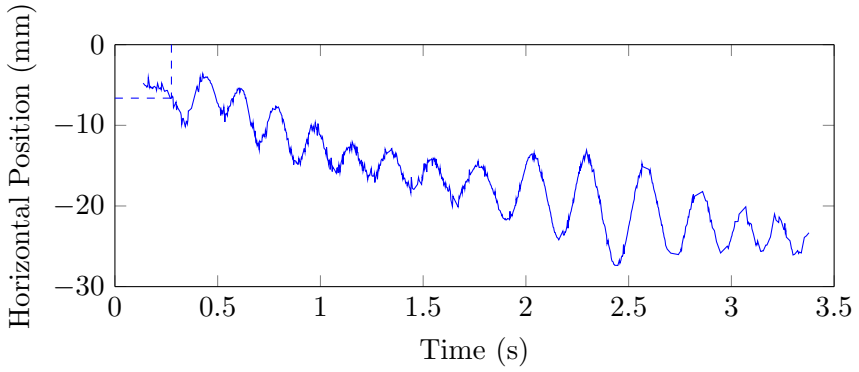

(a) Measured bubble path, with onset of oscillation at $Re \approx 200$

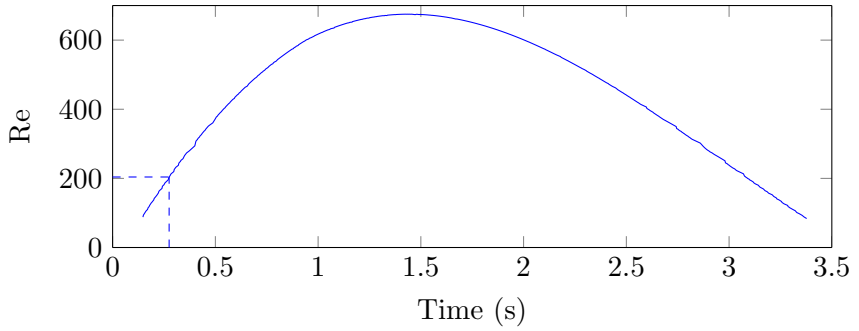

(b) Change in Re during the bubble rise, with onset of path oscillation at $Re \approx 200$

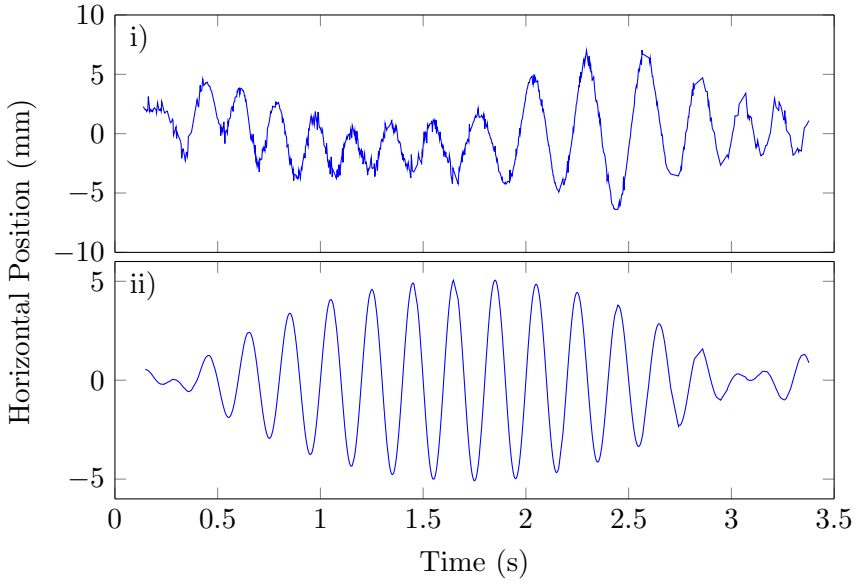

(c) Comparison between i) measured and de-trended bubble horizontal position and ii) predicted bubble horizontal position Okawa (2003), as shown in equation 6.1

Figure 6.11: Effect of Re on onset of bubble path oscillation for bubble 'C' shown in figure 6.9a

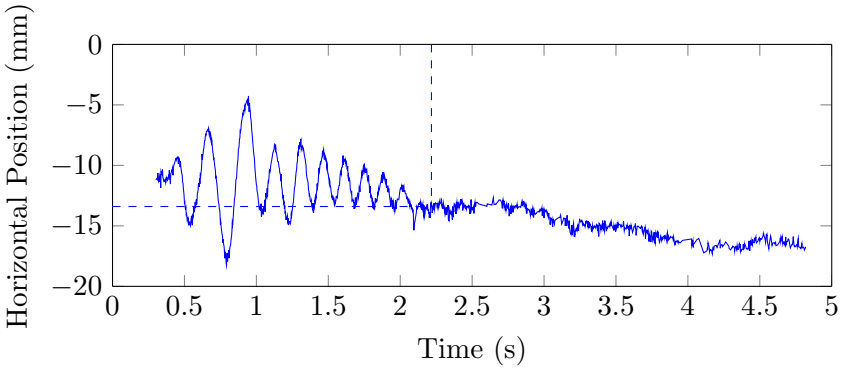

(a) Measured bubble path, with onset of oscillation at $Re \approx 600$

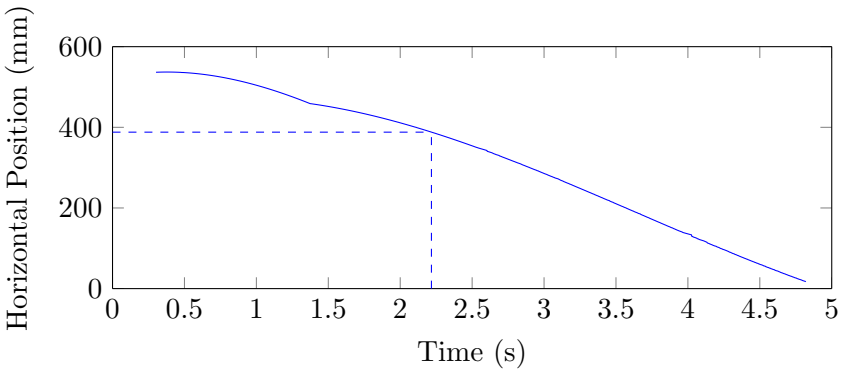

(b) Change in Re during the bubble rise, with onset of path oscillation at $Re \approx 600$

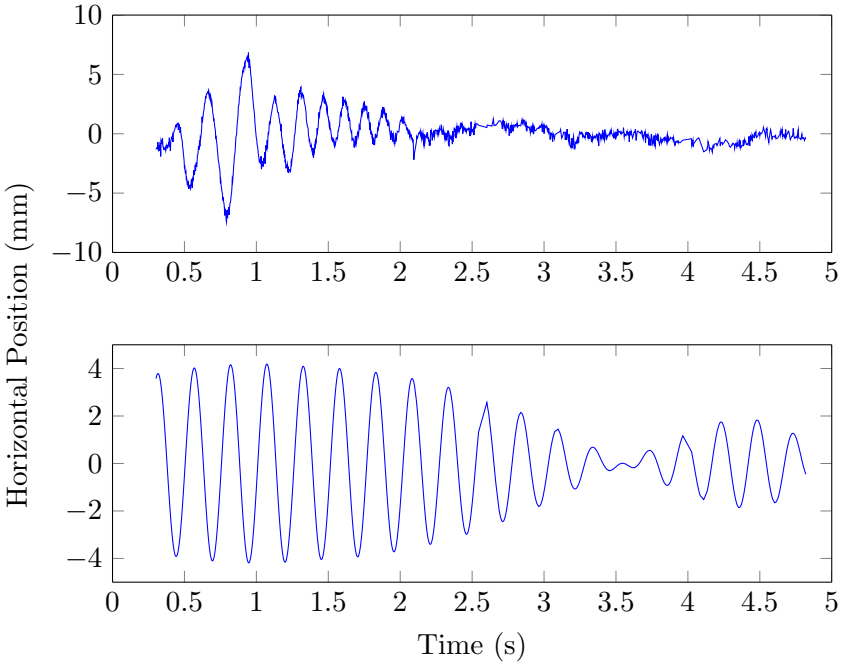

(c) Comparison between i) measured and de-trended bubble horizontal position and ii) predicted bubble horizontal position from Okawa (2003), as shown in equation 6.1

Figure 6.12: Effect of Re on onset of bubble path oscillation for bubble 'D' shown in figure 6.9b

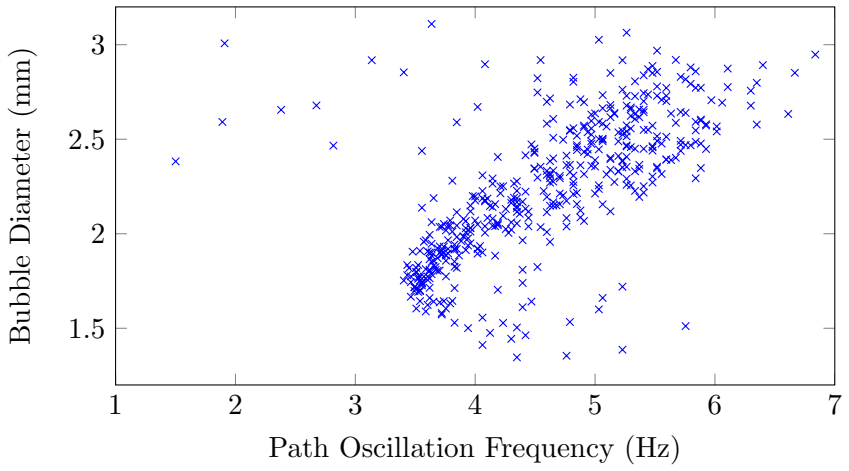

Figure 6.13: Comparison between bubble path oscillation frequency and bubble diameter

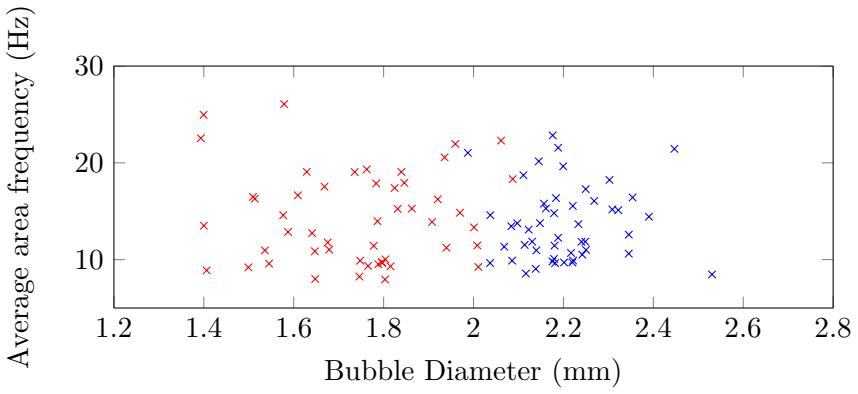

(a) Frequency of surface area oscillations

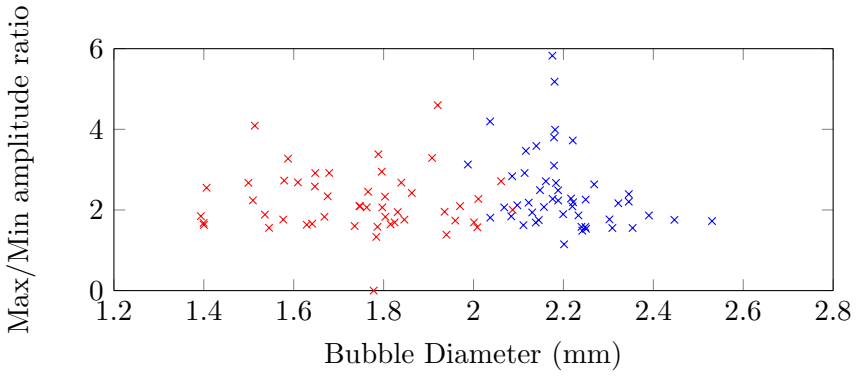

(b) Amplitude of surface area oscillations

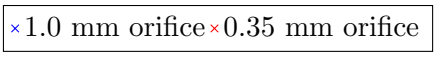

Figure 6.14: Surface area oscillations of bubbles produced with 0.35 and 1.0 mm nozzles

aspect ratio. This shows poor agreement with the measured values from this work. Okawa (2003) also found poor agreement between their measured aspect ratio values and the relation from Wellek et al. (1966) for larger bubbles, however there was better agreement for smaller bubbles. The proposed relation from Okawa (2003) provides a significantly improved fit to the experimental data, although this is only applicable for bubbles with $Eo < 1$.

Figure 6.15b shows the difference between the measured aspect ratio and the predicted values from the relations shown in equations 2.20 - 2.21, in chapter 2.4, which use the We to estimate the aspect ratio. All relations overestimate the aspect ratio, although at larger We the relation from Moore (1965) becomes closer to the measured aspect ratio of bubbles found in the current work. Grace et al. (1976) found that the relations based on the Eo, rather than We better predicted the aspect ratio, which agrees with this work, when comparing figures 6.15a and 6.15b.

As well as the bubble generation procedure, the liquid properties and presence of trace concentrations of surfactants can have a large impact on the bubble characteristics and mass transfer rate. The effect of surfactants has been shown to be greater on smaller bubbles than larger ones.

The effect of increased surfactant concentration on the bubble shape is shown in figure 6.16. A comparison of the aspect ratio relations of Wellek et al. (1966) and Okawa (2003) with the bubble measurements in de-ionised water and synthetic seawater shows a reasonable fit to the relation from Okawa (2003) for $Eo < 0.8$. At values of $Eo > 0.8$ the aspect ratio appears relatively constant for an increase in Eo, up to the measured values of $Eo < 1.7$. The over estimation of the relation from Wellek et al. (1966) is more pronounced in figure 6.16a than figure 6.15a, due to the larger bubble sizes and values of Eo considered in figure 6.16a. This supports the findings from Okawa (2003) who found that Wellek et al.'s empirical relation overestimated the aspect ratio for larger bubble sizes. As with the orifice size, the Eo relation from Okawa (2003) provides the best approximation for the aspect ratio. The average bubble aspect ratio does not show a noticeable difference between de-ionised water or synthetic seawater; however in liquids with lower surfactant concentrations an effect on the aspect ratio maybe more evident.

As seen in figure 6.15b the empirical relations based on the We provide a poor estimate to the measured values of the aspect ratio in this work. The We includes a term for the square of the bubble rise velocity. The inclusion of the bubble rise velocity in the estimation of the aspect ratio is the likely cause of the discrepancy between the empirical relations and measured values from this work. The empirical relations based on the Eo from Okawa (2003) provides a good estimation for the bubble aspect ratio.

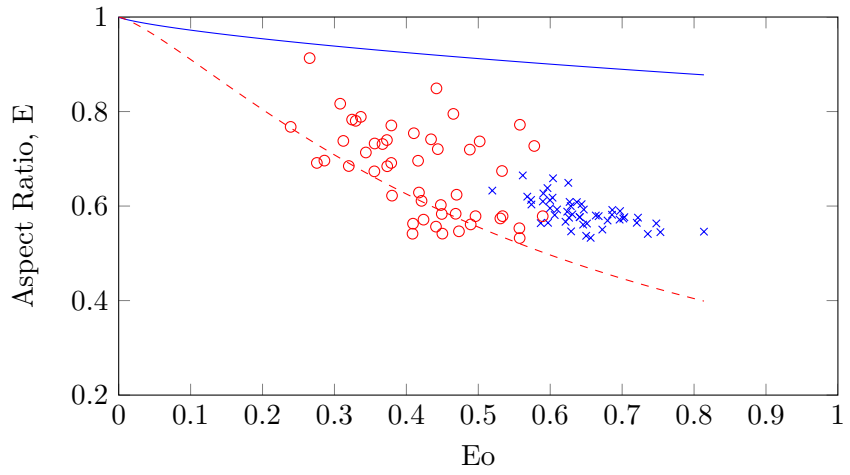

(a) Effect of Eo on aspect ratio of pure CO_2 bubbles produced from 0.35 and 1.0 mm orifices

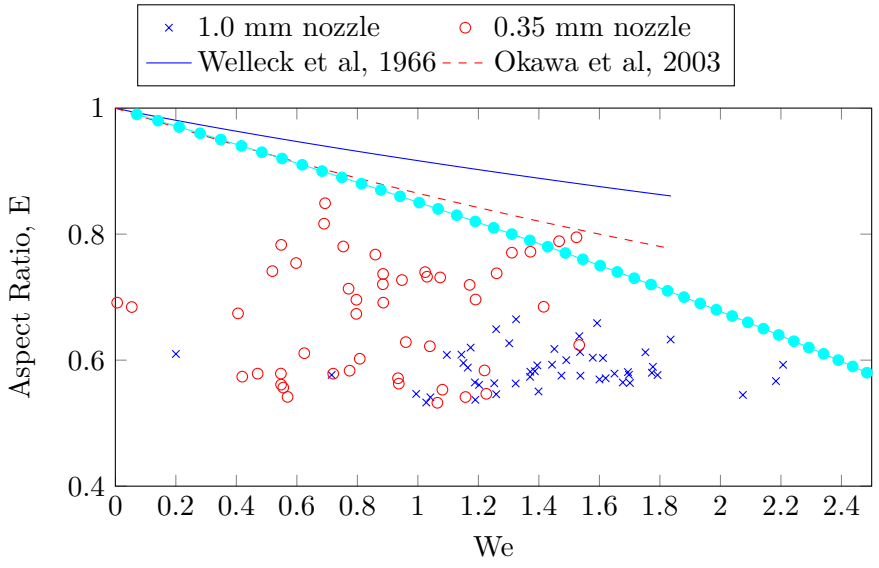

(b) Effect of We on aspect ratio of pure CO_2 bubbles produced from 0.35 and 1.0 mm orifices

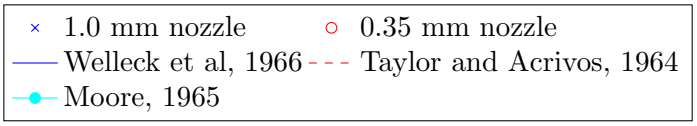

Figure 6.15: Comparison between measured aspect ratio for CO_2 bubbles produced with different orifice sizes and empirical relations based on Eo and We

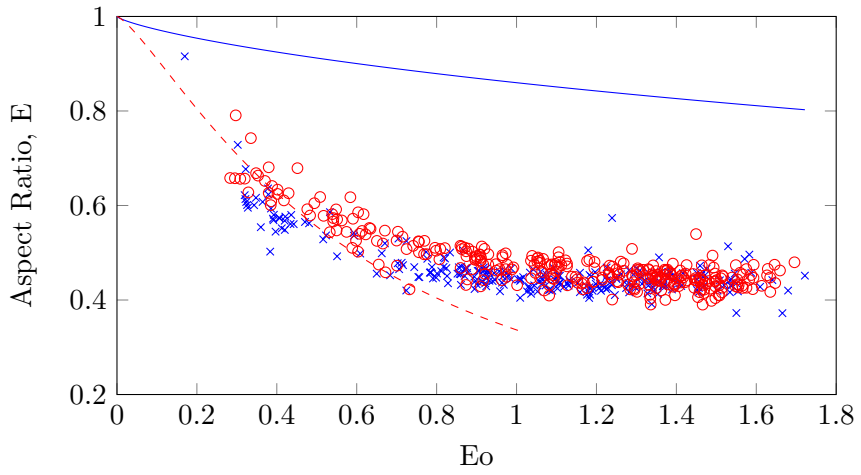

(a) Effect of Eo on aspect ratio in de-ionised water and synthetic seawater, compared with empirical relations

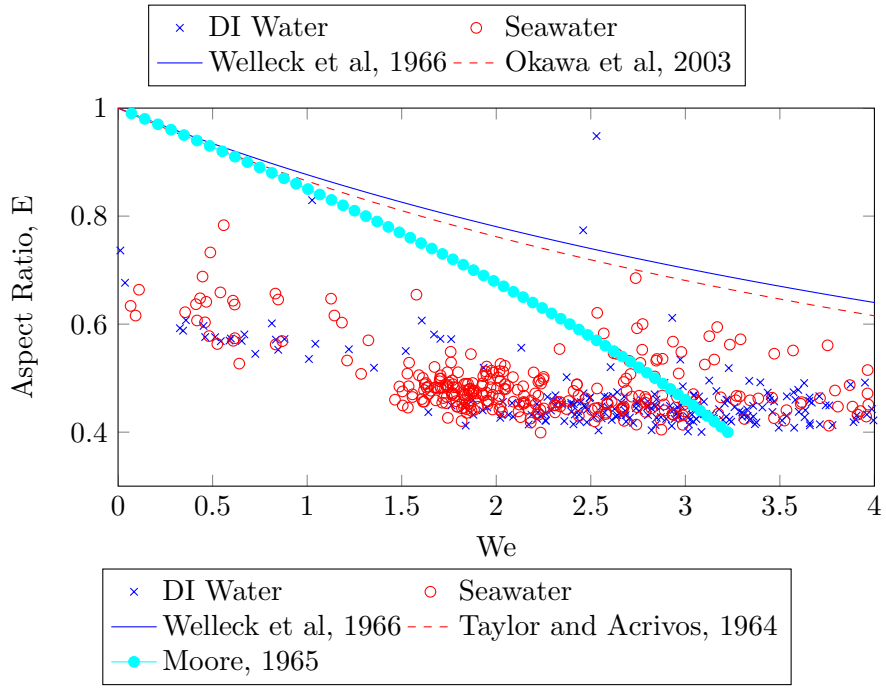

(b) Effect of We on aspect ratio in de-ionised water and synthetic seawater, compared with empirical relations

Figure 6.16: Effect of DI water or synthetic seawater on bubble aspect ratio, E, compared with empirical relations based on Eo and We

6.6 Counter-Diffusion

Along with the mass transfer of CO_2 from the bubble into the liquid, the counter diffusion of the dissolved gases, O_2 and N_2 saturated from the air in the water needs to be considered. The removal of dissolved oxygen (DO) in algal cultivation facilities will help to prevent the inhibitory effects of high DO concentrations on algal cells.

The change in CO_2 concentration within the bubble was measured by capturing the gas from a collection of bubbles at different heights in the bubble column. The CO_2 concentration from the gas sample was then analysed using gas chromatography. The reduction in CO_2 concentration within the bubble is attributed to the counter-diffusion of O_2 and N_2 saturated in the water, desorbing into the gas bubble.

These experiments were conducted with different dissolved concentrations of O_2 and N_2, under atmospheric pressure and room temperature conditions. The difference between the saturated concentrations of O_2 and N_2 in the water and the concentration of the gases in the bubble provides the driving force for mass transfer for desorption into the bubble. The reduction of CO_2 concentration over different sample heights and for different input concentrations is shown in figure 6.17. The blue bars represent the relative CO_2 concentration of the input sample, while the red bars show the relative CO_2 concentration collected at the top of the column (i.e. the ratio of the output to input CO_2 concentration).

Bubbles with an initial CO_2 concentration of 5 - 50 % experienced a larger percentage reduction in CO_2, of between 52 - 69 %, over a 0.8 m rise. This indicates that there

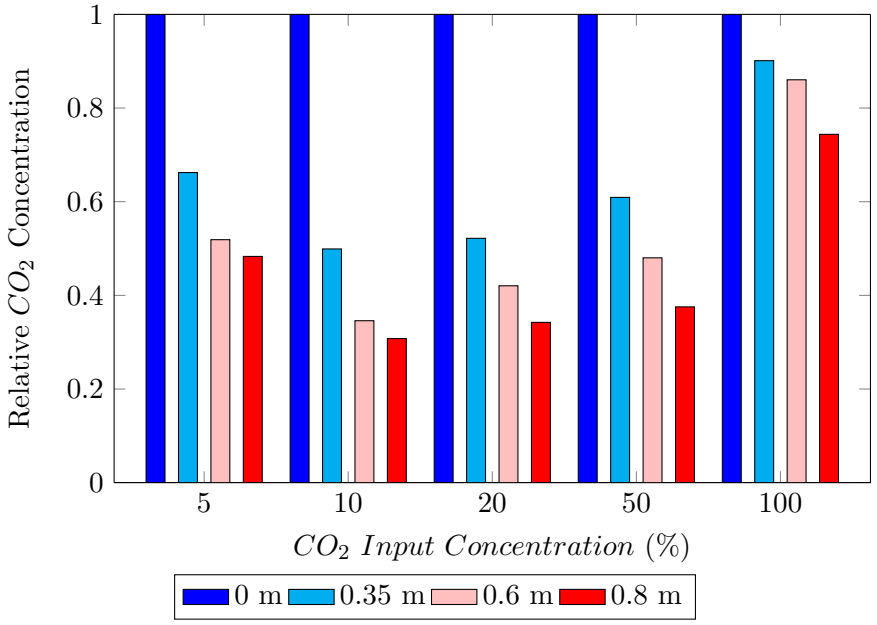

Figure 6.17: Change in gaseous CO_2 concentration at different heights in bubble column

is substantial counter-diffusion from the dissolved N_2 and O_2 from the water into the bubble. The concentration difference, which acts as the driving force for mass transfer from the dissolved O_2 and N_2, reduces with the declining CO_2 concentration in the bubble. Despite the largest concentration difference of O_2 and N_2 occurring with the pure CO_2 bubble, this had a lower reduction in CO_2 concentration over 0.8 m of only 26 %. This is likely because of the smaller average bubble size and thus smaller surface area of the pure CO_2 bubble. This reduced surface area therefore has a considerable effect in reducing the mass transfer of dissolved gases in the water.

A mass balance model was used to simulate the change in bubble volume of a single CO_2 bubble rising in water. This model incorporates empirical relations for the mass transfer coefficient (k_L) from Montes et al. (1999) and Frössling (1938), the bubble rise velocity from Fan and Tsuchiya (1990) and aspect ratio from Okawa (2003). Hamborg et al. (2010) recently validated that the desorption and absorption mass transfer coefficients were the same in a stirred tank reactor. The method of Montes et al. (1999) was therefore used for both the absorption of CO_2 and desorption of O_2 and N_2.

The predicted change in gaseous CO_2 concentration from the mass balance model is shown in figure 6.18, with the CO_2 concentrations shown for the same sampling heights in figure 6.17. The predicted CO_2 concentration shows a similar pattern with a reduction in CO_2 concentration with height. Due to the greater reduction in the bubble surface area, the simulated desorption of N_2 and O_2 is much less with the 100% input CO_2 concentration. In general the predictions for O_2 and N_2 mass transfer are over-estimated compared with the measured results. The predicted mass transfer coefficient took into account the reduction in the mass transfer rate with the changing bubble characteristics, which is discussed in further detail in section 6.7.

6.7 Mass Transfer Rate

Figure 6.19a shows the reduction in the bubble volume, which results from the mass transfer of CO_2 out of the bubble as well as the mass transfer of O_2 and N_2 into the bubble. It should be noted that the mass transfer of gaseous CO_2 from the bubble into the liquid is represented with a negative sign, whereas mass transfer into the bubble is taken as positive. The extent of the counter-diffusion of the O_2 and N_2 can be seen in figure 6.17, where the reduction in the CO_2 gaseous mole fraction is due to the increased concentration of O_2 and N_2. The number of moles of CO_2 within the bubble was calculated using the ideal gas law shown in equation 4.8. After approximately 1.0 s, there is a noticeable kink in the bubble volume, which is caused by the numerical fit for the bubble diameters, d_A and d_B. This discrepancy is carried onto the calculation of the mass transfer rate, shown in figure 6.19b. The change in gradient representing the number of moles of CO_2 results in a localised increase in the mass transfer rate at

approximately 1.0 s. The noise from the mass transfer rate is caused by the variation in the CO_2 concentration in the bubble. This has been smoothed using a median filter, which is shown by the red line in figure 6.19b.

6.7.1 Mass Transfer Coefficient

Figure 6.20 shows an example of the change in the mass transfer coefficient k_L during the rise of two CO_2 bubbles. The change in k_L for a CO_2 bubble with initial diameter, $d_0 \approx 2.9\ mm$ is shown in figure 6.20a. During the rise of this bubble k_L stays reasonably constant, $k_L \approx 4 - 5 \times 10^{-4}\ m\ s^{-1}$, with a slight increase with the reduction of bubble diameter, as the bubble rises up the column. The CO_2 bubble shown in figure 6.20b has an initial diameter, only 0.5 mm smaller, with $d_0 \approx 2.4\ mm$, however the change in k_L is very different. The initial k_L is slightly larger, but this abruptly reduces after approximately 2 s into the bubble rise, with k_L reducing by approximately 1/3 from $k_L \approx 5 \times 10^{-4}\ m\ s^{-1}$ to $k_L < 2 \times 10^{-4}\ m\ s^{-1}$. This illustrates the change between two different mass transfer rates as reported by Schulze and Schlünder (1985a), Schulze and Schlünder (1985b) and Vasconcelos et al. (2002) and shown in figure 6.3. During this transition the bubble interface changes from being mobile, as described by the penetration theory proposed by Higbie (1935), to an immobile interface, which matches the relation from Frössling (1938). The relation between k_L and the bubble diameter is compared with the mobile and immobile gas-liquid interface theories in figure 6.21a, with the bubble rise velocity shown in figure 6.21b. The smaller bubble, $d_0 \approx 2.4\ mm$, has a slightly higher initial velocity, which correlates with the larger, initial k_L. The resulting

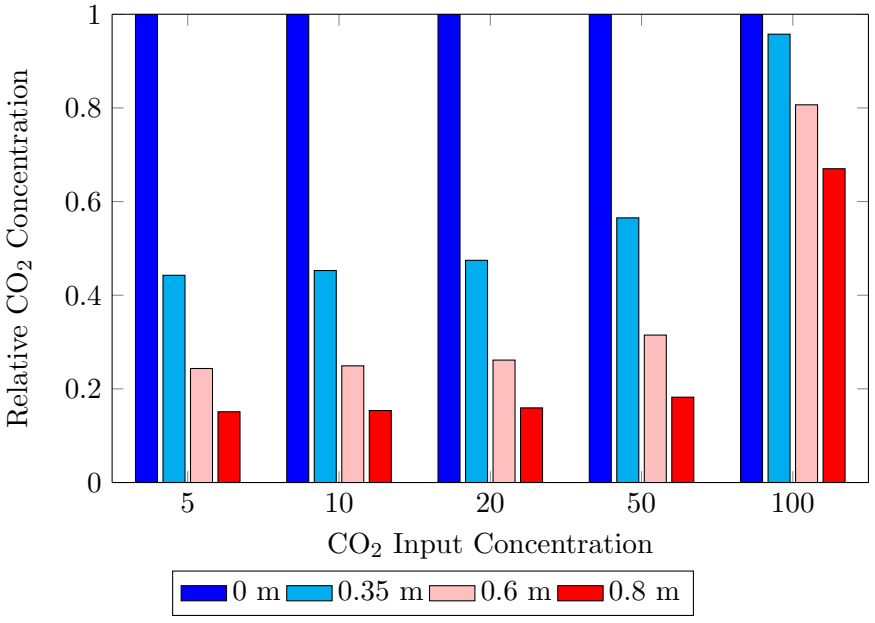

Figure 6.18: Predicted change in gaseous CO_2 concentration in a bubble rising 1.0 m in tap water, relative to the input concentration

mass transfer rate quickly reduces the bubble diameter, which results in a reduced k_L. The rise velocity of both bubbles is similar, with a dip after the initial acceleration, due to the reducing bubble size and surfactant accumulation. The reduced mass transfer rate from the smaller bubble occurs after 1.5 s, at which point the rise velocity is still relatively large. However it is at this point that the bubble path oscillation diminishes, as shown in figure 6.22b. Conversely, the path oscillation of the larger bubble increases at this stage. There is also a difference in the aspect ratio of the two bubbles, shown in figure 6.22. The aspect ratio of the larger bubble is initially lower at $E_0 \approx 0.4$, while for the smaller bubble it is larger at $E_0 \approx 0.5$. Interestingly after 1.5 s, the aspect ratio of the smaller bubble changes from $E \approx 0.65$ to $E \approx 0.8$. This increase in aspect ratio coincides with the reduction in bubble path oscillation and mass transfer rate. The larger bubble has a continually oscillating and increasing aspect ratio, which reaches a maximum of $E \approx 0.7$.

A comparison between the mobile mass transfer rates during the initial bubble rise, and the immobile mass transfer rates at the end of the bubble rise, is shown in figure 6.23. The mass transfer coefficient calculated from the initial mass transfer rate, shown by the blue crosses, has a larger bubble diameter, rise velocity and mass transfer rate.

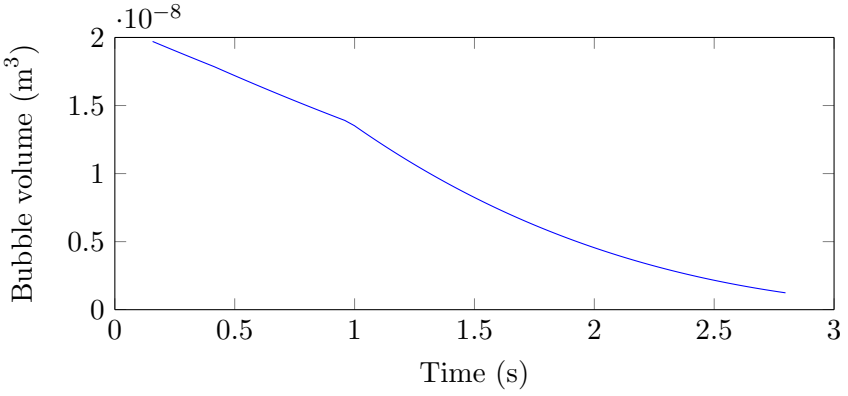

(a) Change in bubble volume during the rise of a CO_2 bubble in tap water

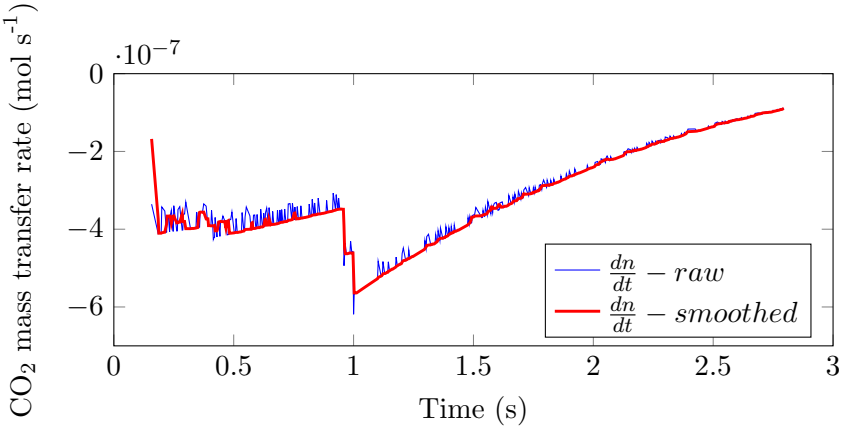

(b) Change in mass transfer rate during the rise of a CO_2 bubble in tap water

Figure 6.19: Change in bubble volume and mass transfer rate from CO_2 bubble

The aspect ratio of these bubbles is smaller, resulting in a more ellipsoidal shape. As the bubble reduces in size its rise velocity reduces and aspect ratio increases. This corresponds to a reduction in the calculated mass transfer coefficient. This comparison provides further evidence that the smaller diameter bubbles have a lower mass transfer coefficient than larger bubbles, at least in liquids with surfactant contamination.

The mass transfer coefficients shown in figure 6.23 are for relatively smaller bubbles, with initial diameter $d_0 < 2.5\ mm$ and which exhibit two distinct mass transfer rates during the 1.0 m rise. Larger bubbles showed only one mass transfer rate, which was characteristic of the mobile gas-liquid interface. For smaller bubbles with initial diameter $d_0 < 2.5\ mm$, the mass transfer coefficient from the first phase is approximately, $4 \times 10^{-4} < k_L < 6 \times 10^{-4}\ m\ s^{-1}$, and in the second phase of mass transfer, the mass transfer coefficient is $2 \times 10^{-4} < k_L < 4 \times 10^{-4}\ m\ s^{-1}$.

Theoretical relations for the mass transfer coefficient k_L, such as Higbies penetration theory, show a constant, or slight increase in k_L with a reduction in bubble diameter, down to a bubble diameter of $d_e \approx 1.0\ mm$, where the k_L then reduces. This can be seen

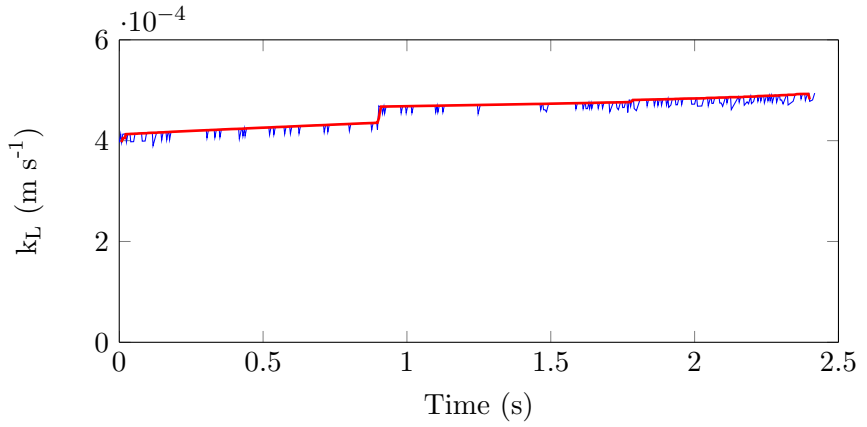

(a) Mass transfer coefficient, k_L for CO_2 bubble with $d_0 \approx 2.9mm$

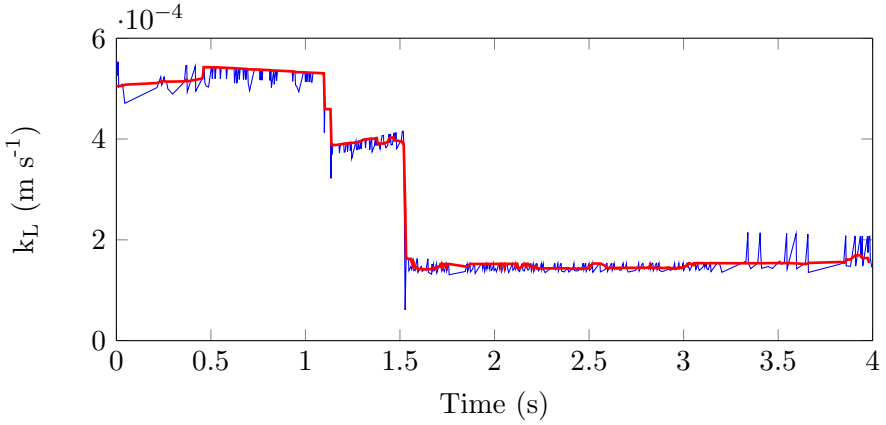

(b) Mass transfer coefficient, k_L for CO_2 bubble with $d_0 \approx 2.4mm$

Figure 6.20: Mass transfer coefficient, k_L for CO_2 bubbles with different initial bubble diameter

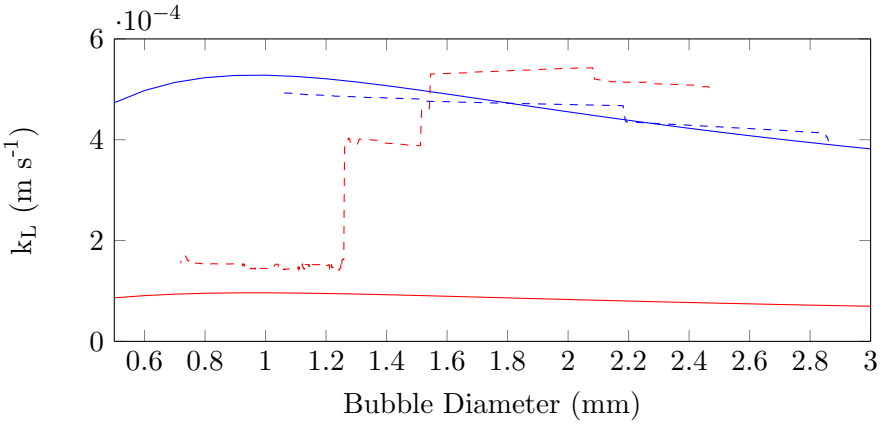

(a) Effect of initial bubble size on mass transfer coefficient, k_L and comparison with empirical relations from Higbie (1935) and Frössling (1938)

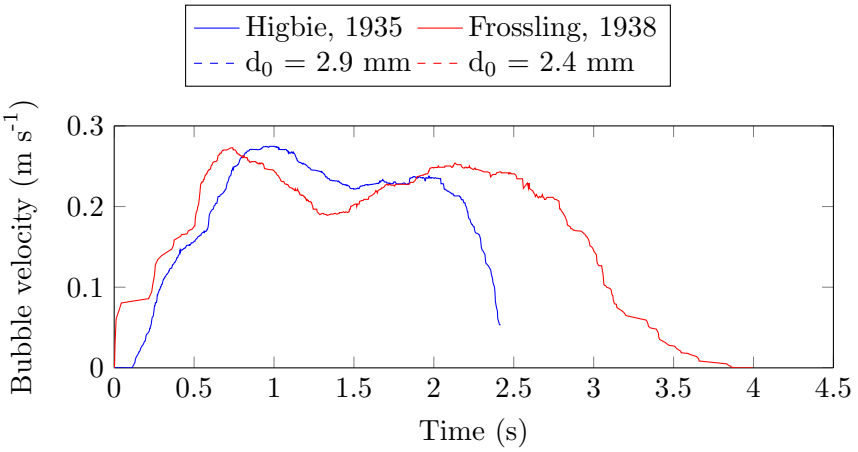

(b) Effect of initial bubble size on bubble rise velocity

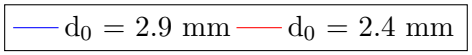

Figure 6.21: Comparison of mass transfer coefficient, k_L, and rise velocity of CO_2 bubbles, with different initial bubble diameter, $d_0 \approx 2.9\ mm$ and $d_0 \approx 2.4\ mm$

from the k_L relations listed in table 2.5 and shown in figure 2.7. This is also seen in this experimental work when looking at a wider range of bubble diameters, as shown in figure 6.24, which compares k_L for CO_2 bubbles in de-ionised water and synthetic seawater. A comparison of the results for bubbles with an average diameter $2.5 < d_e < 3.5\ mm$ shows that, despite a high degree of scattering, k_L increases with reducing bubble diameter. When the bubble diameter $d_e < 2.0mm$ a reduction in bubble diameter results in a reduction in k_L.

For $d_e < 2.0\ mm$, reductions in bubble diameter result in a reduction in k_L. Compared to previous reports in the literature, the reduction in k_L found in the current work occurs at a higher bubble diameter. Most of the proposed relations reported in literature show a reduction in k_L when $d_e < 1.0\ mm$. This may be due to the effects of surfactants, which have a more pronounced effect on smaller bubble sizes. Leonard

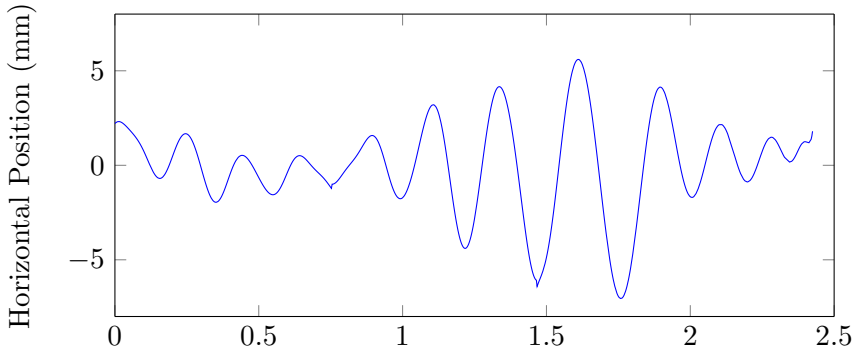

(a) Horizontal bubble position of CO_2 bubble with $d_0 \approx 2.9\ mm$

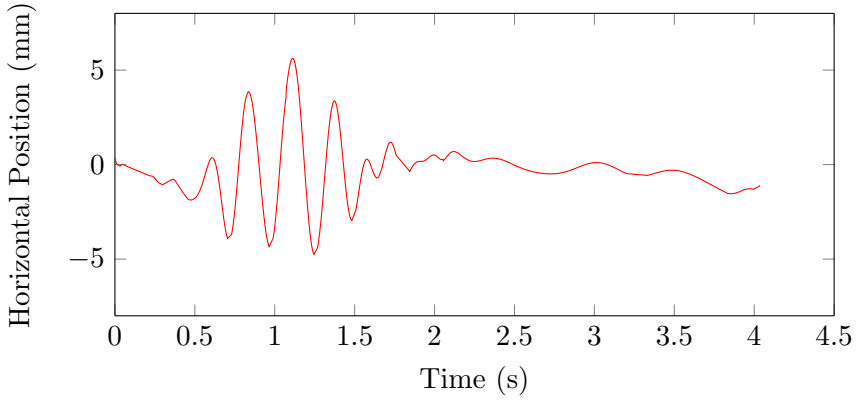

(b) Horizontal bubble position of CO_2 bubble with $d_0 \approx 2.4\ mm$

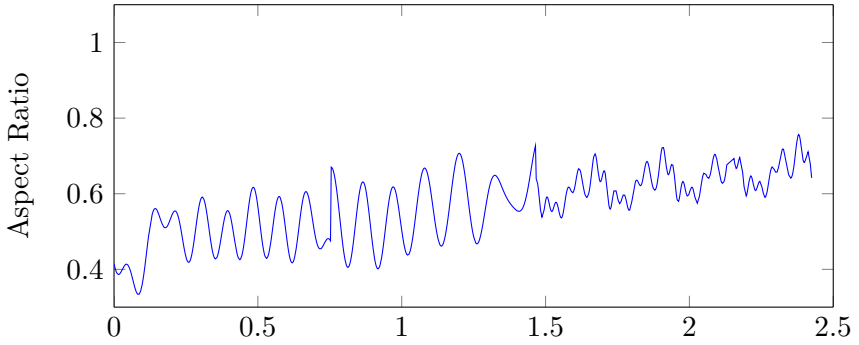

(c) Bubble shape fluctuation of CO_2 bubble with $d_0 \approx 2.9\ mm$

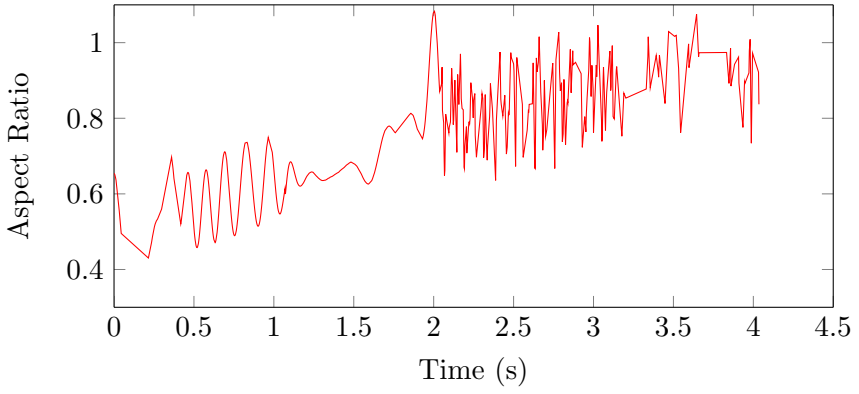

(d) Bubble shape fluctuation of CO_2 bubble with $d_0 \approx 2.4\ mm$

Figure 6.22: Comparison between bubble shape fluctuation and bubble path oscillation of CO_2 bubbles with different initial diameters; $d_0 \approx 2.9\ mm$ and $d_0 \approx 2.4\ mm$

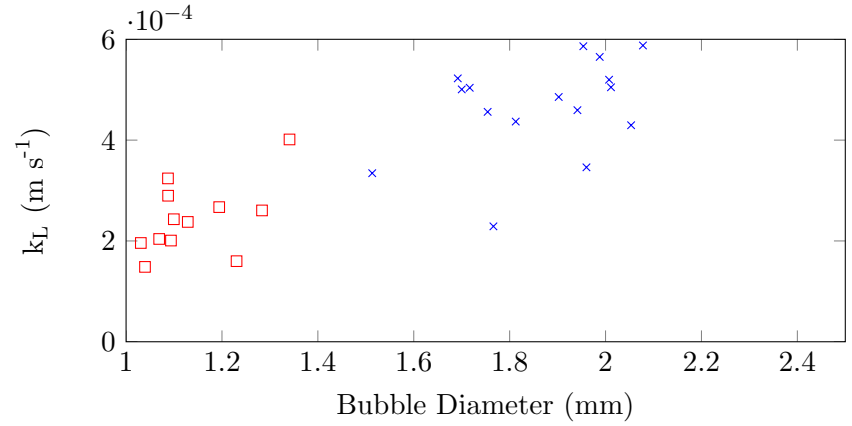

(a) Mass transfer coefficient, k_L with bubble diameter

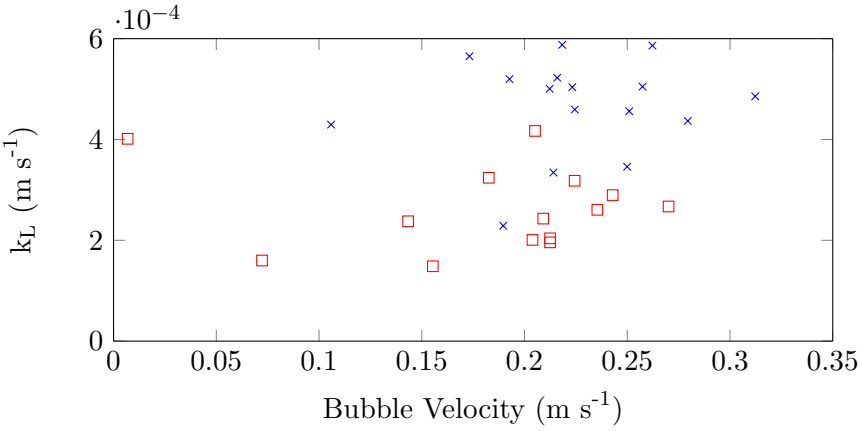

(b) Mass transfer coefficient, k_L with rise velocity

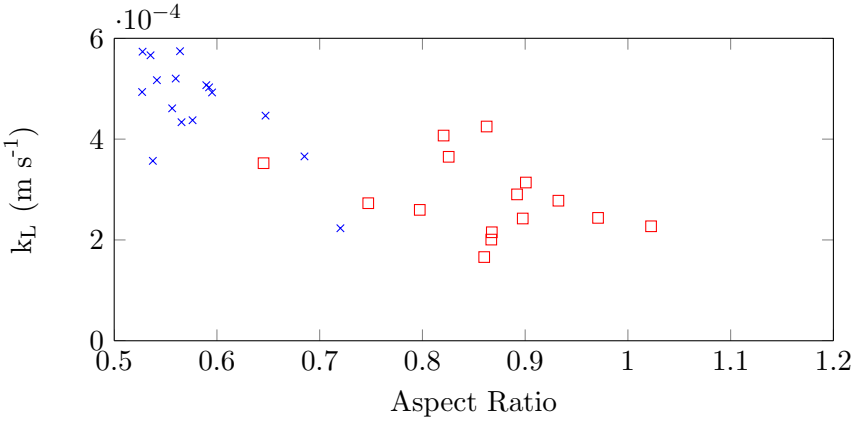

(c) Mass transfer coefficient, k_L with aspect ratio

Figure 6.23: Mass transfer coefficient, k_L of bubbles produced with 0.35 mm orifice, with initial bubble diameter $d_0 < 2.5\ mm$

and Houghton (1963) and Alves et al. (2005) reported that surfactants have a greater effect on inhibiting the velocity, bubble oscillations and mass transfer of smaller bubbles, particularly for $d_e < 2.0\ mm$. The effect of surfactants and the relation between d_e and k_L has also been reported by Clift et al. (1978), who recognised that in pure systems the value of k_L increases with reducing bubble diameter, but not in contaminated systems. They also noted that the large scatter in mass transfer relations for bubble sizes $2.0 < d_e < 4.0\ mm$ is due to several factors, including: the different measurement systems used to obtain the data, bubble generation techniques and the purity of the liquid phase.

Contaminated systems cause oscillations in the bubble to be induced at a lower Re values, with $Re_{CR} \approx 200$, compared to $Re_{CR} \approx 800$ for pure systems. This causes the onset of oscillations to start earlier, and oscillating bubbles increase the mass transfer rate. A further increase in surfactant concentration would also have the effect of dampening the bubble oscillations, however, thus reducing the mass transfer rate in comparison to

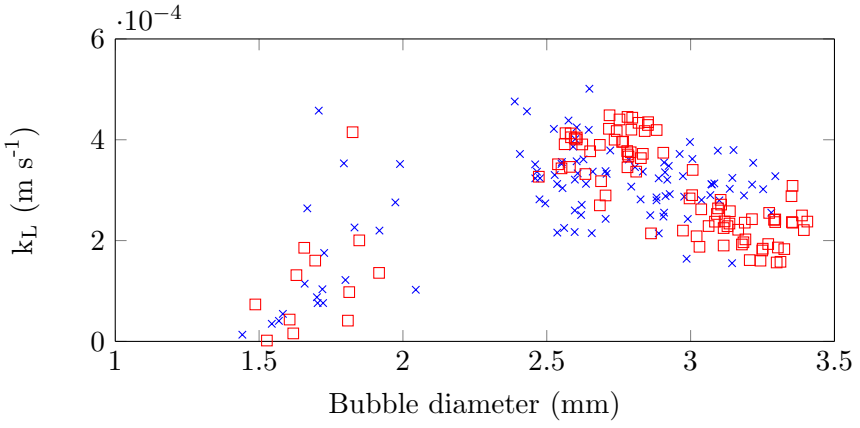

(a) Comparison with bubble diameter and mass transfer coefficient

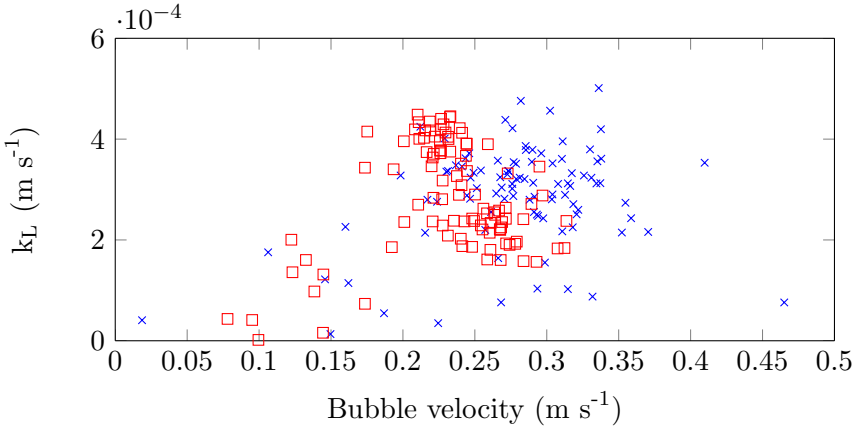

(b) Comparison with bubble velocity and mass transfer coefficient

Figure 6.24: Effect of bubble diameter and rise velocity in distilled water or synthetic seawater on the mass transfer coefficient, k_L

pure systems where $Re > 800$. Surfactants have a large and complex effect on bubble characteristics and mass transfer rate; this is particularly the case for bubble sizes of $2.0 < d_e < 4.0\ mm$, and results in a wide range of predicted k_L values for these regimes. Many of the k_L relations currently used rely on the bubble rise velocity, an increase of which results in a clear increase with k_L, as seen in figure 6.24b.

Figure 6.25 compares relations for k_L in the literature for the rise of single bubbles with the current experimental results from bubbles produced by the 1.0 mm and 0.35 mm orifices. It is clear that the measurements from these experiments show two different stages of mass transfer. A mobile gas-liquid interface is exhibited for smaller bubbles ($d_0 < 2.5\ mm$) during the initial bubble rise, and for at least the first 1.0 m rise for larger bubbles ($d_0 > 2.5\ mm$). This matches the penetration theory proposed by Higbie (1935), which is based on the relation $k_L \propto \sqrt{D}$. Results based on Higbie's penetration theory are shown in figure 6.25A and in comparison to other relations from literature, provides a reasonable estimate of the average k_L from experimental data. The second mass transfer rate was noticed at the end of the rise of small bubbles (with $d_0 < 2.5\ mm$) and has a closer fit with the rigid particle theory from Frössling (1938). This is shown in figure 6.25B and under predicts the average mass transfer rate for the vast majority of the bubbles.

As with the mass transfer relations shown in figure 2.7, there is also a large spread in k_L from these experiments. The changing bubble characteristics and thus mass transfer rates will be a major cause of this wide range of k_L values, particularly for bubbles which exhibit the transition from Higbies penetration theory to Frössling's rigid particle theory. Empirical relations developed by Lochiel and Calderbank (1964) for spherical and ellipsoidal bubbles with mobile interfaces are compared with the measured k_L from this work in figures 6.25C and D. Considering the bubble size, the ellipsoid is a better approximation of the bubble shape; and the ellipsoid relation, shown in figure 6.25D provides a better fit to the experimental data, which has a similar fit to Higbies theory. The empirical relation proposed by Johnson et al. (1969) shown in figure 6.25E under estimates k_L in comparison to the measured data. This relation was developed from experimental results which measured the total change in gas and liquid volume during the bubble rise in a 3.0 m bubble column. This relation was developed typically for larger bubbles, although it shows some agreement for the bubble sizes measured in this work. Finally, the relation proposed by Montes et al. (1999) takes into consideration oscillations of the bubble, and appears to provide a reasonable fit to the experimental data in figure 6.25F.

The mass balance model, using only the mass transfer coefficient from Montes et al. (1999) compares the predicted k_L and number of moles of CO_2 within the bubble in figure 6.26. The left axis, shown in blue shows the number of moles of CO_2 and k_L, shown in red is plotted against the right axis. The model used the average initial diameter from the experimental results, with $d_0 \approx 3.1\ mm$. The modelled mass transfer rate is larger

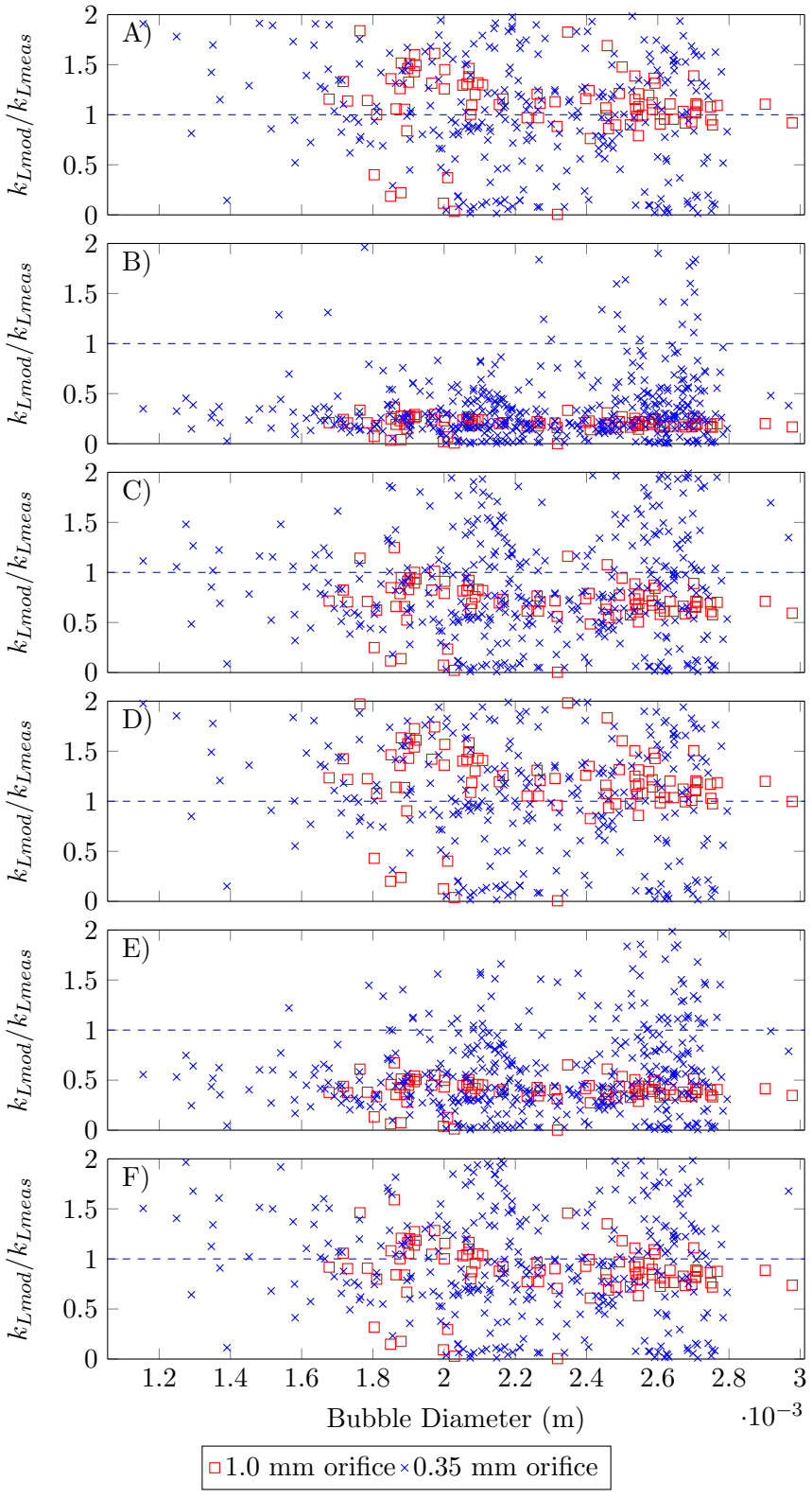

Figure 6.25: Comparison between modelled mass transfer coefficient k_{Lmod} and measured mass transfer coefficient, k_{Lmeas} with bubble diameter for different empirical relations. Measurements taken in tap water with 0.35 and 1.0 *mm* orifice. Compared with models from; A) Higbie (1935) B) Frössling (1938) C) Lochiel and Calderbank (1964) (spheres) D) Lochiel and Calderbank (1964) (Oblate ellipsoids) E) Johnson et al. (1969) F) Montes et al. (1999)

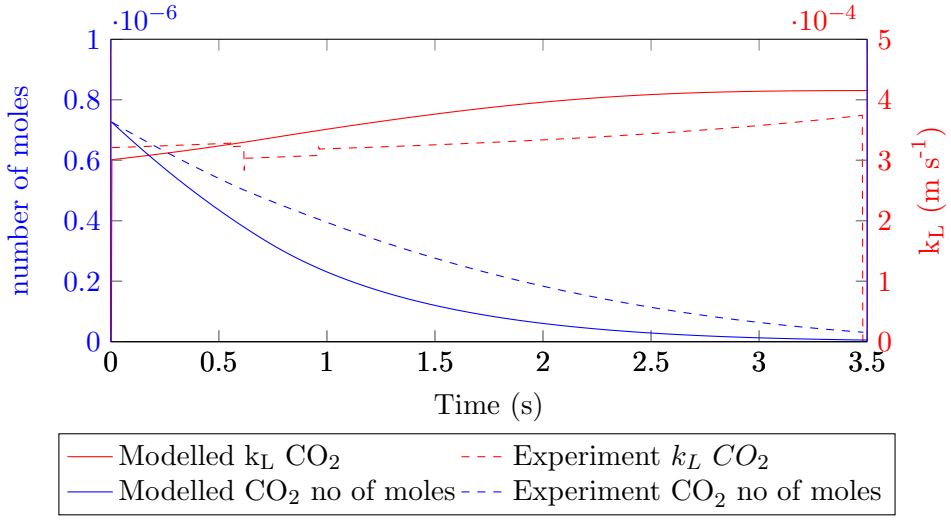

Figure 6.26: Comparison between predicted and modelled number of moles of CO_2 and mass transfer coefficient, k_L

than the measured value. The relation from Montes et al. (1999) provided the best fit for the average mass transfer rate for a range of bubble sizes averaged over the 1.0 m rise in tap water. This was only the average value, however, and the differences during the bubble rise are clear to see from figure 6.26. This also highlights the fact that if the experiments had been conducted over a different rise height, the average k_L would be different because of the dynamically changing mass transfer rate.

Figure 6.27 compares the modelled and experimental bubble diameters. When averaged over the 1.0 m rise, the model provides a reasonable estimate for the bubble diameter; however the initial rate of reduction in the bubble size is over-estimated compared to the averaged experimental data. The predicted bubble size becomes closer to the measured bubble size at the top of the 1.0 m rise, due to the reduction in the mass transfer rate from the smaller bubble surface area and reduction in the concentration driving force of CO_2. Comparison of the average experimental bubble rise velocity and the predicted velocity from Fan and Tsuchiya (1990) shows a clear difference. The model overestimates the average velocity at the beginning and at the end, and under-estimates the velocity during the middle section of the bubble rise. This demonstrates the dynamic changes in bubble velocity over the course of its rise, due to the changing bubble size and increasing concentration of surfactants attached to the bubble surface. The relation from Fan and Tsuchiya (1990) assumes a contaminated bubble surface, hence a reduced rise velocity. Over the course of the 1.0 m rise, the average predicted bubble velocity provides a reasonable estimate for the observed velocity.

With smaller CO_2 bubbles the relations for the mass transfer coefficient and bubble rise velocity are not as accurate. An example of this is seen in figure 6.28a which shows a large deviation between the predicted and measured k_L. This confirms the importance of utilising the correct relation for k_L for the changing bubble characteristics which can

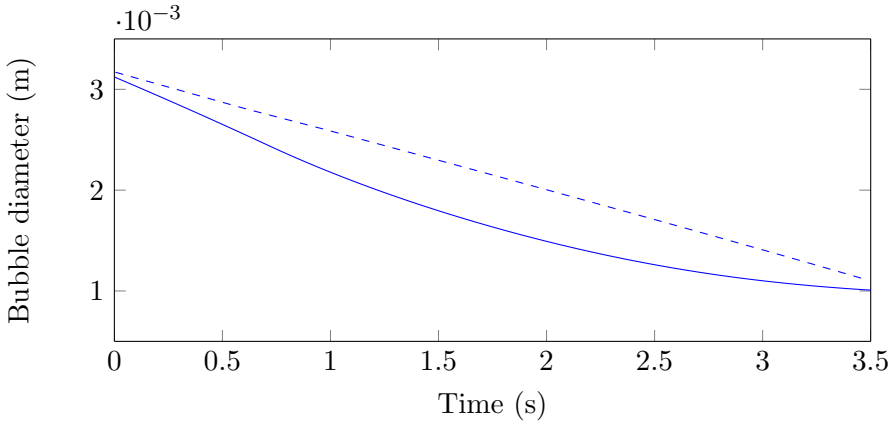

(a) Comparison between modelled and experimental bubble diameter

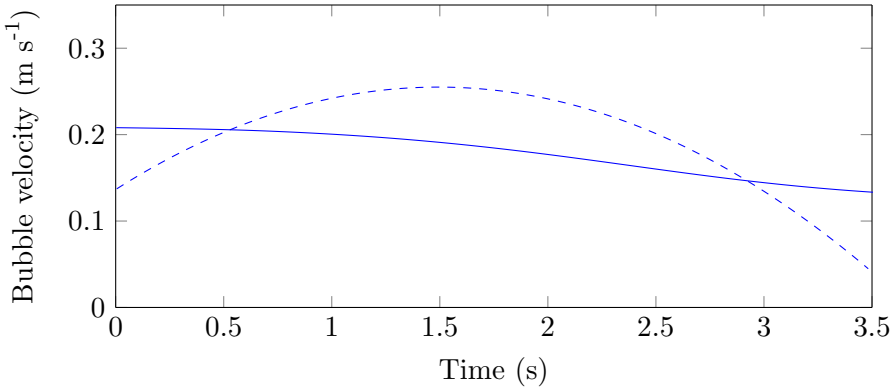

(b) Comparison between modelled and experimental bubble velocity

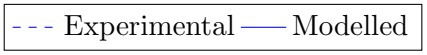

Figure 6.27: Comparison between modelled and predicted bubble diameter and rise velocity

otherwise over-estimate k_L for smaller bubbles. This is particularly exacerbated by the higher inhibition from surfactants on smaller bubbles.

Vasconcelos et al. (2003) showed that the transition bubble diameter (d^*) for the change from a mobile to an immobile gas-liquid interface, increases with initial bubble diameter, (d_0). In these experiments the range of initial bubble diameters was reasonably small and the initial bubble diameter which resulted in the transition between mobile and immobile gas-liquid interface was approximately constant, with $d^* \approx 1.3\ mm$. For a pure CO_2 bubble rising in 1.0 m of tap water, an initial bubble diameter $d_0 <= 2.5\ mm$ would reach this transition diameter. This is supported from the results by Vasconcelos et al. (2003). This transition has been incorporated into the mass balance model, where k_L is calculated using Frössling's equation shown in table 2.5 when $d_e < d^*$. Figure 6.28b shows the resulting prediction of k_L and the number of CO_2 moles within the bubble using this modification. Figure 6.28c compares the predicted bubble volume, incorporating the immobile k_L for $d_e < d^*$ ($MT\ Model$ #2). This provides a significant improvement on the predicted bubble size utilising the single k_L ($MT\ Model$ #1),

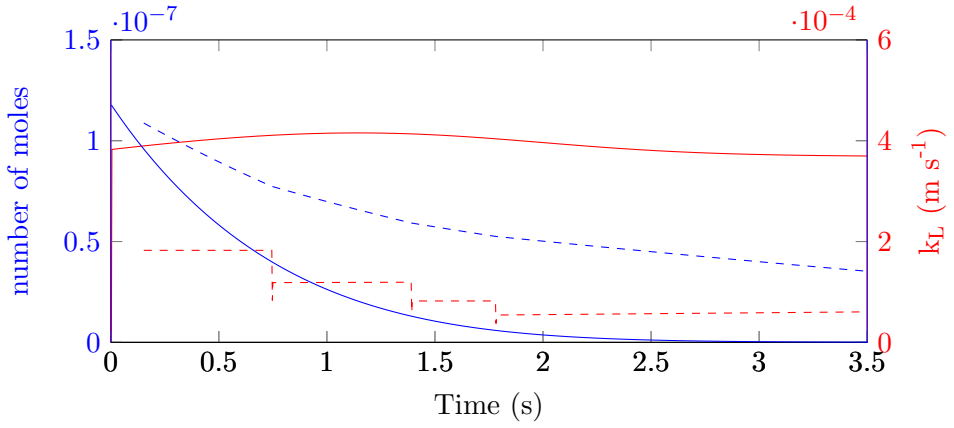

(a) Comparison between measured and predicted number of moles of CO_2 in bubble and mass transfer coefficient, k_L, using mass transfer model # 1 with $d_e \approx 1.7mm$

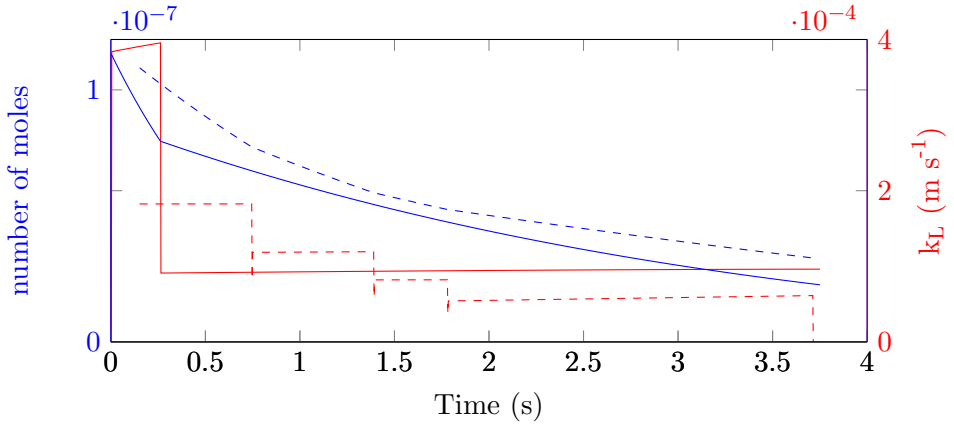

(b) Comparison between measured and predicted number of moles of CO_2 in bubble and mass transfer coefficient, k_L, using mass transfer model # 2 with $d_e \approx 1.7mm$

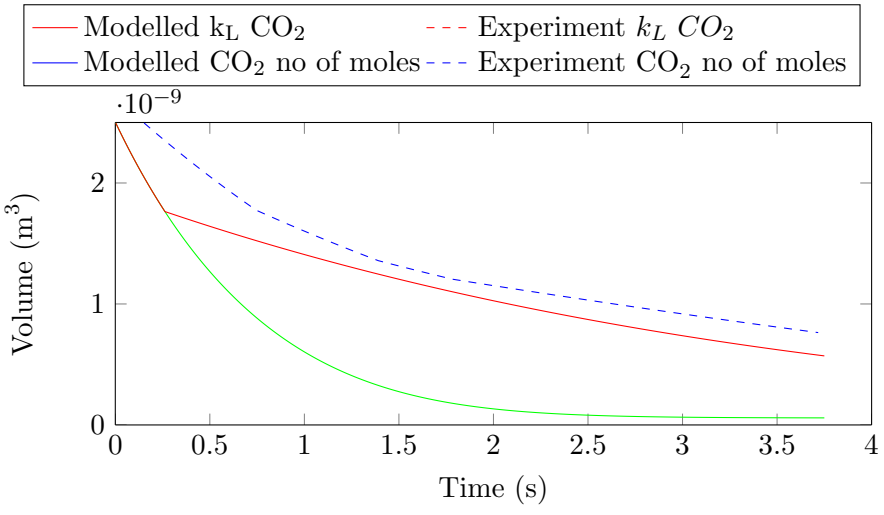

(c) Comparison between predicted and measured bubble volume

Figure 6.28: Comparison between modelled and measured bubble volume change and mass transfer coefficient, k_L

although as for the prediction of the larger bubble diameter, during the middle stages of the 1.0 m bubble rise the model over-estimates the mass transfer.

Similar experiments conducted with O_2 in tap water by Alves et al. (2004) showed k_L relations for the mobile interface agreed well with their results. This suggests that, despite significant concentrations of surfactants in tap water, the gas-liquid interface is still considered mobile in terms of mass transfer. A discrepancy is evident between definitions in the literature for mobile and immobile interfaces for the mass transfer and contaminated and clean systems for the bubble velocity. In terms of the bubble rise velocity, de-ionised water and tap water and in fact any system open to the atmosphere are considered contaminated, resulting in a significantly reduced rise velocity. This does not seem to be so extreme with mass transfer, where a gas-liquid interface contaminated with a surfactant concentration can still provide a mobile interface in terms of Higbies mass transfer coefficient. Provided the surfactant concentration is not too large, there may be a benefit in sustaining a mobile mass transfer rate at a lower rise velocity, which would increase bubble residence time and allow for a longer period of contact between the gas and liquid phase. There are also discrepancies regarding the definition of contaminated and clean systems based on whether experiments are conducted with single bubbles or bubble swarms.

6.7.2 Input Gas Concentration

The measured mass transfer coefficients for different gaseous CO_2 concentrations are shown in figure 6.29. The experiments for the 100 % CO_2 case include those from the 0.35 mm orifice and the 1.0 mm orifice, which show a larger range of bubble diameters. The experiments conducted with 75 %, 50 % and 25 % CO_2 show similar values of k_L, although with a larger spread in results. This could be due to the larger proportional

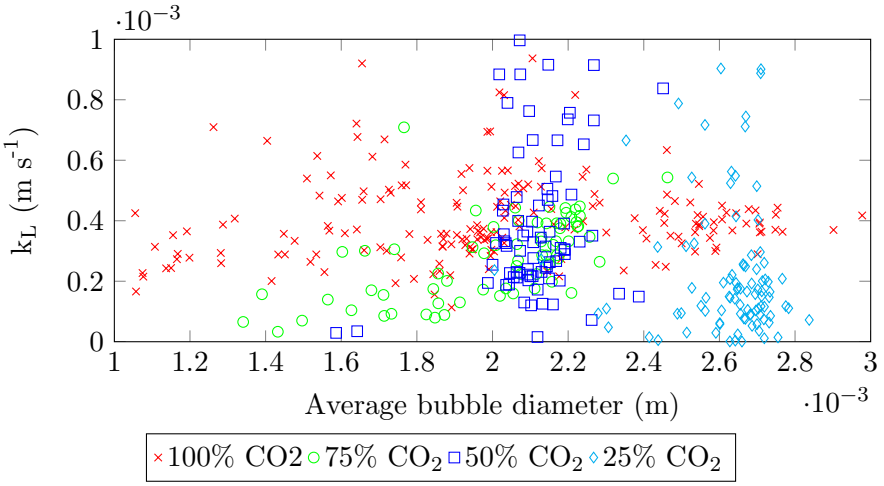

Figure 6.29: Effect of average bubble diameter and input CO_2 gas concentration on mass transfer coefficient, k_L

error in these experiments, which have a lower total change in bubble volume and thus a greater error relative to the difference in bubble volume. The experiments conducted with 75 %, 50 % and 25 % CO_2 bubbles also had a larger average bubble diameter, with a larger gas-liquid contact area for the counter diffusion of O_2 and N_2. As seen in figure 6.17 this increases the desorption of the dissolved gases, further reducing the change in bubble volume.

A comparison between the average measured and the predicted volume change from the mass balance model are shown in figure 6.30. For the input CO_2 gas concentrations of 100 % and 75 %, the predicted volume change under-estimates the mass transfer during the course of the bubble rise. For lower CO_2 concentrations of 50 % and 25 %, the model over-estimates the CO_2 mass transfer and reduction in bubble volume. The model provides a better prediction for the higher CO_2 concentrations. This could perhaps be due to the experimental error: because of the greater volume change, the relative error for 100 % CO_2 bubbles will be lower than for bubbles containing 25 or 50 % CO_2. Another explanation for the larger difference between the predicted bubble volumes for lower CO_2 concentrations is due to the under-prediction of the counter-diffusion of saturated O_2 and N_2 from the water into the bubble. In comparing the predicted and measured CO_2 concentrations from figures 6.17 and 6.18, the model gave a better prediction for the CO_2 concentration, when the initial concentration was higher. An under-prediction in the O_2 and N_2 counter-diffusion would result in a smaller predicted bubble volume as seen in figure 6.30.

Another possible explanation resulting in a lower mass transfer rate for lower CO_2 concentrations maybe higher gas resistance, as a result of the lower concentration of

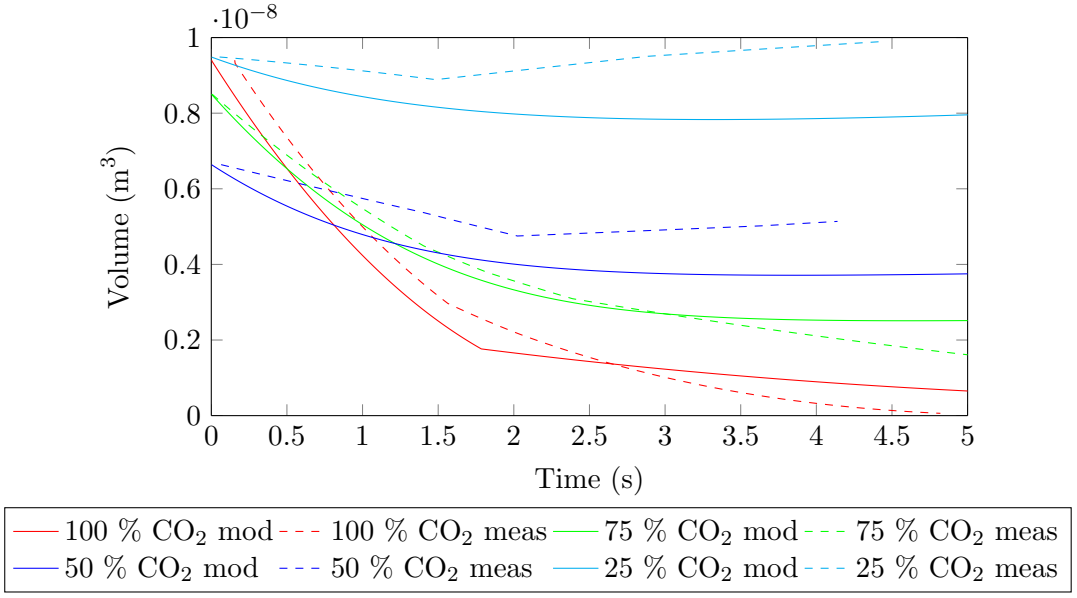

Figure 6.30: Comparison between predicted and measured volume change of a bubble with varying input CO_2 concentration

CO_2 within the bubble. The gas diffusivities for CO_2, O_2 and N_2 are approximately 10^4 greater than their respective diffusivities in water. Because of this the gas phase resistance is assumed negligible in comparison to the liquid phase resistance. It has been shown, however, that surfactants reduce the internal circulation within the bubble, Leonard and Houghton (1963), Clift et al. (1978), which would increase the gas phase resistance, although the magnitude of this effect is difficult to determine.

6.7.3 Counter-Diffusion

The counter-diffusion of gases was investigated by sparging N_2 and O_2 into the water prior to single bubble experiments. During the N_2 saturation experiments DO concentrations reached 0.2 $mg\ L^{-1}$, and up to 36.3 $mg\ L^{-1}$ for the 400 % O_2 saturation experiments. Due to the low concentration of CO_2 in the atmosphere, in all of these experiments the dissolved concentration of CO_2 was assumed to be negligible. Figure 6.31 shows that despite elevated concentrations of DO, the reduction in the bubble volume does not change significantly. There is a slightly larger volume reduction during the saturated N_2 experiments than with super-saturated O_2 (400% O_2) and air saturation (100% O_2) experiments. This suggests a slightly higher counter-diffusion from the O_2 than N_2. This would be expected due to the higher liquid diffusivity of O_2 in water than N_2. From the mass transfer theories the relation for k_L is proportional to the liquid diffusivity of the gas to the power of 1/2 for mobile gas-liquid interfaces, or 2/3 for immobile interfaces. The diffusivities of CO_2, O_2 and N_2 in water at 293 K are compared in table 2.4 in chapter 4.2.4.

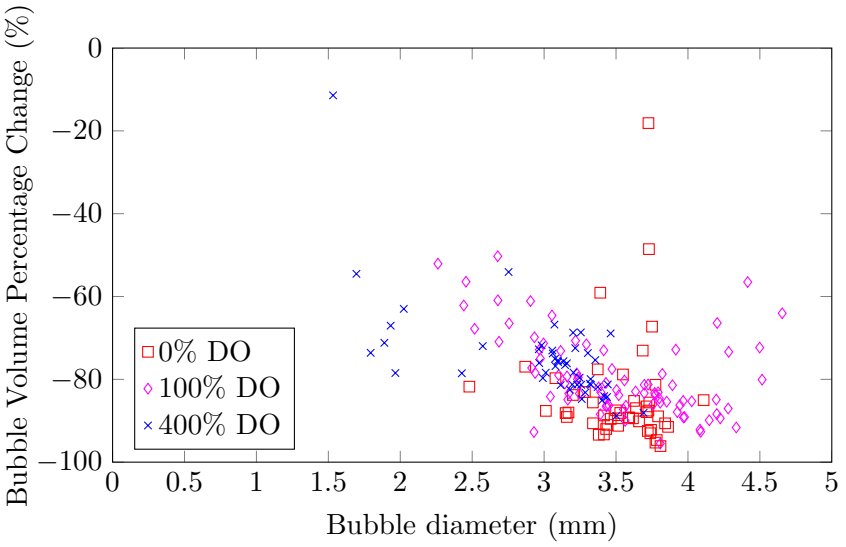

Figure 6.31: Percentage change in bubble volume with different saturated concentrations of dissolved N_2 and O_2

Taking k_L for O_2 and N_2 from equation 4.12 and the values in table 2.4, both in chapter 4.2.4, the mass balance model estimates a volume difference of 3 % for a bubble with $d_0 = 3.0\ mm$ containing 100 % CO_2, dissolving in 1.0 m of water saturated with 0 % O_2 and for 400 % O_2. This agrees with the small difference found in the experimental work, as shown in figure 6.31, and confirms the small effect saturated concentrations of O_2 or N_2 have on the bubble volume, in comparison with the mass transfer of CO_2.

Chapter 7

Multiple-Bubble Results

7.1 Introduction

This chapter presents the results from experiments conducted with a continuous gas flow, producing a bubble swarm from a diffuser. The bubble characteristics and mass transfer of a single bubble are compared with those found from a bubble swarm. The effect of gas and liquid flow rates, as well as CO_2 input concentration and DO concentration are also investigated in this section.

7.2 Bubble Size

Figure 7.1 shows the distributions of the chord length measured by the optical fibre probe at the bottom and top of the bubble column. The experimental runs with 10 % and 20 % CO_2 concentrations show similar distributions throughout the length of the bubble column. There will be an increase in bubble size at the top of the column due to the reduced hydrostatic pressure. This is greater than the mass transfer for a bubble with 10 % CO_2, as can be seen by the increase in bubble chord length distribution (CLD) in figure 7.1a. There is a more noticeable reduction in bubble CLD for 50 % and 100 % CO_2 bubbles. This is particularly noticeable for the 50 % CO_2 bubble, which had a smaller initial bubble distribution than the 100 % CO_2 measurements, and results in almost half of the detected bubbles at the top of the column having a chord length below 0.5 mm. It is interesting to compare the BSD shown in figure 7.1 to the BSD obtained for the single bubbles in figure 6.1. The clear reduction in BSD for 100 % CO_2 bubbles measured from the image analysis is not as apparent in figure 7.1.

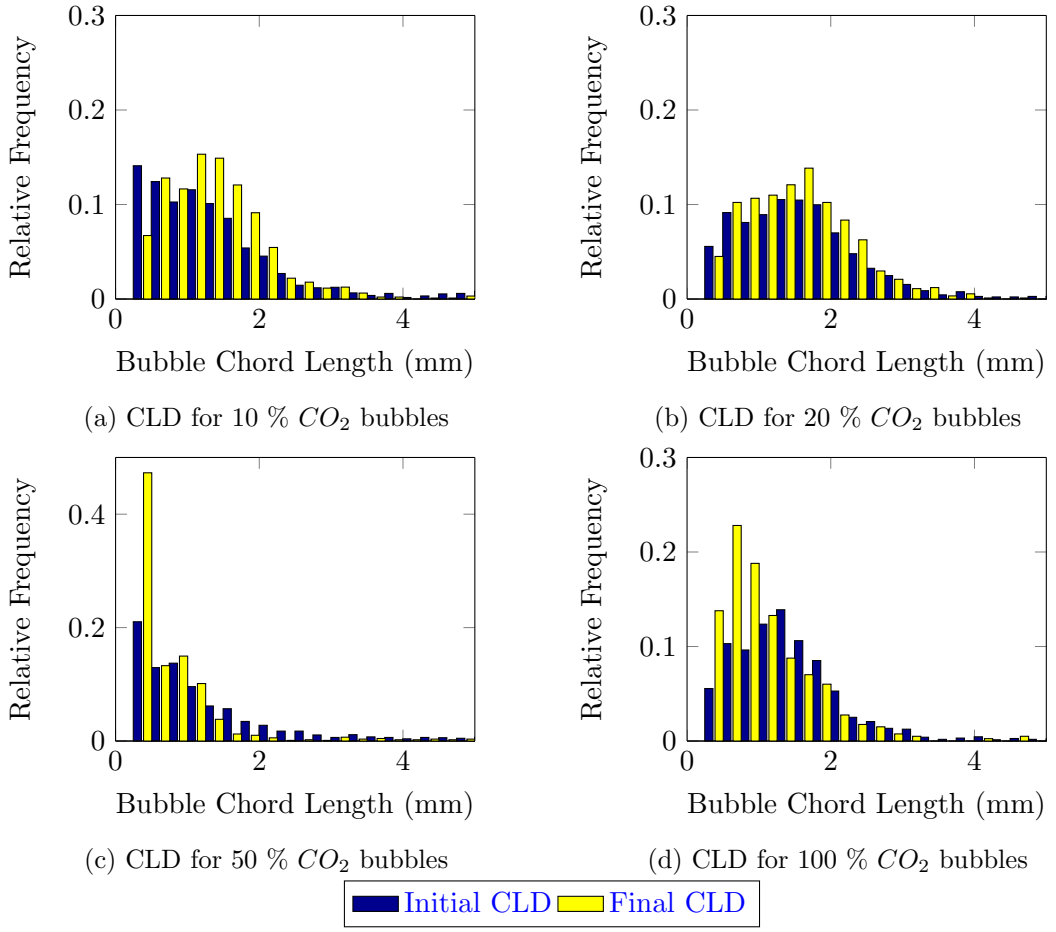

Figure 7.1: Comparison of initial and final bubble chord length distribution (CLD) measured by the optical fibre probe

Figure 7.2 shows the transformed BSD for the CLD shown in figure 7.1. The blue line represents the initial BSD. The increase in bubble size with 10 % CO_2 bubbles is evident in figure 7.2a. The 20 % CO_2 bubble shows little change in the bubble size, while there are reductions in the BSD for the 50 % and 100 % CO_2 bubbles.

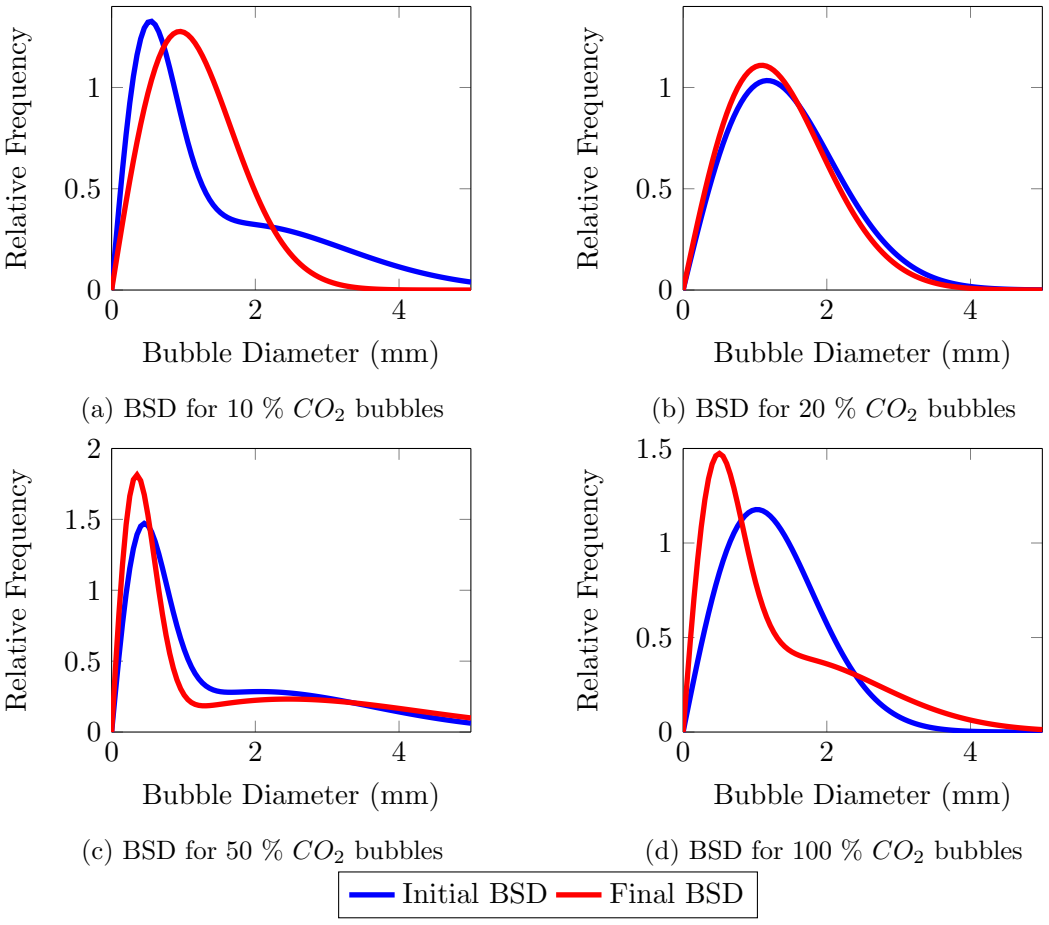

(a) BSD for 10 % CO_2 bubbles

(b) BSD for 20 % CO_2 bubbles

(c) BSD for 50 % CO_2 bubbles

(d) BSD for 100 % CO_2 bubbles

Figure 7.2: Comparison of initial and final bubble size distribution (BSD) measured by the optical fibre probe

7.3 Bubble Velocity

Figure 7.3 shows the variation in average bubble rise velocity recorded by the optical fibre sensors in a bubble swarm. The rise velocities are recorded at different vertical positions in a 1.0 m bubble column. The figure presents the results for a range of input CO_2 concentrations; with the dashed line showing the line of best fit for the range of CO_2 concentrations. A very similar trend in the single bubble rise velocity was shown in figure 6.4, with an initial fast acceleration, followed by a slower increase and then a reduction in bubble velocity. The average velocity from the bubble swarm is slightly higher than the average velocity from the single bubbles. The average rise velocity of single bubbles did not exceed 0.3 $m\ s^{-1}$, while, on average, this is exceeded during the maximum portion of the bubble rise in the bubble swarm.

The comparison of the rise velocity of different sized CO_2 bubbles rising in tap water is shown in figure 7.4. These results were measured for a superficial gas velocity of $u_G = 1 \times 10^{-3}\ m\ s^{-1}$. When compared to the single bubble relations the average rise velocity of the bubble swarm ranges from the relation by Fan and Tsuchiya (1990) for surfactant contaminated liquids and exceeds the relation by Tomiyama et al. (1998) for un-contaminated liquids. The largest rise velocity was measured at an average bubble diameter $d_e \approx 2.0\ mm$. The measurements of the bubble rise velocity for single bubbles were also greater than the predicted rise velocity. The average rise velocities for bubbles within a bubble swarm are not noticeably larger than the average rise velocity of single bubbles.

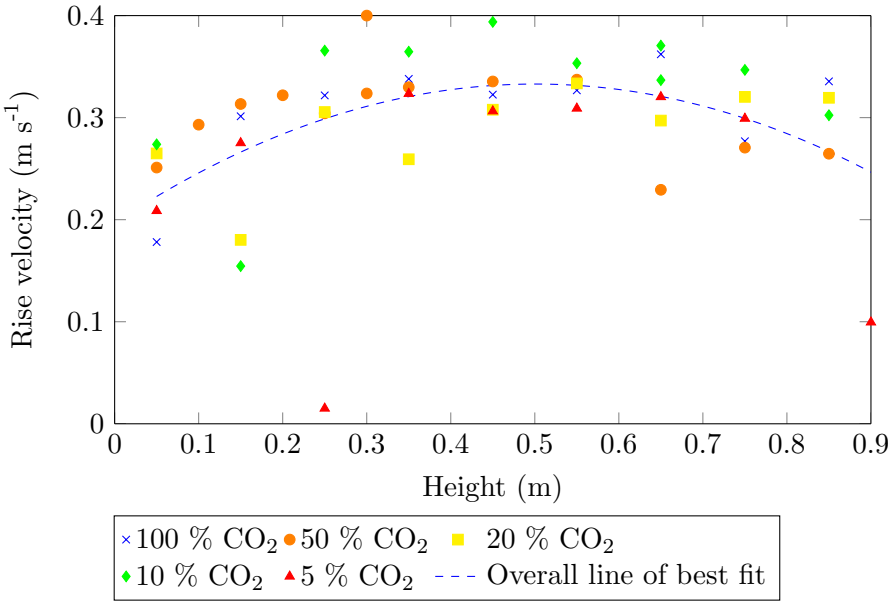

Figure 7.3: Average bubble rise velocity for different CO_2 concentrations rising in tap water

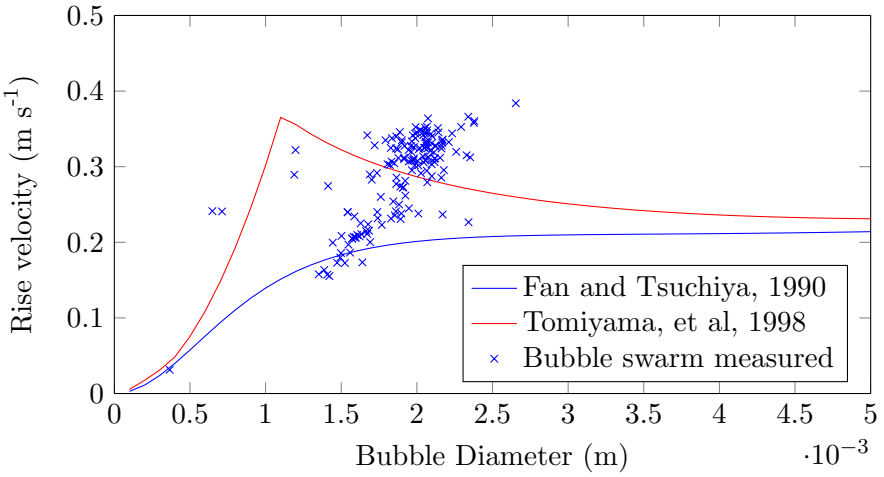

Figure 7.4: Rise velocity of bubbles within a bubble swarm in tap water

Figure 7.5 shows the measured bubble rise velocity for different superficial gas velocities and CO_2 concentrations. The different coloured marks represent superficial gas velocities of 0.5, 1.0 and 2.0×10^{-3} $m\ s^{-1}$. For the range of superficial gas velocities tested there does not seem to be a consistent relation between the bubble rise velocity and bubble diameter, either overall or with different superficial gas velocities.

Analysis of one of the effects of bubble-bubble interactions, which will occur in a bubble swarm is shown in figure 7.6. The sequence of images shown are taken 0.1 s apart and show the changing position of two air bubbles as they rise in water. The two bubbles have similar diameters, of $d_e = 2.20\ mm$ for the bubble shown in the higher position at 0.0 s bubble and $d_e = 2.47\ mm$ for the lower bubble. Over the course of the 0.8 s rise shown in figure 7.6, the lower bubble eventually catches up with the higher bubble. Koynov and Khinast (2005) investigated the motion of the trailing bubble and observed that it responds to vortex shedding from the preceding bubble, with 'jumps' in the vertical position, resulting in continuous acceleration and deceleration of the trailing bubble until it reaches the higher bubble.

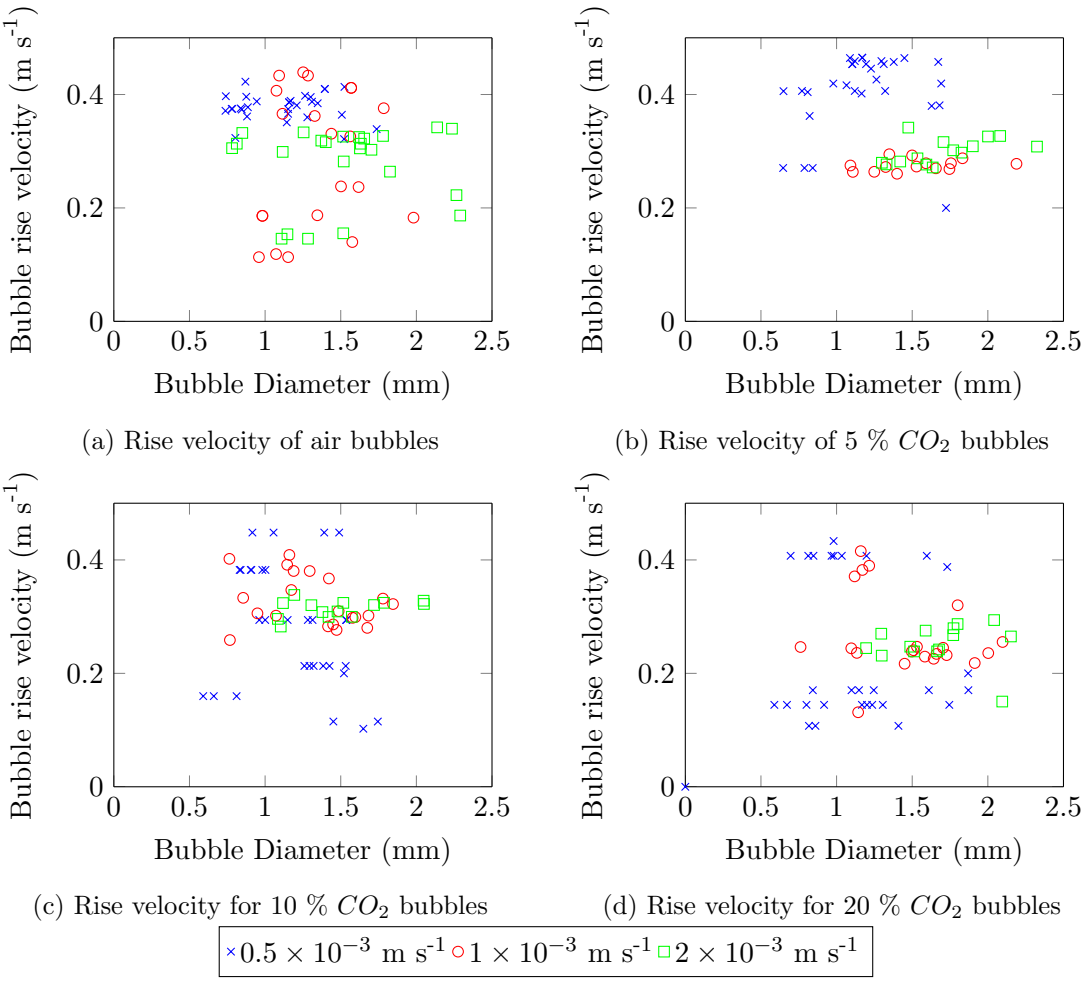

(a) Rise velocity of air bubbles

(b) Rise velocity of 5 % CO_2 bubbles

(c) Rise velocity for 10 % CO_2 bubbles

(d) Rise velocity for 20 % CO_2 bubbles

Figure 7.5: Comparison of bubble rise velocity with superficial gas velocity

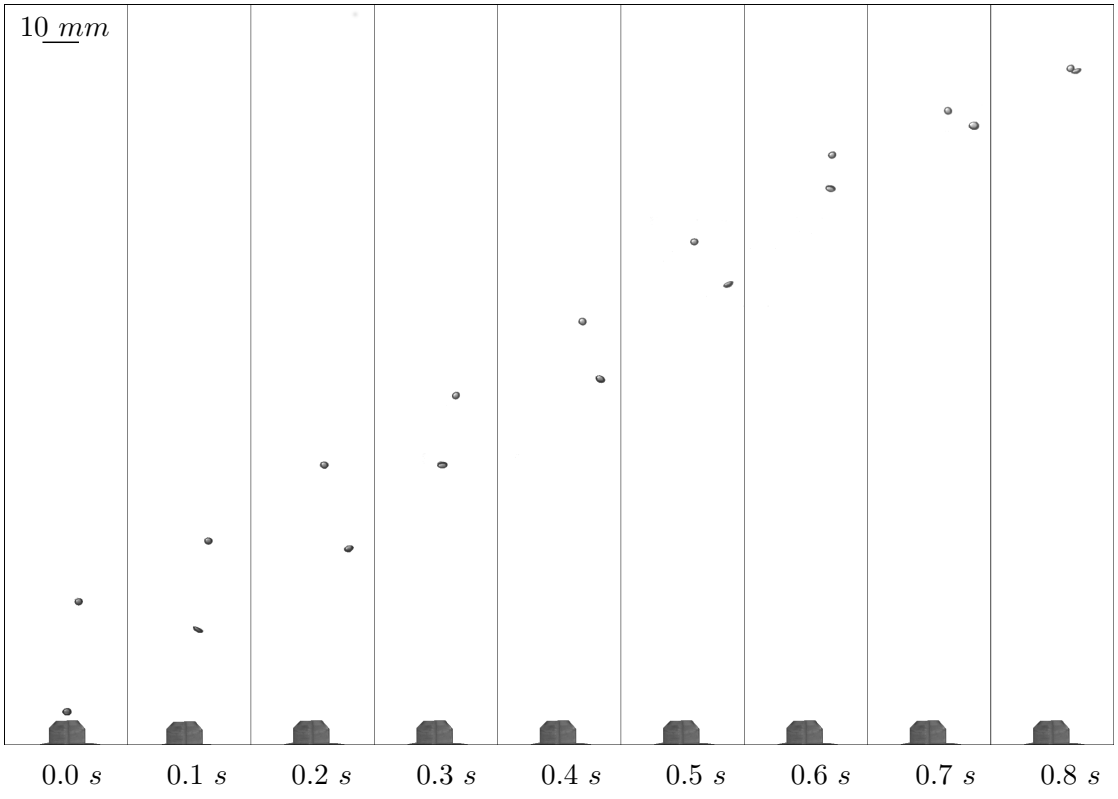

Figure 7.6: Visualisation of a bubble rising in the path of a preceding bubble

7.4 Gas Holdup

Figure 7.7 shows the axial profile of the gas holdup measured in the centre of the bubble column, as calculated from the time difference measurements shown in equation 5.3 and described in chapter 5.2. The reduction in gas holdup with height is due to the radial spreading of the gas phase as it rises up the bubble column. The radial profile of the gas holdup has not been investigated in this study, although this has been extensively studied previously, by Shah et al. (1982), Kawase and Moo-Young (1987), Chabot and de Lasa (1993) and Kantarci et al. (2005). The radial profile of the gas holdup is dependent on the liquid viscosity, the column diameter and the superficial gas velocity (u_G). For bubble columns with a larger diameter, the gas holdup profile becomes flatter. Some of the proposed estimates for the gas holdup from literature, such as the relation proposed by Akita and Yoshida (1973) take into account the column diameter. The gas holdup shown in figure 7.7 reduces from the maximum value at the base of the bubble column to a minimum value after approximately 0.3 m. The small increase in gas holdup after 0.3 m is likely due to bubble coalescence, which has been previously reported to cause an increase in gas holdup with axial position, Majumder et al. (2006). A comparison between the superficial gas velocities, shows an increase in gas holdup with velocity. This is a result of the greater volume of gas per volume of reactor. The relationship between the gas-holdup and u_G is dependent on the flow regime; Kawase et al. (1992) describe this as the reason for the range of exponents used to relate the gas holdup and u_G in relations found in the literature.

Figure 7.8 compares the results for the relations shown in table 2.2 in chapter 2.4 with the localised gas holdup measurements from the optical fibre probe. The gas holdup

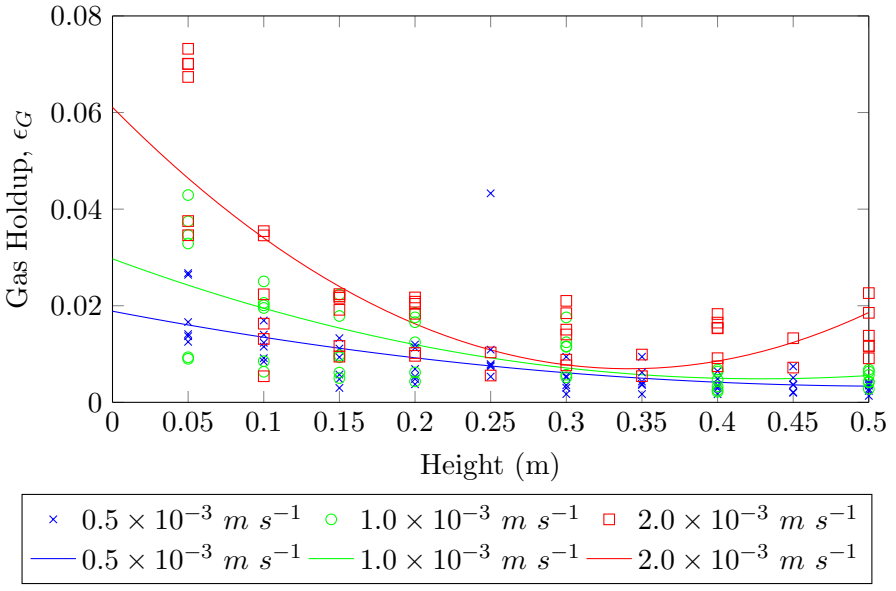

Figure 7.7: Variation of gas holdup, ϵ_G, along the height of the bubble column with air sparged through water at different superficial gas velocities, u_G

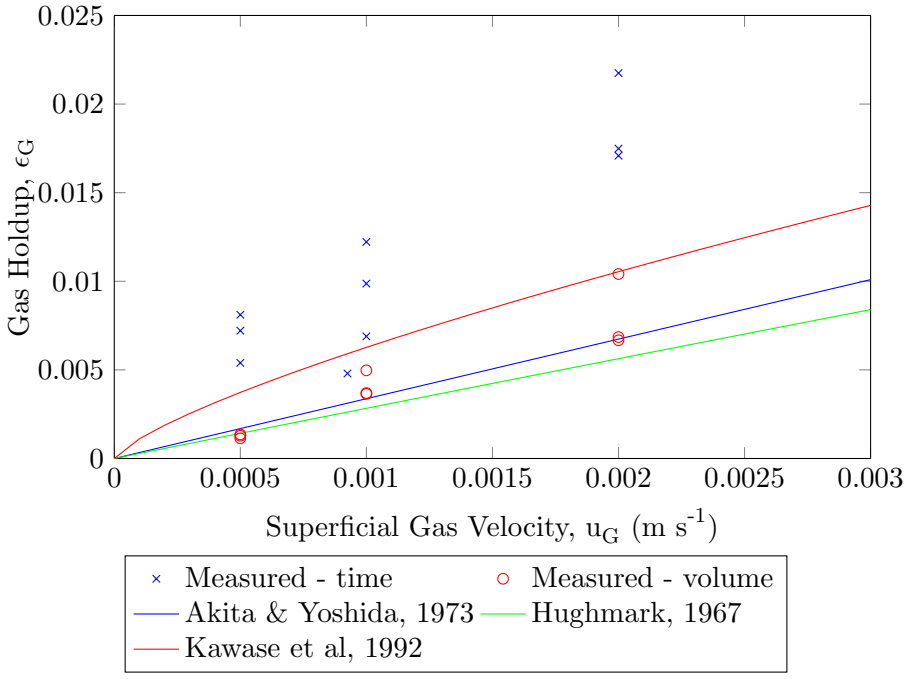

Figure 7.8: Effect of superficial gas velocity, u_G, on gas holdup, ϵ_G

can also be calculated from the bubble size distribution, as shown by equation 7.1. The number of bubbles per unit volume of reactor, N, was calculated from equation 7.2 where u_G is the superficial gas velocity, V_b is the bubble volume and $\bar{u}_b$ is the average bubble rise velocity. The bubble volume was also calculated from the bubble size distribution, shown in equation 7.3. The gas holdup calculated from equation 7.1 using the bubble size distribution is included in figure 7.8, represented by the red circles. The localised gas holdup calculated from the time difference of the optical fibre sensors is shown by the blue crosses.

$$\epsilon_G = \frac{\pi}{6} N \int_0^\infty d_b^3 P_S(d_B) \mathrm{d}d_B \tag{7.1}$$

$$N = \frac{u_G}{V_b \bar{u}_b} \tag{7.2}$$

$$V_b = \frac{\pi}{6} \int_0^\infty d_b^3 P_S(d_B) \mathrm{d}d_B \tag{7.3}$$

The measured values for the gas holdup shown in figure 7.8 represent the average gas holdup over the axial distance of the bubble column. There is a large variation in the measured gas holdup values, which shows the variation in the localised measurements. All the relations and the measured values show a clear increase in the gas holdup with superficial gas velocity. Gas holdup measurement from the time fraction method using equation 5.3 is a more direct method and is consistently higher than the volume-based

distribution method from equation 7.1. The time-based measurement from the optical fibre is a localised measurement and, although it is averaged over the axial direction, it is not averaged in the radial direction. The over-estimation from these measurements is therefore not surprising, considering the higher gas holdup in the centre of the bubble column. The volume distribution method shows a closer fit to the empirical relations. As well as being more representative of the global gas holdup, the relations shown in figure 7.8 used similar approaches to determine the gas holdup. Akita and Yoshida (1973) used an image analysis method to obtain the bubble size distribution and then used the volume distribution to find the gas holdup.

Figure 7.9 shows the variation in gas holdup with different input CO_2 concentrations. Increasing the CO_2 concentration of the gas flow immediately reduces the gas holdup at the base of the column. This is evident comparing the scenario with air and 20% CO_2, although the comparison between 5 % and 10 % CO_2 is less clear. At higher axial positions in the column the difference in gas holdups between the different CO_2 concentrations is reduced. This is similar to the comparison of the superficial gas velocity, where there was a clear difference at the base of the column, but after a height of 0.30 m this difference is not so evident. Interestingly the increase in gas holdup towards the top of the column is more pronounced with the air bubbles, than with higher CO_2 input concentrations. This is likely to be due to the mass transfer which reduces the bubble volume for the 20 % CO_2 bubbles and thus, reduces the gas holdup. There is also less likelihood of coalescence with smaller bubbles, as they will have a reduced volume and lower probability of bubble collisions.

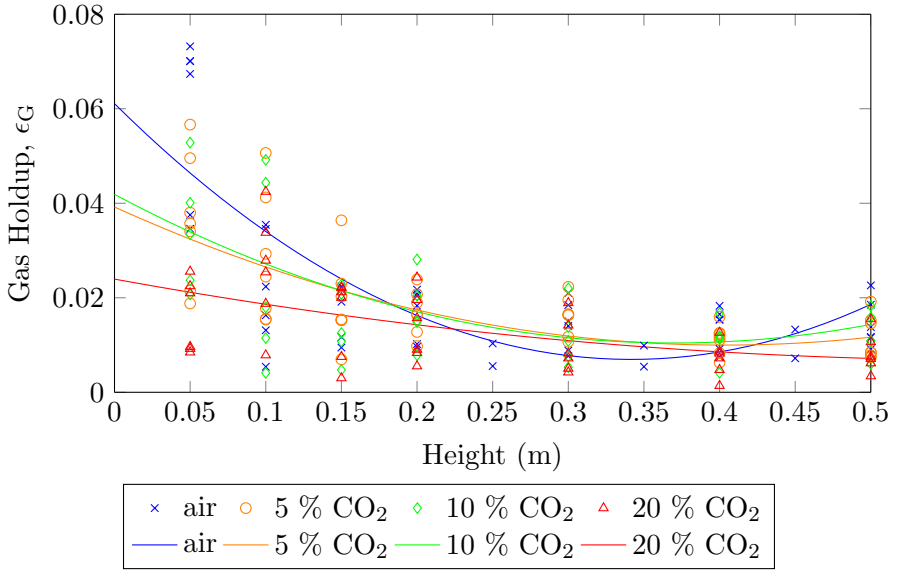

Figure 7.9: Effect of input CO_2 concentration on localised gas holdup (ϵ_G)

7.5 Mass Transfer

The mass transfer rate was calculated from the change in gas volume as estimated from equation 7.3. This was combined with the gas pressure, calculated from equation 4.9, and the ideal gas law to estimate the number of moles in the gas phase. The change in CO_2 concentration, measured from collected gas samples, was combined with the total number of gaseous moles to find the number of moles of CO_2 in the bubble. The average time taken for the bubble to ascend through the bubble column was calculated from the average bubble velocity. Then, in a similar way to the mass transfer calculations for a single bubble, a mass balance of the gaseous CO_2 was carried out to find the change in number of moles of CO_2 with time.

The average equivalent bubble diameter measured at different heights with the optical fibre probe is shown in figure 7.10 for CO_2 input concentrations from $10 - 100$ %. The average initial bubble size shown in the figure is $d_{vs} \approx 2.7\ mm$, where d_{vs} is the average volume-surface bubble diameter, shown in equation 2.13. Figures 7.10a and 7.10b, show similar size changes in bubble diameter, with a slight reduction noticeable for CO_2 input concentrations of 10 and 20 %. In figures 7.10c and 7.10d the bubble equivalent diameter shows a clearer reduction to approximately 2.1 mm and below 1.0 mm for 50% and 100% CO_2 concentrations, respectively.

Figure 7.11 compares the average change in volume for a single CO_2 bubble and the average bubble within a bubble swarm. The recorded changes in bubble volume from the image analysis and optical fibre probes for the single bubble and bubble swarm appear to be similar. The average initial bubble diameters shown in figure 7.11 are 3.2 mm and 3.4 mm for the average single bubble and bubble swarm, respectively.

The mass transfer coefficient (k_L) was calculated by dividing the mass transfer rate (dn/dt) by the saturated CO_2 concentration difference ($C^* - C_0$) and the interfacial area (α). For a bubble swarm the interfacial area was taken as the volumetric interfacial area ($m^2\ m^{-3}$) calculated from equation 7.4.

$$\alpha = 6\frac{V_b}{d_{vs}} \tag{7.4}$$

The k_L values from the bubble swarm are shown in red in figure 7.12a and compared with the single bubble measurements shown in blue. The maximum k_L values from this work were measured with $d_e \approx 2.5\ mm$; where the difference between the k_L for single bubbles and bubble swarms is most evident. For single bubbles k_L reaches a maximum $k_L \approx 6 \times 10^{-4}\ m\ s^{-1}$ which is lower than k_L measured in bubble swarms with $k_L \approx 8 \times 10^{-4}\ m\ s^{-1}$. In this work the maximum k_L in bubble swarms was measured at the maximum average bubble diameter from this work, $d_{vs} \approx 2.6\ mm$. For the range of bubble sizes in bubble swarms studied in this work there is a consistent increase in k_L

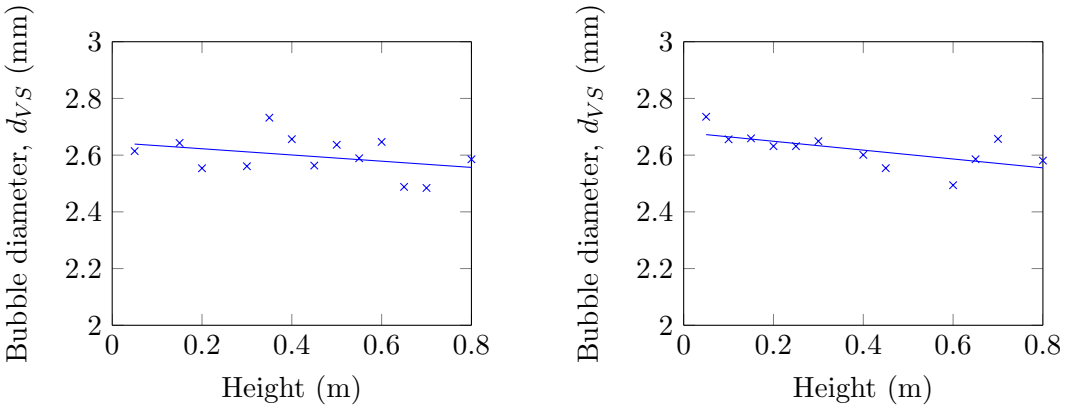

(a) 10% CO_2 concentration

(b) 20% CO_2 concentration

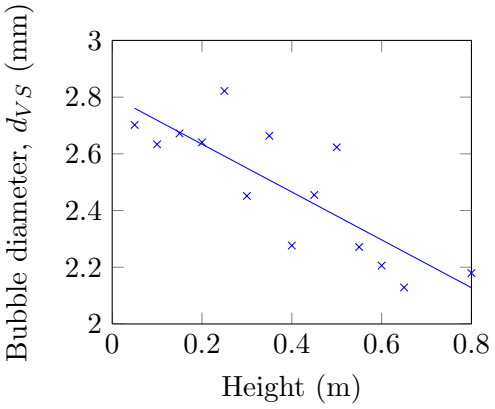

(c) 50% CO_2 concentration

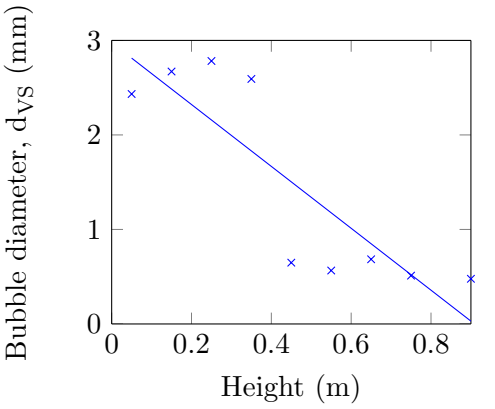

(d) 100% CO_2 concentration

Figure 7.10: Change in bubble diameter with different input CO_2 concentrations

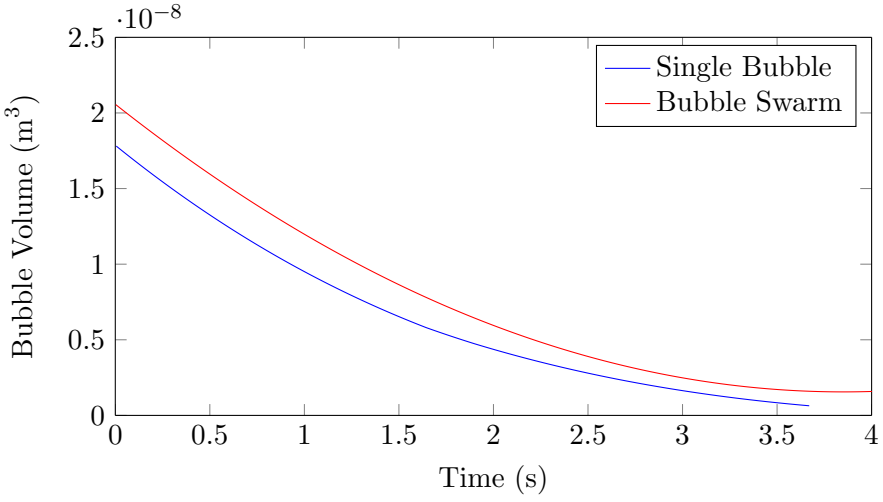

Figure 7.11: Average change in bubble volume for single CO_2 bubbles and bubble swarm

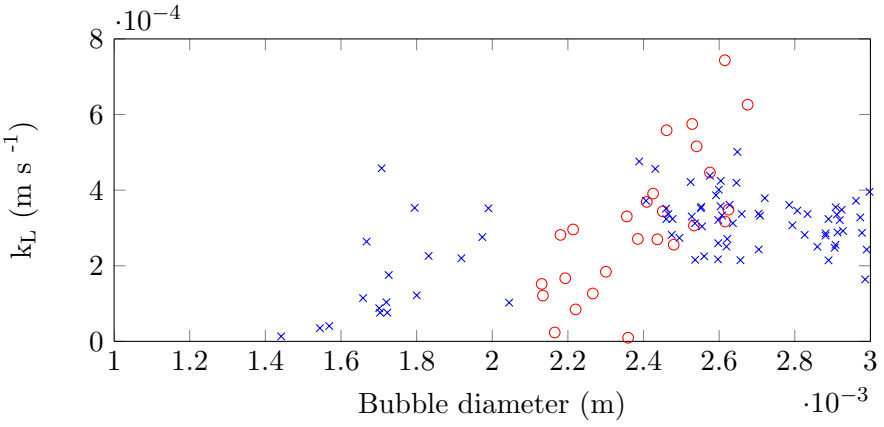

(a) Effect of bubble diameter on the measured mass transfer coefficient, k_L

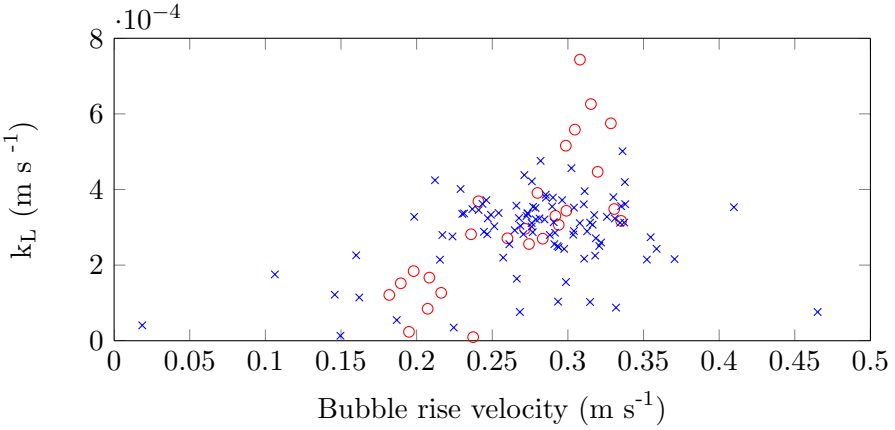

(b) Effect of the bubble rise velocity on the measured mass transfer coefficient, k_L

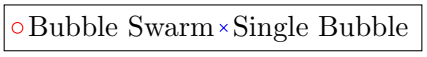

Figure 7.12: Comparison of mass transfer coefficient (k_L) measured in bubble swarms and single bubbles

with d_e. There was also an increase in k_L with d_e for single bubbles, which reached a maximum at $d_e > 2.5\ mm$ and k_L remained approximately constant for greater bubble sizes.

Figure 7.12b compares the measured k_L values for single bubbles and bubble swarms with the average bubble rise velocities. The bubble rise velocity in bubble swarms was shown to be greater than single bubbles in figure 7.3; this could have an effect on increasing k_L. A comparison between the average bubble rise velocities in figure 7.12b does not show a clear distinction between the bubble rise velocities of single bubbles and bubbles within a bubble swarm. There is a clearer relation, however, between the bubble rise velocity and k_L for bubble swarms, than single bubbles. The average bubble velocities do not show the detail of the localised bubble velocity. During the bubble ascent the maximum bubble rise velocity may be larger in bubble swarms, however this cannot be identified by comparing the average values.

Figure 7.13 compares the values of k_L determined from the bubble swarm experiments

with mass transfer relations from the literature which have been applied to bubble column reactors. The relations from Higbie (1935) and Frössling (1938) have also been included as they provide the basis of the different mass transfer relations from bubbles. As with the single bubble experiments Higbie's theory provides a reasonable approximation for the average measured values of k_L, while the theory from Frössling underestimates the average k_L, shown in figure 7.13A and 7.13B, respectively. Empirical relations from Calderbank and Moo-Young (1961) and Akita and Yoshida (1974) shown in figures 7.13C and 7.13D also provide reasonable estimations for the measured k_L values, while the relations proposed from Hughmark (1967b) and Nedeltchev et al. (2007) in figures 7.13E and 7.13F both underestimate the k_L measured in this work.

From the experiments with single CO_2 bubbles in the current work, a bubble with $d_0 < 2.5\ mm$ was found to exhibit two different mass transfer rates during a 1.0 m rise in water. The second stage of the mass transfer was lower, following Frössling's theory for a rigid particle. To account for the two stages of mass transfer, the single bubble model was adapted to include two mass transfer rates; the higher mass transfer rate from Montes et al. (1999), suitable for larger bubbles $d_e > 1.3\ mm$, and the lower mass transfer rate from Frössling (1938), for smaller bubbles. Figure 7.14 shows the measured change in bubble volume for the average 100 % CO_2 bubble, (for which the average bubble diameter is shown in figure 7.10d). The solid blue line represents the line of best fit for the experimental measurements of the change in bubble volume, while the dashed red line represents the single bubble model, incorporating both mass transfer rates from Montes et al. (1999) and Frössling (1938). The black dashed and dotted lines illustrate the bubble volume calculated with k_L from Higbie (1935) and Frössling (1938), respectively. The theory from Frössling for rigid particles predicts a considerably lower mass transfer rate and volume reduction. The relation from Montes et al. used in the model is similar to the penetration theory from Higbie, but provides a slightly better prediction. It can be seen that the model based on the results from the single bubble experiments also provides a reasonable estimate for bubble volumes with 100 % CO_2 in a bubble swarm. This is not so clear at lower CO_2 concentrations, however.

Figure 7.15 compares the change in bubble volume with single bubbles and bubbles in a bubble swarm, for different CO_2 concentrations. The average volume of single bubbles is shown by the dashed lines, and the volume of bubbles in a bubble swarm is shown by the solid lines. In all cases there is a greater reduction in bubble volume for the bubbles in a bubble swarm. This is more noticeable at reduced CO_2 input concentrations. With an input concentration of 10 % CO_2, the single bubbles show an increase in volume, while the bubbles in a swarm remain approximately the same volume. For 20 % CO_2, the bubbles in the swarm show a clear reduction in volume, although there is only a minimal reduction in volume for a single isolated bubble. This suggests a possible lower mass transfer rate for CO_2, or higher mass transfer rate for O_2 or N_2 for single bubbles, which is particularly evident at lower input CO_2 concentrations.

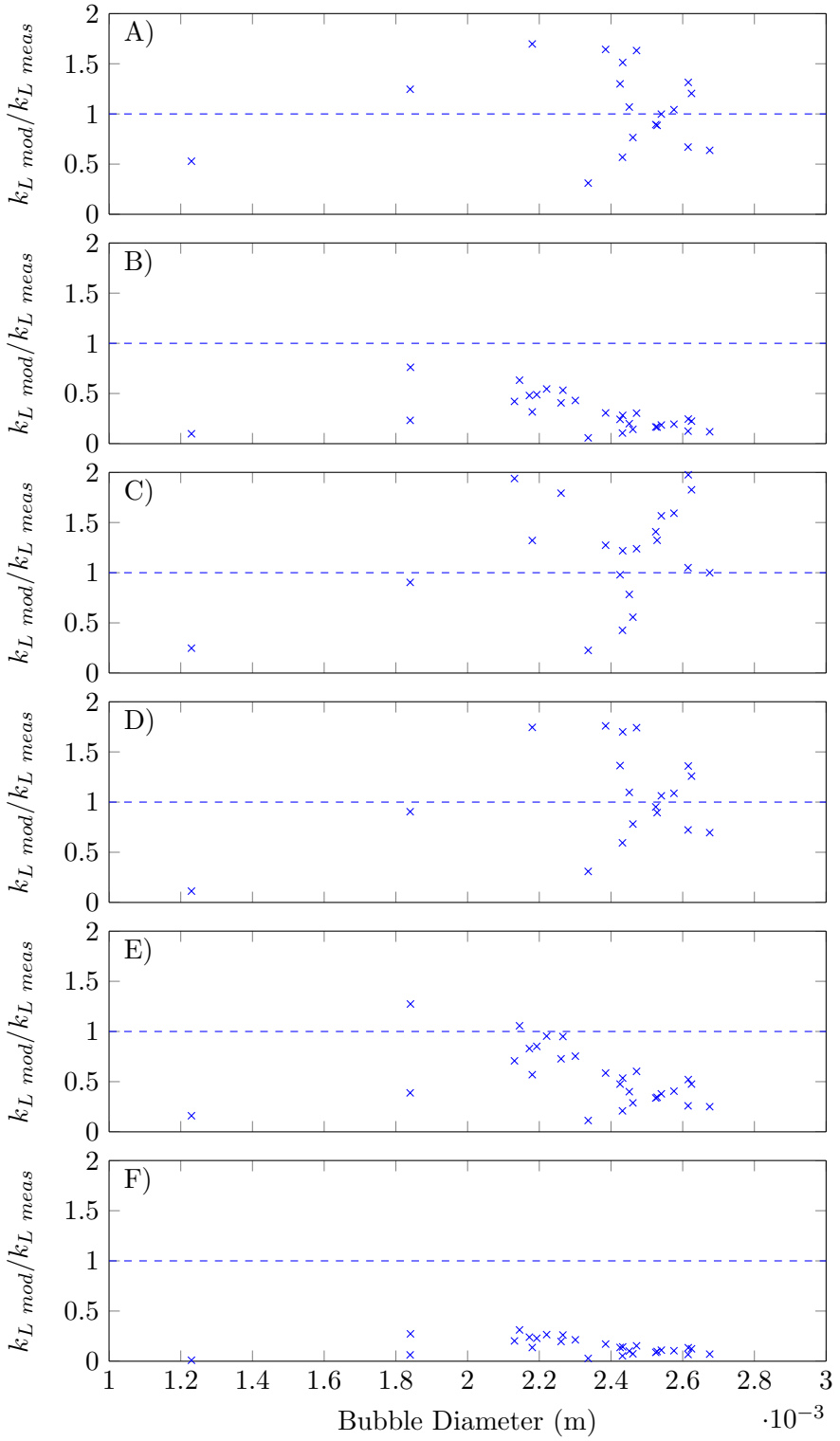

Figure 7.13: Mass transfer coefficient (k_L) measurements compared with models from A) Higbie (1935) B) Frössling (1938) C) Calderbank and Moo-Young (1961) D) Akita and Yoshida (1974) E) Hughmark (1967b) F) Nedeltchev et al. (2007)

In addition to the bubble volume measurements, gas samples were collected at the input and output of the bubble column. These were then analysed to find the change in CO_2 concentration. Figure 7.16 shows the output concentrations of CO_2 relative to the input concentration. In comparison to the change in CO_2 concentration of single bubbles shown by figure 6.17 in chapter 6.6, there is a greater reduction of CO_2 concentration within a bubble swarm. The single bubble experiments showed a reduction to approximately 40 % of the input concentration, with an input concentration from $5-50$ % CO_2,

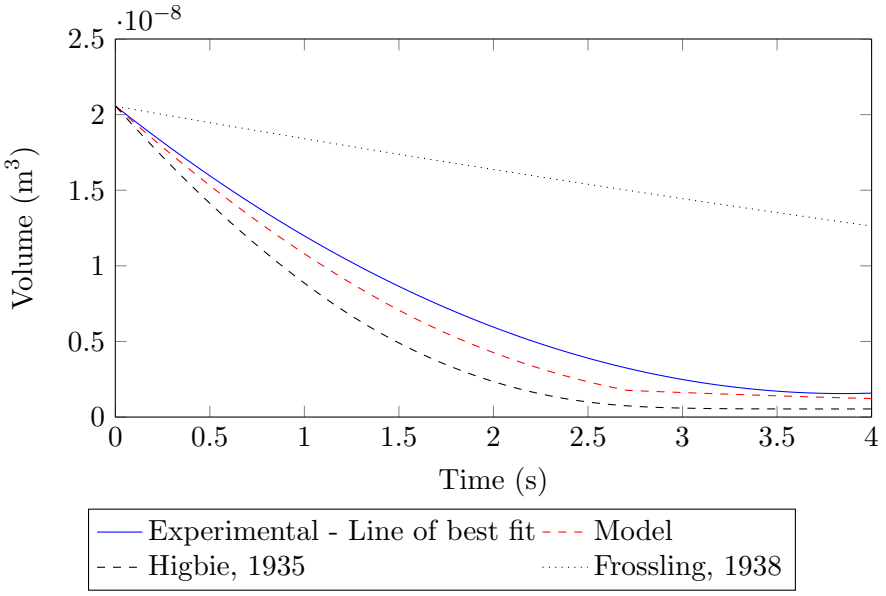

Figure 7.14: Comparison between predicted and measured change in bubble volume for a 100 % CO_2 bubble

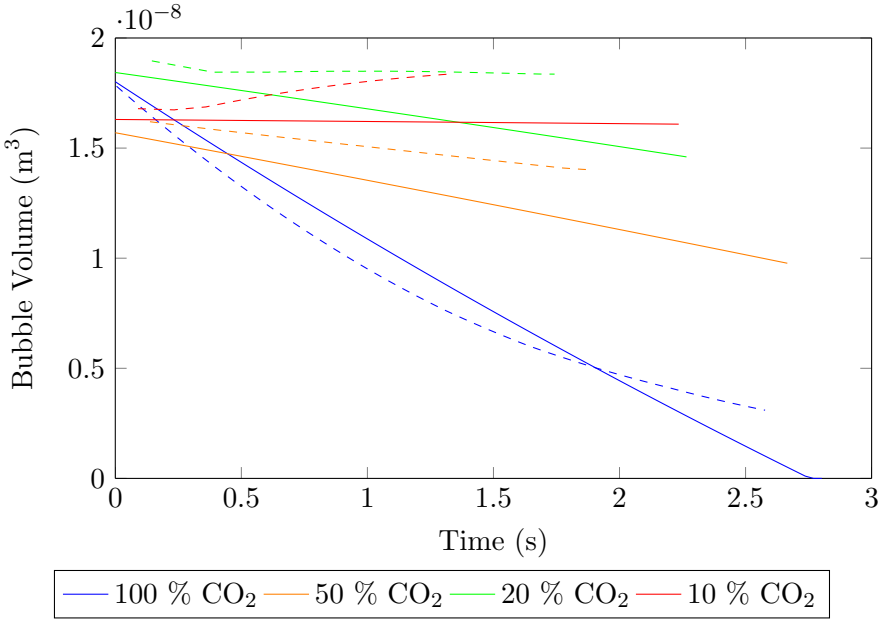

Figure 7.15: Average change in volume of single bubbles and bubbles rising in a swarm, —- Bubble Swarm, - - - - Single Bubble

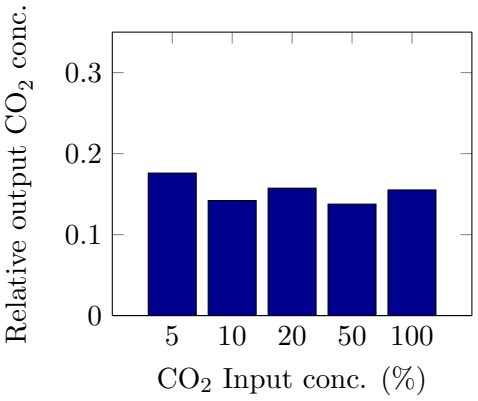

(a) Relative CO_2 concentration at 0% saturation DO

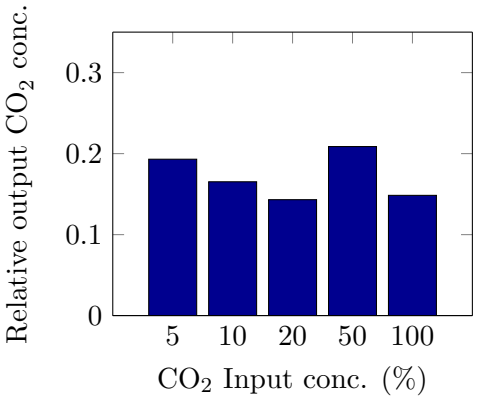

(b) Relative CO_2 concentration at 100% saturation DO

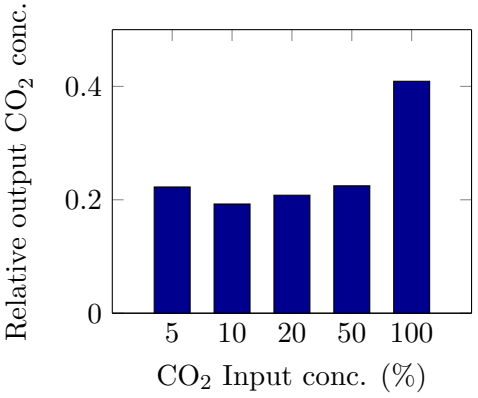

(c) Relative CO_2 concentration at 200% saturation DO

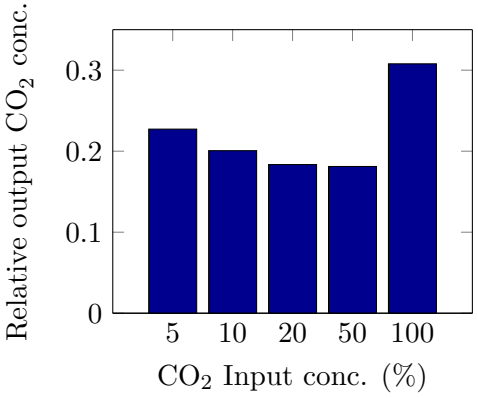

(d) Relative CO_2 concentration at 300% saturation DO

Figure 7.16: Output CO_2 concentration, relative to input concentration, at different saturated dissolved oxygen (DO) concentrations

however in bubble swarms this reduces to approximately 20 %. This result is also reasonably consistent, despite varying DO concentrations in the liquid. The reduction in CO_2 concentration is also significantly lower for the bubbles containing 100 % CO_2. With single bubbles, an input CO_2 concentration of 100 % led to a greater reduction in bubble size and surface area and a lower desorption of O_2 and N_2. This resulted in a higher output CO_2 concentration of approximately 75 % CO_2. In a bubble swarm, this output CO_2 concentration reduced significantly to between $15 - 40$ % of the input value. This supports the pattern from the bubble volume measurements, which suggests that the mass transfer rate for CO_2 is greater for bubbles within a bubble swarm. The bubble swarm results compared with the single bubble measurements were conducted in a semi-batch experiment, with a stagnant liquid phase. The turbulence generated from the bubble swarm could be the reason for the increase in mass transfer rate. Increased turbulence would increase the gas-liquid interface velocity and promote mass transfer.

For bubble input concentrations of $5 - 50$ % CO_2 there is no clear trend in reduction of CO_2 concentration at different DO concentrations. The range of output values typically

varies between 15−25 % of the input CO_2 concentration. The output CO_2 concentration is higher for bubbles with an initial concentration of 100 % CO_2 absorbing into water with an elevated DO concentration of 200 % and 300 % saturation levels. This lower difference in CO_2 reduction is most likely due to a reduced surface area for single bubbles. In bubble swarms, there may also be a contribution from the induced bubble turbulence. For smaller bubbles, including bubbles containing 100 % CO_2 which rapidly reduce in size, the induced turbulence would be expected to be smaller than larger bubbles. This reduced turbulence could then result in a reduced mass transfer rate from the bubble. This could be a contributing factor to the increased CO_2 concentration seen for bubbles containing 100 % CO_2, although this does not explain why this occurs at an increased DO concentration.

A comparison can be made between the counter-diffusion of O_2 and N_2. As noted in chapter 6.7.3, O_2 has a higher gas diffusivity and solubility than N_2. Considering Higbie's theory with $k_L \propto \sqrt{D_L}$ a higher gas diffusivity results in a greater k_L; a larger solubility would also increase the concentration difference driving the mass transfer. A higher DO concentration in the water would therefore be expected to increase the counter-diffusion into the bubble. This would be measured by a greater depletion of the CO_2 in the bubble. From the results shown in figure 7.16, however, an increase in DO concentration does not have a noticeable affect on CO_2 concentration in the bubble. The increased gas diffusivity and solubility of O_2 over N_2 is not large enough to observe a difference.

The mass transfer of O_2 from the liquid phase into the gas phase is important in algal cultivation media, due to the elevated DO concentrations as a result of micro-algal photosynthesis. In micro-algal cultivation media the partial pressure of saturated gases will be larger and thus the counter-diffusion would be expected to be higher. In the experiments in this work, the O_2 was saturated in the water by bubbling, this would also displace the saturated N_2. As a result of this the saturated concentration of N_2 reduces when the saturated concentration of O_2 increases in these experiments. In algal cultivation media, however, the O_2 is introduced from the algal cells without displacing the dissolved N_2, resulting in a higher partial pressure of dissolved gases. This would create a higher concentration driving force for the counter-diffusion of saturated gases.

Figure 7.17 shows two scenarios with bubbles containing 100 % CO_2 and 20 % CO_2 absorbing into water saturated with atmospheric level of DO (in figure 7.17a) and an elevated DO concentration of 300 % of atmospheric levels (in figure 7.17b). This is shown for both measurements from a single bubble and a bubble swarm, along with the predicted volume change by the mass balance model. The single bubble, bubble swarm and predicted volume change are closer together under the atmospheric DO concentration. As observed previously in figure 7.15, the bubbles within the bubble swarm consistently show a greater reduction in bubble volume, than the single bubbles. The predicted bubble volume change is reasonable for a DO concentration at atmospheric

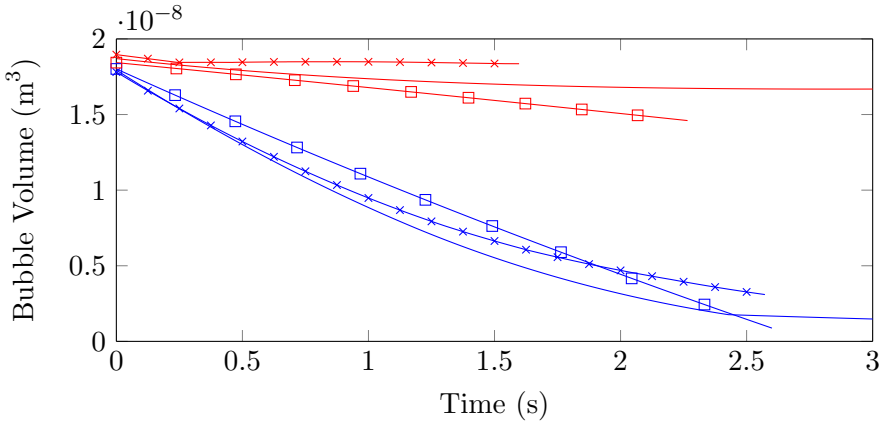

(a) Change in average bubble volume, with *DO* saturation concentration

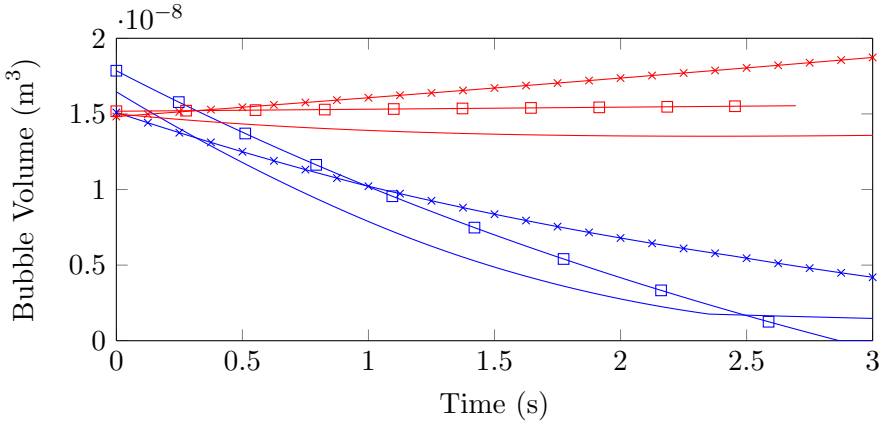

(b) Change in average bubble volume, with 300% *DO* saturation concentration

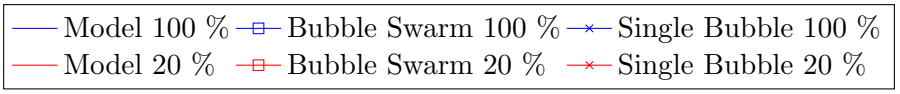

Figure 7.17: Change in bubble volume with different CO_2 concentration, at different saturated dissolved oxygen (DO) concentrations

saturation conditions, however at an elevated DO concentration the mass balance model over-estimates the reduction in bubble volume. This suggests the model underestimates the mass transfer of O_2 from the liquid into the bubble.

The predicted output CO_2 concentrations for different CO_2 input concentrations absorbing into water for different DO concentrations is shown in figure 7.18. The blue bars in figure 7.18 show the predicted output CO_2 concentration using the mass balance model, as calculated with the two k_L values from Montes et al. (1999) and Frössling (1938) (Model # 2). This was used to model the CO_2 concentration for single bubbles, as shown previously in figure 6.18. The red bars shown in figure 7.18 show the predicted change in CO_2 concentration within the bubble, calculated using only one k_L from Montes et al. (1999) (Model # 1). For input CO_2 concentrations between $5-50$ % model #1 and model # 2 predict very similar output concentrations, approximately $10-15$ % of the input value. For bubbles with an input concentration of 100 % CO_2 model #1 predicts a closer output CO_2 concentration to that measured in the bubble

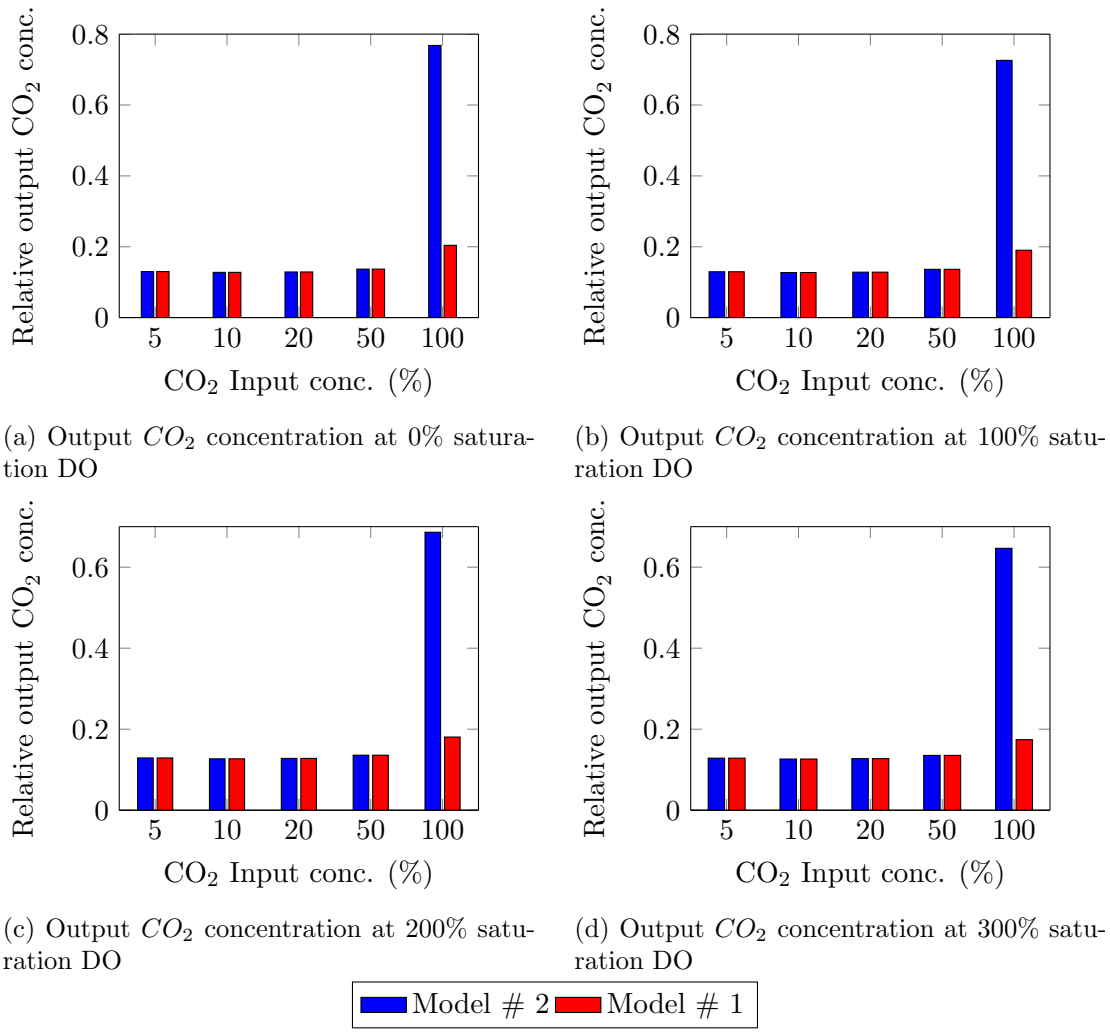

(a) Output CO_2 concentration at 0% saturation DO

(b) Output CO_2 concentration at 100% saturation DO

(c) Output CO_2 concentration at 200% saturation DO

(d) Output CO_2 concentration at 300% saturation DO

Figure 7.18: Modelled CO_2 concentration, relative to input concentration, at different saturated dissolved oxygen (DO) concentrations

swarm. In this case model #1 predicts an output concentrations of approximately 15 %, which is closer to the measured output concentrations of $20 - 40$ %, than the prediction from model # 2 which predicts an output concentration of approximately 70 %. This suggests that just taking the k_L from Montes et al. and not considering the reduced mass transfer rate from Frössling, provides a closer approximation to the mass transfer in bubble swarms.

The differences in the change in volume between the mass transfer coefficients calculated from Frössling (1938) and Montes et al. (1999) (Model #2) and only Montes et al. (1999) (Model #1) are shown in figure 7.19. Because the CO_2 concentration will be larger in the model #2 estimate there is only a minimal difference between the bubble volume predictions from model #1 and model #2. This shows that despite a reduction in bubble size, it appears that the k_L in bubble swarms remains at a higher value. This suggests that the reduction in k_L with smaller bubble sizes is less pronounced in bubble swarms. This is possibly due to the reduced effect of surfactants on changing the bubble

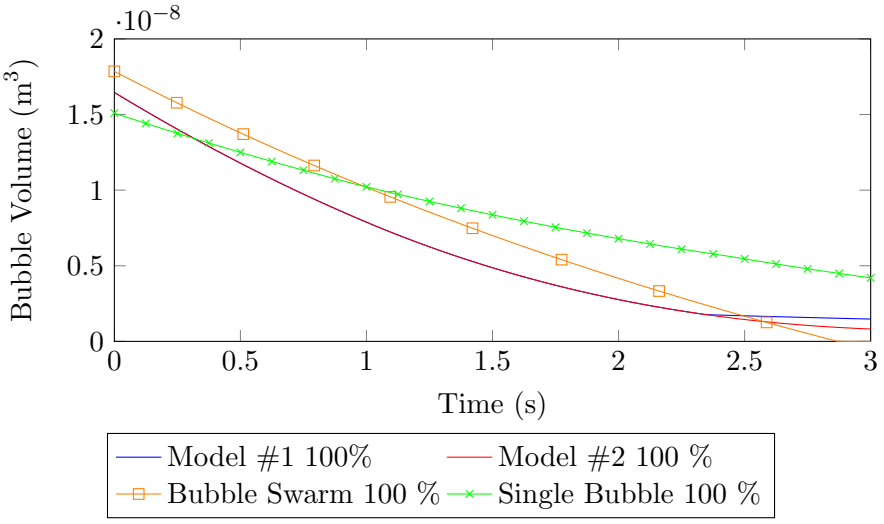

Figure 7.19: Predicted and measured bubble volume

properties to behave as a rigid sphere, in a bubble swarm. The increased turbulence in bubble swarms may be a factor in reducing the surfactant attachment. Alternatively, the increased number of bubbles and surface area in a bubble swarm may reduce the concentration of surfactants per bubble and thus reduce the effect surfactants have on the mass transfer.

Chapter 8

Conclusions & Future Work

The current design of mass transfer systems for gas bubbles absorbing into a liquid is mainly restricted to the use of empirical relations which involve a high level of uncertainty. This is due to a lack of understanding of the interactions of gas bubbles and the liquid phase and of how this affects the mass transfer. This work set out to investigate and to enhance our understanding of the mass transfer of CO_2 from concentrated sources such as flue gases into the aqueous phase, for use in applications such as micro-algal biomass cultivation systems.

8.1 Single Bubble

The experiments conducted in the current work used high speed imaging to study the bubble characteristics and mass transfer from a single bubble and showed a distinct transition between two mass transfer rates. The initial mass transfer rate occurs when the gas-liquid interface is mobile, which corresponds to bubbles in the surface tension-dominated regime following the theory of Higbie (1935). The latter mass transfer rate has a lower value and is applicable for immobile gas-liquid interfaces, such as bubbles in the presence of surfactants in the viscous-dominated regime, as approximated by the rigid particle theory of Frössling (1938). A transition in mass transfer rate has been previously observed by Schulze and Schlünder (1985a), Schulze and Schlünder (1985b), Vasconcelos et al. (2002) and Alves et al. (2005). These authors performed experiments where a bubble was kept stationary by a downflow of liquid and the change in bubble size was measured. The current work showed this transition occurring with a free rising CO_2 bubble in tap water, and demonstrated that it took place during the first 1.0 m rise with $d_0 \leq 2.5$ mm.

The results obtained in this work strongly reinforce the importance of the bubble generation process and rise velocity for surfactant accumulation and mass transfer rate.

The orifice size was shown to affect the initial bubble rise velocity, with a smaller orifice resulting in an increase in velocity and mass transfer rate. Smaller bubbles are more susceptible to the effects of surfactants, which result in a significant reduction in the bubble rise velocity and mass transfer rate. In this work, this was observed in comparisons between bubbles produced with different gas flow rates and orifice sizes. Deformations of the bubble shape from the bubble generation process were observed, which are known to affect the aspect ratio and cause path oscillations thus potentially improving the mass transfer, Martín et al. (2011).

The average measured mass transfer coefficients obtained in the current work were compared with relations available from the literature. The closest fit was provided by the relation proposed by Montes et al. (1999), based on the penetration theory by Higbie (1935). The relation of Montes et al. (1999) was used in a simple finite difference model developed in the current work to calculate the mass balance around a single bubble. The model provided a reasonable estimate when averaged over the 1.0 m rise height; however the changing properties of the bubble resulted in inaccuracies when compared to the experimental results. A discrepancy between the predicted bubble volume and experimental results was particularly evident for smaller bubble sizes, which would undergo a transition from the surface tension dominated regime to the viscous dominated regime. By assuming the relation for k_L from Montes et al. (1999) the mass transfer was over-estimated for bubbles with $d_0 < 2.5\ mm$, hence a modification was proposed which applied k_L from Frössling's theory when $d_e < 1.3\ mm$.

The results of this work therefore highlight the difference in the mass transfer from single bubbles with a mobile or immobile gas-liquid interface. For CO_2 absorption this was particularly noticeable and is dependent on the surfactant concentration, initial bubble size and velocity. The different mass transfer theories from Higbie (1935) to approximate k_L for the mobile interface and Frössling (1938) for the immobile interface were successfully applied to describe the two bubble characteristics. Using both of these mass transfer theories in a simple mass balance model developed in the current work provided a better approximation of the mass transfer from a single bubble, than assuming a single relation for k_L.

8.2 Bubble Swarm

Results from other researchers have indicated the benefits surfactants may have on mass transfer in bubble swarms. Despite this benefit, it is still unclear in the previous literature whether the mass transfer rate from bubble swarms with surfactant contamination would be better approximated by the penetration theory by Higbie (1935) or the rigid particle theory by Frössling (1938).

In the current work the bubble characteristics and mass transfer rate in bubble swarms were investigated by combining bubble size measurements using optical fibre sensors with measurements of the CO_2 concentration from gas samples analysed by gas chromatography. The average bubble rise velocity was observed to be larger for a bubble swarm than for single bubbles. This was established by comparing the average bubble velocities measured with the optical fibre sensors in a bubble swarm, as well as from observation of high speed images of bubbles rising in the path of preceding bubbles. This provides further data to support the view that bubbles accelerate as they rise in the wake of preceding bubbles, as previously suggested by Krishna et al. (1999a) and Koynov and Khinast (2005).

Further analysis comparing the change in CO_2 concentration and bubble volume showed greater mass transfer in bubble swarms compared to single bubbles. For bubbles containing 100 % CO_2 the volume reduction of single bubbles and bubbles within a bubble swarm were approximately the same. The reduction in CO_2 concentration, however, was greater in bubbles within a bubble swarm. The measured output CO_2 concentration was approximately $15 - 40$ % in bubble swarms, and > 75 % with single bubbles. For lower input CO_2 concentrations of $5\ \% - 50\ \%$ CO_2 the reduction in CO_2 concentration was also greater. The output CO_2 concentration in bubble swarms was approximately 20 % of the input value, whereas for single bubbles this was approximately 40 %. For these lower input CO_2 concentrations the volume reduction in bubble swarms was also larger than single bubbles, reinforcing the higher mass transfer rate of CO_2 observed in bubble swarms. This is the first time differences in mass transfer have been quantified between single bubbles and bubble swarms with different input gas concentrations.

As a result of the greater reduction in CO_2 concentration and bubble volume the k_L values for bubble swarms were observed to be larger than for single bubbles. The maximum k_L for both single bubbles and bubble swarms was measured at a bubble diameter $d_e \approx 2.5\ mm$. An average maximum k_L for single bubbles was measured as $k_L \approx 6 \times 10^{-4}\ m\ s^{-1}$, and for bubble swarms as $k_L \approx 8 \times 10^{-4}\ m\ s^{-1}$. The relation of increasing k_L values with d_e was also evident, and at lower bubble sizes the difference in k_L values for single bubbles and bubble swarms was less noticeable. The average measured k_L values in bubble swarms showed reasonable agreement with theoretical values from the penetration theory by Higbie (1935), when the higher rise velocity in bubble swarms was taken into account. This current work provides evidence to explain why the mass transfer is lower in single bubbles than in bubble swarms. For larger bubble sizes, this is partly due to the higher bubble rise velocity, which results in a higher value of k_L. For smaller bubble sizes, however, the transition to the immobile gas-liquid interface was not as apparent in bubble swarms as in single bubbles. This transition to the immobile gas-liquid interface is due to surfactant accumulation which for a given type of aqueous solution has a larger inhibitory effect on the mass transfer rate from single bubbles, than for bubble swarms.

The difference between the measured values of k_L for single bubbles and bubble swarms was more noticeable at a lower input CO_2 gas concentration. At a lower CO_2 concentration, single bubbles had a lower k_L value than bubble swarms. This indicates that there may be a contribution from the gas phase resistance, despite the relatively high diffusivity coefficient in the gas phase, compared to the liquid phase. This was not as apparent in the bubble swarms, which suggests the increased effect of surfactants on single bubbles may be a contributing factor.

The mass balance model developed in the current work provided a closer approximation to the single bubble properties when it adopted two relations for k_L for the mobile and immobile gas-liquid interface, respectively. For changes in bubble size corresponding to a transition into the viscous-dominated regime, the reduction in mass transfer in bubble swarms was less than in single bubbles. As a result the version of the mass balance model which estimated k_L using only Higbie's penetration theory, and not including the reduction in k_L from Frössling's theory, provided a better approximation to the experimental results for bubble swarms. This outcome shows that the penetration theory by Higbie (1935) is suitable for bubble swarms, while single bubbles rising in aqueous solutions will be more susceptible to surfactants and can be approximated with a combination of Frössling's theory for smaller bubbles (in this case $d_e < 1.3\ mm$) and the theory by Higbie (1935) for larger bubbles.

This supports the view that in the same aqueous phase, surfactants have a reduced effect on the mass transfer rate in bubble swarms, and provides evidence for the mechanism of increased turbulence reducing the attachment of surfactants. The larger gas-liquid contact area will also have an effect in reducing the surfactant to area ratio and the concentration of surfactants on the bubble's surface. The current work has thus advanced our understanding of the differences between mass transfer from single bubbles and bubble swarms, and identified several issues that can now be clarified by further work as discussed below.

8.3 Future Work

There are still many unanswered questions regarding the mass transfer from single bubbles and bubble swarms, particularly associated with the recent advances in the production of micro- and nano-bubbles. The advantages of smaller bubbles with an increased residence time and volumetric surface area are apparent. The study of the bubble characteristics of smaller bubbles may require the development of more sensitive measurement techniques. Further experimental work covering a wider range of bubble sizes would prove very useful for the comparison and design of mass transfer equipment.

The effect of surfactants on the gas-liquid interface and mass transfer is also an interesting area, where further investigation would be very worthwhile. In particular

investigation into exactly how surfactants reduce the mass transfer would be valuable. This could be explored by investigating the importance of liquid turbulence for mass transfer. Similar studies could be conducted to the single bubble measurements in this work, but attempting to induce turbulence around the bubble to understand the impact this has on mass transfer. The results of this work may help to shed further light on the higher mass transfer rate in bubble swarms rather than single bubbles.

Further experimental work investigating the surfactant concentration in bubble swarms would be interesting, particularly into the effects of k_L on the ratio of surfactant concentration to gas-liquid volumetric area in industrial applications. These experiments could be conducted with micro-algal cultures, with measurement of the surfactant concentration during the micro-algal growth cycle. Also further investigation into the bubble path oscillation and role this has on mass transfer would be valuable. The bubble path oscillation has been shown to improve mass transfer in single bubbles, although the importance of this in bubble swarms may not be as significant. The role of bubble path oscillations may be to limit the attachment of surfactants to the bubble surface, which would extend the time in which the mobile gas-liquid interface perseveres as the bubble rises through a contaminated liquid.

References

F G Acién Fernández, J M Fernández, J J Magán, and E Molina. Production cost of a real microalgae production plant and strategies to reduce it. *Biotechnology Advances*, 30(6):1344–1353, 2012a.

F G Acién Fernández, C V González-López, J M Fernández Sevilla, and E Molina Grima. Conversion of CO_2 into biomass by microalgae: how realistic a contribution may it be to significant CO_2 removal. *Applied microbiology and biotechnology*, 96(3):577–586, 2012b.

K Akita and F Yoshida. Gas Holdup and Volumetric Mass Transfer Coefficient in Bubble Columns Effects of Liquid Properties. *Industrial Engineering Chemical Process Design Development*, 12(1):76–80, 1973.

K Akita and F Yoshida. Bubble Size, Interfacial Area, and Liquid-Phase Mass Transfer Coefficient in Bubble Columns. *Industrial & Engineering Chemistry Process Design & Development*, 13(1):84–91, 1974.

E Alvarez, J M Correa, J M Navaza, and C Riverol. Theoretical prediction of the mass transfer coefficients in bubble columns operating in churn-turbulent flow regime.Study in Newtonian and non-Newtonian fluids under different operation conditions. *Heat and Mass Transfer*, 37:343–350, 2001.

S Alves, C Maia, and J Vasconcelos. Gas-liquid mass transfer coefficient in stirred tanks interpreted through bubble contamination kinetics. *Chemical Engineering and Processing*, 43(7):823–830, 2004.

S S Alves, S P Orvalho, and J M T Vasconcelos. Effect of bubble contamination on rise velocity and mass transfer. *Chemical Engineering Science*, 60:1–9, 2005.

J B Angelo, E N Lightfoot, and D W Howard. Generalization of the Penetration Theory for Surface Stretch: Application to Forming and Oscillating Drops. *AIChE Journal*, 12(4):751–760, 1966.

W Bai. *Experimental and Numerical Investigation of Bubble Column Reactors*. PhD thesis, Eindhoven University of Technology, 2010.

John R. Benemann, R.P. Goebel, J.C. Weissman, and D.C. Augenstein. Microalgae as a source of liquid fuels. Technical report, U.S. Department of Energy, Fairfield, California, U.S., 1982.

J.R Benemann and W.J Oswald. Systems and economic analysis of microalgae ponds for conversion of CO2 to biomass. Technical report, 1996.

F. Bischof, M. Sommerfeld, and F. Durst. The determination of mass transfer rates from individual small bubbles. *Chemical Engineering Science*, 46(12):3115–3121, 1991.

M Borowitzka. Commercial production of microalgae: ponds, tanks, tubes and fermenters. *Journal of Biotechnology*, 70:313–321, 1999.

M.A Borowitzka. Culturing microalgae in outdoor ponds. In R.A Anderson, editor, *Algal Culturing Techniques*. Burlington, US, 2005.

C Boyer, A Duquenne, and G Wild. Measuring techniques in gas–liquid and gas–liquid–solid reactors. *Chemical Engineering Science*, 57(16):3185–3215, 2002.

G Bozzano and M Dente. Shape and terminal velocity of single bubble motion: a novel approach. *Computers and Chemical Engineering*, 25:571–576, 2001.

G Brenn, V Kolobaric, and F Durst. Shape oscillations and path transition of bubbles rising in a model bubble column. *Chemical Engineering Science*, 61(12):3795–3805, 2006.

R J Brunson and R M Welleck. Mass Transfer Within Oscillating Liquid Droplets. *The Canadian Journal of Chemical Engineering*, 48:267–274, 1970.

J S Burlew. *Algal Culture: From laboratory to pilot plant*. Carnegie Inst. Washington Publ, 1953.

P H Calderbank and M Moo-Young. The continuous phase heat and mass transfer properties of dispersions. *Chemical Engineering Science*, 16:39–54, 1961.

P.H. Calderbank and A.C. Lochiel. Mass transfer coefficients, velocities and shapes of carbon dioxide bubbles in free rise through distiled water. *Chemical Engineering Science*, 19:485 – 503, 1964.

F Camacho Rubio, F G Acién Fernández, J A Sánchez Pérez, F G Garc\'ia Camacho, and E Molina Grima. Prediction of dissolved oxygen and carbon dioxide concentration profiles in tubular photobioreactors for microalgal culture. *Biotechnology and bioengineering*, 62(1):71–86, 1999.

A Cartellier and E Barrau. Mono fiber optical probes for gas detection and gas velocity measurements: conical probes. *International Journal of Multiphase Flow*, 24:1265–1294, 1998.

Alain Cartellier. Optical probes for local void fraction measurements: Characterization of performance. *Review of Scientific Instruments*, 61(2):874, 1990. ISSN 00346748. doi: 10.1063/1.1141457. URL http://scitation.aip.org/content/aip/journal/rsi/61/2/10.1063/1.1141457.

Alain Cartellier. Simultaneous void fraction measurement, bubble velocity, and size estimate using a single optical probe in gasliquid two-phase flows. *Review of Scientific Instruments*, 63(11):5442, 1992. ISSN 00346748. doi: 10.1063/1.1143416. URL http://scitation.aip.org/content/aip/journal/rsi/63/11/10.1063/1.1143416.

A P Carvalho and F X Malcata. Transfer on carbon dioxide within cultures of micro algae: Plain bubbling versus hollow-fibre modules, 2001.

G P Celata, F D'Annibale, P Di Marco, G Memoli, and A Tomiyama. Measurements of rising velocity of a small bubble in a stagnant fluid in one- and two-component systems. *Experimental Thermal and Fluid Science*, 31(6):609–623, 2007.

A H G Cents, D W F Brilman, G F Versteeg, P J Wijnstra, and P P L Regtien. Measuring bubble, drop and particle sizes in multiphase systems with ultrasound. *AIChE Journal*, 50(11):2750–2762, 2004.

J Chabot and H I de Lasa. Gas holdups and bubble characteristics in a bubble column operated at high temperature. *Industrial & Engineering Chemistry Research*, 32(11): 2595–2601, 1993.

H Chaumat, A M Billet-Duquenne, F Augier, C Mathieu, and H Delmas. Mass transfer in bubble column for industrial conditions—effects of organic medium, gas and liquid flow rates and column design. *Chemical Engineering Science*, 60(22):5930–5936, 2005.

N. Chernov. *Circular and Linear Regression: Fitting Circles and Lines by Least Squares*. Chapman & Hall/ CRC, Boca Raton, U.S, 2010.

R Clift, Grace J.R., and Weber M.E. Ellipsoidal Fluid Particles. In *Bubbles, Drops and Particles*, pages 169–202. Courier Corporation, 1978.

B Cuenot, J Magnaudet, and B Spennato. The effects of slightly soluble surfactants on the flow around a spherical bubble. *Journal of Fluid Mechanics*, 339:25–53, 1997.

P V Danckwerts. Significance of liquid-film coefficients in gas absorption. *Industrial & Engineering Chemistry*, 43(6):1460–1467, 1951.

P.V. Danckwerts. Absorption from bubbles of dilute gas. *Chemical Engineering Science*, 20:785 – 787, 1965.

A W G de Vries. *Path and Wake of a Rising Bubble*. PhD thesis, University of Twente, 2001.

H Dong, X Wang, L Liu, X Zhang, and S Zhang. The rise and deformation of a single bubble in ionic liquids. *Chemical Engineering Science*, 65(10):3240–3248, 2010.

J Doucha, F Straka, and K Lívanský. Utilization of flue gas for cultivation of microalgae Chlorella sp.) in an outdoor open thin-layer photobioreactor. *Journal of Applied Phycology*, 17(5):403–412, 2005.

P C Duineveld. The rise velocity and shape of bubbles in pure water at high Reynolds number. *Journal of Fluid Mechanics*, 292:325–332, 1995.

C. Dyer-Smith. Biofuels from algae, parlimentary office of science and technology. Technical report, 2011. URL http://www.parliament.uk/briefing-papers/post-pn-384.pdf.

EC. On the promotion of the use of energy from renewable sources and amending subsequently repealing directives, 2009. URL http://eur-lex.europa.eu/legal-content/en/ALL/?uri=CELEX:32009L0028.

K Ellingsen and F Risso. On the rise of an ellipsoidal bubble in water: oscillatory paths and liquid-induced velocity. *Journal of Fluid Mechanics*, 440:235–268, 2001.

P Ern, F Risso, D Fabre, and J Magnaudet. Wake-Induced Oscillatory Paths of Bodies Freely Rising or Falling in Fluids. *Annual Review of Fluid Mechanics*, 44:97–121, 2012.

D J Euh, B J Yun, and C H Song. Benchmarking of the five-sensor probe method for a measurement of an interfacial area concentration. *Experiments in Fluids*, 41:463–478, 2006.

Liang-shih Fan and Katsumi Tsuchiya. *Bubble wake dynamics in liquids and liquid-solid dispersions*. 1990.

Bruno S Ferreira, Helena L Fernandes, Alberto Reis, and Marília Mateus. Microporous hollow fibres for carbon dioxide absorption: mass transfer model fitting and the supplying of carbon dioxide to microalgal cultures. *Journal of Chemical Technology & Biotechnology*, 71(1):61–70, 1998.

A Fitzgibbon, M Pilu, and R B Fisher. Direct least square fitting of ellipses. *IEEE Transactions on Pattern Analysis and Machine Intelligence*, 21(5):476–480, 1999.

C Fleischer, S Becker, and G Eigenberger. Detailed modeling of the chemisorption of CO_2 into NaOH in a bubble column. *Chemical Engineering Science*, 51(10):1715–1724, 1996.

J Francois, N Dietrich, P Guiraud, and A Cockx. Direct measurement of mass transfer around a single bubble by micro-PLIFI. *Chemical Engineering Science*, 66(14):3328–3338, 2011.

N Frössling. Übber die verdünstung fallenden trop fen (Evaporation of falling drops). *Gerlands Beitrage zur Geophysik von Gerland*, 52:170–216, 1938.

A Frumkin and V G Levich. On surfactants and interfacial motion. *Zhurnal Fizicheskoi Khimii*, 21:1183–1204, 1947.

W Gander, G H Golub, and R Strebel. Least-squares fitting of circles and ellipses. *Bit Numerical Mathematics*, 34(4):558–578, 1994.

G.R Garbarini and C. Tien. Mass Transfer from Single Gas Bubble - A Comparative Study on Experimental Methods. *The Canadian Journal of Chemical Engineering*, 47 (1):35 – 41, 1969.

A M Gaudin. *Flotation*. McGraw Hill, from \cite{Clift1978}, 1957.

C G Golueke, W J Oswald, and H B Gotaas. Anaerobic digestion of algae. *Applied microbiology*, 5(1):47–55, 1957.

C V González-López, F G Acién Fernández, J M Fernández-Sevilla, J F Sánchez Fernández, and E Molina Grima. Development of a process for efficient use of CO 2 from flue gases in the production of photosynthetic microorganisms. *Biotechnology and Bioengineering*, 109(7):1637–1650, 2012.

J R Grace, T Wairegi, and T H Nguyen. Shapes and velocities of single drops and bubbles moving freely through immiscible liquids. *Transactions of the Institute of Chemical Engineers*, 54:167–173, 1976.

R.M. Griffith. Mass transfer from drops and bubbles. *Chemical Engineering Science*, 12:198–213, 1960.

J U Grobbelaar, L Nedbal, L Tichy, and L Setlik. Variation in some photosynthetic characteristics of microalgae cultured in outdoor thin-layered sloping reactors. *Journal of Applied Phycology*, 7(2):175–184, 1995.

J.U Grobbelaar. Algal nutrition. In A. Richmond, editor, *Handbook of Microalgal Culture: Biotechnology and Applied Phycology*, pages 97–115. Blackwell, 2004.

W L Haberman and R K Morton. An Experimental Investigation of the drag and shape of air bubble rising in various liquids. Technical report, US Navy Department, 1953.

E S Hamborg, S R A Kersten, and G F Versteeg. Absorption and desorption mass transfer rates in non-reactive systems. *Chemical Engineering Journal*, 161(1-2):191–195, 2010.

J F Harper, D W Moore, and J R A Pearson. The effect of the variation of surface tension with temperature on the motion of bubbles and drops. *Journal of Fluid Mechanics*, 27(2):361–366, 1967. ISSN 0022-1120. doi: 10.1017/S0022112067000370.

A R Heath, P D Fawell, P A Bahri, and J D Swift. Estimating Average Particle Size by Focused Beam Reflectance Measurement (FBRM). *Particle Particle Systems Characterization*, 19(2):84, 2002.

R. Higbie. The rate of absorption of a pure gas into still liquid during short periods of exposure. *Transactions of the American Institute of Chemical Engineers*, 31(2), 1935.

N H Hoang, D J Euh, B J Yun, and C Song. A new method of relating a chord length distribution to a bubble size distribution for vertical bubbly flows. *International journal of multiphase flow*, 71:23–31, 2015.

G A Hughmark. Holdup and Mass Transfer in Bubble Columns. *Industrial & Engineering Chemistry Process Design and Development*, 6:218–220, 1967a.

GA Hughmark. Mass and Heat Transfer from Rigid Spheres. *AIChE Journal*, 13(6): 1219–1221, 1967b.

M. Ishii and T.C. Chawla. Local drag laws in dispersed two-phase flow. 1979.

I Iwasaki, Q Hu, N Kurano, and S Miyachi. Effect of extremely high-CO_2 stress on energy distribution between photosystem I and photosystem II in a 'high-CO_2' tolerant green alga, Chlorococcum littorale and the intolerant green alga Stichococcus bacillaris. *Journal of Photochemistry and Photobiology B:Biology*, pages 184–190, 1998.

M Jimenez, N Dietrich, J R Grace, and G Hébrard. Oxygen mass transfer and hydrodynamic behaviour in wastewater: Determination of local impact of surfactants by visualization techniques. *Water Research*, 58:111–121, 2014.

H Jin, M Wang, and R A Williams. Analysis of bubble behaviors in bubble columns using electrical resistance tomography. *Chemical Engineering Journal*, 130:179–185, 2007.

A.I. Johnson, F. Besik, and A.E. Hamielec. Mass Transfer from a single rising bubble. *The Canadian Journal of Chemical Engineering*, 47(559 - 564), 1969.

N Kantarci, F Borak, and K O Ulgen. Bubble column reactors. *Process Biochemistry*, 40:2263–2283, 2005.

S Karimipour and T Pugsley. A critical evaluation of literature correlations for predicting bubble size and velocity in gas-solid fluidized beds. *Powder Technology*, 205(1-3):1–14, 2011.

Y Kawase and M Moo-Young. Theoretical prediction of gas hold-up in bubble columns with Newtonian and non-Newtonian fluids. *Industrial & Engineering Chemistry Research*, 26:933–937, 1987.

Y. Kawase, S. Umeno, and T. Kumagai. The prediction of gas hold-up in bubble column reactors: newtonian and non-newtonian fluids. *The Chemical Engineering Journal*, 50:1–7, 1992.

B Ketheesan and N Nirmalakhand an. Development of a new airlift-driven raceway reactor for algal cultivation. *Applied Energy*, 88(10):3370–3376, 2011.

S L Kiambi, A M Duquenne, A Bascoul, and H Delmas. Measurements of local interfacial area: Application of bi-optical fibre technique. *Chemical Engineering Science*, 56: 6447–6453, 2001.

A Koynov and J G Khinast. Mass Transfer and Chemical Reactions in Bubble Swarms with Dynamic Interfaces. *AIChE Journal*, 51(10):2786–2800, 2005.

R Krishna, J W A De Swart, J Ellenberger, G B Martina, and C Maretto. Gas holdup in slurry bubble columns: Effect of column diameter and slurry concentrations. *AIChE Journal*, 43(2):311–316, 1997.

R Krishna, M I Urseanu, J M van Baten, and J Ellenberger. Rise velocity of a swarm of large gas bubbles in liquids. *Chemical Engineering Science*, 54(2):171–183, 1999a.

R Krishna, M I Urseanu, J M Van Baten, and J Ellenberger. Wall effects on the rise of single gas bubbles in liquids. *International Communications in Heat and Mass Transfer*, 26(6):781–790, 1999b. ISSN 07351933. doi: 10.1016/S0735-1933(99)00066-4.

V Kuhnhenn, J Krägel, U Horstmann, and R Miller. Surface shear rheological studies of marine phytoplankton cultures-Nitzschia closterium, Thalassiosira rotula, Thalassiosira punctigera and Phaeocystis sp. *Colloids and surfaces.B, Biointerfaces*, 47(1): 29–35, 2006.

V Kuhnhenn-Dauben, D A Purdie, U Knispel, H Voss, and U Horstmann. Effect of phytoplankton growth on air bubble residence time in seawater. *Journal of Geophysical Research*, 113(C6):1–17, 2008.

A A Kulkarni. Mass Transfer in Bubble Column Reactors: Effect of Bubble Size Distribution. *Industrial & Engineering Chemistry Research*, 46:2205–2211, 2007.

Sailesh B. Kumar, Davood Moslemian, and Milorad P. Duduković. Gas-holdup measurements in bubble columns using computed tomography. *AIChE Journal*, 43 (6):1414–1425, 1997. ISSN 0001-1541. doi: 10.1002/aic.690430605. URL http://doi.wiley.com/10.1002/aic.690430605.

R Lau, W Peng, G Q Yang, and L Fan. Gas - Liquid Mass Transfer in High-Pressure Bubble Columns. *Industrial & Engineering Chemistry Research*, pages 1302–1311, 2004.

A Lecuona, P A Sosa, P A Rodríguez, and R I Zequeira. Volumetric characterization of dispersed two-phase flows by digital image analysis. *Measurement Science and Technology*, 11:1152–1161, 2000.

T G Leighton. *The Acoustic Bubble*. Academic Press, London, 1st edition, 1994.

J.H. Leonard and G Houghton. Mass transfer and velocity of rise phenomena for single bubbles. *Chemical Engineering Science*, 18:133 – 142, 1963.

W. K. Lewis and W. G Whitman. Principles of gas absorption. *Industrial and Engineering Chemistry*, 1924. ISSN 0019-7866. doi: 10.1021/ie50180a002.

W Liu and N N Clark. Relationships between distribution of chord lengths and distributions of bubble sizes including their statistical parameters. *International journal of Multiphase flow*, 21(6):1073–1089, 1995.

A.C. Lochiel and P.H. Calderbank. Mass transfer in the continuous phase around axisymmetric bodies of revolution. *Chemical Engineering Science*, 19:471 – 484, 1964.

J.R. Loudon, P.H. Calderbank, and I. Coward. The influence of insoluble gases on the absorption and desorption rates of freely rising bubbles of soluble gas in liquids. *Chemical Engineering Science*, 21:614–618, 1966.

K Lunde and R J Perkins. Shape Oscillations of Rising Bubbles. *Applied Scientific Research*, 58:387–408, 1998.

S K Majumder, G Kundu, and D Mukherjee. Bubble size distribution and gas-liquid interfacial area in a modified downflow bubble column. *Chemical Engineering Journal*, 122:1–10, 2006.

R Manasseh, A Bui, J Sand ercock, and A Ooi. Sound emission processes on bubble detachment. In *Proc.of 14th Australian Fluid Mech.Conf.*, pages 857–860, Adelaide, 2001.

C C Maneri and P F Vassallo. Dynamics of Bubbles Rising in Finite and Infinite Media. Technical report, American Institute of Chemical Engineers, 2000.

C S Marangoni. Sul principio della viscosita superficiale dei liquidi stabilito dalsig. J. Plateau. *Nuovo Cimento*, Ser. 2(5/6):239–273, 1872.

D Marshall and T E Stanton. On the eddy system in the wake of flat circular plates in three dimensional flow. *Proceedings of the Royal Society*, 130(813):295–301, 1930.

M Martín, F J Montes, and M A Galán. Numerical calculation of shapes and detachment times of bubbles generated from a sieve plate. *Chemical Engineering Science*, 61:363–369, 2006.

M Martín, F J Montes, and M A Galán. Oxygen transfer from growing bubbles: Effect of the physical properties of the liquid. *Chemical Engineering Journal*, 128(1):21–32, 2007.

M Martín, F J Montes, and M A Galán. Mass transfer from oscillating bubbles in bubble column reactors. *Chemical Engineering Journal*, 151(1-3):79–88, 2009.

M Martín, M A Galán, R L Cerro, and F J Montes. Shape oscillating bubbles: hydrodynamics and mass transfer - a review. *Bubble Science, Engineering & Technology*, 3 (2):48–63, 2011.

B.J.H Mathews. *The rate of air-sea CO2 exchange: chemical enhancement and catalysis by marine microalgae*. PhD thesis, University of East Anglia, 1999.

C McGlade and P Ekins. The geographical distribution of fossil fuels unused when limiting global warming to 2 \,ˆ{\circ}C. *Nature*, 517(7533):187–190, 2015.

J L McGrew, T L Rehm, and R G Griskey. The effect of temperature induced surface tension gradients on bubble mechanics. *Applied Scientific Research*, 29(1):195–210, 1974. ISSN 0003-6994. doi: 10.1007/BF00384144. URL http://dx.doi.org/10.1007/BF00384144.

P C Mena. *Mass transfer and hydrodynamics in multiphase systems*. PhD thesis, Faculty of Engineering, University of Porto, 2005.

H D Mendelson. The Prediction of Bubble Terminal Velocities from Wave Theory. *AIChE Journal*, 13(2):250–252, 1967.

J L Mendoza, M R Granados, I de Godos, F G Acién Fernández, E Molina Grima, S Heaven, and C J Banks. Oxygen transfer and evolution in microalgal culture in open raceways. *Bioresource technology*, 137:188–195, 2013.

J J Milledge. Commercial application of microalgae other than as biofuels: a brief review. *Reviews in Environmental Science and Biotechnology*, 2010.

A S Miron, F C Garc\'ia, A C Gomez, E Molina Grima, and Y Chisti. Bubble-Column and Airlift Photobioreactors for Algal Culture. *AIChE Journal*, 46(9), 2000.

Y Mizushima and T Saito. Detection method of a position pierced by a single-tip optical fibre probe in bubble measurement. *Measurement Science and Technology*, 23(8):1–18, 2012.

Y Mizushima, A Sakamoto, and T Saito. Measurement technique of bubble velocity and diameter in a bubble column via single-tip optical-fiber probing with judgment of the pierced position and angle. *Chemical Engineering Science*, 100:98–104, 2013.

E Molina Grima, J Fernández, F G Acién, and Y Chisti. Tubular photobioreactor design for algal cultures. *Journal of biotechnology*, 92(2):113–31, December 2001. ISSN 0168-1656. URL http://www.ncbi.nlm.nih.gov/pubmed/11640983.

E Molina Grima, E H Belarbi, F G Acién Fernández, A Robles Medina, and Y Chisti. Recovery of microalgal biomass and metabolites: Process options and economics. *Biotechnology Advances*, 20(7-8):491–515, 2003.

F J Montes, M A Galan, and R L Cerro. Mass transfer from oscillating bubbles in bioreactors. *Chemical Engineering Science*, 54:3127–3136, 1999.

D W Moore. The velocity of rise of distorted gas bubbles in a liquid of small viscosity. *Journal of Fluid Mechanics*, 23(04):749–766, 1965.

M Motarjemi and G J Jameson. Mass transfer from very small bubbles: the optimum bubble size for aeration. *Chemical Engineering Science*, 33(11):1415–1423, 1978. ISSN 0009-2509. doi: 10.1016/0009-2509(78)85190-2. URL http://www.sciencedirect.com/science/article/pii/0009250978851902.

G Mougin and J Magnaudet. Path Instability of a Rising Bubble. *Physical Review Letters*, 88(1):14502, 2001.

A A Mouza, G K Dalakoglou, and S V Paras. Effect of liquid properties on the performance of bubble column reactors with fine pore spargers. *Chemical Engineering Science*, 60(5):1465–1475, 2005. ISSN 00092509. doi: 10.1016/j.ces.2004.10.013.

F L Muller and J F Davidson. On the effects of surfactants on mass transfer to viscous liquids in bubble columns. *Chemical Engineering Research and Design*, 73:291–296, 1995.

S Nedeltchev, U Jordan, and A Schumpe. Correction of the penetration theory based on mass-transfer data from bubble columns operated in the homogeneous regime under high pressure. *Chemical Engineering Science*, 62(22):6263–6273, 2007.

NREL. Impact of ethanol blending on u.s. gasoline prices, national renewable energy laboratories. Technical report, National Renewable Energy Laboratory, US, 2008.

Met Office. UK Climate. URL http://www.metoffice.gov.uk/.

T Okawa. Temperature effect on single bubble rise characteristics in stagnant distilled water. *International Journal of Heat and Mass Transfer*, 46:903–913, 2003.

R K Pachauri and L A Meyer. Climate Change 2014: Synthesis Report.Contribution of Working Groups I, II and III to the Fifth Assessment Report of the Intergovernmental Panel on Climate Change. Technical report, IPCC, Geneva, Switzerland, 2014.

R H Perry and D W Green. *Perry's Chemical Engineers' Hand book*. McGraw Hill, New York, 8th edition, 2008.

F Peters and C Els. An experimental study on slow and fast bubbles in tap water. *Chemical Engineering Science*, 82:194–199, 2012.

A Prakash, A Margaritis, H Li, and M A Bergougnou. Hydrodynamics and local heat transfer measurements in a bubble column with suspension of yeast. *Biochemical Engineering Journal*, 9:155–163, 2001.

R Putt, M Singh, S Chinnasamy, and K C Das. An efficient system for carbonation of high-rate algae pond water to enhance CO_2 mass transfer. *Bioresource Technology*, 102(3):3240–3245, 2011.

J J Quinn, M Maldonado, C O Gomez, and J A Finch. Experimental study on the shape – velocity relationship of an ellipsoidal bubble in inorganic salt solutions. *Minerals Engineering*, 55:5–10, 2014.

J A Ramirez and R H Davis. Mass transfer to a surfactant covered bubble or drop. *AIChE journal*, 45(6):1355–1358, 1999.

A Richmond, S Boussiba, A Vonshak, and R Kopel. A new tubular reactor for mass production of microalgae outdoors. *Journal of Applied Phycology*, 5(3):327–332, 1993.

D. Rosso. *Mass Transfer at Contaminated Bubble Interfaces*. PhD thesis, 2005.

D Rosso, D L Huo, and M K Stenstrom. Effects of interfacial surfactant contamination on bubble gas transfer. *Chemical Engineering Science*, 2006.

M Rüdisüli, T J Schildhauer, S M A Biollaz, and J R Van Ommen. Monte Carlo simulation of the bubble size distribution in a fluidized bed with intrusive probes. *International Journal of Multiphase Flow*, 44:1–14, 2012.

A Saboni, S Alexand rova, M Karsheva, and C Gourdon. Modeling and simulation of the polymeric nanocapsule formation process. *AIChE Journal*, 57(7):405–410, 2011.

S S Sadhal and R E Johnson. Stokes flow past bubbles and drops partially coated with thin films.Part 2.Thin films with internal circulation – a perturbation solution. *Journal of Fluid Mechanics*, 126:237–250, 1983.

P G Saffman. On the rise of small air bubbles in water. *Journal of Fluid Mechanics*, 1: 249–275, 1956.

T Saito, K Matsuda, Y Ozawa, S Oishi, and S Aoshima. Measurement of tiny droplets using a newly developed optical fibre probe micro-fabricated by a femtosecond pulse laser. *Measurement Science and Technology*, 20(11):1–12, 2009.

N Sakai, Y Sakamoto, N Kishimoto, N Chihara, and I Karube. Chlorella strains from hot springs tolerant to high temperature and high CO_2. *Energy Conversion Management*, 36(6):693–696, 1995.

A Sakamoto and T Saito. Computational analysis of responses of a wedge-shaped-tip optical fiber probe in bubble measurement. *The Review of scientific instruments*, 83 (7):75107, 2012.

A Sam, C O Gomez, and J A Finch. Axial velocity profiles of single bubbles in water/ frother solutions. *International journal of mineral processing*, 47:177–196, 1996.

D L Sanchez, J H Nelson, J Johnston, A Mileva, and D M Kammen. Biomass enables the transition to a carbon-negative power system across western North America. *Nature Climate Change*, pages 1–5, 2015.

Saskpower. Saskpower, 2015. URL http://www.saskpowerccs.com/ccs-projects/boundary-dam-carbon-capture-project/.

P Savic. Circulation and distortion of liquid drops falling through a viscous medium, 1953.

G. Schulze and E.U Schlünder. Physical absorption of single gas bubbles in degassed and preloaded water. *Chemical Engineering and Processing: Process Intensification*, 1985a. ISSN 02552701. doi: 10.1016/0255-2701(85)80002-7.

G. Schulze and E.U Schlünder. The effect of multicomponent diffusion on the mass transfer during absorption of single gas bubbles. *Chemical Engineering and Processing: Process Intensification*, 1985b. ISSN 02552701. doi: 10.1016/0255-2701(85)80018-0.

C D Serdula and M R Loewen. Experiments investigating the use of fiber-optic probes for measuring bubble-size distributions. *Oceanic Engineering, IEEE Journal of*, 23 (4):385–399, 1998.

Y.T Shah, B.G Kelkar, S.P Godbole, and W.D Deckwer. Design Parameters Estimations for Bubble Column Reactors. *AIChE Journal*, 28(3):353 – 375, 1982.

J Sheehan, T Dunahay, J Benemann, and P Roessler. A Look Back at the US Department of Energy's Aquatic Species Program: Biodiesel from Algae. Technical report, National Renewable Energy Laboratory, 1998.

L Shen, X Song, M Iguchi, and F Yamamoto. A method for recognizing particles in overlapped particle images. *Pattern Recognition Letters*, 21(1):21–30, 2000.

T.K Sherwood, R.L Pigford, and C.R Wilke. *Mass Transfer*. McGraw Hill, New York, 1975.

Solazyme. Solazyme Fuels, 2013. URL http://solazyme.com/fuels.

P Spolaore, C Joannis-Cassan, E Duran, and A Isambert. Commercial applications of microalgae. *Journal of bioscience and bioengineering*, 101(2):87–96, 2006.

M Stohr, J Schanze, and A Khalili. Visualization of gas–liquid mass transfer and wake structure of rising bubbles using pH-sensitive PLIF. *Experiments in Fluids*, 2009.

Ordnance Survey. Terrain Data. URL https://www.ordnancesurvey.co.uk/opendatadownload/products.html.

Y Tagawa, S Takagi, and Y Matsumoto. Surfactant effect on path instability of a rising bubble. *Journal of Fluid Mechanics*, 738:124–142, 2013.

F Takemura and A Yabe. Gas dissolution process of spherical rising gas bubbles. *Chemical Engineering Science*, 53(15), 1998.

G Taubin, F Cukierman, S Sullivan, J Ponce, and D J Kriegman. Parametrizing and fitting bounded algebraic curves and surfaces. *Proceedings 1992 IEEE Computer Society Conference on Computer Vision and Pattern Recognition*, pages 3–8, 1992.

T D Taylor and A Acrivos. On the deformation and drag of a falling viscous drop at low Reynolds number. *Journal of Fluid Mechanics*, 18(3):466–476, 1964.

M Tokumura, M Baba, and Y Kawase. Dynamic modeling and simulation of absorption of carbon dioxide into seawater. *Chemical Engineering Science*, 62(24):7305–7311, 2007.

A Tomiyama, I Kataoka, I Zun, and T Sakaguchi. Drag Coefficients of Single bubbles under Normal and Micro Gravity Conditions. *The Japan Society of Mechanical Engineers International Journal*, 41(2):472–479, 1998.

A Tomiyama, G P Celata, S Hosokawa, and S Yoshida. Terminal velocity of single bubbles in surface tension force dominant regime. *International Journal of Multiphase Flow*, 28(9):1497–1519, 2002.

UN. Millennium Development Goals, 2015. URL http://www.un.org/millenniumgoals/.

J M T Vasconcelos, S P Orvalho, and S S Alves. Gas-Liquid Mass Transfer to Single Bubbles: Effect of Surface Contamination. *AIChE journal*, 48(6):1145–1154, 2002.

J M T Vasconcelos, J M L Rodrigues, S C P Orvalho, S S Alves, R L Mendes, and A Reis. Effect of contaminants on mass transfer coefficients in bubble column and airlift contactors. *Chemical Engineering Science*, 58(8):1431–1440, 2003.

P T Vasudevan and M Briggs. Biodiesel production–current state of the art and challenges. *Journal of industrial microbiology & biotechnology*, 35(5):421–430, 2008.

J Vejrazka, M Vercer, S Orvalho, P Sechet, M C Ruzicka, and A Cartellier. International Journal of Multiphase Flow Measurement accuracy of a mono-fiber optical probe in a bubbly flow. *International Journal of Multiphase Flow*, 36:533–548, 2010.

C Veldhuis, A Biesheuvel, and L van Wijngaarden. Shape oscillations on bubbles rising in clean and in tap water. *Physics of Fluids*, 20(4):1–12, 2008.

G B Wallis. The terminal speed of single drops or bubbles in an infinite medium. *International Journal of Multiphase Flow*, 1:491–511, 1974.

J C Weissman and R.P. Goebel. Production of Liquid Fuels and Chemicals by Microalgae. Technical Report March, U.S. Department of Energy, 1985.

J C Weissman, D M Tillet, and R P Goebel. Design and Operation of an Outdoor Microalgae Test Facility, 1989.

J.C. Weissman and R.P Goebel. Design and Analysis of Microalgal Open Pond Systems for the Purpose of Producing Fuels. Technical report, U.S. Department of Energy, Golden, Colorado, U.S., 1987.

L.Y. Wellek, A.K. Agrawal, and A.H.P. Skelland. Shape of liquid drops moving in liquid media. *AIChE Journal*, 12:854 – 862, 1966.

W G Whitman. The two-film theory of gas absorption. *Chemical and Metallurgical Engineering*, 29(4):146–148, 1923.

M Wu and M Gharib. Experimental studies on the shape and path of small air bubbles rising in clean water. *Physics of Fluids*, 14(7):49–52, 2002.

Y Xie and Q Ji. A new efficient ellipse detection method. In *Proceedings on Pattern Recognition, 16th International Conference, IEEE*, volume 2, pages 0–3, 2002.

W Zhang, X Jiang, and Y Liu. A method for recognizing overlapping elliptical bubbles in bubble image. *Pattern Recognition Letters*, 33(12):1543–1548, 2012.

W B Zimmerman, M Zandi, H C H Bandulasena, V Tesa\v r, D J Gilmour, and K Ying. Design of an airlift loop bioreactor and pilot scales studies with fluidic oscillator induced microbubbles for growth of a microalgae Dunaliella salina. *Applied Energy*, 88 (10):3357–3369, 2011.